Perturbative perspectives on the Phase diagram of Quantum ChromoDynamics

Jan Maelger

université PARIS-SACLAY

université PARIS DIDEROT PARIS 7

ÉCOLE POLYTECHNIQUE UNIVERSITÉ PARIS-SACLAY

NNT : 2019SACLX050

Thèse de doctorat

Perturbative perspectives on the Phase diagram of Quantum ChromoDynamics

Thèse de doctorat de l'Université Paris-Saclay
préparée à Ecole Polytechnique

Ecole doctorale n°576 particules hadrons énergie et noyau : instrumentation, image, cosmos et simulation (Pheniics)
Spécialité de doctorat : physique des particules

Thèse présentée et soutenue à Palaiseau, le 10 Octobre, 2019, par

JAN MAELGER

Composition du Jury :

Christoph KOPPER Professeur, Ecole Polytechnique (CPHT)	Président
David H. DUDAL Professeur, KU Leuven (Kulak K. Campus)	Rapporteur
Jan M. PAWLOWSKI Professeur, Ruprecht-Karls-Univ. Heidelberg (ITP)	Rapporteur
Marcela PELÁEZ Professeur, Univ. de la República, Montevideo	Examinateur
Urko REINOSA Chargé de Recherche au CNRS, Ecole Polytechnique (CPHT)	Directeur de thèse
Julien SERREAU Maître de Conférences, Univ. Paris Diderot (APC)	Co-directeur de thèse

To doubt everything, or, to believe everything, are two equally convenient solutions; both dispense with the necessity of reflection.

Henri Poincaré

Life is really simple, but we insist on making it complicated.

Confucius

Acknowledgements

The undertaking of a PhD thesis is a multi-layered labyrinth, the navigation of which is threefold challenging: academic, administrative and social. Without considerable support in all of these categories, any prospective candidate is doomed to fail, and I owe an immense amount of gratitude to a wealth of people for guiding me through this particular process. These few words can barely reflect the investment I have received on their behalf and merely serve as a small symbolic token of my appreciation.

At the core, and thus meriting to be listed first, are my supervisors Urko Reinosa and Julien Serreau, both of whom I want to thank for their countless support related to this work and beyond. Starting from the rather unusual way I came into the PhD position not having passed through one of the infamous M2 internships, they have taken a chance on me and from the beginning nurtured me academically in a very caring environment. In this respect, the tutoring they have passed on to me is by all means far beyond average, with them being available for patient discussion at virtually all times. They have truly mastered handling the racor sharp edge of on the one hand pushing and guiding a PhD student to fruitful analyses while on the other hand creating an atmosphere, in which any student is permitted sufficient liberty of pursuing and developing their own lines of thought. All results presented in this manuscript have been obtained in collaboration with both Urko and Julien.
In the immediate surroundings of the supervisors are the remaining collaborators of the Curci-Ferrari model, notably M. Peláez, M. Tissier and N. Wschebor. Exceptionlessly, they too have gone above and beyond to properly integrate myself into the team forces and their treatments were coined by an unquestionable spirit of collegiality, respect and support.

Throughout all of the PhD, I have enjoyed a joint affiliation between CPHT at Ecole Polytechnique and APC at Univ. Paris Diderot. Despite spending only half my time in either lab, I have always felt as a full member of both, in all its associated facets. The members of each group have certainly facilitated such a welcoming and inclusive work environment, from the researchers over the administrative staffs to the IT support teams. I want to thank all members, who I have had the pleasure of crossing paths with in the past three years for their helpfulness and consideration.

An integrable part of any student's journey to doctorship is founded in the interaction with fellow students. I must say that I have been extraordinarily fortunate in encountering a vast amount of tenderhearted (next to) office mates and most have long surpassed the threshold from temporary companions to dear friends. Thank you all for the entertaining and enjoyable time.

Outside my home universities, I have met many interesting people in various conferences, workshops and doctoral schools, which are the occasions at which one truly appreciates the the full depth of the scientific drive, expressed through an international togetherness and an almost child-like open-mindedness towards others and new ideas. I want to cordially extend my thankfulness to all participants and especially organizers at such events for enabling a well-balanced enriching experience throughout the PhD.

In similar fashion, I also want to express my explicit gratitude towards the Ecole Doctorale Pheniics, who have not only provided a steady source of income, but also supported students in several directions, most notably administratively and via the organization of cross-topic and networking events.

Last but not least, I am extremely grateful to all the distinguished members of my PhD committee, who honor me with their presence. A further explicitation also goes to the referees of the manuscrpit for the undertaking the exhaustive task and for providing feedback, guidance and helping in the final stages of the write-up.

My final special mention belongs to my family and friends, who have ever since supported me throughout all endeavors, during and prior to the thesis, and without their willingness to cope with my numerous idiosyncrasies, I most definitely would not have come even half as far. With all that I am, I love you.

List of Publications

- Maelger J., Reinosa U., Serreau J.
  Perturbative study of the QCD phase diagram for heavy quarks at nonzero chemical potential: Two-loop corrections
  Phys.Rev. D97 (2018) no.7, 074027

- Maelger J., Reinosa U., Serreau J.
  Universal aspects of the phase diagram of QCD with heavy quarks
  Phys.Rev. D98 (2018) no.9, 094020

- Maelger J., Reinosa U., Serreau J.
  Rainbows in the QCD Phase Diagram
  arXiv:1903.04184

- Maelger J., Reinosa U., Serreau J.
  Rainbows with non-trivial Background
  In preparation

- Maelger J.
  Introduction to the Curci-Ferrari Model : Results and Open Questions
  JRJC 2018 Proceedings

List of Presentations

- *2+1 Heavy Quark QCD Phase Transition in Massive Landau-DeWitt Gauge*, Pheniics Fest, LAL, Orsay - 30/31 May 17 - Poster
- *2+1 Heavy Quark QCD Phase Transitions in Massive Landau-DeWitt Gauge*, Journée des doctorants, APC, Univ Paris Diderot - 15 November 17
- *Phase Transitions in Quantum Chromodynamics*, PhD Day, CPHT, Ecole Polytechnique - 6 February 18
- *Heavy quark QCD phase diagram at two-loop order in perturbation theory*, From correlation functions to QCD phenomenology, Heraeus-Seminar, Bad Honnef - 4 April 18
- *Heavy quark phase diagram at two-loop order in perturbation theory*, Rencontre de Physique des Particules, Paris - 11 April 18
- *On the QCD Phase Diagram with Heavy Quarks*, QCD under extreme conditions, ECT*, Trento - 4 June 18
- *QCD phase diagram with heavy quarks: Universal aspects in one-loop models and extension to 2-loop in Curci-Ferrari*, Strong and Electroweak Matter, Barcelona - 29 June 18
- *Generic features of the heavy quark QCD phase diagram in one-loop models and 2-loop Curci-Ferrari*, Cold Quantum Coffee, Heidelberg - 3 July 18
- *Introduction à Curci-Ferrari : Résultats et questions ouvertes*, Journées de Rencontres des Jeunes Chercheurs, Lège-Cap-Ferret - 18 October 18
- *QCD from Perturbation Theory: Curci-Ferrari & Gribov-Zwanziger*, PhD Day, CPHT, Ecole Polytechnique - 15 November 18
- *QCD from Perturbation Theory: Curci-Ferrari & Gribov-Zwanziger*, Journée des doctorants, APC, Univ Paris Diderot - 16 November 18
- *Towards the QCD Phase Diagram from the Curci-Ferrari Model*, GDR QCD, Ecole Polytechnique - 28 November 18
- *On the QCD phase diagram with light quarks from the Curci-Ferrari Model*, Rencontre de Physique des Particules, Clermont-Ferrand - 25 January 19
- *Update on the recent research on the chiral transition from the Curci-Ferrari Model*, shared student seminar, APC Theory Group, Paris - 2 April 19

Abstract

Unravelling the structure of the QCD phase diagram and its many aspects such as (de)confinement and chiral symmetry breaking, is one of the big challenges of modern theoretical physics, and many approaches have been devised to this aim. Since perturbation theory is believed to cease feasibility at low energy scales, these approaches treat the relevant order parameters, the quark condensate and the Polyakov loop, non-perturbatively. However, it is also well-established that the starting point for perturbation theory, the Faddeev-Popov gauge-fixing procedure, is inherently ill-defined in the infrared due to the presence of Gribov copies. In this context, a modified perturbative approach based on the Curci-Ferrari Lagrangian has been introduced, where a phenomenologically motivated effective gluon mass term is added to the Landau gauge-fixed action. Prior to the beginning of the thesis, this approach had proven extremely fruitful in its descriptions of (unquenched) Yang-Mills correlation functions and thermodynamics at (non)zero temperature and density.

Throughout the thesis, we extend this analysis to the entire phase structure of QCD and QCD-like theories and test the validity of the model in various regimes of interest. For instance, to further a previous one-loop study in the regime of heavy quark masses, we compute the two-loop quark sunset diagram in the presence of a non-trivial gluon background in a finite temperature and density setting. We come to the conclusion that the physics underlying center symmetry is well-described by our perturbative model with a seemingly robust weak-coupling expansion scheme. Furthermore, we study the regime of light quarks by means of a recently proposed resummation scheme which exploits the presence of actual small parameters in the Curci-Ferrari description of infrared QCD. In the quark sector, this leads to the renown rainbow equations. We extend this first-principle setup to nonzero temperature, chemical potential, and gluon background. We perform a first qualitative analysis of the prediction of the model concerning the possible existence of a critical endpoint in the QCD phase diagram by using a simplified version of these general equations. Our results nicely fit in the the vast array of values present in the literature.

Résumé

La Chromodynamique Quantique est une théorie quantique de champs (QCD) qui décrit l'interaction forte du Modèle Standard de la Physique des Particules. Ses particules fondamentales sont les six quarks (up, down, strange, charm, bottom, top) et les gluons. La QCD est également une théorie de jauge de type non-abelienne, basée sur le groupe SU(3). Les quarks forment le secteur massif de la théorie et ils possèdent un spin de 1/2. Les gluons, en revanche, sont sans masse et étant les particules de jauge ils transmittent la force forte. Les gluons sont caractérisés par un spin de 0. Les quarks sont des fermions et les gluons des bosons, et ils obéissent chacun aux propriétés statistiques associées. Une composante essentielle de la QCD est le concept de charge de couleur qui fait distinguer la QCD de l'Electrodynamique Quantique (QED) et qui permet aux gluons d'auto-interagir. C'est grâce à cette auto-interaction que la QCD a une structure complexe et intéressante. Une propriété célèbre est le Confinement, qui fait qu'à basse énergie les quarks n'apparaissent jamais comme des particules libres, mais sont toujours groupés dans des états singuliers en couleur, appelés hadrons. En augmentant les énergies, on observe la formation du Quark-Gluon Plasma, dans lequel les particules colorées existent comme constituants libres. A température et densité finies, on obtient un diagramme des phases de la QCD riche et intéressant.
L'étude de ce diagramme des phases de la Chromodynamique Quantique (QCD) et des transitions associées, y compris le déconfinement et restauration de la symétrie chirale, représente des défis majeurs pour la physique moderne et nombreuses sont les approches théoriques qui visent à en sonder les multiples facettes. Du fait de l'intensité de l'interaction forte dans les régimes d'énergie pertinents pour les transitions susmentionnées, ces approches sont en général de nature non-perturbative, la théorie des perturbations étant réputée inapplicable à ces échelles.
Il est, cependant, bien établi que le point de départ de la théorie usuelle des perturbations, basée sur la procédure de fixation de jauge de Faddeev-Popov, est ambigu à ces basses échelles (ambiguïté de Gribov basée sur l'existence des copies). Dans ce contexte, une approche perturbative modifiée, basée sur le Lagrangien de Curci et Ferrari, a été proposée, via l'ajout phénoménologique d'un terme de masse effectif pour le gluon en jauge de Landau. Par construction, cette approche capture bien le comportement de découplage dans le secteur gluonique, qui est vu et établi par des nombreuses simulations de QCD sur réseau. Le modèle a été testé avec succès, notamment dans sa capacité à reproduire les fonctions de corrélation de la théorie Yang-Mills (et de la QCD dans la limite de quarks lourds autour du point Yang-Mills) et de la thermodynamique à température et potentiel chimique non nuls.
Dans cette thèse, nous avons testé la robustesse de ces résultats en évaluant la structure de phase de la QCD avec des quarks lourds au deuxième ordre de la théorie des perturbations dans le modèle de Curci-Ferrari et en comparant nos résultats à ceux d'approches non-perturbatives. Nos résultats indiquent que, dans ce régime de quarks lourds, le diagramme de phases est contrôlé perturbativement.
Nous avons également étendu notre étude au cas de la QCD avec des quarks légers en utilisant un schéma de resommation qui exploite la présence de petits paramètres (notament la valeur du couplage en secteur purement gluonique et l'inverse du nombre de couleurs) dans le régime infrarouge de la QCD. Dans le secteur des quarks, cette démarche donne lieu à la resommation des fameux diagrammes dits "arc-en-ciel". Ici, nous généralisons ce formalisme à température et densité non nulles et en présence d'un champ de fond gluonique. Nous réalisons une toute première étude qualitative des prédictions du modèle Curci-Ferrari concernant l'existence possible d'un point critique dans le diagramme de phases de QCD sur la base d'une version simplifiée des équations générales ainsi obtenues. Nos résultats sont en bon accord qualitatif avec ceux des nombreuses approches existantes.

Table of Contents

Part I

General considerations

1 Introduction

The theory of Quantum Chromodynamics (QCD) is the part of the Standard Model which describes the strong interactions. The fundamental particles of QCD are the six quarks, up, down, strange, charm, bottom and top, the respective anti-quarks, as well as the gluon, which is its mediating, force-carrying particle. Aside from spin 1/2 for the quarks and spin 1 for the gluons, each of the QCD particles exhibits a non-trivial color charge labelled by either red, green or blue. In field theory language, QCD is a non-abelian gauge theory with gauge group SU(3), and the possible interaction vertices, three-gluon, four-gluon and quark-gluon, come with a proportionality factor which we call the coupling constant, g, g^2 or g respectively. It is important to note that the value of this coupling constant depends on the energy scale E of the interaction, $g(E)$.

One of the most celebrated properties of QCD is asymptotic freedom [1, 2], which means that for very large energy values, calculations are generally well-controlled perturbatively in a weak coupling expansion, if one accounts for non-converging asymptotic series and potentially necessary resummations. Whenever applicable, perturbation theory is extremely powerful and usually a theoretical physicist's first line of attack. So too in the realm of high energy QCD, for instance in studying collider phenomenology, heavy-ion collisions or the evolution of (generalized) distribution functions with the momentum scale. Moreover, for sufficiently large energy density values, one expects the fundamental particles of QCD to coexist almost freely as non-trivial color charges in a phase characterized by a bath of weakly coupled constituents, labelled the Quark-Gluon-Plasma (QGP).

In contrast, in the standard picture of infrared (IR) QCD, upon sufficiently lowering the energy scale towards hadronic scales, perturbation theory in form of a weak coupling expansion formally breaks down, which is regarded as the onset of non-perturbative QCD. Eventually, one encounters the infamous Landau pole, which marks the location (Λ_{QCD}) on the energy axis at which the coupling diverges. Λ_{QCD} is scheme-dependent, but typically lies around a value of 300 MeV [3, 4, 5, 6].

In order to gain insight into the underlying dynamics in the IR, one resorts to non-perturbative methods, which have been developed in the last four decades to a high degree of sophistication. These comprise, but are not limited to, Lattice QCD [7, 8, 9, 10, 11, 12], analytic approaches, such as Dyson-Schwinger Equations (DSE) [13, 14, 15, 16, 17, 18] and the Functional Renormalization Group (FRG) [19, 20, 21, 22, 23, 24, 25, 26, 27].

Experimentally, for high energies, there has been some recent progress in the creation of the QGP in the laboratory [28, 29]. On the other hand, in the low energy regime, one observes that quarks[1] are confined into color-singlet bound states. This fundamental property of Nature is known as confinement. This strongly-interacting hadronic matter is expected to exhibit a rich phase structure under extreme conditions of sufficiently large energy, baryonic densities or magnetic fields *etc.* Understanding its thermodynamic properties is the goal of many heavy-ion collision experiments at RHIC, CERN, FAIR, NICA and J-PARC [30, 31, 32, 33, 34, 35, 36] and has vast implications on other fields of physics, *e.g.* early universe cosmology and astrophysics [37, 38, 39].

Confinement in QCD has only ever been demonstrated on the lattice, and whether or not it is permitted from first-principle continuum methods remains to present one of the most studied open questions in physics. Difficulties in this search arise from various directions (to be discussed below), but already begin with the identification of an appropriate order parameter for the transition between the

[1] With the exception of the top quark, which is too heavy to hadronize.

QGP and the confined phase. The most prominent candidate is the Wilson loop, which, in practice, bears the obstacle of being incredibly hard to compute analytically. Therefore, many viable replacement candidates have been proposed, most notably the Polyakov and 't Hooft loops as well as the study of correlation functions [40, 41, 42, 43, 44, 45, 46, 47, 48, 49].

While confinement largely remains unsolved analytically, it is well-established that QCD allows for two crossovers, one associated to chiral symmetry restoration and one to center symmetry breaking, which is related to deconfinement [48, 50, 51, 52]. To firmly uncover the associated phase diagram of QCD at nonzero temperature T and baryonic chemical potential μ_B is a substantial undertaking of theoretical research [53, 54, 55, 56]. A major open question in this respect is the possible existence of a critical endpoint (CEP) in the (T, μ_B) plane, which terminates a first order line starting off on the μ_B-axis, as well as studying its signatures [16, 57, 58, 59, 60, 61, 62, 63, 64, 65, 66, 67, 68]. A large ensemble of theoretical frameworks have been developed to explore the phase structure of this QCD matter in thermodynamic equilibrium, from lattice Monte Carlo simulations [69, 70, 71, 72, 73] to numerous continuum approaches either in QCD [74, 75, 76, 77, 78, 79, 80, 81, 82] or based on low-energy effective models [83, 84, 85, 86, 87, 88]. The former entail the advantage of describing the full and exact non-perturbative dynamics of the theory, and upon taking the continuum limit, its results basically only succumb to statistical errors. On the other hand, lattice studies are (so far) restricted to not too large baryonic chemical potential μ_B since standard Monte Carlo importance sampling algorithms are severely plagued by the infamous sign problem at nonzero μ_B [64, 89]. Attempts to circumvent the sign problem on the lattice have been devised but remain to present limited to a density regime of $\mu_B/T \lesssim 1$, in which no CEP has been observed [54, 60, 90, 91, 92, 93, 94, 95, 96]. Contrarily, the strong sign problem of the lattice is most easily avoided in continuum approaches, where one gains direct access to averaged quantities, such as correlation functions, with the caveat (to be discussed later) that physical solutions correspond to saddle points of the relevant potential instead of minima. However, the price to pay is that analytic approaches necessarily rely on approximation schemes or model building that must be tested in reliable situations, *e.g.*, in situations where guidance from lattice QCD exists. Moreover, these continuum approaches face the supplementary challenge of capturing the relevant degrees of freedom, which in the IR are not only quarks and gluons but also bound states [97, 98]. In this context, we remark that an enticing proposal has been to equip lattice findings for the quenched gauge dynamics with explicit quark contributions in the form of (approximate) nonperturbative functional methods [76, 99, 100, 101, 102]. Existing studies account for mesonic degrees of freedom (in some cases baryons have been included [102]) and consent on a CEP with relatively large density $\mu_B/T \gtrsim 3$. A complementary line of attack relies on phenomenological, Nambu-Jona-Lasinio (NJL) or Quark-Meson models (QM) which inherit various degrees of sophistication: For instance accounting for beyond-mean-field mesonic fluctuations or linking to various aspects of the glue dynamics via a non-trivial dependence on the Polyakov loop, *etc* [58, 103, 104, 105, 106]. These model-based studies typically predict a CEP located at comparatively larger values of μ_B/T. However, the precise values differ significantly from one study to another. Due to the underlying nonperturbative character of the problem in question, the approximations employed in approaches of this type commonly lack a systematic ordering principle. In fact, it is not uncommon to explore the entire phase space on the grounds of truncations which are adjusted against lattice benchmarks at $\mu_B = 0$, *i.e.*, far from the location where a critical point is found.

A further insightful research thread is the exploration of QCD–like theories by means of altering the values of certain parameters, such as the number of colors (N_c) and flavors (N_f) as well as the quark masses (M_f), *etc*. An investigation of the phase structure in such an extended parameter space is twofold merited. On the one hand, it is interesting in its own right and provides a rich theoretical playground. On the other hand, any gained understanding has the potential to enrich our knowledge of the phase diagram of the physical theory itself. A notorious example is given by the Columbia Plot, which broadcasts the phase structure of color SU(3) in dependence of the isospin symmetric degenerate up and down quark mass, $M_u = M_d$, as well as the strange quark mass, M_s [90, 106, 107, 108, 109, 110].

For physical quark masses and in case of zero chemical potential, first principle lattice simulations unambiguously demonstrate a smooth crossover from a mostly confined to a mostly deconfined phase, accompanied by a restoration of chiral symmetry [52, 72, 111]. The corresponding crossover temperatures, defined as the point of steepest as-/descent of the associated order parameters, are observed to be similar, from which one expects a non-trivial interplay between the two transitions [52, 69]. The deconfinement crossover sharpens for increasing quark masses towards second order at a critical mass value, above which the transition is of first order. An opposite pattern is supposed to happen with the chiral transition in the scenario of decreasing quark masses: the chiral transition becomes of first order below a critical value of the quark masses [107]. Although this first order nature is not firmly established yet [64, 65, 112], it

is the expected behavior of a theory with at least three light quark flavors. In contrast, the intrinsics of a theory with two light quarks are more subtle due to the interplay of the axial anomaly [107].

While physical observables are inherently gauge invariant quantities, their explicit computation in continuum approaches typically requires specifying a particular choice of gauge. In principle, the same calculation of any observable should be performed in several gauge choices to verify the result's invariance. The pathway to implementing a chosen gauge configuration is via gauge fixing, most prominently the Faddeev-Popov (FP) procedure. The various gauge choices can be classified, where each class inherits its own strengths and shortcomings. Notorious examples are axial or covariant gauges, such as the Landau or Feynman gauge. Axial gauges typically lead to tremendously difficult gluon propagators and a formulation without manifest Lorentz covariance. Therefore, covariant gauges are the more popular and more natural choices. However, it has long been proven that the starting point for perturbation theory for covariant gauges, the FP procedure, while well-defined in the ultraviolet (UV), becomes increasingly invalid in the IR due to non-complete gauge fixing and the presence of so-called Gribov copies [113, 114, 115, 116, 117, 118]. The latter are the multiple intersections of the submanifold induced by the gauge fixing condition with individual gauge orbits, and the infinite number of copies renders the usual calculation of correlation functions via generating functionals and path integrals ill-defined [119]. Thus, alternative IR QCD approaches have been pursued, in which one tries to control the Gribov ambiguity by one of three main strategies.[2] Either by restricting the space of gauge configurations to be integrated over in the generating functional to a less problematic subregion, leading to the well-known (refined) Gribov-Zwanziger action (GZ) [120, 121, 122, 123, 124, 125]. Or by averaging over Gribov copies yielding a one-parameter class of non-linear covariant gauges and a local and renormalizable action [126, 127, 128]. Or, finally, by phenomenologically accounting for the IR effects of the Gribov copies in the form of an effective gluon mass term, leading to the Curci-Ferrari (CF) model [129, 130, 131]. In all scenarios, one modifies the FP (Landau) gauge-fixed action and proceeds to a perturbative analysis of the theory at hand. Historically the most studied case in the literature is the Landau gauge which thus enables many comparisons with existing findings of non-perturbative methods. It is important to note that in this context, the gluon mass term is an effective operator, and the CF model is seen as an effective model for an underlying (unknown) theory in which one fully controls the Gribov ambiguity. However, this underlying theory must satisfy certain properties induceable from the nature of the Gribov copies themselves, and we can ensure that the deformation operator, in this case the gluon mass term, aligns with these underlying features. In particular, the Gribov copies yield a (soft) breaking of BRST invariance and they are a mere IR effect which leaves the UV intact. As can easily be checked, a gluon mass term corresponds to the simplest deformation of the FP Lagrangian in agreement with these properties [129, 130, 131].

Despite its (explicit but soft) breaking of BRST symmetry, the CF model is still perturbatively renormalizable and its perturbative expansion is controlled down to the deep IR: The non-zero gluon mass leads to a screening effect of the standard perturbative Landau pole and additionally, the (running) gauge coupling persists at a moderate value at all momentum scales [126, 130, 132], as observed in lattice simulations [133, 134].

Furthermore, the principal motivation of the gluon mass term in the CF model comes from the decoupling behavior of the gluon propagator, as observed in Landau gauge-fixed lattice simulations, present both in Yang-Mills (YM) as well as unquenched QCD, both in the vacuum [133, 134, 135, 136, 137, 138, 139, 140, 141, 142, 143] and at finite temperature [144, 145, 146, 147, 148]. A large panel of continuum studies have confirmed this picture [118, 149, 150, 151, 152, 153, 154, 155, 156, 157, 158, 159]. This serves as a further indication of the difficulties of standard FP theory to describe IR QCD, and the fact that the gluon propagator attains a finite value at vanishing momentum essentially introduces an effective mass term.

A series of recent papers has investigated the predictions made by a perturbative analysis within the CF model for the ghost, gluon, and quark two- and three-point functions at one-loop level. Overall, one finds an impressive agreement with corresponding lattice data, given the simplicity of the computaions involved [130, 131, 160, 161, 162, 163]. More recently, the calculation of the pure gauge gluon and ghost propagators has been extended to two-loop level [164]. Beyond its theoretical justification and motivation, this supports the CF model as a valid effective theory able to perturbatively capture some essential dynamics underlying IR (Landau-gauge) QCD.

At finite temperature, it is well-understood that Landau gauge formulae have to be enhanced by a

[2] On a lattice, one picks one copy by hand for each gauge configuration, leading, for instance, to the so-called minimal Landau gauge. Of course, on a lattice, gauge-fixing is not necessary, but possible and sometimes performed to better compare with and guide continuun approaches.

non-trivial gluon background related to the Polyakov loops, elevating the analysis to so-called Landau-DeWitt gauge (LdW) [74]. In this respect, the perturbative approach of the CF model is characterized by a substantial efficiency in grasping known aspects of the QCD phase diagram with heavy quarks at nonzero temperature and chemical potential. For instance, a simple one-loop calculation correctly encodes the order of the (de)confinement transition in pure YM theories [165]. The respective two-loop corrections were computed in Ref. [166, 167] and shown to lead to a quantitative improvement as compared to the one-loop results. This is true not only for the numerical value of the transition temperature, but also for curing some (but not all) of the unphysical features of thermodynamical observables encountered at the one-loop level. Furthermore, an unquenched scenario of heavy dynamical quarks has been discussed in Ref. [168], in which similarly a simple one-loop calculation reproduces the rich phase structure and produces numbers for the critical line within the Columbia plot in quantitative agreement with lattice data.

Comparatively, the thermal phase structure of the light quark sector is more intricate. This is due to the fact that unlike the pure gauge couplings, the quark-gluon coupling becomes significant in the IR [169]. Here, it was previously shown that the CF model allows for a systematic expansion scheme in terms of small parameters given by $1/N_c$ as well as the pure gauge couplings, while simultaneously resumming over the non-perturbative quark-gluon one. For the quark propagator, at leading order, this amounts to eliminating all diagrams except the infinite series resummed by the well-known rainbow equation [170]. Its predictions for the QCD vacuum have been demonstrated to be in qualitative and quantitative agreement with dynamical chiral symmetry breaking.
In this thesis, we set out to study the entire range of the Columbia plot from the CF model and explore its predictions for the resulting phase structure. In particular, we extend the analysis in the heavy quark regime to two-loop level and in the light quark corner we generalize the description in terms of the rainbow equations to finite temperature and density, and in the presence of a non-trivial background.

The manuscript is structured as follows. In Chap. 2, we outline some general features and concepts that will frequently be employed throughout the various discussions in this report. For instance, we recall some of the basic formalism of the symmetries dominating QCD transitions, *i.e.* chiral and center symmetry. Additionally, we give a more detailed description of the state of the art on the Columbia Plot and the QCD phase diagram. Furthermore, in chapter 3, we describe the foundations of the CF model and its extension to finite temperature and density. In all subsequent chapters of the present thesis, we present the results of original research. In Chap. 4, we discuss the heavy quark physics from the viewpoint of the CF model at two-loop level and verify explicitly the robustness of the associated perturbative expansion in that domain. Further, in Chap. 5, we discuss generic features of the heavy quark corner of the Columbia Plot which are ubiquitously displayed in a wide class of models entailing a quark contribution at one-loop order. In Chap. 6, we formally derive the most general rainbow equations at $T \neq 0, \mu_B \neq 0$ and in dependence of a non-trivial gluon background and in agreement with all constraints imposed by the symmetries of the thermal system on the Dirac tensorial form of the quark propagator. Thereafter, we discuss a simplified version of these equations in order to gain a first insight on their qualitative prediction of the phase diagram and pave the way to a future, more complete study. We showcase and compare our findings in different approximation schemes. Finally, in Chap. 7, we attempt a unique description combining both the light and the heavy quark dynamics, based on a particular approximation scheme detailed in the previous chapter, which is supplemented with a non-trivial gluonic background contribution. Lastly, we conclude in Chap. 8. Technical computations and additional material can be found in the various appendices.

2 Generalities

2.1 Basics of thermal field theory

In this very elementary—by no means exhaustive—primer to thermal field theory we solely present the concepts and quantities which are fundamental to the further conduction of this report and which shall be heavily exploited therein. For a fully documented and very pedagogic introduction to the nuances of finite temperature field theory the reader is referred to Ref. [171, 172, 173, 174].

Since during the entirety of the manuscript, we are only ever concerned with static configurations rather than real-time equilibrium quantities (*e.g.* decay rates) or the real-time evolution of off-equilibrium observables, we choose to only work in the imaginary time formalism. While the study of real-time dynamics (in and out of equilibrium) is itself worthwhile and insightful, such an endeavor is left for research beyond the scope of this thesis.

Starting from a zero temperature Minkowski action $\int_x \mathcal{L}_M(x)$ with $x = (t, \vec{x})$, the finite temperature imaginary time formalism is obtained upon applying the following recipe.[1] One rotates the Minkowski time direction according to $t = -i\tau$. Further, the new Euclidean time direction is compactified to a finite interval $\tau \in [0, \beta]$, where $\beta = 1/T$ is the inverse temperature. The Minkowski action has turned into

$$i \int_x \mathcal{L}_M(x) \to - \int_0^\beta \mathrm{d}\tau \int_{\vec{x}} \mathcal{L}_E(\tau, \vec{x}).$$

This compactification comes with consistency requirements on the field content, in particular the necessity of satisfying boundary conditions at 0 and β in Euclidean time. Bosonic fields are periodic, $\varphi(\beta, \vec{x}) = \varphi(0, \vec{x})$, while fermionic fields are anti-periodic, $\psi(\beta, \vec{x}) = -\psi(0, \vec{x})$.

To summarize, the partition function takes the form[2]

$$\mathcal{Z} = \int_{\mathrm{PBC}} \mathrm{D}\varphi \int_{\mathrm{APBC}} \mathrm{D}\bar{\psi}\,\mathrm{D}\psi \exp\left\{ - \int_0^\beta \mathrm{d}\tau \int_{\vec{x}} \mathcal{L}_E \right\}. \tag{2.1}$$

In turn, the (anti)periodicity of the fields in configuration space restricts the associated structure of the Fourier transforms in momentum space. In particular, it is easily checked that the fields $\tilde{\varphi}(K)$ and $\tilde{\psi}(P)$, the Fourier-transformed momentum-space counterparts of φ and ψ, must have bosonic and fermionic four-momenta of the type $K = (\omega_n, \vec{k})$ and $P = (\hat{\omega}_n, \vec{p})$, where we have introduced the Matsubara frequencies

$$\omega_n = 2\pi T\, n\,, \tag{2.2}$$
$$\hat{\omega}_n = 2\pi T (n + 1/2)\,, \tag{2.3}$$

for $n \in \mathbb{Z}$. Any formal integration over the entire momentum space becomes an infinite sum over all Matsubara frequencies combined with a three-dimensional spatial momentum integral. In this context,

[1] We stress that many subtleties are omitted at this stage, for instance that for Dirac fields one also redefines the matrices γ_μ. Or that for gauge fields one rotates the temporal component of the gauge field as well.

[2] Here, (A)PBC stands for (anti-)periodic boundary conditions.

we fix the notations for these bosonic and fermionic Matsubara sum-integrals:

$$\int_Q F(Q) \equiv T\sum_{n\in\mathbb{Z}} \mu_r^{2\epsilon} \int \frac{d^{d-1}q}{(2\pi)^{d-1}} F(\omega_n, q), \tag{2.4}$$

$$\int_{\hat{P}} F(P) \equiv T\sum_{n\in\mathbb{Z}} \mu_r^{2\epsilon} \int \frac{d^{d-1}p}{(2\pi)^{d-1}} F(\hat{\omega}_n, p), \tag{2.5}$$

with μ_r an arbitrary renormalization scale in dimensional regularization and $d = 4 - 2\epsilon$.

In the following, we detail how Matsubara sums are commonly computed throughout this report. For most complex functions F, a formula for bosonic Matsubara sums is given by

$$T\sum_{n=-\infty}^{\infty} F(i\omega_n) = -\sum_{\zeta_j} \mathrm{Res}\big(F(\zeta)\, n(\zeta), \zeta_j\big), \tag{2.6}$$

where n denotes the Bose-Einstein distribution function, $n(x) = \frac{1}{e^{x/T}-1}$, the sum runs over all poles ζ_j of the function $F(\zeta)$, and $\mathrm{Res}(F,\zeta)$ is the residue of F at position ζ.

Similarly, fermionic Matsubara sums are performed according to

$$T\sum_{n=-\infty}^{\infty} F(i\hat{\omega}_n) = \sum_{\zeta_j} \mathrm{Res}\big(F(\zeta)\, f(\zeta), \zeta_j\big), \tag{2.7}$$

with f denoting the Fermi-Dirac distribution function, $f(x) = \frac{1}{e^{x/T}+1}$. A proof for both formulae, alongside a sufficient condition for the function F, is sketched in appendix A.

In most physical situations, the given formulae can be applied. They represent one of the simplest ways of computing Matsubara sums. In the rare case where one comes across a function F for which the above cannot be utilized, there exists another (more cumbersome) formula given in Ref. [171].

Finally, we give some useful relations involving the distribution functions. For instance, we have

$$n(x \pm i\omega_n) = n(x)\,, \qquad f(x \pm i\omega_n) = f(x)\,, \qquad f(x \pm i\hat{\omega}_n) = -n(x)\,, \tag{2.8}$$

and it is easily checked that

$$f(-x) + f(x) = 1 \qquad \text{and} \qquad n(-x) + n(x) = -1\,. \tag{2.9}$$

2.2 QCD at finite temperature and chemical potential

At finite temperature $T = 1/\beta$ and quark chemical potential $\mu = \mu_B/3$, in the imaginary time formalism, the Euclidean action of QCD in d dimensions with N_c colors and N_f quark flavors is given by

$$S_{\mathrm{QCD}} = \int_x \left\{ \frac{1}{4} F^a_{\mu\nu} F^a_{\mu\nu} + \sum_{f=1}^{N_f} \bar{\psi}_f (\not{D} + M_f + \mu\gamma_0)\psi_f \right\}, \tag{2.10}$$

where we have defined $\int_x \equiv \int_0^\beta d\tau \int d^{d-1}x$. The field-strength tensor is

$$F^a_{\mu\nu} \equiv \partial_\mu A^a_\nu - \partial_\nu A^a_\mu + g f^{abc} A^b_\mu A^c_\nu\,, \tag{2.11}$$

where g denotes the bare coupling constant, f^{abc} the structure constants of the SU(N_c) gauge group, and

$$\mathcal{D}_\mu \psi \equiv (\partial_\mu - igA_\mu)\,\psi\,, \tag{2.12}$$

with $A_\mu \equiv A^a_\mu t^a$ a color matrix, t^a the generators of the algebra su(N_c) in the fundamental representation. We choose the normalization

$$\mathrm{tr}\; t^a t^b = \frac{1}{2}\,\delta^{ab}\,. \tag{2.13}$$

We leave the Dirac and color indices of the quark fields implicit and ψ_f and $\bar{\psi}_f$ are understood in the common sense as column and line bispinors, respectively. The Euclidean Dirac matrices γ_μ are related to the standard Minkowski matrices (in the Weyl representation) as $\gamma_0 \equiv \gamma^0_M$ and $\gamma_i \equiv -i\gamma^i_M$. They are hermitian and satisfy the anticommutation relations $\{\gamma_\mu, \gamma_\nu\} = 2\delta_{\mu\nu}$.

In our (unusual) convention, a positive value of μ corresponds to an excess of anti-quarks over quarks. Throughout this report, we shall restrict to the physical scenario of $N_c = 3$. Thus the (anti-)fundamental representations for quarks and anti-quarks are **3** and $\bar{\mathbf{3}}$ respectively, and the t^a are simply given by the well-known Gell-Mann matrices. Similarly the gluons live in the adjoint representation **8**, in which the generators are determined from the structure constants f^{abc} themselves.

2.2.1 Center Symmetry

Given the (anti-)periodic nature of the bosonic (fermionic) fields in the imaginary time formalism in section 2.1, the fields in Eq. (2.10) satisfy

$$A_\mu(\tau+\beta,\vec{x}) = A_\mu(\tau,\vec{x})\,, \qquad \psi(\tau+\beta,\vec{x}) = -\psi(\tau,\vec{x})\,, \qquad \bar{\psi}(\tau+\beta,\vec{x}) = -\bar{\psi}(\tau,\vec{x})\,. \tag{2.14}$$

For an arbitrary gauge transformation

$$A_\mu \to U\,A_\mu\,U^\dagger - \frac{i}{g}(\partial_\mu U)\,U^\dagger\,, \qquad \psi \to U\,\psi\,, \qquad \bar{\psi} \to \bar{\psi}\,U^\dagger\,, \tag{2.15}$$

with $U \in \mathrm{SU}(3)$, the action in (2.10) is invariant, but the (anti-)periodicity is generally broken and the corresponding partition function

$$\mathcal{Z} = \int_{\mathrm{PBC}} \mathcal{D}A \int_{\mathrm{APBC}} \mathcal{D}\bar{\psi}\mathcal{D}\psi\, e^{-S_{\mathrm{QCD}}} \tag{2.16}$$

becomes non-invariant.[3] Therefore, transformations as in (2.15) only constitute a symmetry of the theory if the boundary conditions are respected. In order to avoid this conundrum, one restricts the allowed form of elements $U \in \mathrm{SU}(3)$ to the largest possible subset leaving the boundary conditions at $\tau = \beta n$ $(n \in \mathbb{Z})$ intact, which is satisfied if the gauge transformations are themselves periodic, $U(\tau+\beta,x) = U(\tau,x)$.

At this point it is beneficial to consider the gluonic and fermionic content separately, since pure YM theory additionally permits for a larger set of gauge transformations preserving the PBC in the format

$$U(\tau+\beta,x) \quad = \quad z_k\,U(\tau,x)\,, \tag{2.17}$$

where z_k is an element of the center subgroup of SU(3), $z_k \in \mathbb{Z}_3 = \{e^{2\pi\,ik/3}\mathbb{1}_3\,|\,k = 0,1,2\}$. Gauge transformation based on (2.17) with $k \neq 0$ are called twisted and induce an exact symmetry of the pure YM theory. Contrarily, in an unquenched scenario, this symmetry is explicitly broken. However, for sufficiently heavy quarks, the center transformations (2.17) remain an approximate symmetry which constrains the dynamics.

It was demonstrated in Ref. [48, 175, 176] that an appropriate order parameter for the center symmetry in YM theories is given by the averaged Polyakov loops defined as

$$\ell \equiv \frac{1}{3}\mathrm{tr}\left\langle P\exp\left(ig\int_0^\beta d\tau A_0^a t^a\right)\right\rangle, \tag{2.18}$$

$$\bar{\ell} \equiv \frac{1}{3}\mathrm{tr}\left\langle \bar{P}\exp\left(-ig\int_0^\beta d\tau A_0^a t^a\right)\right\rangle, \tag{2.19}$$

where P and $\bar{P}$ denote path and antipath ordering, respectively. For intact charge conjugation invariance at vanishing chemical potential or in pure YM theory, one has $\ell = \bar{\ell}$. Under a twisted transformation, the Polyakov loop transforms as $\ell \to z_k\,\ell$ and, therefore, it is apparent that an unbroken center symmetry immediately enforces $\ell \equiv 0$. Likewise, observing $\ell \neq 0$ indicates a spontaneously broken symmetry. Similarly for $\bar{\ell}$. Due to the explicit breaking of center symmetry by the inclusion of quarks, this association formally breaks down. For sufficiently heavy quarks, the Polyakov loops still serve as approximate order parameters where $\ell \ll 1$ now indicates an almost symmetric phase.

Invoking Gauss' law, it was argued in Ref. [40, 48, 49] that the averaged Polyakov loops can be interpreted in terms of the free energies $(F_q\,, F_{\bar{q}})$ of the thermal bath in presence of a static color (anti)charge:

$$\ell \propto e^{-\beta F_q}\,, \qquad \bar{\ell} \propto e^{-\beta F_{\bar{q}}}\,. \tag{2.20}$$

Similar relations can be derived for more involved free energies, for instance of a static pair of test charges, $F_{q\bar{q}}$. However, we shall not consider these here. The proportionality factor missing in (2.20) to turn both relations into equations is actually given by $e^{\beta F_0}$, where F_0 is the free energy of the system in absence of a static test charge. This detail will become of significance in section 4.3, but can safely be ignored at this stage. Equations (2.20) establish the connection between center symmetry and the deconfinement transition, since a vanishing Polyakov loop corresponds to a center symmetric phase as well as a formally

[3] Strictly speaking, the partition function is ill-defined since it scales with the (infinite) volume of the gauge group, but this holds irrespective of the boundary conditions of the field content. In a discretized form, Eq. (2.16) is well-defined but non-invariant for non-preserved (anti-)periodicity of the fields.

infinite free energy, clearly indicating the (infinite) reluctance of the bath to accomodate an isolated static color charge. Contrarily, for a finite value of the Polyakov loops, entering a single static color charge into the bath is permitted. Therefore, the phase of a broken center symmetry is equally associated to deconfinement.

Finally, we mention that the entire formalism above can be extended to other gauge groups than SU(3) and other representations beyond the fundamental **3** and $\overline{\mathbf{3}}$. However, despite this extension being virtuous in many situations [167, 177, 178, 179, 180], it shall not be employed in this report.

2.2.2 Chiral Symmetry

Having described the intrinsics of center symmetry in the previous section, we now turn to chiral symmetry, which is the other symmetry of relevance for the QCD phase diagram permitted by the action in (2.10). More specifically, in case of a massless fermionic sector, $M_f = 0$, the action remains invariant under transformations of the flavor group $\mathrm{U}(N_f)_L \otimes \mathrm{U}(N_f)_R$. With

$$\bar{\psi} = \begin{pmatrix} \bar{\psi}_L & \bar{\psi}_R \end{pmatrix} \qquad \text{and} \qquad \psi = \begin{pmatrix} \psi_L \\ \psi_R \end{pmatrix}, \tag{2.21}$$

or, by definition, $\psi_{L/R} = \frac{1}{2}(1 \mp \gamma_5)\,\psi$, we have

$$\psi_{L/R} \to g_{L/R}\,\psi_{L/R}\,, \tag{2.22}$$

for some elements $g_{L/R} \in \mathrm{U}(N_f)_{L/R}$. Similarly for $\bar{\psi}_{L/R}$.

This framework can be transferred to a description in terms of the group

$$\mathrm{U}(N_f)_V \otimes \mathrm{U}(N_f)_A \;=\; \mathrm{U}(1)_V \otimes \mathrm{U}(1)_A \otimes \mathrm{SU}(N_f)_V \otimes \mathrm{SU}(N_f)_A\,, \tag{2.23}$$

where

$$\psi_V \equiv \psi_L + \psi_R = (P_L + P_R)\psi = \psi \tag{2.24}$$

$$\psi_A \equiv \psi_R - \psi_L = (P_R - P_L)\psi = \gamma_5\psi \tag{2.25}$$

Here, V stands for vector and A for axial. The $\mathrm{U}(1)_V$ part corresponds to Baryon number conservation and is always satisfied. Infamously, the $\mathrm{U}(1)_A$ displayed by the action at tree-level gets anomalously broken by quantum corrections in form of the quark-loop triangle diagram [181, 182, 183]. One remains with the symmetry group

$$\mathrm{SU}(N_f)_V \otimes \mathrm{SU}(N_f)_A\,, \tag{2.26}$$

where the group elements induce transformations of the form

$$\begin{cases} \psi \to e^{i\Theta^a t^a}\,\psi \\ \bar{\psi} \to \bar{\psi}\,e^{-i\Theta^a t^a} \end{cases} \qquad \text{for } \mathrm{SU}(N_f)_V \tag{2.27}$$

and similarly

$$\begin{cases} \psi \to e^{i\Theta^a t^a \gamma_5}\,\psi \\ \bar{\psi} \to \bar{\psi}\,e^{i\Theta^a t^a \gamma_5} \end{cases} \qquad \text{under } \mathrm{SU}(N_f)_A\,. \tag{2.28}$$

In fact, it can be shown that global vectorial symmetry cannot be broken [184]. Contrarily, in the QCD vacuum, one observes the axial part $\mathrm{SU}(N_f)_A$ to be spontaneously broken, which yields a finite, dynamically generated quark mass, called the constituent mass and which explains the relative lightness of the pion in the hadron spectrum. An appropriate order parameter for this spontaneous breaking of chiral symmetry is given by the quark condensate $\sigma \equiv \langle\bar{\psi}\psi\rangle$.

In a non-idealized scenario with finite bare quark masses, the mass term $\bar{\psi}M\psi$ explicitly breaks this chiral symmetry. However, if the corresponding masses are numerically small, then this breaking is soft and (2.26) remains an approximate symmetry. In the same spirit, the quark condensate remains an approximate order parameter for the spontaneous breaking of chiral symmetry.

As a side note, for physical quark masses, chiral symmetry is severely broken for the heavy flavors charm, top and bottom. On the other hand, in the light sector for up, down and strange it remains

reasonably accurate. Therefore, the spontaneous breaking of flavor SU(3) leads to the creation of 8 pseudo-scalar Goldstone bosons corresponding to the 8 broken generators. Since there is an additional explicit breaking of chiral symmetry due to the non-vanishing current quark masses, these Goldstone bosons are not massless, but very light. They are associated to the octet of pion, eta and kaon mesons. Interestingly, the observed constituent quark masses in the QCD vacuum are much larger than the respective current values. Based on these chiral symmetry considerations, a very powerful effective field theory has been developed for scales below the resonance region, where the set of relevant degrees of freedom reduces to the lightest mesons and hadrons. This effective approach, labelled chiral perturbation theory, is tremendously accurate and has significantly enhanced our understanding of the low energy regime of QCD [185].
Finally, we mention that the above considerations trivially extend to a finite temperature setting, where the high temperature symmetric phase is characterized by a restoration of the spontaneously broken $\mathrm{SU}(N_f)_A$ symmetry.

2.2.3 The Columbia Plot

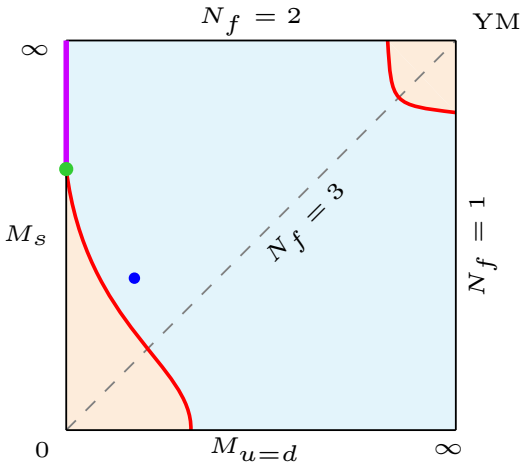

Figure 2.1: Most prominent version of the Columbia Plot at zero chemical potential. The order of the phase transition is depicted in dependence of the quark masses $(M_{u=d}, M_s)$, as described in the main text. It exhibits a first order region in the bottom left and top right corner, corresponding to very light and very heavy quarks.

In the previous two sections we have introduced the two symmetries that play an important role for the QCD phase diagram in two opposite regimes, *i.e.* the center symmetry breaking for heavy quark masses and chiral symmetry restoration for light quarks. In this respect, it is very insightful to indicate the nature of the respective transitions in dependence of the quark mass, which is thereby varied as a free parameter. The resulting diagram is a mere theoretic construct, called the Columbia Plot, shown in Fig. 2.1. Conventionally, one considers a semi-degenerate scenario with a strange quark mass, M_s, and the isospin symmetric up and down degenerate masses $M_{u=d}$. All masses are varied from 0 to ∞, with $M_{u=d}$ on the abscissa and M_s on the ordinate. Consequently, the chiral limit can be found in the bottom left corner of the Columbia Plot [112, 186, 187, 188, 189, 190].

As mentioned in section 2.2.1 already, taking the quark masses to infinity corresponds to a freeze out of the associated degrees of freedom and in this quenched limit one therefore recovers the pure gauge SU(3) Yang-Mills theory in the top right corner. Similarly, the bottom right corner corresponds to an infinite up and down mass, which are thus frozen out, and a massless strange quark. This is a theory with $N_f = 1$ in the chiral limit. Similarly, the top left corner signifies chiral $N_f = 2$.

The Columbia Plot, as illustrated in Figs. 2.1, 2.2 and 2.3, has to be understood as an idealized picture in dependence of the dimensionful quark masses $M_{u=d}$ and M_s. This is due to the absence of a relevant reference scale and thus, practically, a more natural variable to consider is, for example, the ratio M/Λ_{QCD}. There are, of course, subtleties related to the proper definition of the quark masses—which is not a physical observable[4]—but they are irrelevant for the present discussion.

In addition to analytic considerations [48, 175], lattice QCD simulations have conclusively proven a first order transition in YM theory in the top right corner [191]. By continuity, this first order

[4] In this respect, a more physical version of the Columbia plot would be in terms of the pion and kaon masses [106]. The question of properly defining the quark masses will be discussed in chapter 4.

transition must transfer over into a small region around the YM point, described by an unquenched theory with decreasingly heavy quark masses. The more the quark masses are decreased, the more the first order transition becomes weaker and eventually it turns second order for some critical mass values [192]. This boundary line separates the first order region from a regime of smooth crossovers. The physical point, *i.e.* the point in the Columbia plot corresponding to physical values of the quark masses, lies in this crossover region. This observation has been exhaustively demonstrated by lattice QCD simulations [52, 53, 193, 194] and verified by various models [195, 196, 197], which all find a pseudo-critical temperature[5] around 150-170 MeV.

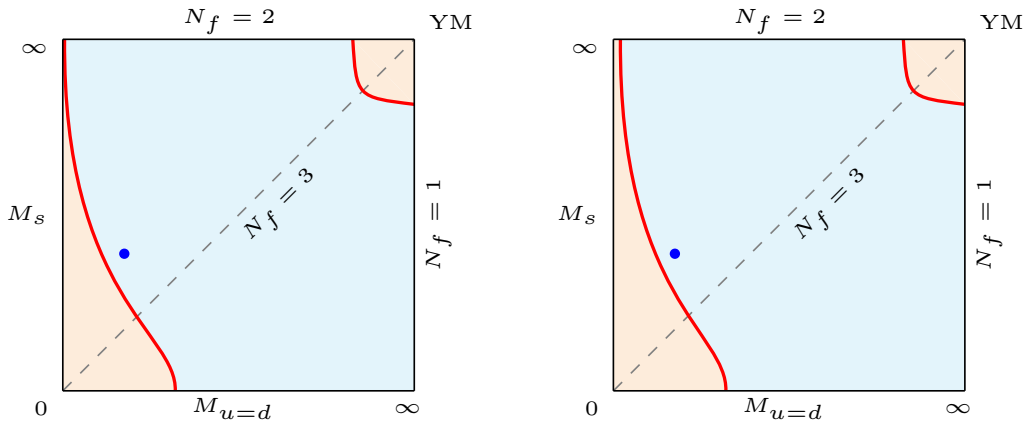

Figure 2.2: Two alternatives to Fig. 2.1 for the upper end of the light quark boundary line. In the first case it terminates exactly in the top left corner, whereas in the second it reaches further to enlarge the first order region to some finite range in the $N_f = 2$ theory.

Unfortunately, the implementation of chiral or even very light fermions on the lattice is technically extremely challenging. This is why, to present, there is still no final consensus from the lattice community on the nature of the Columbia Plot in the light quark regime. Supportingly, one also relies on model descriptions and symmetry-based universality arguments for insight [107]. The most prominent estimate is that for lower and lower masses the smooth crossover becomes steeper and steeper until, once again, one hits a further second order line. Beyond lies a first order region including the chiral point in the bottom left corner of the Columbia Plot. The shape of this light quark critical boundary line is heavily disputed [198]. Various possibilities are shown in Figs. 2.1 and 2.2. In the most prevalent scenario there exists a tricritical point $(0, M_s^{\text{tric}})$, $0 < M_s^{\text{tric}} < \infty$, which terminates the $Z(2)$ critical line and is connected to the top left corner by an $O(4)$ critical line; see Fig. 2.1. In other versions the $Z(2)$ boundary line extends to either the $N_f = 2$ chiral point itself [Fig. 2.1, left] or even beyond to include the top left corner within the first order region [Fig. 2.1, right]. Model calculations, especially towards the $N_f = 2$ chiral point in the top left corner, heavily depend on the role of the chiral anomaly and the inclusion of beyond-mean-field fluctuations in the order parameter [106, 107, 112, 199, 200, 201, 202].

On the other hand, while the above-mentioned picture with a first order region around the chiral point in the bottom left corner is largely accepted as fact in the community, it is not conclusively proven and questioned in recent lattice QCD studies [203]. To present, when taking the continuum limit of vanishing lattice spacing, all lattice findings are still compatible with a critical chiral $N_f = 3$ point and no first order region at all [203]. Thus, it seems clear that if the light quark first order region exists, it must be tiny, a fact for which the approach we follow in chapter 6 provides a possible consistent explanation. This alternative version is illustrated in Fig. 2.3 and immediately contradicts the conclusions of Ref. [107], which are based on a perturbative RG analysis of an effective matrix model. It should be mentioned, however, that an effective approach of this type assumes the order of the transition to be determined solely from the mesonic degrees of freedom and thus treats the gauge contributions at mean-field level. Interestingly enough, in Ref. [204], it was demonstrated that example theories exist where neglecting gauge fluctuations leads to an erroneous result for the transition order. In particular, it was shown that gauge fluctuations have the potential to render a formerly first order transition critical. While not

[5]Here, the pseudo-critical temperature is defined as the value of extremal first derivative in the Polyakov loop as a function of temperature.

permitting proof in either direction, this study, at the very least, questions the reliability of Ref. [107] for QCD. These analytic considerations, together with inconclusive lattice findings, make the version of the Columbia Plot displayed in Fig. 2.3 a possibility that has yet to be discarded.

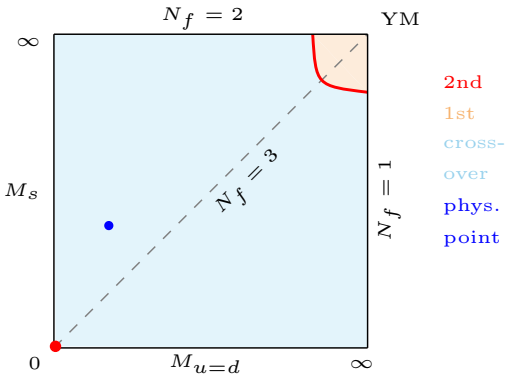

Figure 2.3: This version of the Columbia Plot does not exhibit a first order region in the light quark regime. Instead, there is a second order critical point in the chiral limit in the lower left corner. The nature of this critical point, *i.e.* its universality class as well as the possible existence of a critical line connecting to the $N_f = 2$ chiral point is then an open question. To present, this version is still very much a viable possibility that has not been ruled out (yet), as explained in the main text.

The Columbia Plot can be extended by a further dimension to non-zero values of the chemical potential squared, in the following labelled the 3D Columbia Plot [91, 191, 205, 206]. Its projected shape along the $N_f = 3$ degenerate line is given in Fig. 2.4. The possible values of μ^2 range from $-\infty$ to $+\infty$. However, one restricts the analysis to $-T^2\pi^2/9$ to $+\infty$ due to the Roberge-Weiss symmetry of the theory at imaginary chemical potential $\beta\mu = i\pi/3$ [205, 207], beyond which the physics of any interval $\mathrm{Im}\,\mu \in [k\pi/3, (k+1)\pi/3]$ can be uniquely linked back to $\mathrm{Im}\,\mu \in [0, \pi/3]$. This possibility is based on an interplay of center and abelian transformations combined with charge conjugation.

It is paramount to note that Monte Carlo important sampling techniques are not directly applicable at $\mu^2 > 0$, such that in this regime one has to estimate the projected phase structure. This is due to the fact that for non-zero real values of the chemical potential lattice QCD simulations suffer from the infamous sign problem [208, 209]. The sign problem manifests itself in the non-positivity of the fermion determinant in the functional integral. This then leads to a probabilistically ill-defined weight factor that renders standard importance sampling algorithms inapplicable. The sign problem can be circumvented for sufficiently small values of the chemical potential, however becomes fundamentally prohibitive as one reaches deeper into the regime of real μ values. In this respect, it is to be noted that recent efforts from the lattice community have succeeded in enlarging the domain of reliability of their findings [210, 211, 212, 213]. On the contrary, for imaginary values of the chemical potential the sign problem is absent. Also, in the heavy quark region, the sign problem can be circumvented by an expansion around the quenched theory in inverse powers of the quark masses [214].

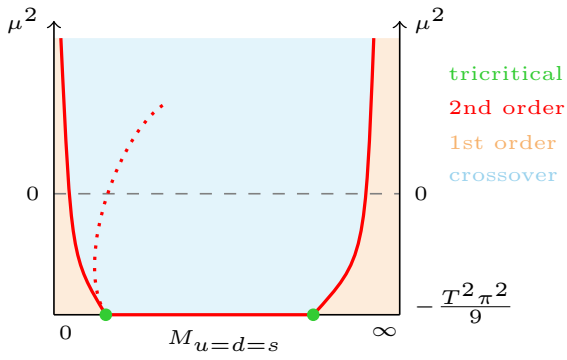

Figure 2.4: We show a crosscut of the 3D Columbia Plot along the direction of three degenerate quark masses. In the most prevalent scenario the light quark critical line behaves as shown by the respective solid red line. However, a different curvature resulting in a bending as indicated by the red dotted line is also possible. A back-bending of this type would allow for a CEP in the QCD phase diagram shown in Fig. 2.5.

The second order boundary lines at $\mu = 0$ extend to critical surfaces, which still separate first order regions from smooth crossovers. It is firmly established that the curvature of the heavy quark critical surface is such that for increasing values of μ^2 it bends towards the YM point. It is therefore apparent that this critical surface will never intersect the line (as a function of μ) above the physical point. On the other hand, the curvature of the critical surface in the light quark corner (if it exists), remains unknown and a bending towards the physical point is not ruled out [90]. This question is of tremendous

significance for the possible existence of a CEP in the QCD phase diagram, as explained in section 2.2.4.

For a very inclusive and pedagogic discussion of the various aspects of the Columbia Plot, from both continuum and lattice viewpoints, the reader is also referred to Ref. [209].

As a final remark, one might inquire the necessity to study the Columbia Plot in the first place since only the physical point is of actual physical relevance. On the other hand, given the above-outlined structure of the Columbia Plot, it is apparent that the dynamics underlying the physical point itself is continuously related to the non-trivial physics of either the heavy or light quark regime. Therefore, understanding each of these theoretic extremes enables or at least enlarges our control of the situation at the physical point. In this respect, it is virtuous to pursue model descriptions capable of spanning the whole Columbia plot.

2.2.4 The QCD Phase Diagram

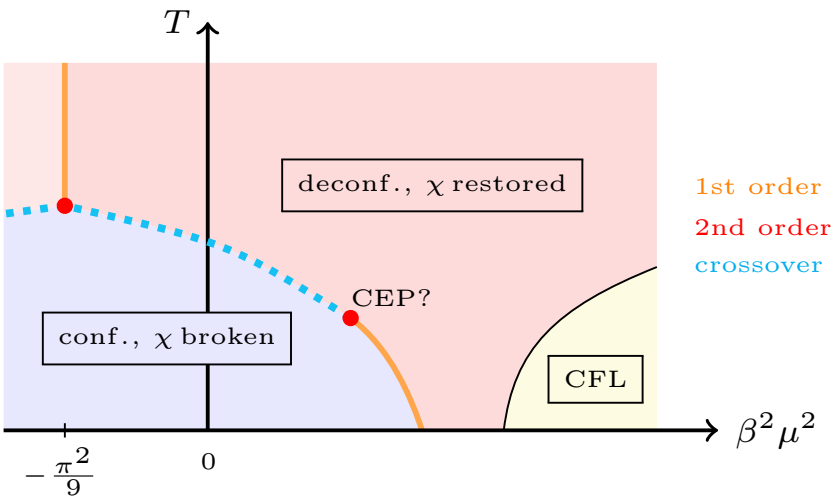

Figure 2.5: We outline the qualitative structure of the QCD phase diagram. The physically relevant regime corresponds to non-negative values of μ^2. Here, in the lower left corner for sufficiently small values of T and μ, QCD exhibits a mostly confined and mostly chirally broken phase (light blue). In the opposite regime of sufficiently high T and μ values, the associated phase is characterized to be mostly deconfined and mostly chirally restored (light red). Finally, in the lower right corner for high μ and low T values exist(s) the superconducting color-flavor-locked phase(s) (light yellow). The indicated nature of the respective transitions between these phases depends on the exact location within the diagram. As outlined in the main text, the phase diagram smoothly connects to a priori non-physical imaginary values of the chemical potential. In principle, one could imagine alterations to the imaginary μ regime in a scenario where the light quark critical surface in the 3D Columbia plot intersects the physical point. However, as argued in the previous section, given the small size of the respective first order region in the light quark corner, this is very unlikely.

Having presented the Columbia Plot in the previous section 2.2.3, we are now in the position to discuss the QCD phase diagram. In contrast to the Columbia Plot, the QCD phase diagram is characterized by the quark masses restricted uniquely to physical values. One then depicts the various phases attained by the system in dependence on chemical potential and temperature. A schematic representation is shown in Fig. 2.5.

The realm of imaginary values of chemical potential does again correspond to an unphysical scenario, which is nonetheless continuously connected to the physical case of real μ values, as shown in Fig. 2.5. Its phase structure is discussed further below.

Excluding non-physical imaginary μ values, the part of the phase diagram that is actually firmly established from first principle approaches is limited to the temperature axis for $\mu = 0$. In the absence of well-controlled lattice QCD results, insight into the thermodynamic nature of the system at finite (real) chemical potential is attempted from various angles. On the one hand there are numerous first principle non-perturbative methods [15, 16, 17, 97, 101] as well as effective models capturing purely the

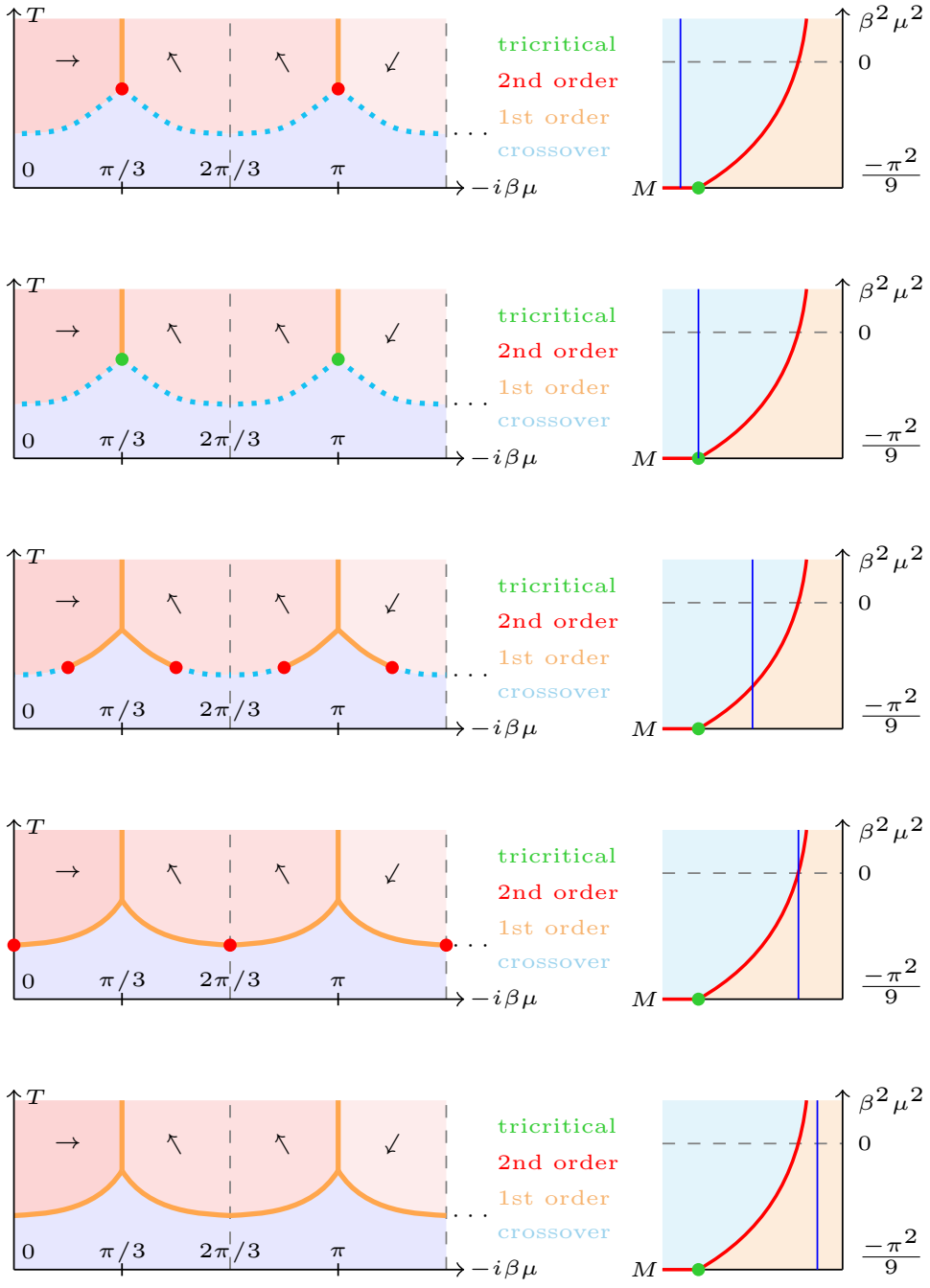

Figure 2.6: We show various facets of the phase diagram in dependence on temperature and imaginary chemical potential for different choices of the degenerate $N_f = 3$ quark mass. Thereby we have focussed on the heavy quark regime, where for comparisons the bottom right corner of Fig. 2.4 is depicted on the right of each respective plots. There, the thin blue line indicates the chosen quark mass in each case.

(supposedly) relevant degrees of freedom [30, 88, 86, 195, 215, 216, 217, 218, 219]. On the other hand, one exploits the fact that phase diagram for imaginary μ is smoothly related to the real μ side, as shown in Fig. 2.5. This has the benefit that lattice QCD computations are no longer hampered by the sign problem and the results can, in principle, be extrapolated over by (numerical) analytic continuation. In practice, this is also limited to not-too-large values of the chemical potential.

At vanishing chemical potential, QCD admits a crossover for both the chiral and the deconfinement order parameters with a pseudo-critical temperature around 150-170 MeV. This crossover line extends

inwards for increasing μ and decreasing T values and might end at a CEP. The existence and possible location of this CEP is subject to vast research efforts from both experimental [220, 221, 222, 223] as well as theoretical studies [15, 16, 17, 58, 66, 97, 101, 111, 188, 195, 215, 216, 217, 224, 225, 226, 227, 228, 229, 230, 231, 232]. The CEP then connects via a first order line to the axis of zero temperature. Finally, for very large density values and small temperatures, one expects superconducting phases which are characterized by color-flavor-locking. Since they are of no further importance in this report beyond this stage, we merely point the interested reader to relevant literature [233, 234, 235, 236]. Similarly, our discussion shall neglect any effects from the nuclear liquid-gas transition, which is in principle situated within the (mostly) confined phase [237, 238].

Despite turning the results unphysical again, it is nonetheless interesting to study the effects on Fig. 2.5 upon relaxing the restriction to purely physical quark mass values. In particular, this is illustrated in the regime of imaginary chemical potential in Fig. 2.6. For pictorial simplicity and to enable comparisons with Fig. 2.4, we only consider the case of three degenerate masses. Also, when exploring the space of possible values of $M_{u=d=s}$, we restrict to the heavy quark regime, as indicated by the respective small plots on the right hand sides of Fig. 2.6, which correspond to the bottom rightmost part of Fig. 2.4. Similar pictures could of course be obtained in the light quark corner, where however the possible back-bending of the critical surface could lead to non-trivial alterations.

The phase diagram at imaginary μ is periodic with period $2i\pi T$ and essentially consists of two phases. At large enough quark mass, these are a mostly confined and mostly chirally broken phase in light blue and a mostly deconfined and mostly chirally restored phase in light red. The nature of their mutual transition depends on the value of the quark mass, as explained below and shown in Fig. 2.6. Independently of the quark mass, there exist first order transition lines for chemical potential values $iT(2n+1)\pi/3$, $n \in \mathbb{N}$. These first order transition lines are controlled by the Roberge-Weiss symmetry mentioned in previous sections. If crossing one of these lines, one still remains in a mostly deconfined and mostly chirally restored phase corresponding to a different element of the center subgroup Z_3 of SU(3). This is indicated by slightly distinct shades of red and the small arrows, which represent the respective elements of the center group.

As invoked above, the order of the confinement and chiral transition at imaginary chemical potential heavily depends on the quark mass. For $N_f = 3$ degenerate values in the intermediate range close to the physical point, $M_{u=d=s} < M^{\text{tric}}_{u=d=s}$, the resulting diagram coincides with the top left of Fig. 2.6. Then, moving closer towards the heavy quark regime, for some $M_{u=d=s} = M^{\text{tric}}_{u=d=s}$, one eventually encounters the situation depicted in the second top row of Fig. 2.6. Here the tricritical points are connected to the Roberge-Weiss first order lines mentioned above and via crossover lines with each other. For increasing masses $M^{\text{tric}}_{u=d=s} < M_{u=d=s} < M^{c,\mu=0}_{u=d=s}$, the tricritcal points split into two second order points moving off along the formerly crossover lines in either direction, leaving behind a first order line. The former tricritical point has now become a triple point where three first order lines meet. This image continues, until for some quark mass value $M^{c,\mu=0}_{u=d=s}$, the second order points hit μ values $2iT\pi\, n/3$, $n \in \mathbb{N}$, merge and then vanish thereafter. For even larger quark masses, $M_{u=d=s} > M^{c,\mu=0}_{u=d=s}$, there only remain first order lines in the phase diagram, as sown in the bottommost row of Fig. 2.6.

The vicinity of the tricritical point, *i.e.* the behavior of the second order points near the tricritical point, is well-described by a simple mean field scaling analysis [91]:

$$\frac{M_c(\mu_i)}{T_c(\mu_i)} = \frac{M_{\text{tric.}}}{T_{\text{tric.}}} + K\left[\left(\frac{\pi}{3}\right)^2 - \left(\frac{\mu_i}{T_c}\right)^2\right]^{\frac{2}{5}}, \tag{2.29}$$

where K is some constant, μ_i is defined as the imaginary part of μ and the subscripts $u = d = s$ have been dropped for simplicity.

This particular scaling law can be analytically continued to real values of chemical potential and thus serves as an example of the usefulness of studying the a priori unphysical regime of imaginary μ and circumventing the sign problem (provided the scaling extrapolates into the real chemical potential region). This shall be tested explicitly within the CF model in section 4.2.

3 The Curci-Ferrari Model

The original research conducted throughout the present thesis, presented in the subsequent chapters, is based almost exclusively (with one exception) on the CF model. In this chapter, we introduce the basic features and properties of the CF model, which we then rely on continuously in later stages. Despite the fact that these later analyses only use the CF model in a finite temperature setting, many of its fundamental characteristics are best illustrated already at zero temperature in a simplified scenario; see section 3.1. Thereafter, in section 3.2, we present some aspects that are specific to the nonzero temperature setting of the CF model, such as the introduction of a non-trivial gluon background, the necessary elevation to Landau-DeWitt gauge, the existence of Weyl chambers, the nature of the root-weight diagram and the resulting Feynman rules.

3.1 Fundamentals at zero Temperature

The CF model is a phenomenologically motivated effective theory for the low energy regime of QCD, where a gluon mass term is added to the FP Landau gauge-fixed Lagrangian. At zero temperature and in Euclidean space, the latter is given by

$$\mathcal{L}_{\mathrm{CF}} = \frac{1}{4}(F^a_{\mu\nu})^2 + \bar{\psi}(\gamma_\mu \mathcal{D}_\mu + M)\psi + \mathcal{L}_{\mathrm{FP}} + \frac{1}{2}m^2(A^a_\mu)^2\,, \tag{3.1}$$

where, in the Landau gauge, defined by $\partial_\mu A^a_\mu = 0$, the FP term writes as

$$\mathcal{L}_{\mathrm{FP}} = \partial_\mu \bar{c}^a D_\mu c^a + i h^a \partial_\mu A^a_\mu \tag{3.2}$$

with c and $\bar{c}$ denoting the ghost fields and h is the Nakanishi-Lautrup Lagrange multiplier used to enforce the particular gauge configuration of choice. The Langrangian (3.1) is a particular case of the class of Curci-Ferrari Lagrangians [129].

The model was first introduced by Curci and Ferrari in 1976 [129], who simply pursued the most general Lagrangian consistent with certain symmetries obtained after imposing the FP procedure. In the general case, their construction involves a class of nonlinear gauges, the Curci-Ferrari-Delbourgo-Jarvis gauges, and also features a mass term for the ghost fields. It was shown in Ref. [129, 239], that this model (including an arbitrary ghost mass) breaks the nilpotent Bechi-Rouet-Stora-Tyutin (BRST) symmetry of the FP Lagrangian, but nonetheless possesses a modified, nonnilpotent BRST symmetry and remains perturbatively renormalizable.

In 2011, motivated by a large influx of lattice results on the decoupling behavior of the Landau gauge gluon propagator in the IR limit, Tissier and Wschebor proposed the Lagrangian (3.1) as an effective starting point for a modified perturbative expansion. While a nonzero value of the gluon propagator at vanishing momentum is guaranteed in the CF model, it is a nontrivial question whether the model is capable to reproduce the momentum dependence of both the gluon and ghost correlation functions. This was indeed confirmed in Ref. [131] by one-loop effects, where a remarkable agreement with lattice numerics is observed, see Fig. 3.1.

In parallel, Serreau and Tissier (ST) identified an alternative theoretical motivation for the gluon mass term [126]. It has long been proven that Gribov copies spoil the typical calculation of Green's

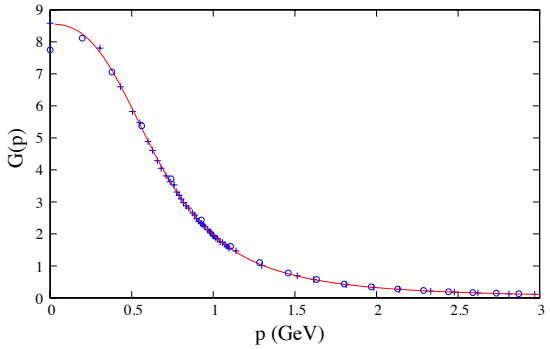

Figure 3.1: Fitted one loop gluon propagator within the YM CF model (red) from [131] against lattice YM simulations [134, 159] (blue). The fitted value of $m \approx 500$ MeV for the gluon mass is kept constant in all further (one-loop) computations of the CF model.

functions via path integral methods in the IR regime [115, 119]. This illustrates the fact that, although the UV dynamics is well-described by the FP Lagrangian, this alignment gets severely broken in the IR. While the explicit in-detail effects of the Gribov copies remain to present a delicate issue in analytic approaches, many of their properties are well understood in the case of the Landau gauge [116]. For instance, choosing a particular copy leads to non-invariance of the gauge-fixed theory under BRST symmetry. Also, the presence of the copies does not alter the UV structure of the theory. ST propose a gauge-fixing procedure involving an average over Gribov copies with a nonflat weight (a flat weight corresponds to FP). The weight proposed in [126] introduces an effective gluon mass, which appears here as a gauge-fixing parameter.

In order to demonstrate self-consistency of the perturbative treatment of the CF model, a one-loop RG flow diagram was computed in Ref. [126, 132] for pure YM, see Fig. 3.2. In the plane spanned by the two running parameters, the coupling g and the rescaled gluon mass $\tilde{m} \equiv m/\mu_r$, it was established that the physical, positive quadrant is separated by a single separatrix (scaling-type solution) into two qualitatively distinct regimes linked to the (repulsive) Gaussian UV fixed point. The first region, which is the one containing the standard FP Lagrangian without a gluon mass term, is characterized by RG flows which suffer from a Landau pole and thus inhibit perturbative control in the IR. Here, one eventually has to resort to non-perturbative methods for a sensible description of the physics at long distances. On the other hand, there exists a second region, labelled IR-safe, in which the associated RG flows do no longer suffer from a Landau pole. Despite the fact that the coupling constant g might become large along IR-safe trajectories, it was shown that the effective loop-expansion parameter is of the form $\frac{\lambda}{1+\tilde{m}^2}$, where $\lambda = \frac{g^2 N_c}{16\pi^2}$; see Ref. [132]. Interestingly, it is found that decoupling-type Lattice QCD simulations follow a trajectory deep within this IR-safe regime. For the trajectory which best describes lattice data at one-loop, this expansion parameter never exceeds values of around 0.4, thus permitting perturbation theory at all momentum scales down to the deep IR.

We also mention that an extension of this analysis to two-loop order in YM has recently been performed [164], which shows a convincing quantitative improvement of the one-loop results and an excellent agreement with lattice calculations of the ghost and gluon propagators.

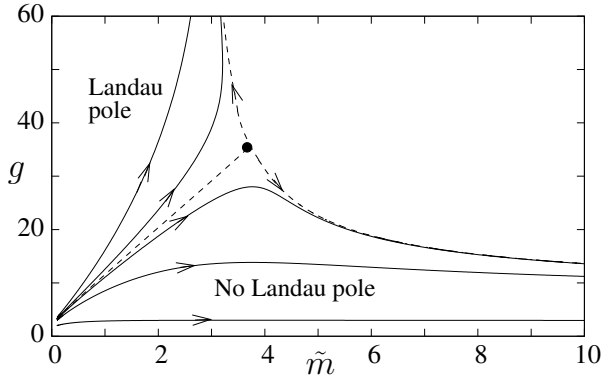

Figure 3.2: One loop RG flow of the coupling and rescaled gluon mass in the CF model, taken directly from Ref. [126]. The scaling separatrix is denoted by the dashed line, connecting a UV fixed point in the origin with a gaussian IR fixed point. Not depicted are flows disconnected from the UV fixed point

The CF model has been applied to the calculation of various two- and three-point correlation functions in an overall reasonable agreement with lattice QCD findings, both for YM at one-loop [131, 160, 163] and at two-loop order [164], but also for heavy quark QCD at one-loop level [161, 162]. These works enlist nicely into the existing set of model-based output for IR QCD available in the literature. The main advantage these perturbative studies inherit over long-established non-perturbative analytic approaches

is their conceptual simplicity of the underlying systematic expansion in the coupling. Thus, improvements to the numerical findings in form of higher order corrections are, in principle, envisionable and in all cases studied so far, including the respective two-loop corrections has indeed lead to a better description of the dynamics, signaling a robust expansion.

Furthermore, one can also study the case of QCD with light quarks. Here, however, one encounters an obstacle related to the observation that the quark-gluon coupling is significantly IR-enhanced compared to the pure gauge counterparts [169]. Hence, a naive perturbative expansion treating all couplings on equal footing is no longer expected to work well and, indeed, it fails. Instead, Ref. [170] has proposed a systematic approximation scheme in the CF model which is non-perturbative in the quark-gluon coupling while simultaneously double-expanding in the pure gauge couplings as well as in the inverse number of colors. Implementing this recipe - labelled as "rainbow-improved" (RI) in Ref. [170] - for all diagrams contributing to the quark self-energy, it can be shown that the leading order (LO) terms embody the resummation of the well-known rainbow diagrams [240, 241, 242, 243], with the gluon propagator corresponding to the tree-level CF propagator. In Ref. [170], it was demonstrated that the vacuum CF version of the rainbow equations successfully describes the dynamical symmetry breaking.

3.1.1 Fixing the gluon mass m

Superficially, it appears as though there is an extra parameter in the CF model in form of the gluon mass supplementary to the ones present in QCD or the standard FP Lagrangian. Ideally, the gluon mass term would be a dynamically generated quantity whose value is determined via that of the coupling. In practice, a precise scenario for such dynamical mass generation is still missing and we fix the gluon mass by fitting the calculated gluon propagator against corresponding lattice data and then keep it fixed for any further calculation. The optimal value is typically around 500 MeV.

3.2 Landau-DeWitt Gauge at finite Temperature

We remark that the CF model is originally twofold motivated in a zero temperature setting, from the Gribov ambiguities and the observed decoupling-behavior in lattice studies. It is regarded as an effective theory capturing the essence of the underlying physics at zero temperature. Any model can of course be transfered to a finite temperature scenario, however, whether or not this model in question remains aligned with the physics at finite temperature as well is a non-trivial question. While one does in fact observe the decoupling-type behavior of the Landau gauge gluon propagator in finite temperature analyses [148, 244, 245], a respective study of the Gribov ambiguity is more intricate due to the more complicated topological structure of the phase space [246]. Thus, the applicability of the CF model at finite temperature remains a semi-implicit assumption.

At finite temperature, it is crucial to work in a choice of gauge with manifest center symmetry and which permits to go beyond simply pure Landau gauge. One such choice of gauge is the so-called Landau-DeWitt (LdW) gauge [74, 247, 248, 249], where one splits the gluon field A^a_μ into a background $\bar{A}^a_\mu$ and a fluctuating component a^a_μ, such that $A^a_\mu = \bar{A}^a_\mu + a^a_\mu$. In this case, the LdW gauge-fixing condition reads

$$(\bar{D}_\mu a_\mu)^a = 0\,, \tag{3.3}$$

with $\bar{D}^{ab}_\mu \equiv \delta^{ab}\partial_\mu + g f^{acb}\bar{A}^c_\mu$ the background covariant derivative in the adjoint representation.

In summary, the Euclidean action of the CF model at finite temperature, $S_{\rm CF}$, is constructed from the respective QCD counterpart in (2.10), $S_{\rm QCD}$, supplemented with the necessary FP gauge-fixing terms and the gluon mass term. It reads

$$S_{\rm CF} = S_{\rm QCD} + \int_x \left\{(\bar{D}_\mu \bar{c})^a (D_\mu c)^a + i h^a (\bar{D}_\mu a_\mu)^a\right\} + \int_x \frac{1}{2} m^2 a^a_\mu a^a_\mu\,, \tag{3.4}$$

where c^a, $\bar{c}^a$ and h^a denote respectively the ghost, anti-ghost and Nakanishi-Lautrup fields. The covariant derivative in the adjoint representation is given by $D_\mu\varphi^a \equiv \partial_\mu\varphi^a + g f^{acb} A^c_\mu \varphi^b$, with g the bare coupling, as before. The advantage of the background field formalism is that the massless version of the gauge-fixed Lagrangian (3.4) possesses a formal gauge invariance with respect to gauge transformations of the background field. The latter allow one to encode the center transformations despite having fixed a gauge. The CF extension (3.4) of the LdW gauge-fixed Lagrangian adds a mass term to the fluctuating part

only in order to maintain this important property.[1] Indeed, (3.3) is invariant under

$$\bar{A} \to U\bar{A}U^\dagger - \frac{i}{g}U\partial U^\dagger\,, \qquad \varphi \to U\varphi U^\dagger\,, \tag{3.5}$$

for $\varphi = \{a, c, \bar{c}, h\}$.

For each temperature T, one chooses the background such that the expectation value of the fluctuating component, $\langle a^a_\mu \rangle$, vanishes in the limit of vanishing sources. In practice, for pure YM,[2] this corresponds to locating the absolute minimum[3] of the functional $\tilde{\Gamma}[\bar{A}]$ defined as $\tilde{\Gamma}[\bar{A}] \equiv \Gamma[\bar{A}, \langle a \rangle = 0]$, where $\Gamma[\bar{A}, \langle a \rangle]$ is the effective action for $\langle a \rangle$ in the presence of $\bar{A}$ [74, 167]. It is an easy check that center transformations leave this functional $\tilde{\Gamma}[\bar{A}]$ invariant, which means that center symmetry is manifest during each undertaken step.[4] Hence, one gains control over the deconfinement transition by monitoring when the background values associated to minima of $\tilde{\Gamma}[\bar{A}]$ depart from their center-symmetric (confining) values. In this respect, the value of the background field at the minimum serves as a genuine order parameter. For more details, see Refs. [167, 252]. Since any minimum has to respect the symmetries of the system at finite temperature, one can restrict the subspace of configurations $\bar{A}$ to temporal and homogenous backgrounds

$$\bar{A}_\mu(\tau, \mathbf{x}) = \bar{A}_0 \delta_{\mu 0},$$

upon which the functional $\tilde{\Gamma}[\bar{A}]$ reduces (up to a Euclidean volume factor) to an effective potential $V(\bar{A}_0)$ for the constant matrix field $\bar{A}_0$. Furthermore, due to global color symmetry, it is always possible to rotate this matrix $\bar{A}_0$ into the Cartan subalgebra[5] (CSA)

$$\beta g \bar{A}_0 = r_3 \frac{\lambda_3}{2} + r_8 \frac{\lambda_8}{2}\,, \tag{3.6}$$

where λ_3 and λ_8 are the diagonal Gell-Mann matrices. $V(\bar{A}_0)$ is reduced to a mere function of two variables $V(r_3, r_8)$. The non-trivial question how to self-consistently implement the components $r_{3/8}$ in various situations of interest and which values they can attain in practice is the object of discussion in the following section.

We also point out that, in the high temperature limit, the potential $V(r_3, r_8)$ can be computed in a loop-expansion outwith the CF model in pure FP theory [253].

3.2.1 Self-Consistent Background and Weyl Chambers

It was shown in Refs. [168, 254], that depending on the nature of the chemical potential, either real or imaginary, the self-consistent choices of the background components r_3 and r_8 follow distinct formats. In this short subsection, we briefly recall the key features and refer the reader to the respective Refs. [168, 254] for more detail.

Whenever the chemical potential is imaginary, it is easily shown that the background effective potential $V(r_3, r_8)$ becomes a real function upon taking $r \equiv (r_3, r_8)$ in the plane $\mathbb{R} \times \mathbb{R}$. In this case, the self-consistent backgrounds correspond to the absolute minima of the effective potential over $r \in \mathbb{R} \times \mathbb{R}$. Since the effective potential is invariant under (periodic) gauge transformations[6] which preserve the form of the background in Eq. (3.6), the r-plane is divided into physically equivalent cells, known as *Weyl chambers*. In practice, it is sufficient to restrict the analysis to one of these chambers, for instance the equilateral triangle of edges $(0, 0)$ and $2\pi(1, \pm 1/\sqrt{3})$, which we refer to as the *fundamental* Weyl chamber, shown in Fig. 3.3. Within this fundamental Weyl chamber, the confining value of the background components is located at the point $r = (4\pi/3, 0)$, the center of the triangle. Moreover, all charge conjugation invariant states lie on the median $r_8 = 0$. One deduces that for vanishing chemical potential the physical point can be identified by restricting completely to this median axis. For non-zero values of imaginary chemical potential, the physical point moves away from the axis $r_8 = 0$ within the fundamental Weyl chamber.

[1] A mass term for the compete gluon field is easily implemented but spoils the said center symmetry.

[2] Including dynamical quarks is trivial in the heavy quark limit, where chiral symmetry breaking effects are irrelevant [250, 251].

[3] This property assumes the positivity of the functional integral measure. For a discussion in the pure YM case, the reader is referred to Ref. [167].

[4] More precisely, center symmetry is explicitly broken by the gauge-fixing. However, the background field permits to maintain some formal gauge invariance, which then encodes a remnant of center symmetry.

[5] Here of su(3), but in principle of any gauge algebra in question.

[6] These include particular global color rotations, known as Weyl transformations.

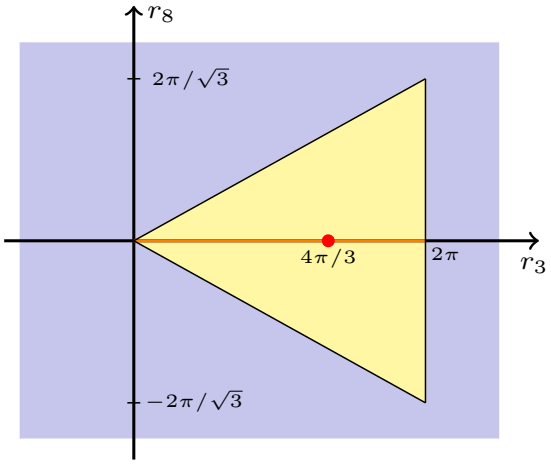

Figure 3.3: We illustrate the fundamental Weyl Chamber in light yellow in the plane spanned by the background components (r_3, r_8). The charge conjugation invariant states are given by the orange line on the $r_8 = 0$ axis, and the confining point at $(4\pi/3, 0)$ is shown in red.

Contrarily, for real chemical potentials, it was outlined in Ref. [168] that the effective potential requires consideration over the variables $(r_3, r_8) \in \mathbb{R}\times i\mathbb{R}$ such that $V(r_3, r_8)$ remains real-valued (whereas it is not anymore over $\mathbb{R}\times\mathbb{R}$) and the space of r is preserved under the requirement of self-consistent backgrounds. However, in such a configuration, the physical point is associated to a saddle-point and in the presence of multiple such saddle points, it is not well-defined which one to identify as the physical state of the system.[7] In Ref. [168], this ambiguity is viewed as a remnant of the sign problem in continuum approaches. In the same reference, it is also suggested that the appropriate criterion might be to opt for the deepest saddle-point. This choice is certainly well-motivated at $\mu = 0$—where one can equivalently choose either of the above spaces for r—and, by extension, to small real μ. Throughout this manuscript, we shall implement this very criterion as well.

In the literature, one can find similar discussions at real chemical potential in terms of the Polyakov loops ℓ and $\bar{\ell}$ [255, 208], as well as linking them to the background presented here [254]. Note that analytically continuing in r_8 to imaginary values formally corresponds to taking the variables ℓ and $\bar{\ell}$ as real and independent. The necessity of complex background components was equally mentioned in the context of saddle point approximations in Refs. [256, 257]. Another approach commonly employed in the literature is to simply take r_3 and r_8 real (or correspondingly in terms of the Polyakov loops) and to neglect the imaginary part of the potential by hand [77, 258]. However, as argued in [168, 259] and explained in section 4.3, this approach misses some of the essential physics. In particular, it completely neglects any effects of explicit breaking of charge conjugation by the nonzero chemical potential.

3.2.2 Root and Weight Diagram

In this section, we illustrate the various color modes, quarkonic and gluonic, summarized in the so-called root and weight diagram, shown in Fig. 3.4, which originates in considerations of the su(3) algebra generators t^a in the respective representations.

For non-trivial background in Eq. (3.6), it is convenient to decompose the field content in Eq. (3.4) along suitable bases which diagonalize the adjoint and fundamental background covariant derivatives $\bar{D}^{ab}_\mu \equiv \delta^{ab}\partial_\mu + gf^{acb}\bar{A}^c_\mu$ and $\bar{\mathcal{D}}_\mu \equiv \partial_\mu - igA^a_\mu t^a$. To treat the former, one introduces a Cartan-Weyl basis $\{t^\kappa\}$ in the su(N_c) Lie algebra. The parameters κ exist in two categories: Either $\kappa = 0^{(j)}$ is a *zero* or $\kappa = \alpha$ is a root. In case of a zero, the corresponding $t^{0^{(j)}}$'s span the CSA, where j samples over the various zeroes. In case of a root the t^α's simultaneously diagonalize the action of the elements of the CSA in the adjoint representation:

$$[t^{0^{(j)}}, t^\alpha] = \alpha_j t^\alpha \,. \tag{3.7}$$

Naturally, the roots $\alpha \equiv (\alpha_j)$ are vectors with the same number of (real) components as elements in the CSA. It is standard practice to represent them in the space $\mathbb{R}^{d_C}$, where d_C denotes the dimension of the CSA. By themselves, they form the so-called root diagram of the algebra. Upon specifying to SU(3), there

[7] This is in contrast to the case of an imaginary chemical potential, where standard arguments based on the (assumed) positivity of the integration measure dictate that the physical point corresponds uniquely to the absolute minimum of the background effective potential.

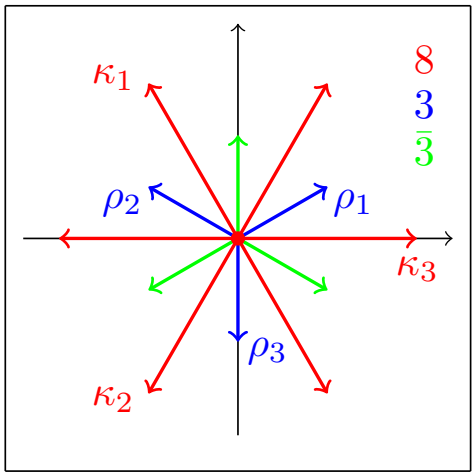

Figure 3.4: Diagram displaying the six roots and three plus three weights as vectors in the space of the Cartan subalgebra. The x-axis corresponds to r_3 and the y-axis to the r_8-direction. Roots in red sit in the adjoint representation and the weights in blue are in the fundamental representation **3** of SU(3), whereas the ones in green are in the anti-fundamental one, $\bar{\mathbf{3}}$.

are two zeros $0^{(3)}$ and $0^{(8)}$ to which correspond the generators $t^{0^{(3)}} = \lambda_3/2$ and $t^{0^{(8)}} = \lambda_8/2$. Additionally, on encounters six roots, which are given by $\pm(1,0)$, $\pm(1,\sqrt{3})/2$ and $\pm(1,-\sqrt{3})/2$ as illustrated in Fig. 3.4.

For quarks in the fundamental representation, because the $t^{0^{(j)}}$'s are hermitian matrices, one can choose an orthonormal vector basis $\{|\rho\rangle\}$ with $\langle\rho|\sigma\rangle = \delta_{\rho\sigma}$ such that the action of these generators is simultaneously diagonalized:

$$t^{0^{(j)}}|\rho\rangle = \rho_j|\rho\rangle\,, \tag{3.8}$$

where the ρ's, defined as $\rho \equiv (\rho_j)$, are called the weights of the (fundamental) representation. The weights entail the same number of (real) components ρ_j as the roots and allow for a depiction on the same root-weight diagram.[8] The fundamental representation **3** permits three nondegenerate weights $(1,1/\sqrt{3})/2$, $(-1,1/\sqrt{3})/2$ and $(0,-1/\sqrt{3})$, whereas for the anti-fundamental representation the weights are given by a global sign flip, *i.e.* $-(1,1/\sqrt{3})/2$, $(1,-1/\sqrt{3})/2$ and $(0,1/\sqrt{3})$. These vectors are depicted in Fig. 3.4.

For notational convenience in the subsequent chapters, we allocate specific labels to some of the weights and roots (which shall be in fact the only ones needed in practice, all others will be accounted for by symmetry requirements):

$$\rho_1 \equiv \frac{1}{2}\begin{pmatrix}1\\ \frac{1}{\sqrt{3}}\end{pmatrix}, \quad \rho_2 \equiv \frac{1}{2}\begin{pmatrix}-1\\ \frac{1}{\sqrt{3}}\end{pmatrix}, \quad \rho_3 \equiv -\begin{pmatrix}0\\ \frac{1}{\sqrt{3}}\end{pmatrix}, \tag{3.9}$$

and the roots

$$\kappa_1 \equiv \frac{1}{2}\begin{pmatrix}-1\\ \sqrt{3}\end{pmatrix}, \quad \kappa_2 \equiv -\frac{1}{2}\begin{pmatrix}1\\ \sqrt{3}\end{pmatrix}, \quad \kappa_3 \equiv \begin{pmatrix}1\\ 0\end{pmatrix}, \tag{3.10}$$

such that

$$\kappa_1 + \kappa_2 + \kappa_3 = 0\,, \tag{3.11}$$

as well as

$$\rho_3 = \rho_1 + \kappa_2, \quad \rho_1 = \rho_2 + \kappa_3, \quad \rho_2 = \rho_3 + \kappa_1, \tag{3.12}$$

and likewise, with $\bar{\rho}_i \equiv -\rho_i$,

$$\bar{\rho}_3 = \bar{\rho}_1 - \kappa_2, \quad \bar{\rho}_1 = \bar{\rho}_2 - \kappa_3, \quad \bar{\rho}_2 = \bar{\rho}_3 - \kappa_1, \tag{3.13}$$

which all satisfy cyclic (notational) permutivity. We also define $\kappa_{-1} = -\kappa_1$.

[8] The vectors $|\rho\rangle$ and ρ differ in meaning and origin. The former are vectors in the space over which the representation acts. The latter are the vectors of eigenvalues ρ_j in Eq. (3.8).

3.2.3 Feynman Rules in Landau-deWitt Gauge

Throughout this thesis, the only Feynman rules in the LdW gauge which will be actively called upon stem from the fermion sector: the free quark propagator and the quark-gluon vertex as well as the free gluon propagator to be used in the fermion sunset. Therefore, these are the only ones that shall be detailed at this point. For a complete discussion of the remaining quantities in the gauge sector, the reader is referred to Ref. [166] for the gauge group SU(2) specifically and, for a generic gauge group with semi-simple Lie algebra, to Ref. [167]. Prior to the beginning of the thesis, the explicit forms of the propagators were known in Ref. [168], which we briefly revoke in the current setting. On the other hand, the formula for the quark-gluon vertex had to be established, see Ref. [259].

With the particular decompositions of the various fields in (3.4) introduced in the previous section, *i.e.* the Cartan-Weyl basis and the vectors $|\rho\rangle$, the Feynman rules can be expressed in a simple manner. For instance, the momentum space free gluon propagator is found as

$$\langle a_\mu^{-\kappa}(Q')\, a_\nu^{\kappa}(Q)\rangle = (2\pi)^d \delta^{(d)}(Q+Q') \frac{P^\perp_{\mu\nu}(Q_\kappa)}{Q_\kappa^2 + m^2}\,, \tag{3.14}$$

where we make use of the bosonic generalized momentum

$$Q^\mu_\kappa \equiv Q^\mu + \delta^{\mu 0}\, T\, r_\kappa\,, \tag{3.15}$$

with $Q_\mu = (\omega_n, \vec{q})$ and $\omega_n = 2\pi n T$ a bosonic Matsubara frequency. We also denote $r_\kappa \equiv r\cdot\kappa = r_3\kappa_3 + r_8\kappa_8$ and remark that $Q^\kappa = -(-Q)^{-\kappa}$.

For the fermion part, after decomposing the color structure of the Grassmann fields via

$$\bar\psi_f = \sum_\rho \bar\psi_{f\rho}\, \langle\rho|\,, \qquad \text{and} \qquad \psi_f = \sum_\rho \psi_{f\rho}\, |\rho\rangle\,, \tag{3.16}$$

where $\psi_{f\rho}$ is a bispinor without color structure, the tree-level quark propagator is easily determined as

$$\langle \psi_{f\rho}(P')\bar\psi_{f\rho}(P)\rangle = (2\pi)^d \delta^{(d)}(P+P') \frac{i\not{P}_\rho + M_f}{P_\rho^2 + M_f^2}\,, \tag{3.17}$$

where M_f denotes the quark mass of flavor f. In analogy to (3.15) we have introduced[9] the fermionic generalized four-momentum

$$P^\nu_\rho \equiv P^\nu + \delta^{\nu 0}\,(T\, r_\rho + i\mu)\,, \tag{3.18}$$

with $P^\nu \equiv (\hat\omega_n, \vec{p})$ and $\hat\omega_n = 2\pi(n+1/2)T$ a fermionic Matsubara frequency. Also $r_\rho \equiv r\cdot\rho$.

In Eq. (3.18), the fermionic frequency P^0_ρ is not only shifted by $T\, r_\rho$ but also by $i\mu$, illustrating that the action of a temporal abelian gluonic background can be interpreted as an imaginary chemical potential, and vice versa. Whenever $\mu \neq 0$, one has $P^\rho \neq -(-P)^{-\rho}$, unless one simultaneously changes the sign of the chemical potential, $\mu \to -\mu$.

Lastly, we treat the quark-gluon vertex, which in the action $-S$ (we have included the prefactor minus sign in the exponential within the expression for the generating functional) originates from the interaction term

$$i\bar\psi_f a^\kappa t^\kappa \psi_f = \sum_{\rho,\sigma} i\bar\psi_{f\sigma} a^\kappa \langle\sigma|t^\kappa|\rho\rangle \psi_{f\rho}\,. \tag{3.19}$$

where we have again used the color decompositions in (3.16). It is easily verified that the associated Feynman rule is given by

$$ig\,\delta(P+Q+P')\,\gamma_\mu t^\kappa_{\sigma\rho}\,, \tag{3.20}$$

with $t^\kappa_{\sigma\rho} \equiv \langle\sigma|t^\kappa|\rho\rangle$, where all momenta are either in- or outgoing, and σ denotes an outgoing weight while ρ and κ are an ingoing weight and root respectively. We draw attention to

$$\begin{aligned} t^{0^{(j)}} t^\kappa\, |\rho\rangle &= [t^{0^{(j)}}, t^\kappa]\, |\rho\rangle + t^\kappa t^{0^{(j)}}\, |\rho\rangle \\ &= (\kappa+\rho)_j\, t^\kappa\, |\rho\rangle\,, \end{aligned} \tag{3.21}$$

[9] We use the greek letters μ and ν to denote Lorentz indices, ρ and σ to denote the weights of the fundamental representation and κ to denote the zeros and roots of the algebra. Note that μ primarily refers to the chemical potential when it is not a sub/superscript. For simplicity, we use the same notation for bosonic and fermionic four-momenta, and to ensure clarity, we shall (mostly) reserve the letters Q and K to bosonic momenta and the letters P and L to fermionic ones.

which means that $t^\kappa|\rho\rangle$ is either 0 or collinear to $|\rho+\kappa\rangle$. In particular, the nonvanishing elements of $t^\kappa_{\sigma\rho}$ satisfy the color conservation rule $\sigma = \rho + \kappa$. By extension, all elements of the color tensor

$$\mathcal{D}_{\sigma,\rho\kappa} \equiv t^\kappa_{\sigma\rho} t^{-\kappa}_{\rho\sigma} = \mathcal{D}_{\rho,\sigma(-\kappa)}\,, \tag{3.22}$$

must vanish unless $\sigma = \rho + \kappa$.

Finally, we outline some useful relations encountered when summing over the various color modes, *e.g.*, in Feynman diagrams. For instance, one finds that

$$\sum_{\rho\kappa} \mathcal{D}_{\sigma,\rho\kappa} = C_F\,, \qquad \text{and similarly} \qquad \sum_{\sigma\rho} \mathcal{D}_{\sigma,\rho\kappa} = T_F\,, \tag{3.23}$$

where C_F is the quadratic Casimir of the fundamental representation, which equals 4/3 in SU(3), and T_F is the normalization of the generators in the fundamental representation, chosen as 1/2 in Eq. (2.13).

3.2.4 Background field and the Deconfinement Transition

We are now in the position to discuss the relation between the background field in (3.6) and the Polyakov loops ℓ and $\bar{\ell}$. Based on their definitions in (2.18) and (2.19), the loops can be expanded in the coupling, as functions of the physical values of the background field components r_3 and r_8. At leading order, this yields the well-known formula

$$\ell = \frac{e^{-i\frac{r_8}{\sqrt{3}}} + 2\cos(r_3/2)\, e^{i\frac{r_8}{2\sqrt{3}}}}{3} + \mathcal{O}\left(g^2\right). \tag{3.24}$$

For pure YM, the next-to-leading order (NLO) correction to ℓ has been worked out in Ref. [167]; see Eq. (87) of that reference. Fortunately, at NLO, the YM expression coincides with the corresponding unquenched counterpart. This is due to the fact that explicit quark loops only appear at NNLO and thus at NLO the mere effects of dynamical quarks enter the Polyakov loops indirectly via the altered physical values of r_3 and r_8. The explicit expression of ℓ in terms of r_3 and r_8 remains, however, applicable.

For the anti-Polyakov loop $\bar{\ell}$ in (2.19) one could, of course, derive a similar expression to (3.24) from first principles. However, provided one carefully accounts for the nature of the variable r_8 and the chemical potential μ (real or imaginary), its results can directly be deduced from the corresponding expression for ℓ. In particular, as detailed in section 3.2.1, for $\mu \in i\mathbb{R}$, the background components are real, $r_{3,8} \in \mathbb{R}$, and therefore $\bar{\ell} = \ell^*$ [168], in agreement with the general discussion of Ref. [208]. At leading order, this results in

$$\bar{\ell} = \frac{e^{i\frac{r_8}{\sqrt{3}}} + 2\cos(r_3/2)\, e^{-i\frac{r_8}{2\sqrt{3}}}}{3} + \mathcal{O}\left(g^2\right). \tag{3.25}$$

Similarly, the NLO correction to $\bar{\ell}$ is found simply as the complex conjugate of Eq. (87) of Ref. [167]. On the other hand, for a real chemical potential, one finds the appropriate expression of $\bar{\ell}$ by analytically continuing the formula in Eq. (3.25) (and likewise for the NLO counterpart) from $r_8 \in \mathbb{R}$ to $r_8 \in i\mathbb{R}$. It is straightforward at LO and a little more cumbersome at NLO to check that this continuation yields $\bar{\ell} \in \mathbb{R}$ for real μ, as must be the case based on general arguments [168, 208]. Further, it can be shown that this recipe of analytic continuation coincides with the first-principle computation of $\bar{\ell}$ directly in a background setting of $(r_3, r_8) \in \mathbb{R} \times i\mathbb{R}$, for instance along the lines of Ref. [167].

A phase of confined static charges ($\ell = 0$) is associated to the center symmetric point $(r_3, r_8) = (4\pi/3, 0)$ in the fundamental Weyl chamber. In an unquenched scenario, center symmetry is explicitly broken and this association of background position to symmetry does no longer hold. Nonetheless, a position in close proximity of $(4\pi/3, 0)$ still implies $F_q \approx \infty$ and can therefore still be attributed to a confining phase.

Part II

Heavy Quark QCD

4 Curci-Ferrari Model at Two-Loop Order

In the following two chapters we study the physics of center symmetry and the deconfinement transition in the heavy quark regime by means of a perturbative expansion. In this respect, our results indicate an valid description of the underlying dynamics.

The purpose of this chapter is to compute the two-loop corrections to a one-loop CF analysis [168] (which we briefly recall in section 4.1) of the heavy quark corner of the Columbia Plot. To this end, it is essential to compute the correction terms obtained from the quark-sunset diagram in the presence of a non-trivial gluon background in LdW gauge at finite temperature and density. We outline this calculation and its renormalization in section 4.2. Our results for the phase diagram at vanishing, imaginary and real chemical potential are gathered in section 4.3, where, overall, we find an improved agreement with lattice data due to the two-loop corrections as compared to leading-order findings. Additionally, based on simple thermodynamic arguments, we demonstrate that the nonmonotonous behavior of the Polyakov loops as functions of (real) chemical potential does not conflict with their interpretation in terms of quark and anti-quark free energies, which clarifies recent claims in the literature. Finally, in section 4.4, we critically analyze the thermodynamic stability of the system at two-loop order. As previously observed in the pure YM case [166, 167], two-loop corrections cure some unphysical features encountered at one-loop order. Finally, some concluding remarks will be given in section 4.5. The work presented in this chapter has been published in Ref. [259].

4.1 Review of the one-loop results

In this section, we briefly recall the analysis of the CF model at one-loop level and refer the reader to Ref. [168]. At one loop order, the background field effective potential takes the form

$$V^{(1)}(r,T,\mu) \quad = \quad V_g^{(1)}(r,T) + V_q^{(1)}(r,T,\mu)\,. \tag{4.1}$$

The pure-glue one-loop contribution to the potential, which we have denoted by $V_g^{(1)}(r,T)$, reads in its most simplified form [167, 165]:

$$V_g^{(1)}(r,T) = \frac{3}{2}\mathcal{F}_m(r) - \frac{1}{2}\mathcal{F}_0(r), \tag{4.2}$$

with

$$\mathcal{F}_m(r) = \frac{T}{\pi^2}\sum_\kappa \int_0^\infty dq\, q^2 \ln\left[1 - e^{-\beta\varepsilon_q + i r_\kappa}\right], \tag{4.3}$$

where $\varepsilon_q = \sqrt{q^2+m^2}$. Similarly, the one-loop quark term [250, 251, 168, 88], denoted $V_q^{(1)}(r,T,\mu)$, is given by

$$V_q^{(1)}(r,T,\mu) = \sum_{f,\rho} V_f^{(1)}(\mu - iT r_\rho), \tag{4.4}$$

R_{N_f}	$N_f = 1$	$N_f = 2$	$N_f = 3$
CF1 [168]	6.74	7.59	8.07
DSE [77]	1.42	1.83	2.04
Matrix [88]	8.04	8.85	9.33
Lattice [191]	7.23	7.92	8.33

Table 4.1: We review the one-loop results of the heavy quark critical line in the Columbia plot, in terms of the critical ratios $R_{N_f} \equiv [M_c/T_c](N_f)$, as compared to the findings of some literature studies.

with the contribution of a single quark flavor f in a definite color state at nonzero chemical potential μ being

$$V_f^{(1)}(\mu) = -\frac{T}{\pi^2}\int_0^\infty \mathrm{d}q\, q^2 \left\{ \ln\Big[1 + e^{-\beta\left(\varepsilon_q^f + \mu\right)}\Big] + \ln\Big[1 + e^{-\beta\left(\varepsilon_q^f - \mu\right)}\Big] \right\}, \tag{4.5}$$

where $\varepsilon_q^f = \sqrt{q^2 + M_f^2}$. In the above formulae, ρ and κ denote, as usual, the weights and roots in the fundamental and adjoint representations of SU(3); see section 3.2 for definitions.

It is remarkable that the simple one-loop expression (4.1) in the present CF model reproduces the whole complexity of the phase diagram described in section 2.2.3 and 2.2.4, both at real and imaginary chemical potential. Moreover, the numerical values of the various quantities of interest (temperature, quark masses) at the (tri)critical points are in very good agreement with lattice results. A respective sample in the case of vanishing chemical potential is presented in Tab. 4.1 and further results are summarized in the various tables presented in section 4.3. Note that the values $\mathcal{R}_{N_f}$ obtained with CF1 in Tab. 4.1 do not depend on the parameters of the model (m and g).

4.2 Two-loop corrections from the Quark-Sunset Diagram

We now consider the inclusion of the two-loop quark contribution to the background field effective potential, $V_q^{(2)}(r,T,\mu)$, represented by the quark sunset diagram shown in Fig. 4.1. Meanwhile, the YM two-loop contribution, denoted $V_g^{(2)}(r,T)$, has already been computed in Refs. [166, 167] and will not be recalled here.

Once the terms associated to the diagram in Fig. 4.1 are computed in section 4.2.1, it is

$$V^{(1+2)}(r,T,\mu) \quad = \quad V^{(1)}(r,T,\mu) + V_g^{(2)}(r,T) + V_{\mathrm{q}}^{(2)}(r,T,\mu), \tag{4.6}$$

where $V^{(1)}(r,T,\mu)$ is readily found in Eq. (4.1). In appendix B.4, we outline consistency checks of our calculations using the symmetries of the full potential $V^{(1+2)}$, after having dealt with renormalization and various possible schemes in section 4.2.2.

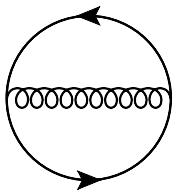

Figure 4.1: Quark sunset diagram representing the $\mathcal{O}(g^2)$ two-loop correction $V_{\mathrm{q}}^{(2)}(r,T,\mu)$ due to dynamical heavy quarks in the perturbative expansion (4.6) of the background field effective potential.

The gluon mass at two-loop order takes a slightly different value than at one-loop level. This is not surprising, given the particular way it is fixed against lattice calculations of the pure YM gluon propagator at the appropriate order in the loop expansion. Refer to section 3.1.1 for more information. At one-loop level the value is $m = 500$ MeV as compared to $m = 540$ MeV at two-loop,[1] together with a coupling of $g = 4.9$.

4.2.1 Quark sunset contribution $V_{\mathrm{q}}^{(2)}(r,T,\mu)$

Let us now use the Feynman rules listed in section 3.2 to establish the expression corresponding to the (two-loop) quark sunset diagram in Fig. 4.1. In the process, the UV divergences are accounted

[1] Here, in the unquenched theory, these values of m and g are kept the same as the ones employed in the quenched two-loop study [167] to simplify comparisons. Furthermore, a value of $g = 4.9$ seems to naively rule out any perturbative expansion. However, as outlined in Ref. [132], the true loop-expansion parameter in the CF model is $\lambda/(1+\tilde{m}^2(\mu_r))$ with $\tilde{m}^2(\mu_r) = m^2/\mu_r^2$ and $\lambda = g^2 N_c/(16\pi^2)$. For the flow best reproducing lattice results at one-loop, it never exceeds 0.4.

for in dimensional regularization with $d = 4 - 2\epsilon$. With the conventions introduced in section 2.1 for denoting bosonic and fermionic Matsubara sum-integrals by $\int_Q f(Q)$ and $\int_{\hat{P}} f(P)$ respectively, the full contribution from the quark sunset diagram is found as

$$V_q^{(2)}(r,T,\mu) = -\frac{g^2}{2}\sum_f \sum_{\sigma\rho\kappa} \mathcal{D}_{\sigma,\rho\kappa} \int_{\hat{P}} \int_Q G_m(Q^\kappa) G_{M_f}(P^\rho) G_{M_f}(L^\sigma)\, P^\perp_{\mu\nu}(Q^\kappa) \times \mathrm{tr}\left[\gamma_\mu (i\not{P}^\rho + M_f)\gamma_\nu (i\not{L}^\sigma + M_f)\right], \tag{4.7}$$

where $L^\sigma = P^\rho + K^\kappa$. For more information on the tensor $\mathcal{D}_{\sigma,\rho\kappa}$ as well as the entire color structure involved, refer to section 3.2.

We point out that (4.7) is a particular case of the more involved expression (B.1) in appendix B, where the quark sunset is computed in a generic setting with color-dependent fermion masses. In contrast, the quark masses of (4.7) are color- and thus background-independent. The detailed calculation of the Matsubara sums and momentum integrals is described in appendix B. Here, we give a brief summary.

First, we reduce the trace structure and rewrite $V_q^{(2)}(r,T,\mu)$ as a combination of scalar-type integrals, for instance in terms of the tadpoles

$$J_m^\kappa \equiv \int_Q G_m(Q^\kappa)\,, \quad \tilde{J}_m^\kappa \equiv \int_Q Q_0^\kappa G_m(Q^\kappa)\,, \quad J_M^\rho \equiv \int_{\hat{P}} G_M(P^\rho)\,, \quad \tilde{J}_M^\rho \equiv \int_{\hat{P}} P_0^\rho G_M(P^\rho)\,, \tag{4.8}$$

as well as the scalar sunset

$$S_{mMM}^{\kappa\rho\sigma} \equiv \int_{\hat{P}} \int_Q G_m(Q^\kappa) G_M(P^\rho) G_M(L^\sigma)\,. \tag{4.9}$$

With these definitions, we obtain

$$\begin{aligned} V_q^{(2)}(r,T,\mu) = -\frac{g^2}{4}\mathrm{tr}\mathbb{1}\sum_f \sum_{\sigma\rho\kappa} \mathcal{D}_{\sigma,\rho\kappa} \Bigg\{ &(d-2)\Big[J_m^\kappa \left(J_{M_f}^\rho + J_{M_f}^\sigma \right) - J_{M_f}^\rho J_{M_f}^\sigma \Big] \\ &+ \frac{2}{m^2}\Big[\left(\tilde{J}_0^\kappa - \tilde{J}_m^\kappa \right)\left(\tilde{J}_{M_f}^\rho - \tilde{J}_{M_f}^\sigma \right) \Big] + \Big[(d-2)m^2 + 4M_f^2 \Big] S_{mM_fM_f}^{\kappa\rho\sigma} \Bigg\}. \end{aligned} \tag{4.10}$$

We stress that dealing with the trace structure in this manner leaves an overall factor $\mathrm{tr}\mathbb{1}$, which shall be important in managing renormalization in dimensional regularization in the next section 4.2.2. Thus, we leave it generic for now.

In a second step, we evaluate the Matsubara sums involved in the scalar-type integrals. In so doing, it is convenient (for renormalization purposes later) to group together all terms containing the same amount of either Bose–Einstein and/or Fermi-Dirac distribution functions, indicated hereafter by $(\#n)$. We stress that the pure vacuum contribution, without thermal factors $(0n)$, is independent of the background, temperature, and chemical potential and is thus systematically discarded. This is justified since the neglected vacuum terms do not impact the in-medium analysis of any thermodynamic observable. Eventually, we arrive at

$$\begin{aligned} V_q^{(2)}(r,T,\mu) = &-g^2\mathrm{tr}\mathbb{1}\sum_f \Bigg\{ \frac{1}{4}\Big[(d-2)J_{M_f}(0n) + \frac{1}{2}\left[(d-2)m^2 + 4M_f^2 \right] I_{M_fM_f}(0n) \Big] \sum_\kappa J_m^\kappa(1n) \\ &+ \frac{C_F}{2}\Big[(d-2)\left[J_m(0n) - J_{M_f}(0n) \right] + \left[(d-2)m^2 + 4M_f^2 \right] I_{M_fm}(0n) \Big] \sum_\rho J_{M_f}^\rho(1n) \Bigg\} \\ &- \frac{g^2}{2}\mathrm{tr}\mathbb{1}\sum_f \sum_{\sigma\rho\kappa} \mathcal{D}_{\sigma,\rho\kappa} \Bigg\{ \Big[J_{M_f}^\rho(1n) + J_{M_f}^\sigma(1n) \Big] J_m^\kappa(1n) - J_{M_f}^\rho(1n) J_{M_f}^\sigma(1n) \\ &+ \frac{1}{m^2}\left[\tilde{J}_0^\kappa(1n) - \tilde{J}_m^\kappa(1n) \right]\Big[\tilde{J}_{M_f}^\rho(1n) - \tilde{J}_{M_f}^\sigma(1n) \Big] + (m^2 + 2M_f^2) S_{mM_fM_f}^{\kappa\rho\sigma}(2n) \Bigg\}, \end{aligned} \tag{4.11}$$

which is the expression given in Eq. (B.15), minus the subtracted vacuum terms. As explained in appendix B, the UV divergences occur in the $(0n)$ pieces[2] of the scalar-type integrals and it thus follows that the

[2]The thermal part of the scalar sunset also includes UV divergences, however they can be rewritten in the form of a $(0n) \times J(1n)$ contribution.

first two lines contain $1/\epsilon$ poles that have to be accounted for.[3] Their renormalization is discussed in the subsequent section 4.2.2. On the other hand, all terms in the last two lines are UV finite.

Once Eq. (4.11) is renormalized, as detailed in the following section, it is interesting to study its behavior in various parameter regimes, for example for small or large values of temperature or chemical potential. Explicit expansions of these types can be useful for many situations of physical interest, such as early universe cosmology or dense astrophysical objects (neutron stars *etc.*), and their respective full discussions can be found in appendix D.

Furthermore, $V_q^{(2)}(r,T,\mu)$ as given in Eq. (4.11), as well as its renormalized version, together with the scalar-type integrals it features, all satisfy a selection of symmetries, that provide important cross-checks for our calculations. Finally, it is precisely in terms of these symmetries that a further simplification to the last two lines of (4.11) can be achieved. For instance, we note that κ either constitutes a zero $0^{(j)}$ or a root α. The sum over all κ's can therefore be split into these two cases. For the former, *i.e.* $\kappa = 0^{(j)}$, we immediately have $\rho = \sigma$ and $\mathcal{D}_{\rho,\rho 0^{(j)}} = \rho_j^2$. Since $J_m^{0^{(j)}}(1n)$, $\tilde{J}_m^{0^{(j)}}(1n)$ and $S_{mMM}^{0^{(j)}\rho\rho}(2n)$ are all j-independent, we obtain, in SU(3), where $\rho^2 = 1/3$, for the first piece of the last two lines of Eq.(4.11),

$$-2g^2 \sum_f \sum_\rho \rho^2 \Big\{ J_{M_f}^\rho(1n) \Big[2J_m^0(1n) - J_{M_f}^\rho(1n) \Big] + \big(m^2 + 2M_f^2 \big) S_{mM_f M_f}^{0\rho\rho}(2n) \Big\} . \tag{4.12}$$

In contrast, if $\kappa = \alpha$, no such simplifications occurs. Nonetheless, we remark $\mathcal{D}_{\sigma,\rho\alpha} = \mathcal{D}_{\rho,\sigma(-\alpha)}$, $J^\alpha(1n) = J^{-\alpha}(1n)$, $\tilde{J}^\alpha(1n) = -\tilde{J}^{-\alpha}(1n)$, and $S_{mMM}^{\alpha\rho\sigma}(2n) = S_{mMM}^{(-\alpha)\sigma\rho}(2n)$ enabling the sum over α to be restricted[4] to only one of the two contributions (σ,ρ,α) and $(\rho,\sigma,-\alpha)$. As outlined in section 3.2, SU(3) permits for three such independent contributions.

4.2.2 Renormalization

As mentioned above, the expression (4.11) contains UV divergences and requires renormalization. Alongside the quark sunset diagram shown in Fig. 4.1, one also has to supplement Eq. (4.11) with the associated counterterm diagrams, depicted in Fig. 4.2. A similar procedure has already been performed for the YM two-loop contribution in Refs. [166, 167] and when writing $V_q^{(2)}(r,T)$ in Eq. (4.6), it is understood as a renormalized quantity. By default, all one loop terms $V^{(1)}(r,T,\mu)$ are inherently UV finite (up to an overall vacuum piece) and thus don't require renormalization in the first place. Hence, to render Eq. (4.6) finite, we merely have to account for the divergences occurring in Eq. (4.11). The necessary diagrams to accomplish this task are the counterterm quark loop of the form

$$\begin{aligned} -\sum_f \int_{\hat{P}} \mathrm{tr}(-\delta Z_{\psi_f} i\not{P}_\rho + \delta M_f)(i\not{P}_\rho + M_f) G_{M_f}(P_\rho) &= -\mathrm{tr}\mathbb{1} \sum_f \int_{\hat{P}} (\delta Z_{\psi_f} P_\rho^2 + M_f \delta M_f) G_{M_f}(P_\rho) \\ &= -\mathrm{tr}\mathbb{1} \sum_f M_f (\delta M_f - M_f \delta Z_{\psi_f}) \sum_\rho J_{M_f}^\rho , \end{aligned} \tag{4.13}$$

as well as the counterterm gluon loop

$$\frac{d-1}{2} (\delta m^2 - m^2 \delta Z_A) \sum_\kappa J_m^\kappa . \tag{4.14}$$

The gluon loop is also responsible for the (partial) renormalization of the YM two-loop diagrams treated

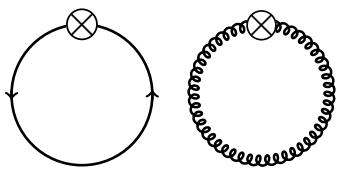

Figure 4.2: Quark and gluon loop counterterm diagrams contributing to the potential in Eq. (4.18) via the expressions in Eqs. (4.13) and (4.14) respectively. The corresponding ghost loop diagram vanishes in dimensional regularization.

in Refs. [166, 167] by resorting to a particular choice of renormalization scheme. The counterterms δm^2 and Z_A can be split as

$$\delta m^2 \equiv \delta m_g^2 + \delta m_q^2 \quad \text{and} \quad \delta Z_A \equiv \delta Z_{A,g} + \delta Z_{A,q} . \tag{4.15}$$

[3] All $1/\epsilon^2$ poles solely appear in the pure vacuum terms of the form $(0n) \times (0n)$ which have been discarded from consideration. Their renormalization amounts to a constant subtraction (defining the zero of energy).

[4] Trivially, this restriction can only be realized if the summand in question does in fact display the above-mentioned symmetry. As can be checked, this is true for the expressions in (4.11).

The terms labelled by a "g" are the pieces that absorb the YM divergences, which shall thus not be re-considered hereafter. It is possible to do so because we intend to keep the same YM renormalization as in Refs. [166, 167] to better enable comparisons and the study of any unquenching effects. In light of this guiding principle, it is imperative that any renormalization condition implemented for the quark contributions, labelled by "q", matches the previous YM renormalization scheme.

We are now in the position to specify the explicit finite and divergent parts in the first two lines of Eq. (4.11) in more detail. In particular, as shown in in appendix B.3, they easily rewrite as[5]

$$-\frac{g^2\mathrm{tr}\,\mathbb{1}}{64\pi^2}\sum_f\left\{m^2\left[\frac{1}{\epsilon}+\ln\frac{\bar{\mu}^2}{M_f^2}\right]+m^2+4M_f^2-2\left(m^2+2M_f^2\right)\mathcal{T}_f\,\arctan\left(\mathcal{T}_f^{-1}\right)\right\}\sum_\kappa J_m^\kappa(1n) \tag{4.16}$$

and

$$+\frac{g^2C_F\mathrm{tr}\,\mathbb{1}}{16\pi^2}\sum_f\left\{m^2-3M_f^2\left[\frac{1}{\epsilon}+\ln\frac{\bar{\mu}^2}{M_f^2}\right]-\left(m^2+2M_f^2\right)\right. \tag{4.17}$$
$$\left.\times\left[2-\frac{m^2}{2M_f^2}\ln\frac{m^2}{M_f^2}-\frac{m^2}{M_f^2}\mathcal{T}_f\,\arctan\left(\mathcal{T}_f\right)\right]\right\}\sum_\rho J_{M_f}^\rho(1n)\,.$$

where we used $\mathcal{T}_f\equiv\sqrt{\frac{4M_f^2}{m^2}-1}$, $\bar{\mu}^2=4\pi\mu_r^2e^{-\gamma}$, with μ_r the renormalization scale and γ the Euler-MacLaurin constant. In a further step, after some algebra, one can verify that the expressions in the curly brackets above can be rewritten as the real part of the quark-loop contribution to the vacuum transverse gluon self-energy $\Pi_q^\perp(Q^2\to-m^2)$ for (4.16), and the one-loop vacuum quark self-energy $\Sigma_f(P^2\to-M_f^2)$ for (4.17), with $\Sigma_f(P)=-iA_f(P^2)\not{P}+M_fB_f(P^2)$. Here, $Q^2\to-m^2$ has to be understood as the analytic continuation from $Q^2>0$ to $Q^2=-m^2-i0^+$ and similarly for $P^2=-M_f^2-i0^+$. In particular, after combination with the counterterm contributions in (4.13) and (4.14), it is from (4.16) and (4.17),

$$\begin{aligned}
V_q^{(2)}(r,T,\mu) &= \frac{d-1}{2}\left[\delta m_q^2-m^2\delta Z_{A,q}+\Pi_q^\perp(Q^2\to-m^2)\right]\sum_\kappa J_m^\kappa(1n) \\
&+ \mathrm{tr}\,\mathbb{1}\sum_f M_f^2\left\{\delta Z_{\psi_f}-\frac{\delta M_f}{M_f}+\left[A_f-B_f\right](P^2\to-M_f^2)\right\}\sum_\rho J_{M_f}^\rho(1n) \\
&- \frac{g^2}{2}\mathrm{tr}\mathbb{1}\sum_f\sum_{\sigma\rho\kappa}\mathcal{D}_{\sigma,\rho\kappa}\left\{\left[J_{M_f}^\rho(1n)+J_{M_f}^\sigma(1n)\right]J_m^\kappa(1n)-J_{M_f}^\rho(1n)J_{M_f}^\sigma(1n)\right. \\
&\qquad\left.+\frac{1}{m^2}\left[\tilde{J}_0^\kappa(1n)-\tilde{J}_m^\kappa(1n)\right]\left[\tilde{J}_{M_f}^\rho(1n)-\tilde{J}_{M_f}^\sigma(1n)\right]+(m^2+2M_f^2)S_{mM_fM_f}^{\kappa\rho\sigma}(2n)\right\}.
\end{aligned} \tag{4.18}$$

We stress that, in writing Eq. (4.18), we have implicitly redefined $V_q^{(2)}(r,T,\mu)$ to denote the renormalized quark sunset contribution to the background effective potential. Similarly we point out that in the first line the flavor sum is hidden inside $\Pi_q^\perp$ and likewise for the factors g^2 in $\Pi_q^\perp$, A_f and B_f.

Another issue we briefly want to raise concerns the $\mathrm{tr}\,\mathbb{1}$ factors, which are not uniquely defined in dimensional regularization and many conventions are *a priori* permissible. The sole requirement to be fulfilled is that upon taking the $\epsilon\to0$ limit, we must have $\mathrm{tr}\,\mathbb{1}\to4$. It is evident that the thermal part of the renormalized potential $V_q^{(2)}(r,T,\mu)$ in Eq. (4.18) must be independent of the chosen convention and always yield the same result in the appropriate limit. In fact, this seems obvious and is easily checked for the explicit expression in Eq. (4.18). On the other hand, it is imperative to consistently implement the same convention both in the computation of the potential and the self-energies and any deviations prohibit a sensible renormalization procedure.

By observation from Eqs. (4.16) and (4.17), the divergent parts of the renormalization factors are fixed as

$$\left[\delta M_f-M_f\delta Z_{\psi_f}\right]_{\mathrm{div}}=-\frac{3g^2C_FM_f}{16\pi^2\epsilon}\,, \tag{4.19}$$

and

$$\left[\delta m_q^2-m^2\delta Z_{A,q}\right]_{\mathrm{div}}=\frac{g^2m^2}{96\pi^2\epsilon}N_f\,\mathrm{tr}\,\mathbb{1}\,. \tag{4.20}$$

[5]For simplicity, we have restricted to the scenario of $M_f>2m$, but the other cases are equally straightforward.

Equivalently,[6] the same finding could have been deduced from the identification via self-energies and their explicit computation in Ref. [161]. Thus, this agreement serves as a consistency check.

With the divergent terms firmly fixed, there remains a choice on the respective finite parts of the counterterms. Here, we shall consider renormalization schemes of the form:

$$0 = \delta m_q^2 + \Pi_q^\perp(0)\,, \tag{4.21}$$

$$0 = \delta Z_{A,q} + \frac{\delta m_q^2 + \Pi_q^\perp(\mu_r^2)}{\mu_r^2}\,, \tag{4.22}$$

$$0 = \delta Z_{\psi_f} + A_f(\hat{\mu}_f^2)\,, \tag{4.23}$$

$$0 = \delta M_f + M_f B_f(\mu_f^2)\,, \tag{4.24}$$

where we insist that these conditions agree with the YM two-loop analogues discussed in Ref. [167]. The presence of the arbitrary scales μ_r, $\hat{\mu}_f$ and μ_f allows for a consideration of various schemes, see below. Note that δm_q^2 is determined irrespective of the values of these scales and one always finds $\delta m_q^2 = 0$.

In the following we consider

$$\mu_r^2 = 1\text{GeV} \qquad \hat{\mu}_f^2 = \mu_r^2 \qquad \mu_f^2 = 0 \qquad \text{"CF2"}\,, \tag{4.25}$$

$$\mu_r^2 = 1\text{GeV} \qquad \hat{\mu}_f^2 = -M_f^2 \qquad \mu_f^2 = -M_f^2 \qquad \text{"CF2 q.o."}\,, \tag{4.26}$$

$$\mu_r^2 = -m^2 \qquad \hat{\mu}_f^2 = 1\text{GeV} \qquad \mu_f^2 = 0 \qquad \text{"CF2 g.o."}\,, \tag{4.27}$$

$$\mu_r^2 = -m^2 \qquad \hat{\mu}_f^2 = -M_f^2 \qquad \mu_f^2 = -M_f^2 \qquad \text{"CF2 f.o."}\,, \tag{4.28}$$

which are all interesting in their own right for some particular reason. The first scenario, labelled "CF2", is the main scheme considered and in which we exert the most confidence. Here, $\mu_r = 1$GeV, in agreement with Ref. [167], and thus the entire gluonic sector of Eq. (4.6) is treated on the same footing. Generically, for arbitrary values of μ_r, the terms in (4.16) result in a polynomial approach ($\sim 1/M_f^2$) to the YM theory when taking the large quark mass limit. Contrarily, all other terms in Eq. (4.18) are exponentially suppressed. It is clear that this polynomial behavior is a direct consequence of the presence of the CF gluon mass. This is based on the fact that for vanishing gluon mass, $m = 0$, BRST symmetry, applied both to the QCD and YM cases, imposes $\Pi_q^\perp(Q^2 = 0) = 0$ and thus the prefactor of $\sum_\kappa J_m^\kappa(1n)$ in Eq. (4.16) vanishes. Hence, one might naturally envision testing the approach to YM in lattice QCD simulations to supply a direct test of the CF model. However, there exists a particular scheme, with $\mu_r^2 = -m^2$, eliminating the terms in (4.16) or, equivalently the first line of (4.18) entirely. Therefore, the polynomial behavior appears to be a scheme-dependent artifact. Letting $\mu_r^2 = -m^2$ corresponds to the gluon on-shell scheme (g.o.) and can be seen as more physical than the choices in (4.25). This is because it parametrizes the theory in terms of the pole of the propagator, which is invariant under renormalization group effects [260].

Analogously, the contributions in (4.17), or the second line of (4.18), can be entirely eliminated upon implementing the quark on-shell (q.o.) scheme for $\hat{\mu}_f^2 = \mu_f^2 = -M_f^2$. Finally, in the full on-shell (f.o.) scheme one evades all terms in either of the first two lines of (4.18). We remark that for the gluon on-shell schemes, keeping $m = 540$ MeV fixed is questionable, since the gluon mass is scheme-dependent, and, moreover, one expects a complex pole in the CF model. Nonetheless, to keep the discussion relatively simple, we chose to use the same mass value throughout all schemes considered. In section 4.3, we discuss some results for all schemes in (4.25)-(4.28) and moreover briefly comment on the effects of allowing for arbitrary values of $\hat{\mu}_f$ and μ_f.

4.3 Results

In this section we finally showcase our two-loop results for the phase diagram and Columbia Plot, as obtained from the potential in Eq. (4.6) with the quark-sunset contribution in the form (4.18), and parameter values $m = 540$ MeV and $g = 4.9$. We consider various values of chemical potential, from vanishing, imaginary to real. In so doing, for zero μ, we also test all four renormalization schemes given in (4.25)-(4.28). For non-zero values of μ, we restrain to the scheme (4.25).

[6] At $T = \mu = 0$, the LdW gauge reduces to the Landau gauge studied in Ref. [161]. Note also that this reference employs a different sign convention for the self-energy.

4.3.1 Vanishing chemical potential

In the simplest case of vanishing chemical potential, one can restrict to the axis $r = (r_3, 0)$ with $r_3 \in [0, 2\pi]$ due to invariance under charge conjugation, see section 3.2. For $\mu = 0$, $r_8 = 0$, the background effective potential $V^{(1+2)}(r_3, T, 0)$ is real and the physical point can self-consistently be identified with its absolute minimum.

In this setup, our results for the heavy quark corner of the Columbia Plot are shown pictorially in Fig. 4.3 and numerically in Tab. 4.2. Qualitatively, they don't change the picture given in the one-loop CF analysis of section 4.1, which has already been in agreement with the content of section 2.2.3. Thus, the focus here lies purely on the quantitative aspects. Firstly, one notices that the second order boundary lines in Fig. 4.3 are significantly pushed towards larger quark masses in the two-loop study. This effect occurs in all renormalization schemes under consideration. We observe that the critical temperatures along the boundary lines are almost constant,[7] Its particular value sits around $T_c/m \approx 0.456$, which is slightly smaller than the YM two-loop (first order) counterpart at $T_c/m \approx 0.474$ [167]. Hence, at both one- and two-loop level, unquenching leads to a lowered critical temperature.

In order to ensure a meaningful comparison between our two-loop findings and other approaches, including the lattice results of Ref. [191], the DSE calculation of Ref. [77] and the matrix model of Ref. [88], we resort to particular quantities introduced as follows. To begin, note that calculations beyond one-loop order necessarily feature a non-trivial quark mass renormalization. While at one-loop order the renormalized mass simply corresponds to the bare mass, $M_{\text{bare}} = M_{\text{ren.}}$, this is no longer true at NLO and one instead deals with $M_{\text{bare}} = Z_M\, M_{\text{ren.}} + C_M$. Here, Z_M denotes the multiplicative renormalization factor, present in all models beyond one-loop, and C_M is an additive one, which is required whenever the employed regulator explicitly breaks chiral symmetry. While this is generically not the case for analytic approaches, in particular not for CF2 or DSE, it is, on the other hand, true for lattice computations. The factor Z_M is N_f-independent at $\mathcal{O}(g^2)$, because quark loops in the quark self-energy only appear at two-loop order and thus at $\mathcal{O}(g^4)$. We deduce that suitable quantities of comparison in two-loop analytic approaches are given by the ratios of critical $R_{N_f} \equiv M_c(N_f)/T_c(N_f)$ values, $R_{N_f}/R_{N_f'}$. This is due to the (partial) cancellation of the renormalization factor Z_M, whose N_f-dependence appears only at NNLO in the form of quark loop contributions. In the same spirit, because C_M is equally N_f-independent at $\mathcal{O}(g^2)$ [261], whenever $C_M \neq 0$, one instead considers ratios defined by

$$Y_{N_f} \equiv \frac{R_{N_f} - R_1}{R_2 - R_1}. \tag{4.29}$$

Both, ratios of R_{N_f} and the quantity Y_{N_f}, are particularly useful since they eliminate renormalization effects of the scheme-dependent quark mass up to higher order corrections.

Furthermore, exploiting the (almost) N_f-independence of T_c, one approximates

$$\frac{R_{N_f'}}{R_{N_f}} \approx \frac{M_c(N_f')}{M_c(N_f)} \tag{4.30}$$

as well as

$$\frac{M_c(N_f) - M_c(N_f')}{M_c(N_f) - M_c(N_f'')} \approx \frac{R_{N_f} - R_{N_f'}}{R_{N_f} - R_{N_f''}}. \tag{4.31}$$

Several remarks are in order concerning the values in Tab. 4.2.
Firstly, we note that while the R_{N_f} values superficially differ non-trivially between distinct continuum approaches, the ratios R_2/R_1 and R_3/R_1 agree rather well. This is especially true for Y_3, which is a less scheme-dependent quantity, as discussed in detail in chapter 5. We insist that the CF results are close to the lattice numbers and that the CF two-loop corrections (at the very least) do not spoil the relatively good one-loop results.

Secondly, we point out that among the four two-loop schemes considered, two pairs very closely resemble one another. These are "CF2" and "CF2 g.o." as well as "CF2 q.o." and "CF2 f.o.", see (4.25)-(4.28). This indicates that a change in the scale μ_f has a very noticeable effect, whereas changing $\hat{\mu}_f$ or μ_r basically leaves the results unaltered. This observation can be confirmed upon considering other scale configurations (while also keeping m and g fixed). We understand these scheme-dependent deviations

[7] We find $\frac{T_c(N_f=3)-T_c(N_f=1)}{T_c(N_f=1)} \approx 0.2\%$. This is significantly smaller than the difference with the pure YM case: $\frac{T_c(N_f=1)-T_c(N_f=0)}{T_c(N_f=0)} \approx 3.8\%$. The latter is due to the fact that the typical fermion mass on the critical line is $M_c/T_c \sim 7-8$ which leads to a significative Boltzmann suppression.

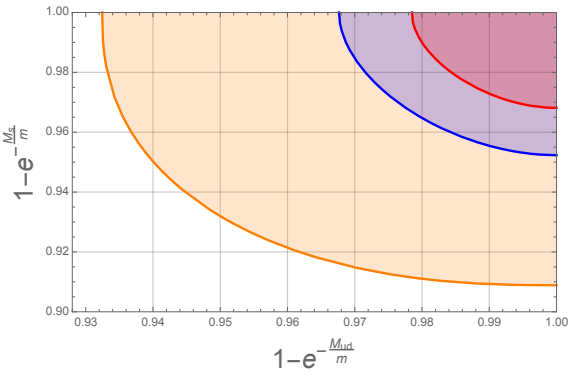

Figure 4.3: We compare the CF one-loop (orange) and two-loop (red for "CF2", blue for "CF f.o.") findings for the critical lines in the upper right hand corner of the Columbia Plot. The boundary lines for the schemes "CF2 g.o." and "CF2 q.o." are not explicitly shown here, but basically lie on top of the red and blue lines respectively, as indicated by the values in Tab. 4.2. This can be understood from (4.24), where the scale μ_f directly impacts the mass M_f (indirect for $\hat{\mu}_f$ and μ_r). The accompanying first order regions are hinted at by the respective lightly colored shades.

$R_{N_f}(0)$	$N_f = 1$	$N_f = 2$	$N_f = 3$	R_2/R_1	R_3/R_1	Y_3
CF1 [168]	6.743	7.586	8.071	1.125	1.197	1.575
CF2 [259]	7.535	8.401	8.899	1.115	1.181	1.575
CF2 g.o.	7.532	8.396	8.892	1.115	1.181	1.574
CF2 q.o.	6.638	7.487	7.975	1.128	1.201	1.575
CF2 f.o.	6.636	7.483	7.970	1.127	1.201	1.575
DSE [77]	1.42	1.83	2.04	1.29	1.43	1.51
Matrix [88]	8.04	8.85	9.33	1.10	1.16	1.59
Lattice [191]	7.23	7.92	8.33	1.10	1.15	1.59

Table 4.2: We showcase our two-loop results computed in the schemes (4.25)-(4.28) against various literature benchmarks in terms of the critical $R_{N_f} = [M_c/T_c](N_f)$ values on the left, as well as their ratios and the quantity Y_3 defined in Eq. (5.15). For the latter, as explained in the main text, scheme and regulator dependences are suppressed and we observe an excellent agreement amongst all approaches, including the lattice.

as stemming from neglecting renormalization group effects when varying the scale over a wide range. Nonetheless, despite the initial disagreement for the R_{N_f} values, the physically most relevant values for Y_3 again match the other literature findings, in particular from lattice QCD, thus ultimately supporting our two-loop findings as robust against scheme dependences.

Thirdly, we stress that the lattice numbers for R_2/R_1 and R_3/R_1 agree very well with the remaining model predictions. *A priori*, this is a non-trivial result, since the lattice QCD study in Ref. [191] uses a chiral symmetry breaking regulator and thus entails a non-zero additive quark mass renormalization. Contrarily for Y_3, this agreement is non-surprising since Y_3 is designed to suppress such additive renormalization effects in the first place. This suggests that the effect of the additive quark mass renormalization may be numerically small.

Fourthly, we briefly comment on the literature continuum approaches. Here, we note an almost perfect agreement of the matrix model with the lattice results for the ratios R_2/R_1, R_3/R_1 and Y_3. For the non-perturbative DSE results, it is impressive how much partially eliminating the scheme dependences improves the numbers towards the lattice counterparts. The remaining numerical disagreement may be attributed to the fact that the DSE analysis, on the one hand, only contains part of the two-loop corrections considered in this chapter and, on the other hand, also includes some higher order contributions, for which the scheme dependence might be more relevant.

Finally, we mention that in the following discussion we shall restrict to the scheme given by (4.25) and disregard the others.

4.3.2 Imaginary chemical potential

For $\mu \equiv i\mu_i \in i\,\mathbb{R}$, taking the background variables real, $r = (r_3, r_8) \in \mathbb{R}^2$, leads to a real-valued potential $V^{(1+2)}(r, T, i\mu_i)$ in Eq. (4.6). Once again, owing to the positivity of the fermion determinant, this allows the identification of the physical value of the background with the absolute minimum of $V^{(1+2)}$. The explicit effect of broken charge conjugation invariance is manifested in non-zero r_8 values; see section 3.2.

$R_{N_f}(i\pi/3)$	$N_f = 1$	$N_f = 2$	$N_f = 3$	R_2/R_1	R_3/R_1	Y_3
CF1 [168]	4.724	5.631	6.145	1.192	1.301	1.567
CF2 [259]	5.472	6.409	6.939	1.171	1.268	1.566
DSE [77]	0.41	0.85	1.11	2.07	2.70	1.59
Matrix [88]	5.00	5.90	6.40	1.18	1.28	1.56
Lattice [191]	5.56	6.25	6.66	1.12	1.12	1.59

Table 4.3: Our two-loop results for the tricritical $R_{N_f}(i\pi/3)$ values are compared with the one-loop and other literature counterparts. We also test the quantities R_2/R_1, R_3/R_1 and Y_3 ,which are less sensitive to regulator and scheme dependences as explained in the main text.

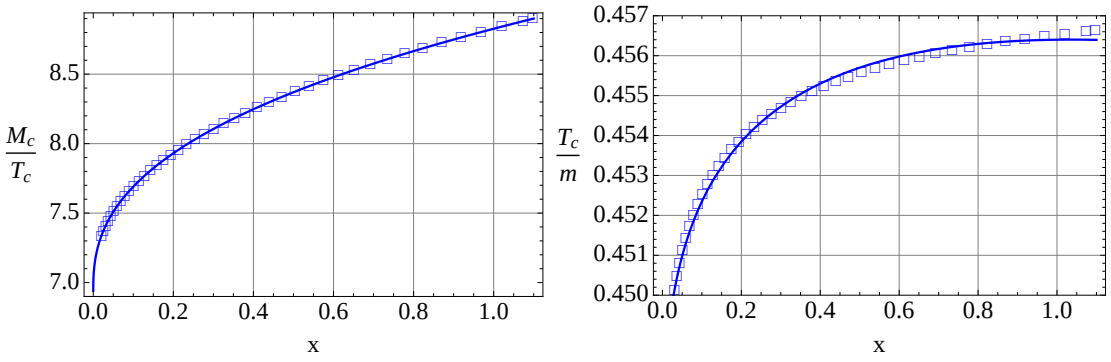

Figure 4.4: **Left:** We depict the critical $R_{N_f=3}$ values as a function of $x \equiv (\pi/3)^2 + (\mu/T_c)^2 = (\pi/3)^2 - (\mu_i/T_c)^2$, in the empty squares. The continuous curve corresponds to the fit (4.33). **Right:** The associated critical temperatures in units of the gluon mass m as a function of x for $N_f = 3$. The curve is given by Eq. (4.34).

Our N_f-dependent results for the tricritical point at $\beta\mu_i = \pi/3$ are shown in Tab. 4.3, yet again in terms of the less scheme-dependent quantities introduced previously, Eqs. (4.30) and (4.31). Many of the comments made concerning the values of Tab. 4.2 at vanishing chemical potential apply here as well. In particular we stress an overall rather good agreement for the Y_3 values, although being slightly less impressive for our perturbative approach than in Tab. 4.2.

As discussed in section 2.2.4, the immediate neighborhood of the tricritcal point can be understood from a simple mean field analysis in terms of an effective ϕ^6-potential with ϕ the actual order parameter (here the phase of the Polyakov loop), which leads to a scaling behavior of the form [91]:

$$\frac{M_c(\mu_i)}{T_c(\mu_i)} = \frac{M_{\text{tric.}}}{T_{\text{tric.}}} + K\Big[\underbrace{\Big(\frac{\pi}{3}\Big)^2 - \Big(\frac{\mu_i}{T_c}\Big)^2}_{\equiv x}\Big]^{\frac{2}{5}} . \tag{4.32}$$

Upon tracking the Z_2 critical points for $N_f = 3$, we obtain the curves shown in Fig. 4.4, and our data points can be fitted against mean-field tricritical scaling laws. We find

$$\frac{M_c}{T_c}(x) \approx 6.939 + 1.888\, x^{2/5} , \tag{4.33}$$

$$\frac{T_c}{m}(x) \approx 0.445 + 0.022\, x^{2/5} - 0.011\, x^{4/5} . \tag{4.34}$$

These fits are shown as solid blue curves in Fig. 4.4. We point out that the additive constant in (4.32) and in (4.33) is nothing but the $R_{N_f}(i\pi/3)$ value, here for $N_f = 3$. This provides an independent way of determining the tricritical values in Tab. 4.3 and thus serves as a consistency check. Similar fits can be obtained for $N_f = 1, 2$ with respective K-values in Eq. (4.33) of $K_{N_f=1} = 1.991$ and $K_{N_f=2} = 1.920$.

4.3.3 Real chemical potential

Finally we discuss the physically most relevant scenario of real chemical potential, where one is faced with a complex potential $V^{(1+2)}(r, T, \mu) \in \mathbb{C}$ if keeping the background components real.

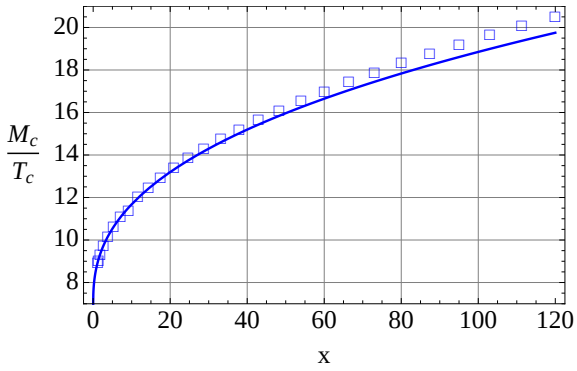

Figure 4.5: The solid curve corresponds to the tricritical scaling fit in Eq. (4.33) extrapolated to the region $\mu^2 > 0$. This is compared with our actual data points (empty squares) for critical $R_{N_f=3}$ values obtained directly at real values of chemical potential.

As explained in chapter 3, we shall follow the strategy proposed in [168], where one chooses $r = (r_3, r_8) \in \mathbb{R} \times i\mathbb{R}$, which results in a real potential and allows for self-consistent backgrounds. In practice, one can restrict the analysis to the parameter space $[0, 2\pi] \times i\mathbb{R}$. In this setup the physical point is associated with a saddle point,[8] leading to the ambiguity of determining the correct one whenever multiple saddle points are present. In our subsequent analysis, we always select the lowest saddle point,[9] which is the recipe outlined in Ref. [168].

Another strategy, followed by some authors, see, e.g., [77, 258], is to artificially set $r_8 = 0$ and search for the absolute minimum of the—then real—potential $V(r_3, 0, T, \mu)$. However, this systematically neglects any effect stemming from the explicit breaking of charge conjugation. Moreover, it is important to stress that this second strategy is at best an approximation for not too large μ since for $\mu \neq 0$ none of the points on the axis $r_8 = 0$ corresponds to an extremum of the potential: $\partial_8 V(r, T, \mu)|_{r_8=0} \neq 0$. We shall compare the results of both strategies in the following.

In Fig. 4.5 we show the critical points for $N_f = 3$ (for increasing values of μ) and compare their coordinates against the fits obtained in Eq. (4.33), which are continued in x to real values of μ. We note a good agreement up to reasonably large values of $x = (\pi/3)^2 + (\mu/T_c)^2 \lesssim 40$. In a further step, it is interesting to analyse the situation at constant chemical potential.[10] In Fig. 4.6, we show the Polyakov loops ℓ and $\bar{\ell}$ together with the corresponding (static) quark and anti-quark free energies as functions of temperature, for $\mu/m = 0.6$. We distinguish three particular cases of the $N_f = 3$ degenerate masses. First, in the top row of Fig. 4.6, the mass value is taken as $M/m = 5.56$, which is sufficiently large to lie within the first order region. Secondly, in the middle panel of Fig. 4.6, we tune the quark mass to be critical, $M = M_c \approx 4.48m$. Finally in the bottom row of Fig. 4.6, we choose a degenerate quark mass value of $M = 3.3m$, deep in the crossover region. Similar plots can be obtained for other N_f-values. We compare our findings to the results obtained by evaluating the Polyakov loops at the minimum of the potential along the axis $r_8 = 0$ (dotted line[11]), as done for example in Ref. [77, 258]. We observe from the top row of Fig. 4.6 (for the particular set of parameter values chosen) that this approximation might lead to significant alterations in the confined phase, especially in terms of the free energies. Similarly, in the middle panel of Fig. 4.6, one observes that upon setting $r_8 = 0$ the deduced critical temperature is slightly underestimated as compared to the one found by ℓ and $\bar{\ell}$ in the saddle-point scenario. However, for the present parameters, this is a small (less than 1 percent) effect, so that this can be considered a good approximation for the critical temperature. A similar conclusion holds for the bottom row of Fig. 4.6.

In the conventions employed in this thesis, $\mu > 0$ corresponds to an excess of anti-quarks over quarks. This situation is representatively illustrated in Figs. 4.6, where we find that the free energy of the thermal bath plus a static antiquark is larger than with a quark. A similar observation on the lattice was interpreted as the quark screening by all the abundant anti-quarks within the heat bath [262]. In all cases of Fig. 4.6 the Polyakov loops overshoot 1 in the high temperature phase, as was also observed for the pure YM theory at two-loop level [254]. In turn, this overshooting leads to negative free energy values. This observation seems unphysical since the free energies have to be understood as free energy differences between the system in presence of a test charge as compared to in absence of the latter [48]. Hence a negative value would mean a destabilization of the vacuum towards a medium with sources.

[8] With a positive (resp. negative) curvature in the r_3 (resp. r_8) direction.

[9] This rule is certainly valid at $\mu = 0$ where one can work equivalently over $\mathbb{R} \times \mathbb{R}$ or $\mathbb{R} \times i\mathbb{R}$ and the physical point lies at $r_8 = 0$. The absolute minimum in the first subspace coincides in this case with the deepest saddle point in the second subspace.

[10] Similar plots to the ones in Fig. 4.6 could be obtained upon fixing the quark mass and varying the chemical potential.

[11] We recall that $\ell = \bar{\ell}$ on the axis $r_8 = 0$.

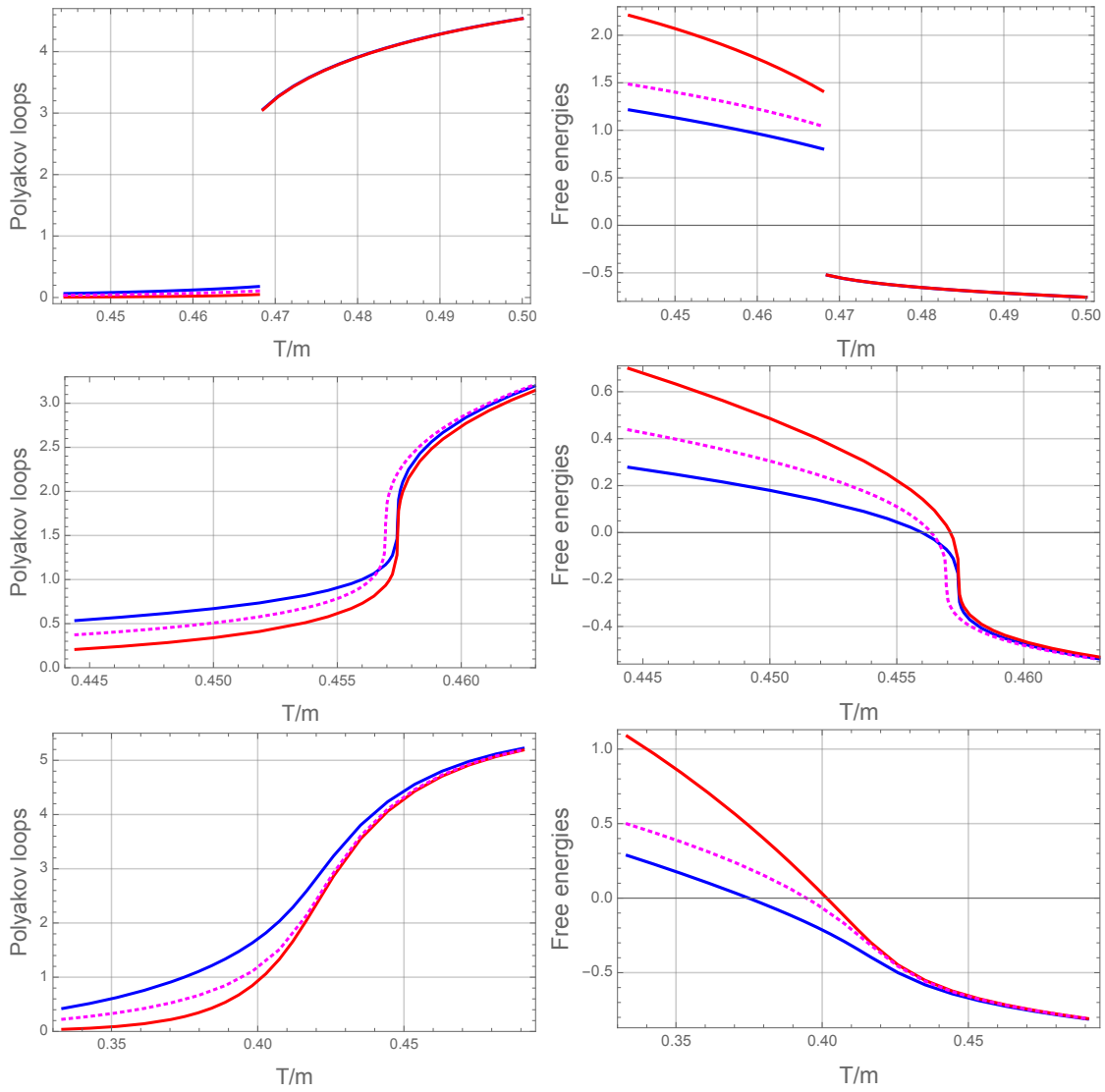

Figure 4.6: **Top:** The Polyakov loops ℓ (blue) and $\bar{\ell}$ (red) and the associated rescaled quark and anti-quark free energies, $\Delta F/m$ and $\overline{\Delta F}/m$, as functions of T/m, as found in the saddle-point approach with a non-zero imaginary background component r_8, for a $N_f = 3$ degenerate quark mass value in the first order region and a positive value of the chemical potential. The dotted lines correspond to the same quantities computed with $r_8 = 0$. We point out that these curves differ in height as compared to the ones shown in Ref. [259], correcting for a slight numerical error. **Middle:** Same setup with a degenerate quark mass tuned to criticality. **Bottom:** Same setup in the crossover region for $M = 3.3m$.

Also, the Polyakov loops outgrowing 1 is troublesome by itself, since by definition in (2.18) and (2.19) they satisfy

$$\ell \;=\; \frac{1}{N}\,\mathrm{tr}\,\langle L\rangle \;=\; \langle\frac{1}{N}\,\mathrm{tr}\,L\rangle\,, \tag{4.35}$$

where for simplicity we have hidden the path ordered exponential along the compact time direction inside the unitary matrix L. Similarly for $\bar{\ell}$, and by N we denote the dimension of the particular representation of the gauge group associated to the loops ℓ and $\bar{\ell}$. Since L is unitary, it immediately follows that $|\mathrm{tr}\,L/N| \leq 1$. The discrepancy of finding $\ell, \bar{\ell} > 1$ for some temperature values can stem from various possible origins.

The first comes from the realization that the weak coupling expansion of ℓ and $\bar{\ell}$ performed in Eq. (3.24) and (3.25) might, at two-loop order, break the unitarity of L. Naturally, one expects unitarity to be reinstated upon expanding to all orders. Thus, problems originating from this option can be seen as an artifact of the perturbative expansion. On the other hand, it is possible that the averaging

procedure $\langle \ldots \rangle$ spoils the bound $|\mathrm{tr}\, L/N| \leq 1$ due to non-positivity of the measure under the functional integral. One can identify two potential sources of such positivity-violation. Gauge fixing terms typically render the integration measure no longer positive definite.[12] Further, one encounters a complex fermion determinant in an unquenched theory at real chemical potential, which is of course related to the fermion sign problem present on the lattice. The latter, however, cannot be the sole origin of the overshooting problem since it is absent at $\mu = 0$ or in the quenched theory.

A third possible explanation is that, when computed in dimensional regularization, the bare Polyakov loops have no reason to satisfy the bounds $|\ell| < 1$ and $|\bar{\ell}| < 1$. Indeed, dimensional regularization is only properly defined perturbatively and it is therefore not clear whether the positivity of the integration measure is preserved by this regularization. Yet another interpretation is that, in a certain sense, the bare Polyakov loops in dimensional regularization can be seen as renormalized Polyakov loops. In particular, dimensional regularization subtracts UV power law divergences which, in the case of the Polyakov loop actually correspond to shifting the free energies by an infinite constant. These subtractions make the loops finite at the present order of approximation, without the need for a renormalization factor (this would remain true at higher orders but one would need to remove subdivergences via renormalization of the coupling). It is then natural to expect that these Polyakov loops have no reason to be bounded by one.

As a further application, it is interesting to investigate the behavior of the Polyakov loops and the associated free energies as functions of the chemical potential at fixed temperature. For instance, we choose the parameters as $T/m = 0.33$ and $M/m = 2.22$, which is sufficiently light to lie within the crossover regime for all values of the (real) chemical potential in the case $N_f = 3$. Our results are shown in Fig. 4.7, where we depict the Polyakov loops as functions of $\hat{\mu} = -\mu$, to cope for our unconventional choice of sign in (2.10), in prevision of the discussion below. Also, we have opted to restrict the employed formulae to the respective one-loop terms in Eqs. (3.24) and (3.25) since the $\mathcal{O}(g^2)$ corrections face the limitations outlined above. In Fig. 4.7, one clearly observes that the loops display a different monotony at small $\hat{\mu}$ but eventually approach 1 together from below. A similar observation was made in Ref. [180], where the nonmonotonous behavior of, in that case, ℓ at small $\hat{\mu}$ have instilled doubts on the validity of the interpretation of the Polyakov loops as exponentials of free energies. In the following, we resolve the confusion upon considering a situation where the charge of the bath at $\hat{\mu} = 0$ is non-zero. On the grounds of simple thermodynamic arguments, we can demonstrate that the interpretation of the logarithms of the Polyakov loops as differences of free energies with respect to that of the bath (free energy costs), leads to the qualitative behavior observed in Fig. 4.7.

We begin by recalling the free energy of the bath, $F = -T \ln \mathrm{tr}\, \exp\{-\beta(H - \hat{\mu}Q)\}$, where Q denotes the baryonic charge. It immediately follows that

$$\frac{\partial F}{\partial \hat{\mu}} = -\langle Q \rangle \quad \text{and} \quad \frac{\partial \langle Q \rangle}{\partial \hat{\mu}} = \beta \left\langle (Q - \langle Q \rangle)^2 \right\rangle > 0 \,. \tag{4.36}$$

If one presumes no external (static) source and if $\hat{\mu} = 0$, then the thermal bath is charge-conjugation invariant, such that $\langle Q \rangle_{\hat{\mu}=0} = 0$. In this situation we can turn on a (positive) chemical potential and find that for any $\hat{\mu} > 0$ the inequalities in Eq. (4.36) imply that $\langle Q \rangle > 0$ and $\frac{\partial F}{\partial \hat{\mu}} < 0$. In other words, the free energy of the bath is a decreasing function of $\hat{\mu}$. However, in a situation in which external sources are present, this deduction no longer holds. Consider the case in which a static quark or anti-quark has been inserted into the system. We define the associated free energies and averaged charges by F_q and $\langle Q \rangle_q = -\partial F_q / \partial \hat{\mu}$ or $F_{\bar{q}}$ and $\langle Q \rangle_{\bar{q}} = -\partial F_{\bar{q}} / \partial \hat{\mu}$ respectively. Note that the latter denote the average charge of the dynamical quarks in the bath itself and do not include the static test charge per se. Since the latter violates charge-conjugation invariance, it is $\langle Q \rangle_{q,\hat{\mu}=0} = -\langle Q \rangle_{\bar{q},\hat{\mu}=0} \neq 0$, even at zero chemical potential. In this respect, the insertion of the static (anti-) quark into the system results in a negative (positive) mean baryonic charge: $\langle Q \rangle_{q,\hat{\mu}=0} < 0$ and $\langle Q \rangle_{\bar{q},\hat{\mu}=0} > 0$.
Eq. (4.36) now leads to

$$\forall \hat{\mu} > 0 \,, \quad \langle Q \rangle_{\bar{q}} > 0 \,, \tag{4.37}$$

whereas on the other hand we have for some $\hat{\mu}_0 > 0$ that

$$\forall \hat{\mu} \in [0, \hat{\mu}_0] \,, \ \langle Q \rangle_q < 0 \quad \text{and} \quad \forall \hat{\mu} > \hat{\mu}_0 \,, \ \langle Q \rangle_q > 0 \,. \tag{4.38}$$

We point out that $\langle Q \rangle_q$ and $\langle Q \rangle_{\bar{q}}$ must be of the same sign for sufficiently large values of $\hat{\mu}$. In terms of free energies, the considerations in Eqs. (4.37) and (4.38) mean that $F_{\bar{q}}$ is monotonously decreasing for

[12] One prominent exception is given by the Gribov-Zwanziger implementation of the Landau gauge in the vacuum.

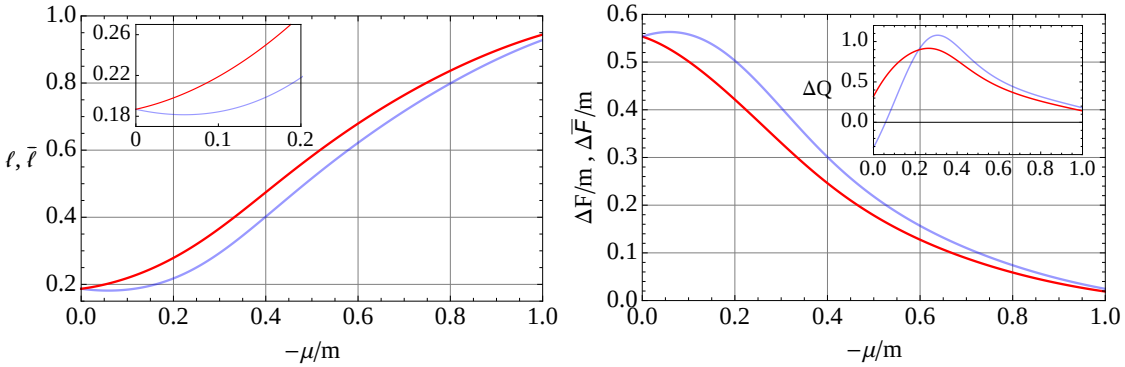

Figure 4.7: We show the Polyakov loops ℓ (blue) and $\bar{\ell}$ (red) together with the associated free energies, both as functions of $\hat{\mu} = -\mu$. The inset on the left zooms in for small $\hat{\mu}$ values surrounding the changing monotony for ℓ. In the inset on the right we showcase the difference of average baryonic charge of the bath in the presence of a test quark (blue) or a test anti-quark (red), with respect to the average charge in the absence of a test charge.

$\hat{\mu} > 0$, while F_q first increases and then decreases. To finally link to the Polyakov loops, we to consider the free-energy differences $\Delta F_q \equiv F_q - F$ and $\Delta F_{\bar{q}} \equiv F_{\bar{q}} - F$, as well as their respective $\hat{\mu}$-derivatives, which are given by $\Delta Q_q \equiv \langle Q \rangle_q - \langle Q \rangle$ and $\Delta Q_{\bar{q}} \equiv \langle Q \rangle_{\bar{q}} - \langle Q \rangle$, with F and $\langle Q \rangle$ the free energy and mean baryonic charge of the bath in absence of a test charge. Since $\langle Q \rangle_{\hat{\mu}=0} = 0$, the signs of ΔQ_q and $\Delta Q_{\bar{q}}$ at small non-zero $\hat{\mu}$ are dominated by those of $\langle Q \rangle_{q,\hat{\mu}=0}$ and $\langle Q \rangle_{\bar{q},\hat{\mu}=0}$. One deduces a different monotony of ΔF_q and $\Delta F_{\bar{q}}$ (and therefore of ℓ and $\bar{\ell}$) at small non-zero $\hat{\mu}$, which shows that the behavior observed in Fig. 4.7 and Ref. [180] is compatible with the thermodynamic interpretation of the Polyakov loops. As a final comment, we also observe that ΔQ_q and $\Delta Q_{\bar{q}}$ go to zero at large values of $\hat{\mu}$, as they must.

4.4 Thermodynamic stability

In this section we analyse the stability of the thermal system (4.6). In principle, there are many ways to proceed, but here our considerations revolve around an interplay of various thermodynamic observables, in particular we investigate the entropy density s as a function of the energy e and charge density q density, $s(e, q)$. Our respective two-loop results are shown in Fig. 4.9 and compared to their one-loop counterparts. We have chosen to depict our findings for a vanishing value of the charge density, however it is easily verified that the situation remains basically unchanged as one varies q. To enable a smoother discussion of the interpretations induced by our results in Fig. 4.9, it is beneficial to first consider an idealized scenario. In this respect, given the observed (almost) q-independence of our findings, it is instructive to consider the case of merely $s(e)$.

Naturally, a stable thermal system will always attain the microstate permitting maximal entropy. This realization implies that any perturbation, *e.g.*, in the form of a redistribution of energy, must result in a reduced value of entropy. In equations, this statement writes as

$$x_1 s(e_1) + x_2 s(e_2) \leq s(x_1 e_1 + x_2 e_2)\,, \tag{4.39}$$

for any $x_{1,2}$ such that $x_1 e_1 + x_2 e_2 = e$. One identifies Eq. (4.39) as a necessary condition for a concave function. However, a generic function $s(e)$ will exhibit locally concave and locally convex pieces, as schematically illustrated in Fig. 4.8. Note that $s(e)$ is by definition strictly monotonically increasing due to its derivative being given by the inverse temperature, $ds/de = 1/T$. Alongside, in Fig. 4.8, we also depict the convex envelope $\bar{s}(e)$. For any value of energy e, whenever $s(e)$ coincides with $\bar{s}(e)$, the system is in a thermodynamically stable state. This is the case for the green pieces of the curve in Fig. 4.8. On the other hand, whenever the function $s(e)$ differs from $\bar{s}(e)$ but still remains (locally) concave, the system is in a metastable configuration, as illustrated by the respective blue parts of the curve. The points of contact between the stable and metastable parts (where the green touches the blue) are the first order transition points the associated slope of $s(e)$ (or $\bar{s}(e)$) corresponds to the inverse transition temperature. This is indicated by the two instances of T_c above the the curve, where the system experiences a finite jump. We point out that there exists a third occurrence of the same transition temperature (same

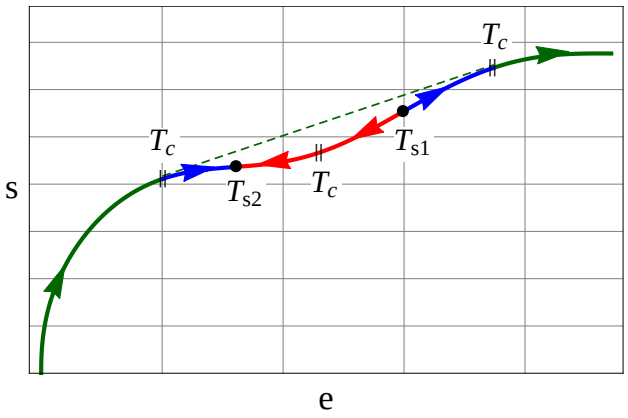

Figure 4.8: Schematic representation of a generic function $s(e)$ (solid curve) corresponding to a thermal system with a first order transition. In green, $s(e)$ agrees with the convex envelope $\bar{s}(e)$ (which continues along the dotted line). In blue the system is meta- and in red it is unstable. The black dots marked by T_{s1} and T_{s2} denote spinodal points. Finally, the arrows point in the direction of evolution of the system with temperature.

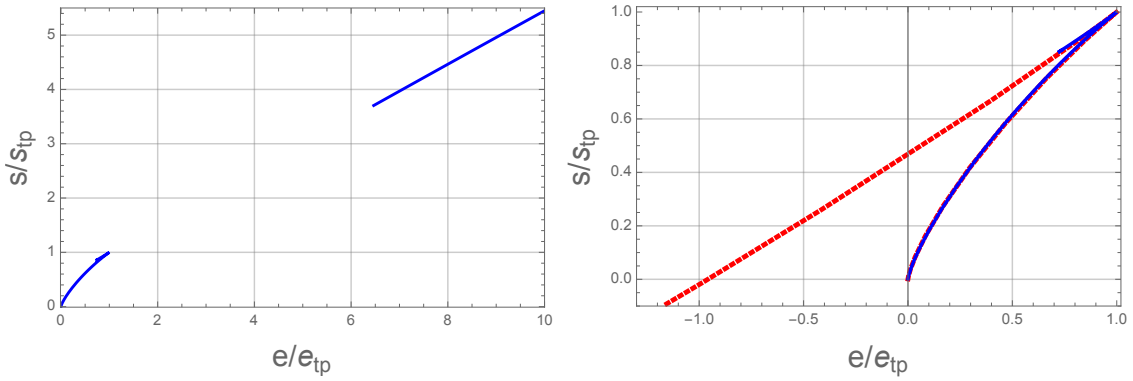

Figure 4.9: **Left:** entropy density vs. energy density at two-loop level for vanishing chemical potential, normalized by the values $s_{\rm tp}$ and $e_{\rm tp}$ at the respective turning points (beginning of the unphysical branches). The discontinuity corresponds to the first order phase transition. **Right:** Comparison of the one- (red) and two-loop (blue) low temperature branches. The unphysical part is significantly reduced at two-loop order and neither s or e explore negative values.

slope), within the red piece, corresponding to a convex part of $s(e)$ and thus an unstable state of the thermal system. Finally, the points of contact between metastable and unstable (blue and red) pieces are identified as spinodal points.
We insist on the fact that the stable parts (green) of $s(e)$ correspond to the absolute minimum of the system's associated (idealized) potential, whereas the metastable (blue) and unstable (red) parts are characterized by a local minimum and maximum respectively.

We are now in the position to return the discussion to the explicit two-loop results for $s(e, q = 0)$ obtained from Eq. (4.6) and shown in Fig. 4.9. For clarity, we have restricted to the pieces of the curve corresponding to the absolute minimum,[13] *i.e.* the analogues of the green parts of Fig. 4.8. Several remarks are in order.

Most importantly, in the confined phase, both at one- and two-loop order, one observes a convex branch just before the first order transition. This branch renders $s(e)$ multivalued and must be unphysical. More severely, in the one-loop case, this already unphysical branch continues into the region of negative energy and entropy values. This is not the case for the two-loop curve, where the respective values remain always positive. A similar observation was made in the case of pure YM in Ref. [166, 167]. Nonetheless, the presence of a multivalued convex branch characterized by $de/dT < 0$ and $ds/dT < 0$ is twofold troublesome: First, owing to

$$U = \frac{1}{Z} \operatorname{tr} H\, e^{-\beta H}\,, \tag{4.40}$$

[13] Recall that for vanishing charge density, the physical point is self-consistently identified as the absolute minimum of the potential. If we turn on a nonzero value of q, the thermal picture in Fig. 4.9 remains unchanged, however one has to remeber to convert the analysis towards saddle points; see section 3.2 for more details.

where Ω is the volume of the thermal system and $U = e\Omega$ its total internal energy, one has

$$\frac{\partial U}{\partial T} = \beta^2 \langle (H - U)^2 \rangle > 0 \,. \tag{4.41}$$

Secondly, we have $dp/de = dp/dT \times dT/de = s \times dT/de$ and since s is positive,[14] a negative value of de/dT implies a negative $dp/de = c_s^2$, with c_s the speed of sound, which is clearly unphysical; see also [263].

In light of the above considerations, we point out that similar issues were encountered in the GZ setting of Ref. [263] and that they might be connected to negative norm states in the partition function [239].

As a final comment, we stress that the magnitude of the unphysical branch in Fig. 4.9 is dramatically reduced upon including the two-loop corrections. In particular, the respective temperature range is reduced from $\Delta T_{1\ell}/m = 0.133$ at one-loop to $\Delta T_{2\ell}/m = 0.095$ at two-loop. This observation might hint at the presence of the unphysical branch being a mere perturbative artifact cured at higher orders.

4.5 Conclusion

We have analysed the phase structure of the heavy quark region of the Columbia Plot in the perturbative CF model at two-loop accuracy. This extends a previous study at one-loop [168] and we find that the inclusion of the NLO corrections does not spoil the qualitative agreement with lattice findings already established at one-loop level. Contrarily, our main result is that, when properly interpreted in terms of less scheme-dependent-quantities, the two-loop findings improve on the one-loop counterparts as compared to lattice values. In particular, assuming the additive renormalization effects on the lattice to be small (see before) and that it makes sense to use the lattice values of $R_{N_f}/R_{N_f'}$ for comparison, we find that the two-loop corrections lead to a numerical improvement, at both vanishing and imaginary chemical potential. Additionally, we have also tested the stability of the thermal system at two-loop level, which was shown to suffer from spurious artifacts at one-loop order (*e.g.* negative entropy or energy density). In line with the pure YM case [166, 167], we have shown that such unphysical features, when they do not simply disappear, are drastically reduced at two-loop order. Further, based on simple thermodynamic considerations, we have clarified the fact that the changing monotony of the Polyakov loops as functions of chemical potential is not in contradiction with their interpretation in terms of quark and anti-quark free energies, as originally suggested in [48].

The results presented in this chapter conclude a series of works on the upper right corner of the Columbia Plot [165, 166, 167, 168, 264, 254]. Overall, our conclusions can be split into three layers. First, we confirm that the perturbative CF model provides an efficient description of the heavy quark physics governed by center symmetry. Secondly, the obtained results are competitive with the findings of nonperturbative approaches present in the literature. For what concerns continuum nonperturbative approaches, this may be put in relation with the observation that existing such approaches implicitely use some version of the CF model, with a bare gluon mass to be adjusted in some way or another [132]. Finally, these considerations support our viewpoint that the studied physical aspects of heavy quark QCD are well under control in a perturbative treatment of a modified massive gauge-fixed Lagrangian.

[14] At two-loop this is always true, and, for this argument, we disregard the one-loop branch with a negative s.

5

Universality in the heavy quark limit: one loop and beyond

In this chapter we discuss the N_f-dependence of the heavy quark regime in the Columbia Plot, as described in section 2.2.3, and outline its universality amongst all one-loop models which are confining at zero temperature. In particular, we give a simple derivation of a fact noticed in the literature, that the entire shape of the second order boundary line is model-independent and, given one model-dependent data point, can be reconstructed in a model-independent way with remarkable accuracy. The argument exploits the fact that, in this region of the Columbia plot, the effect of quarks is Boltzmann suppressed. We further show that the same universality holds for any value of the chemical potential. This illustrates that many essential aspects of the critical line are, to a large extent, independent of the gluon dynamics of the model under investigation, but instead are already guaranteed by the inclusion of the quark content at one-loop level. One additional universal feature is the invariance of the critical temperature with N_f. We test these universal properties on the various one-loop results available in the literature, and we also perform original calculations in Gribov-Zwanziger (GZ) inspired models. We further observe that some universal properties are well satisfied by different calculations beyond one-loop order, including lattice simulations, further comforting the idea that essential aspects of the phase diagram are under perturbative control. Finally, for degenerate quarks, we propose a simple universal law for the flavor dependence of the critical mass-to-temperature ratio, satisfied by all approaches.

In the first section 5.1, we will derive most of the above-mentioned universal features on very general grounds, and in the following section 5.2, we apply and develop these properties further. Thereafter in section 5.3, we detail the various GZ-type models, which underlie some of the results presented in section 5.2. Finally, we conclude in section 5.4.

The content of this chapter encompasses the results presented in Ref. [265], and further includes additional material.

5.1 Derivation of universal aspects

Very generally, assume any potential $V(\ell, \bar{\ell}, M, \mu, T)$ with a quark contribution of the simple one-loop form, *i.e.* in the form of a Tr Ln[1]:

$$V(\ell, \bar{\ell}, T, M, \mu) \quad = \quad \tilde{V}_{\text{glue}}(\ell, \bar{\ell}, T) - \text{Tr}\,\text{Ln}\left(\not{\partial} + M + \mu\gamma_0 - ig\gamma_0\bar{A}\right) \tag{5.1}$$

where ℓ and $\bar{\ell}$ denote the Polyakov loops introduced in section 2.2.1 and M the mass of the N_f degenerate quark flavors. $\bar{A}$ is the matrix-valued gluon background component necessary in order to guarantee a coupling of the quark potential to the Polyakov loop(s) in the first place. Finally, $\tilde{V}_{\text{glue}}$ is any generic potential describing the gluon dynamics under the single assumption that it must be confining[2] so that we have a well-defined starting point when inquiring about the transition and the critical boundary line. We furthermore assume that the latter exists and its associated values of βM are large.

[1] Here Tr denotes a generalized trace over all indices and integration over momenta, whereas Ln stands for a matrix-valued functional logarithm.

[2] Confining in this context simply means that its zero temperature minimum is at $\ell = 0$.

At vanishing chemical potential, $\mu = 0$, we have $\ell \equiv \bar{\ell}$. In the heavy quark limit, one can expand the generic potential in (5.1), given partially by the expressions in (4.4) and (4.5), in large masses, $\beta M >> 1$, which, at leading order, reduces to [88]

$$\beta^4 V(\ell, T, M) = V_{\rm glue}(\ell, T) - 2N_f\, h(\beta M)\, \ell\,, \tag{5.2}$$

where we have defined $V_{\rm glue} \equiv \beta^4 \tilde{V}_{\rm glue}$ and $h(x) = (3x^2/\pi^2)K_2(x)$ with $K_2(x)$ the modified Bessel function of the second kind.

For each N_f, the critical values of ℓ, T and M on the upper critical line in the Columbia plot are determined from the system of equations

$$0 = \partial_\ell V = \partial_\ell^2 V = \partial_\ell^3 V\,. \tag{5.3}$$

In (5.2), we stress that in the heavy quark limit, at vanishing chemical potential, the quark contribution to the potential becomes linear in ℓ, such that

$$2N_f\, h(\beta M) = \partial_\ell V_{\rm glue}\,, \tag{5.4}$$

$$0 = \partial_\ell^2 V_{\rm glue} = \partial_\ell^3 V_{\rm glue}\,. \tag{5.5}$$

The critical values ℓ_c and T_c are found from (5.5), which thus merely depend on $V_{\rm glue}$ and are insensitive to the quark contribution to the dynamics.[3] This implies that the critical temperature β_c^{-1} is essentially constant along the critical line in the Columbia plot, as observed before in matrix model calculations [88, 46] and in lattice simulations [192, 191]. For each value of N_f, Eq. (5.4) yields the critical value of βM, which we denote as $R_{N_f} \equiv \beta_c M_c$ for simplicity. Because ℓ_c and T_c are N_f-independent, the RHS of (5.4) is N_f-independent, from which we deduce

$$\boxed{N_f\, h(R_{N_f}) = N_f'\, h(R_{N_f'})\,.} \tag{5.6}$$

A similar relation was previously worked out in the context of matrix models [88]. We deduce that although the critical values ℓ_c, T_c and R_{N_f} depend on the specific model for $V_{\rm glue}$, the relation (5.6) between the values of R_{N_f} for various N_f is model-independent, at one-loop order. We briefly mention that this extends trivially to the case of nondegenerate quarks and leads to a model-independent, universal form of the critical line. This shall be detailed later in section 5.2.

Let us now turn to the case of non-vanishing chemical potential, $\mu \neq 0$, either real or imaginary.[4] For each value of N_f and for each value of the chemical potential μ, the critical point is determined from the four equations

$$0 = \partial_\ell V = \partial_{\bar{\ell}} V\,, \tag{5.7}$$

$$0 = \partial_\ell^2 V\, \partial_{\bar{\ell}}^2 V - \left(\partial_\ell \partial_{\bar{\ell}} V\right)^2\,, \tag{5.8}$$

$$0 = a^3 \partial_\ell^3 V + 3a^2 b\, \partial_\ell^2 \partial_{\bar{\ell}} V + 3ab^2\, \partial_\ell \partial_{\bar{\ell}}^2 V + b^3\, \partial_{\bar{\ell}}^3 V\,, \tag{5.9}$$

with $a = \partial_{\bar{\ell}}^2 V|_c$ and $b = \partial_\ell \partial_{\bar{\ell}} V|_c$. Together, they fix the four critical values $\ell_c, \bar{\ell}_c, T_c, R_{N_f}$. The first two equations in (5.7) are the gap equations for the order parameters, one each for ℓ and $\bar{\ell}$. The equation in (5.8) is the generalization of $\partial_\ell^2 V = 0$ in (5.3) and imposes that the determinant of the Hessian matrix of V vanishes at the critical point, *i.e.* that it has at least one zero eigenvalue. The final equation in (5.9) then demands that the third directional derivative of V in the direction, in the space spanned by ℓ and $\bar{\ell}$, of the eigenvector associated to the zero eigenvalue vanishes. In so doing, a and b denote the components of this eigenvector.

Upon again considering the potential in (5.1) in the large mass expansion, we find

$$\beta^4 V(\ell, \bar{\ell}, T, M, \mu) = V_{\rm glue}(\ell, \bar{\ell}, T) \;-\; N_f\, h(\beta M)\big(e^{-\beta\mu}\ell + e^{\beta\mu}\bar{\ell}\big)\,. \tag{5.10}$$

We again stress the linearity of the potential in ℓ and $\bar{\ell}$ (in the heavy quark limit), upon which one obtains for (5.7),

$$N_f h(\beta M) = e^{\beta\mu}\, \partial_\ell V_{\rm glue}(\ell, \bar{\ell}, T) = e^{-\beta\mu}\, \partial_{\bar{\ell}} V_{\rm glue}(\ell, \bar{\ell}, T)\,. \tag{5.11}$$

[3] More precisely, quark dependent corrections to ℓ_c and T_c are suppressed by $\exp(-\beta M)$ in the large mass expansion.

[4] For $\mu \in i\,\mathbb{R}$, the Polyakov loops satisfy $\ell^* = \bar{\ell}$. On the other hand, for $\mu \in \mathbb{R}$, both Polyakov loops as real and independent. For a more detailed discussion on the rationale behind these choices, the reader is referred to sections 4.3.3 and 3.2.

Contrarily, the equations in (5.8) and (5.9) are characterized by higher derivatives in ℓ and $\bar{\ell}$ and thus solely feature the gluonic contribution $V_{\text{glue}}(\ell, \bar{\ell}, T)$ and the variables $\ell, \bar{\ell}$ and T. Any explicit dependence on M, μ or N_f has dropped out entirely. Therefore they can be used to define two functions $\ell(T)$ and $\bar{\ell}(T)$ which are (μ, M, N_f)-independent. Moreover, taking the ratio of the RHS's of (5.11) yields

$$e^{-2\beta\mu} = \frac{\partial_\ell V_{\text{glue}}\big(\ell(T), \bar{\ell}(T), T\big)}{\partial_{\bar{\ell}} V_{\text{glue}}\big(\ell(T), \bar{\ell}(T), T\big)}, \tag{5.12}$$

which allows in turn to extract a (M, N_f)-independent relation $\mu(T)$, or equivalently $T(\mu)$, and thus in turn (M, N_f)-independent critical values $\ell_c(\mu) = \ell(T_c(\mu))$ and $\bar{\ell}_c(\mu) = \bar{\ell}(T_c(\mu))$. Similarly to before, this allows one to deduce that the critical temperature is flavor independent (constant along the critical line) for any value of μ. Finally, the only (M, N_f)-dependence enters via the LHS of Eq. (5.11). Considering the ratio for two distinct values of N_f at fixed μ, the respective RHS's cancel and we conclude that Eq. (5.6) still holds, irrespective of the value of the chemical potential μ. Once again, we stress the simple generalizability of Eq. (5.6) to nondegenerate quark mass values to describe the entire critical line, for any μ.

5.2 Applications

Given these previous remarks on universality, our findings can be tested against numerical results for R_{N_f} from various one-loop models, gathered in Tab. 5.1, some of which are taken from the literature and some (labelled GZ) have been developed in this thesis (see section 5.3). A more detailed discussion on the conceptual frameworks, merits, and the validity of the latter models is given in section 5.3. The aim of the present section is to check for the universal features described above, some of which seem robust beyond one-loop order.

$\mu = 0$	R_1	R_2	R_3	R_2/R_1	R_3/R_2	Y_3
Lattice [191]	7.23	7.92	8.33	1.10	1.05	1.59
GZ-A [265]	7.09	7.92	8.40	1.12	1.06	1.58
GZ-B [265]	9.45	10.25	10.72	1.08	1.05	1.58
GZ-C [265]	–	1.33	2.12	–	1.59	–
GZ-0 [265]	4.66	5.56	6.07	1.20	1.09	1.59
Matrix [88]	8.04	8.85	9.33	1.10	1.05	1.59
CF1 [168]	6.743	7.586	8.071	1.125	1.064	1.575
CF2 [259]	7.535	8.401	8.899	1.115	1.059	1.575
DSE [77, 75]	1.42	1.83	2.04	1.29	1.11	1.51
$\beta\mu = i\pi/3$	R_1	R_2	R_3	R_2/R_1	R_3/R_2	Y_3
Lattice [191]	5.56	6.25	6.66	1.12	1.07	1.59
GZ-A [265]	5.02	5.91	6.42	1.18	1.09	1.57
GZ-B [265]	7.51	8.34	8.82	1.11	1.06	1.58
Matrix [46]	5.00	5.90	6.40	1.18	1.08	1.56
CF1 [168]	4.724	5.631	6.145	1.192	1.091	1.567
CF2 [259]	5.472	6.409	6.939	1.171	1.082	1.566
DSE [77, 75]	0.41	0.85	1.11	2.07	1.31	1.59

Table 5.1: R_{N_f} values for $N_f = 1$, 2, and 3 degenerate quark flavors, as computed in various approaches (one-loop models in blue). Top for vanishing and bottom for imaginary chemical potential, $\beta\mu = i\pi/3$. CF1 and CF2 refer to the one- and two-loop calculations within the CF model, see sections 4.1 and 4.2. Similarly GZ-A-0 refer to various versions of the one-loop Gribov-Zwanziger model presented in section 5.3. As described in section 5.3, the models GZ-0 and GZ-C are from the outset not sensible models for the dynamics and are thus not further pursued beyond the upper table. The last two lines of either table gather results beyond one-loop order, as described in the main text. A discussion on how to embed the lattice results into the general one-loop analysis within this chapter can also be found in the main text.

A small remark is in order for the values displayed at imaginary chemical potential, which rather than being critical actually correspond to a tricritical point. The presence of the latter is closely connected to

the Roberge-Weiss symmetry of the potential at $\beta\mu = i\pi/3$, which is summarized in the form

$$V(\ell, \bar{\ell}) = V(e^{i2\pi/3}\bar{\ell}, e^{-i2\pi/3}\ell). \tag{5.13}$$

For a more explicit illustration, change variables to the real-valued x and y such that

$$\ell = e^{i\pi/3}(x - iy) \quad \text{and} \quad \bar{\ell} = e^{-i\pi/3}(x + iy), \tag{5.14}$$

where the Roberge-Weiss symmetry now corresponds to the potential being even in y. One can formally eliminate the x-variable through the condition $\partial_x V = 0$ and obtain a curve $x(y)$ along which one evaluates a reduced potential $V_r(y)$ invariant under the $\mathbb{Z}_2$ transformation $y \to -y$. In this context, the tricritical point corresponds to the vanishing of both the second and the fourth derivatives of $V_r(y)$ at $y = 0$. Practically, in Tab. 5.1, the tricritical values can be determined either by following the boundary line in the Columbia plot as $\beta\mu$ approaches $i\pi/3$ or directly from the reduced potential at $\beta\mu = i\pi/3$. Both methods must yield the same results. However, the former is technically more challenging due to the scaling behavior in the near vicinity of tricriticality.

Finally, as illustrated in Tab. 5.2, we verify that the μ-independent universal Eq. (5.6) is nicely satisfied for all one-loop results in Tab. 5.1, regardless of their aptitude to reproduce the lattice results. Moreover, in both Tabs. 5.1 and 5.2, we also quote some findings that go beyond one-loop order, despite

$N_f\, h(R_{N_f})$	$N_f = 1$	$N_f = 2$	$N_f = 3$
Lattice [191]	0.00684	0.00771	0.00819
GZ-A [265]	0.00767	0.00770	0.00772
GZ-B [265]	0.00105	0.00105	0.00105
GZ-0 [265]	0.05215	0.05237	0.05254
Matrix [88]	0.00349	0.00352	0.00350
CF1 [168]	0.01021	0.01015	0.01020
CF2 [259]	0.00534	0.00515	0.00505
DSE [77, 75]	0.41440	0.67637	0.905327

Table 5.2: Checking Eq. (5.6) explicitly for the various results displayed in Tab. 5.1 at vanishing chemical potential. A similar table can be obtained for $\beta\mu = i\pi/3$. Model GZ-C has already been discarded as physically ill-defined here. The findings in this table give a nice hands-on example of the universality considerations in this section. Whereas the actual numbers in each of the rows are model-dependent, the fact that each column (approximately) agrees is due to the universal character of the quantitiy $N_f\, h(R_{N_f})$.

them satisfying the universal relation (5.6) being *a priori* questionable. While we expect the perturbative corrections to maintain some level of reasonable accuracy, hinting at the fact that the underlying physics of the heavy quark regime might be of perturbative nature itself, the same is not true for the remaining beyond one-loop approaches. Indeed, relation (5.6) remains well-satisfied by CF2, but this is not the case for DSE or the lattice. For DSE, this disagreement is not surprising, since the respective critical ratios R_{N_f} are small, see Tab. 5.1, which implies that the large mass expansion underlying (5.6) is not justified. We insist that R_{N_f} is a scheme-dependent quantity, and the small values obtained in the DSE case are thus *per se* not problematic. As explained in chapter 4, we point out that the (partial) cancelation of scheme-dependences in ratios of the form $R_{N_f}/R_{N_f'}$ leads to a much improved agreement of the DSE findings. However, in terms of the large mass expansions considered in this chapter, they shall not be discussed any further.

We recall the quantities

$$Y_{N_f} \equiv \frac{R_{N_f} - R_1}{R_2 - R_1}\,, \tag{5.15}$$

which as discussed in chapter 4 eliminate nontrivial regulator and scheme dependences between the various approaches at $\mathcal{O}(g^2)$. Numerical results for Y_3 are displayed in Tab. 5.1 and their agreement among all models is remarkable. In the following we demonstrate that this observation can be understood, at one-loop level, on the grounds of the universal relation in Eq. (5.6). In so doing, we also discuss how sensitive (5.6) is against higher order loop corrections to the potential in (5.1). We further comment

on the dependence of (5.6) on NLO corrections coming from the heavy mass expansion performed in Eq. (5.1) to obtain Eqs. (5.2) or (5.10).

Since R_{N_f} is always large, we can approximate the Bessel function by its asymptotic behavior and rewrite Eq. (5.6) as

$$\left(\frac{R_{N'_f}}{R_{N_f}}\right)^{3/2} e^{R_{N_f}-R_{N'_f}} = \frac{N_f}{N'_f}\,, \tag{5.16}$$

which formally defines a function $R_{N'_f}(R_{N_f})$. We can further consider the asymptotic expansion of (5.16), which at leading order up to corrections of order $\mathcal{O}(R_{N_f}^{-1})$ yields the estimate

$$R_{N'_f} - R_{N_f} = \ln\frac{N'_f}{N_f}\,, \tag{5.17}$$

and therefore

$$Y_{N_f} \approx \frac{\ln N_f}{\ln 2}\,, \qquad \text{with} \qquad Y_3 \approx 1.58\,, \tag{5.18}$$

which nicely fits the value quoted in Tab. 5.1. An even better estimate for differences of two R_{N_f}'s is obtained as follows. To first order in $R_{N'_f} - R_{N_f}$, we can rewrite Eq. (5.16) as[5]

$$e^{(R_{N_f}-R_{N'_f})\left(1-\frac{3}{2R_{N_f}}\right)} = \frac{N_f}{N'_f}\,, \tag{5.19}$$

yielding

$$R_{N_f} - R_{N'_f} = \frac{\ln N_f/N'_f}{1-\frac{3}{2R_{N_f}}} \tag{5.20}$$

and the expression Y_{N_f} in (5.18) is unaffected up to higher order corrections of $\mathcal{O}(R_1^{-2})$, which means that Y_{N_f} is a robust quantity. The quality of the approximations (5.17) and (5.20) is tested in Tab. 5.3 where we show the ratio of the respective left and right-hand sides.

values of	of (5.17)			of (5.20)		
LHS/RHS	$(2,1)$	$(3,2)$	$(3,1)$	$(2,1)$	$(3,2)$	$(3,1)$
Lattice [191]	0.99546	1.01118	1.00126	0.80692	0.82910	0.82096
GZ-A [265]	1.19744	1.18383	1.19241	0.97065	0.97243	0.97948
GZ-B [265]	1.154156	1.15916	1.15600	0.98526	0.99697	0.99425
GZ-0 [265]	1.29843	1.25781	1.28344	0.94813	0.94697	0.96628
Matrix [88]	1.16858	1.18383	1.17421	0.97052	0.99350	0.98543
CF1 [168]	1.22629	1.18383	1.21062	0.98394	0.96378	0.98560
CF2 [259]	1.25514	1.23315	1.24703	1.03101	1.02531	1.03685

Table 5.3: Explicit check of Eqs. (5.17) and (5.20). The notation (i,j) in the table header denotes $N_f = i$ and $N_{f'} = j$ in either of the formulae.

As a further application, Eq. (5.6) can immediately be generalized to non-integer values of N_f, meaning non-degenerate quark flavors in the Columbia Plot such that

$$N_f h(R_{N_f}) = 2\,h(R_{u=d}) + h(R_s), \tag{5.21}$$

where $R_{u=d}$ and R_s denote the up, down and strange quark critical mass to temperature ratios respectively. Given (5.21) and one model dependent point for the LHS on the critical boundary line, the entirety of the remaining line can be reconstructed fully independently of the gluonic contribution V_{glue}. Thus the shape of the boundary line is equally a universal property common among all one-loop models. This is illustrated in Fig. 5.1. We mention that, in principle, the reconstruction works upon employing either of the choices $3h(R_3) = 2h(R_2) = h(R_1)$ as input. In practice, all three options yield accurate results,[6] but for technical reasons and a marginally better outcome, we recommend nonetheless to use the value for $N_f = 3$, because it sits in the center of the critical line rather than its edges. To summarize,

[5] To the same order, we could replace R_{N_f} by $R_{N'_f}$ or even by $(R_{N_f} + R_{N'_f})/2$ in the denominator of the exponential.

[6] They are so good that it is not even insightful to show the differences between a reconstructed and exact line, since they are indistinguishable to the naked eye.

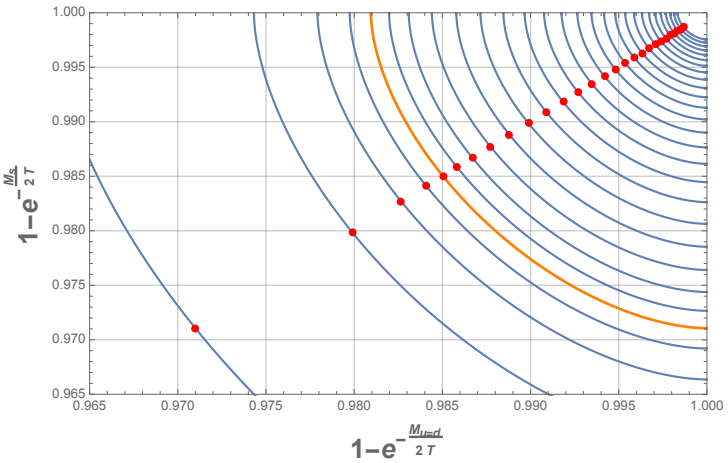

Figure 5.1: Top right corner of the Columbia plot, where the red points are the model-dependent input values for $R_{N_f=3}(\mu)$, with μ real or imaginary, here obtained from the first Gribov-Zwanziger model (GZ-A), see section 5.3 for more details. Then the blue curves are determined uniquely from the condition that $2\,h(R_{u=d}) + h(R_s)$ should remain constant. Finally, the orange curve corresponds to the case of vanishing chemical potential. Increments in between curves are of the order $\beta^2(\Delta\mu)^2 \approx 0.04\,n$, $n \in \mathbb{Z}$, with increasing n towards the top right YM point. All reconstructed curves lie exactly on top of the actual numerical results found in the GZ-A model.

we deduce that while the *location* of the critical line is V_{glue}-dependent via the LHS of Eq. (5.21), the *shape* of the line is then universal, *i.e.* independent of the model V_{glue} at one-loop order. As we have shown above, this is valid regardless of the value of the chemical potential.

Another straightforward generalization of Eqs. (5.6) and (5.17) is to apply them to larger values of $N_f > 3$. These are typically not available in the literature for a vast number of model calculations, and can therefore be seen as predictions based on the present universality considerations. For the models developed ourselves in the subsequent section and the previous chapter, we have computed all values both exactly and from the universal relations in Eq. (5.6) and

$$R_{N_f} = R_1 + (R_2 - R_1)\frac{\ln N_f}{\ln 2} \tag{5.22}$$

or

$$R_{N_f} = R_2 + (R_3 - R_2)\frac{\ln N_f/2}{\ln 3/2}, \tag{5.23}$$

which are easily obtained from Eq. (5.17). Overall, we expect (5.23) to produce slightly more accurate predictions than (5.22), which is intuited from $R_3 > R_2 > R_1$ and, therefore, the large mass expansion should be slightly more justified. All results are summarized in Tab. 5.4.

While the universal relations are overall accurately satisfied, given the displayed precision, for all one-loop results in Tabs. 5.1, 5.2 and 5.4, this is, in contrast, rather not the case for the lattice values, which follow a somewhat different scaling, where the function $h(x)$ is replaced by a simple exponential. The lattice results of Ref. [191, 266] featuring in various tables treat heavy quarks via a combination of expansions, in the strong-coupling and in the so-called hopping parameter κ_f, which depends on the quark flavor. The effective generating functional obtained in this way can then be split into a YM part and a contribution from the heavy quarks, in a similar spirit as in Eq. (5.2), again parametrized by the Polyakov loops and some effective couplings. On the critical line, one then finds the relation

$$N_f\, e^{-\mu/T_c} h_1 = \frac{c}{\cosh \mu/T_c}, \tag{5.24}$$

valid up to higher order corrections, for some constant $c = 0.00075$. The numerical value of c is known from Ref. [266], but will cancel out in the universality calculations considered here. The parameter h_1 is one of the above-mentioned effective couplings and given as an expansion in the hopping parameter via

$$h_1 = \left(2\kappa_f e^{a\mu}\right)^{N_\tau}\left(1 + 6\kappa_f^2 N_\tau \frac{u - u^{N_\tau}}{1-u} + \ldots\right).$$

table of R_{N_f} values	$\mu = 0$					$\beta\mu = \frac{i\pi}{3}$				
	$N_f = 4$	$N_f = 5$	$N_f = 6$	$N_f = 7$	$N_f = 8$	$N_f = 4$	$N_f = 5$	$N_f = 6$	$N_f = 7$	$N_f = 8$
Lattice [191]										
Eq. (5.6)	–	–	–	–	–	–	–	–	–	–
Eq. (5.22)	8.61	8.83	9.01	9.17	9.30	6.94	7.16	7.34	7.50	7.63
Eq. (5.23)	8.62	8.85	9.03	9.19	9.32	6.95	7.18	7.36	7.52	7.65
exact	–	–	–	–	–	–	–	–	–	–
GZ-A [265]										
Eq. (5.6)	8.74	9.00	9.22	9.40	9.55	6.78	7.05	7.28	7.46	7.62
Eq. (5.22)	8.76	9.03	9.25	9.43	9.59	6.81	7.10	7.34	7.54	7.71
Eq. (5.23)	8.74	9.01	9.23	9.41	9.57	6.80	7.08	7.31	7.51	7.67
exact	8.74	9.00	9.22	9.40	9.55	6.78	7.05	7.27	7.46	7.62
GZ-B [265]										
Eq. (5.6)	11.05	11.30	11.51	11.68	11.83	9.16	9.42	9.63	9.81	9.96
Eq. (5.22)	11.06	11.31	11.52	11.70	11.86	9.17	9.43	9.65	9.84	10.0
Eq. (5.23)	11.05	11.30	11.51	11.69	11.84	9.16	9.43	9.64	9.82	9.98
exact	11.05	11.30	11.51	11.68	11.83	9.16	9.42	9.66	9.85	9.96
Matrix [46]										
Eq. (5.6)	9.66	9.92	10.13	10.31	10.46	6.76	7.03	7.25	7.44	7.60
Eq. (5.22)	9.66	9.92	10.13	10.31	10.47	6.80	7.09	7.33	7.53	7.70
Eq. (5.23)	9.67	9.93	10.15	10.33	10.49	6.75	7.03	7.25	7.44	7.61
exact	–	–	–	–	–	–	–	–	–	–
CF1 [168]										
Eq. (5.6)	8.41	8.67	8.89	9.07	9.23	6.50	6.78	7.00	7.19	7.35
Eq. (5.22)	8.43	8.67	8.92	9.11	9.27	6.53	6.82	7.06	7.26	7.43
Eq. (5.23)	8.42	8.68	8.90	9.09	9.25	6.51	6.79	7.02	7.22	7.38
exact	8.41	8.68	8.89	9.07	9.23	6.50	6.78	7.00	7.19	7.35
CF2 [259]										
Eq. (5.6)	9.21	9.47	9.68	9.86	10.01	–	–	–	–	–
Eq. (5.22)	9.27	9.55	9.77	9.97	10.13	7.35	7.65	7.89	8.10	8.28
Eq. (5.23)	9.25	9.53	9.75	9.94	10.10	7.31	7.60	7.84	8.05	8.22
exact	9.25	9.52	9.74	9.92	10.08	–	7.60	7.83	8.02	8.19

Table 5.4: $R_{N_f>3}$ predictions, as obtained from various formulae worked out in the main text, in comparison to the respective in-model findings, whenever they could have been found in the literature. If there are values missing from either Eqs. (5.6), (5.22) or (5.23), then they were indeed attempted, however the universal relation in question failed to provide stable and reliable predictions.

Here N_τ is the number of temporal lattice sites and a the lattice spacing in the temporal direction, which satisfy the relation $aN_\tau = 1/T$. If one only accounts for the leading order term in h_1, and uses the fact that Ref. [266] finds that the hopping parameter scales as $\kappa_f \approx \frac{1}{2}e^{-aM_f}$ on the critical line, it is easily derived that

$$N_f e^{-\beta M_f} = \frac{c}{\cosh \mu/T_c}. \tag{5.25}$$

Based on Eq. (5.25) and the assumption (as was in fact observed) that T_c remains constant on the lattice along the critical line, Eq. (5.17) immediately follows. Subsequently, so do Eqs. (5.22) and (5.23).

5.3 The One-Loop Gribov-Zwanziger Model(s)

We close this chapter with the description of the Gribov-Zwanziger models used in the previous section. These are a simple unquenching of the Gribov-Zwanziger YM models presented in Ref. [125]. First,

we quickly review the YM part, then we detail the added quark contributions and finally interpret the resulting outcomes.

In Refs. [267, 268, 269, 78, 125] it is questioned wether a naive extension of the zero temperature GZ action to nonzero temperature and chemical potential leads to a correct description of the thermodynamic properties of the system. This is related to the fact that GZ quantization and compactifying the time coordinate don't commute and, in LdW gauge, it is to date unknown how to write the action in a form which is invariant under background-gauge transformations. In principle, one needs to consider the finite T and μ version of the generating functional and install the GZ-quantization procedure thereupon. However, this is, so far, an unsurmonted task and model descriptions are thus in order. In this context, Refs. [78, 125] propose[7] a model for the finite temperature GZ action in YM theory which agrees with all the symmetries of the problem:

$$V^{(1)}_{\rm glue}(r,\{m^4_\kappa\},T) \;=\; \frac{d-1}{2}\sum_\kappa \Delta\hat{K}_\kappa(m^4_\kappa,m^4_{\rm vac}) - \frac{d}{4}\sum_\kappa \Delta\hat{K}_\kappa(0,m^4_{\rm vac})\,, \tag{5.26}$$

with

$$\Delta\hat{K}_\kappa(m^4,m^4_{\rm vac}) \;\equiv\; \int_Q^T \ln(Q^4_\kappa+m^4) - \int_Q \frac{m^4}{Q^4+m^4_{\rm vac}}\,, \tag{5.27}$$

where $\int_Q$ denotes the zero temperature analogue of $\int_Q^T$, that is, an d-dimensional integral of momenta Q. Finally, the parameters m^4_κ are color-dependent Gribov parameters which, for familiarity with the CF model, have been labelled like (gluon) square masses. In principle, there could be a different Gribov parameter for each color mode κ, which for SU(3) are detailed in section 3.2. Each Gribov parameter depends implicitly on temperature T as well the background r via its gap equation[8]

$$0 = \frac{\partial V^{(1)}_{\rm glue}(r,\{m^4_\kappa\},T)}{\partial m^4_\kappa}. \tag{5.28}$$

We mention that the scale $m_{\rm vac}$ is fixed from the zero temperature gap equation upon accounting for the running coupling [270]. In the current setup, this is unfortunately not possible and at one-loop level one instead keeps $m_{\rm vac}$ as a scale parameter fixed to 1 GeV. However, we insist that the results for the critical ratios R_{N_f} obtained from the model in Eq. (5.26) are, at one-loop, independent of the chosen value of $m_{\rm vac}$.

Ref. [125] has proposed three scenarii for the Gribov parameters which are compatible with the relevant underlying symmetries. In the previous section, these are denoted by GZ-A, GZ-B, and GZ-C. Additionally, we also consider the naive treatment where one neglects the background dependence of the m_κ's. This scenario is denoted by GZ-0. In summary:

GZ-0: one m^4 independent of r.

GZ-A: all m^4_κ's equal.

GZ-B: all $m^4_{0^{(j)}}$'s equal and all m^4_α's equal.

GZ-C: all $m^4_{0^{(j)}}$'s equal and the m^4_α's different (with, however, $m^4_\alpha = m^4_{-\alpha}$).

At lowest order in their unquenched version, the models (5.26) are equiped with a one-loop fermionic contribution in the form of a trace log:

$$V^{(1)}_{GZ}(r,\{m^4_\kappa\},T,\mu) \;=\; V^{(1)}_{\rm glue}(r,\{m^4_\kappa\},T) + V^{(1)}_q(r,T,\mu) \tag{5.29}$$

with

$$V^{(1)}_q(r,T,\mu) \;=\; -{\rm Tr}\,{\rm Ln}\left(\not{\partial} + M + \mu\gamma_0 - ig\gamma_0\bar{A}\right). \tag{5.30}$$

[7] Both Refs. [78, 125] ultimately reach the same one-loop potential in Eq. (5.26). However the routes are different. While Ref. [125] entails an action characterized by background gauge invariance, the same is not true for the formulae in Ref. [78].

[8] The various color modes lead to non-degenerate gap equations due to the presence of the gluon background.

Having performed the Matsubara sum and angular integration, the quark contribution in (5.30) is given by Eq. (4.4). Given the potential in (5.29), one proceeds to study the thermodynamic properties of the system. At this point, a nontrivial aspect in the calculation comes from the implicit background dependence of the Gribov parameters via Eq. (5.28). Our results for the top right corner of the Columbia Plot are in qualitative agreement with the descriptions of section 2.2.3. Our quantitative results for the (tri)critical points for various N_f and μ values can be found in the tables of section 5.2. There we observe that, among the various one-loop approaches considered here, the degenerate GZ approach, GZ-A, gives the best results as compared to the lattice numbers. We also point out that accounting for the background dependence of the Gribov parameters is crucial. Neglecting the latter leads to much poorer findings as apparent from the values of GZ-0 in Tab. 5.1. Furthermore the non-degenerate case (GZ3) is completely discarded: For $N_f = 1$, one finds a first order phase transition, irrespectively of the value of the quark mass and the values for R_2 and R_3 are too small to be consistent with the heavy quark regime.

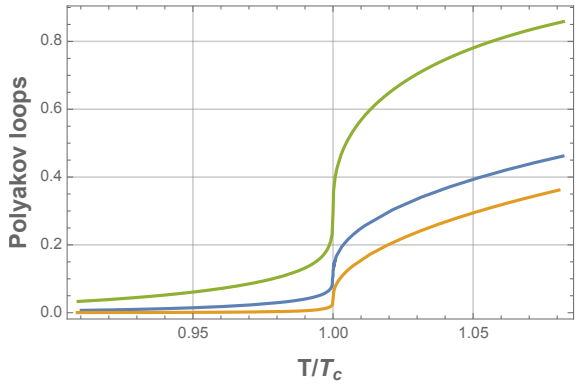

Figure 5.2: Polyakov loops as functions of T/T_c at fixed chemical potential and $N_f = 3$ degenerate quark mass, for various models under consideration, GZ-A (blue), GZ-B (orange) and CF1 (green). In each model, given $\mu/T_c \approx 1.011$ fixed, the respective masses have been tuned to criticality. Naturally, the critical temperatures T_c and masses M_c differ between the models under display.

In Fig. 5.2, we compare Polyakov loops as functions of T/T_c at fixed chemical potential for the GZ-A, GZ-B and CF1 models. We find that $\ell_{\mathrm{CF1}} > \ell_{\mathrm{GZ-A}} > \ell_{GZ-B}$ for all temperatures. Similar plots yielding the same inequalities can be obtained for the respective anti-Polyakov loops. In the confined phase this implies a stronger repulsion of the test charge by the thermal system in the Gribov-Zwanziger than in the CF model. On the other hand, in the deconfined phase, ℓ_{CF1} approaches 1 a lot faster than the corresponding curves for $\ell_{\mathrm{GZ-A}}$ or ℓ_{GZ-B}.

5.4 Conclusion

In the first part of this chapter we have established some ubiquitous features for the dynamics in the heavy quark regime common among all models which treat quarks at one-loop order in the form of a trace log. In particular, we have studied the flavor dependence of the critical line in the top right corner of the Columbia Plot and presented an explanation for the observed constant value of critical temperatures. It was demonstrated that the shape of the critical surface can, independently of the chemical potential, be understood merely on the grounds of the fermionic content of the theory and the gluon dynamics only intervenes in its location. Part of these results had been worked out before in the literature for particular low energy QCD models. Here we have provided a simple explanation which ubiquitously works for all of them and we have generalized to finite (real an imaginary) chemical potential.

We have derived several universal quantities and relations that can serve as useful, easy-access benchmarks or guidelines for model building. Furthermore, the universal concepts were tested against various models, some from the existing literature, others that have been developed in this thesis for this purpose. In the analysis of the latter, which are Gribov-Zwanziger approaches, we have considered several possible schemes for the Gribov parameters which are all in agreement with the underlying symmetries. However, our results disqualify the most intricate scenario of parameters on the basis of unphysical results. All remaining Gribov-Zwanziger-like models are in qualitative agreement with the expected phase pattern in the heavy quark regime and their numerics satisfy the derived universal relations with reasonable accuracy.

Similarly, all one-loop models from the literature considered here comply with the universality picture. However, it is a nontrivial observation that beyond LO approaches follow the same one-loop universality with good accuracy. This, again, hints at the fact that already a simple one-loop analysis in the regime

of heavy quarks (dominated by center symmetry) encodes the essence of the dynamics and that the underlying physics might inherently be of perturbative nature.

Part III

Light Quark QCD

6

Chiral phase transition from the Curci-Ferrari Model

The focus of this chapter lies on the dynamics of light quarks at finite temperature and density in the context of the CF model. As mentioned in the Introduction of this thesis, the light quark sector is strongly coupled in the infrared [169] and necessitates special treatment as compared to the pure gauge or heavy quark dynamics. We rely on the proposal of Ref. [170] which, as recalled below, leads to the CF version of the well-known rainbow equations for the quark propagator, which correctly captures the dynamics of spontaneous chiral symmetry breaking in the vacuum. Our main concern here is to implement this approach at nonzero T and μ and study the predictions of the CF model for the phase diagram in the light quark sector of the Columbia plot, including the physical QCD point. After some general comments on how to imbed this formalism into the framework of the two-particle-irreducible action in section 6.1, we outline the most general Dirac tensor decomposition of the quark propagator allowed by the symmetries of the thermal system in section 6.2. In section 6.3, we extend the rainbow equations in the CF model to finite temperature and density in presence of a nontrivial gluon background, which is the main original aspect of that section. We thus obtain a coupled set of nonlinear integral equations for the quark propagator and the Polyakov loops which, in principle, allows for a unified study of the interplay between the chiral and the deconfinement transitions across the whole Columbia plot, from the light to the heavy quark sector. In section 6.4, we motivate a particular approximation scheme of the rainbow equations, labelled as localization. We further specify two different possible implementations of localization, yielding two simple models for the underlying dynamics. The present chapter, however, focuses mostly on the chiral transition, turning off the background field, as a prototype study. We shall implement a coupling to the Polyakov loop at varying quark masses in the last chapter of the thesis.[1] Finally, in section 6.5, we present our results for the phase structure of the light quark regime as obtained from these two model descriptions. Our results are overall in qualitative agreement with the expected phase pattern and our simple localized rainbow equations predict values of the tricritical point in the chiral limit as well as for the CEP in the vast ballpark of standing literature findings. Lastly, we conclude in section 6.6.

The content of this chapter can partly be found in Ref. [271] and partly adds supplementary material.

6.1 General comments

In order to cope with the strongly coupled infrared dynamics in the quark sector, Ref. [170] proposed a modified loop expansion in the context of the CF model which exploits actual or effective small parameters in the game, namely, the pure gauge coupling and the inverse number of colors.[2] In practice, one performs a double expansion in g_g and $1/N_c$ while simultaneously resumming over g_q at fixed 't Hooft coupling $\lambda = g_q^2 N_c$.

Implementing this recipe for all diagrams contributing to the quark self-energy, it can be shown that the leading order (LO) terms embody the well-known rainbow resummation [240, 241, 242, 243],

[1] This will be sent at a later stage.

[2] In QCD, $N_c = 3$ but it is well known that the $1/N_c$ expansion correctly captures nontrivial aspects of the dynamics already at low values of N_c [272, 273].

illustrated in Fig. 6.1, with the gluon propagator corresponding to the tree-level CF propagator.

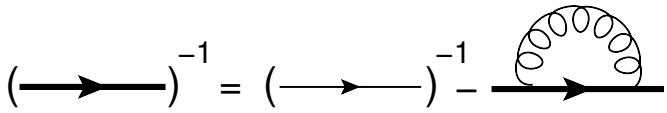

Figure 6.1: Diagrammatic representation of the rainbow equation obtained as the leading order contribution in the systematic rainbow-improved expansion scheme described in the main text.

The rainbow equation in Fig. 6.1 has been abundantly studied over the past four decades in terms of a vast landscape of different approaches which lay the foundations of the present understanding of chiral symmetry breaking and low energy QCD dynamics [16, 274, 275, 276, 277, 278, 279, 280]. However, one typically has to use educated modeling for the gluon propagator and the quark-gluon vertex, e.g., in order to correctly reproduce the quark mass anomalous dimensioun in the UV [16]. In contrast, the systematic approximation scheme of Ref. [170] allows for a consistent treatment of these aspects at the order of approximation considered, e.g., via standard RG improvement. In the latter reference, it was demonstrated that this CF version of the rainbow equations successfully describes the expected pattern of spontaneous chiral symmetry breaking in the vacuum. In a further step, we extend this work to nonzero values of temperature and chemical potential, and—most notably as compared to state-of-art degree of sophistication—we also include a nontrivial background field. We aim to study the QCD phase diagram from the CF model at leading order in this expansion scheme. Schematically, the finite temperature version of the rainbow equation follows the format

$$S^{-1}(P) \quad = \quad S_0^{-1}(P) + g^2 \int_{\hat{Q}}^{T} \gamma_\mu S(Q) \gamma_\nu \, G_{\mu\nu}(P-Q)\,, \tag{6.1}$$

where S and S_0 correspond to the dressed and tree-level Euclidean quark propagators respectively, and $G_{\mu\nu}(K)$ denotes the tree-level CF gluon propagator. We shall dive deeper into the details of this equation in section 6.3.

We also remark that the rainbow resummation can be derived from a two-particle-irreducible[3] (2PI) effective action [281] submitted to the rainbow-improved loop expansion (RILO) of Ref. [170]. The RILO procedure consists in resumming, on top of of the diagrams arising at a given loop order, all higher-loop diagrams which are of the same order in $1/N_c$ or g_g, the pure gauge coupling. For instance, at one-loop order for the effective action, one starts with the gluon and quark one-loop diagrams. The one-loop gluon terms are $\mathcal{O}(N_c^2)$ and the quark loop is $\mathcal{O}(N_c)$. One easily shows that the whole series of ladder diagram with one quark loop and multiple gluon exchanges, illustrated in Fig. 6.2, is of the same order in $1/N_c$ and g_g (only differ by powers of λ_q) and must thus be resummed. Any other diagram is supressed by either $1/N_c$ or λ_g as compared to the one-loop contributions. For instance, the two loop gluon and ghost diagrams are $\mathcal{O}(\lambda_g^2 N_c)$.

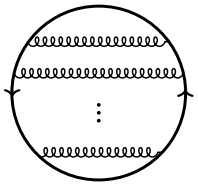

Figure 6.2: Resummed quark loop with multiple gluon exchanges. This diagram contributes at leading order in RILO.

In turn, this can be cast in a partially 2PI effective action of the form

$$\Gamma_{\rm 2PI}[S;r,T,\mu] \quad = \quad V_g(r,T) + V_{\rm q}^{(1+2)}[S;r,T,\mu]\,, \tag{6.2}$$

where $V_g(r,T)$ is the gluonic potential mentioned in chapter 4 and S is the dressed quark propagator to be self-consistently determined (see below) and where the 2PI character only concerns quark lines. In this context, the quark contribution is written

$$V_{\rm q}^{(1+2)}[S;r,T,\mu] \quad = \quad -{\rm Tr\ Ln}\, S^{-1} - {\rm Tr}\, S_0^{-1}\, S + \Phi(S) \tag{6.3}$$

[3]The 2PI effective action involves loop diagrams with lines representing fully dressed propagators and which cannot be disconnected by cutting any two lines.

where the second term on the RHS is present to avoid double counting [282, 283] and where $\Phi(S)$ denotes the quark sunset contribution shown in Fig. 4.1, as computed with the full propagator S,

$$\Phi(S) \,=\, -\frac{1}{2}\,g^2 \int_{\hat{P}\hat{Q}}^{T} \mathrm{tr}\Big(\gamma^\mu\, S(P)\gamma^\nu\, S(Q)\Big) G_{\mu\nu}(P-Q)\,. \tag{6.4}$$

Obviously, the dressed propagator S also depends on color, the background, temperature and chemical potential. However, for simplicity, we abstain from showing its explicit dependences. The quark propagator is obtained from (6.2) as

$$\frac{\delta\Gamma_{2\mathrm{PI}}[S;r,T,\mu]}{\delta S} \;\;=\;\; S^{-1} - S_0^{-1} + \frac{\delta\Phi(S)}{\delta S} \;\;=\;\; 0\,, \tag{6.5}$$

which, at the present order of approximation, is nothing but the rainbow eq. in Fig. 6.1.

The interest of the formulation (6.2) in terms of an effective action stems from the fact that it grabs together the relevant equations for the various order parameters in the game, namely, the quark condensate for chiral symmetry and the Polyakov loops, or, equivalently, the background components $r_3\,\&\,r_8$, for center symmetry. The values of the latter associated to the physical point are determined from their respective gap equations

$$\frac{\partial\Gamma_{2\mathrm{PI}}[S;r,T,\mu]}{\partial r_3} \,=\, 0\,, \qquad\qquad \frac{\partial\Gamma_{2\mathrm{PI}}[S;r,T,\mu]}{\partial r_8} \,=\, 0\,. \tag{6.6}$$

Moreover, the rainbow equation (6.1) constitutes the chiral gap equation yielding the quark propagator S, from which one then gains access to the quark condensate via $\sigma = \langle\bar{\psi}\psi\rangle = -\mathrm{Tr}\,S$.

Analyzing the phase structure and thermodynamics either from the 2PI potential as starting point or based directly on the gap equations must yield the same results. With the sole difference that in the presence of multiple solutions, the potential allows to discriminate and identify the physical one, which is *a priori* not possible from purely the gap equations. While trivial at this point, this correspondence might not hold true anymore as soon as one implements approximations to either the potential or the gap equations, as will become apparent in section 6.4, where several schemes are discussed.

In the next section we deal with the most generic form of the quark propagator as permitted by the symmetries of the system. Thereafter, in section 6.3, we derive the most general form of the rainbow equations in Fig. 6.1.

6.2 Symmetries of the dressed Quark Propagator

Let us analyze which constraints are imposed on the Euclidean quark propagator by the symmetries of the system at finite temperature and chemical potential in the LdW gauge with a non-trivial background.

6.2.1 Color and Flavor Structure

To begin, we deal with the straightforward color decomposition. Writing $\psi(x) = \sum_\rho \psi_\rho(x)\,|\rho\rangle$ and $\bar{\psi}(x) = \sum_\rho \bar{\psi}_\rho(x)\,\langle\rho|$, we have that

$$S(x,y) \,=\, \langle\psi(x)\bar{\psi}(y)\rangle \,=\, \sum_{\rho\sigma} \langle\psi_\rho(x)\bar{\psi}_\sigma(y)\rangle\; |\rho\rangle\,\langle\sigma|\,. \tag{6.7}$$

The propagator is invariant under the global color rotations that leave the background (3.6) invariant. For the quark fields, these are of the form

$$\psi \to \mathrm{U}\,\psi\,, \qquad \bar{\psi} \to \bar{\psi}\,\mathrm{U}^\dagger\,, \tag{6.8}$$

where $\mathrm{U}= e^{\theta_j t^{0(j)}}$, with generators $t^{0(j)}$ in the CSA of SU(N_c). With $t^{0(j)}\,|\rho\rangle = \rho_j\,|\rho\rangle$, we thus have that

$$\langle\psi_\rho(x)\bar{\psi}_\sigma(y)\rangle \,=\, \langle\psi_\rho(x)\bar{\psi}_\sigma(y)\rangle\; e^{i\,\theta\cdot(\sigma-\rho)} \,=\, \langle\psi_\rho(x)\bar{\psi}_\rho(y)\rangle\;\delta_{\rho\sigma}\,. \tag{6.9}$$

Therefore,

$$S(x,y) \,=\, \sum_\rho S_\rho(x,y)\;|\rho\rangle\,\langle\rho|\,, \tag{6.10}$$

where we have identified $S_\rho(x,y) \equiv \langle \psi_\rho(x)\bar{\psi}_\rho(y)\rangle$. A similar relation holds for the flavor structure of the propagator such that

$$S(x,y) = \sum_f S_f(x,y)\,|f\rangle\langle f|\,. \tag{6.11}$$

Now, each flavor-color component $S_{\rho,f}(x,y)$ depends on the background, temperature, and chemical potential. Furthermore, it exhibits a particular Dirac tensor decomposition, as we now explain.

6.2.2 Parity, Charge and Complex Conjugation

The propagator S is a function of both the external frequency and momentum variables ω and $\vec{p}$ and the parameters r, μ and T. We write explicitely the μ and r dependence to exhibit some useful relations below. In an isotropic configuration, the tensor structure of the propagator S is decomposed in the form

$$S(\omega,\vec{p};r,\mu) = S_1\mathbb{1} + S_2\gamma_5 + S_3\gamma_0 + S_4\gamma_0\gamma_5 + S_5\not{\vec{p}} + S_6\not{\vec{p}}\gamma_5 + S_7\gamma_0\not{\vec{p}}\,, \tag{6.12}$$

where $S_i = S_i(\omega,p;r,\mu)$, $p\equiv|\vec{p}|$, $\hat{p}\equiv\vec{p}/p$ and $\not{\vec{p}}\equiv\hat{p}\cdot\vec{\gamma}$. Transforming under parity yields

$$\begin{aligned} S(\omega,\vec{p};r,\mu) &\to \gamma_0 S(\omega,-\vec{p};r,\mu)\gamma_0 \\ &= S_1\mathbb{1} - S_2\gamma_5 + S_3\gamma_0 - S_4\gamma_0\gamma_5 + S_5\not{\vec{p}} - S_6\not{\vec{p}}\gamma_5 + S_7\gamma_0\not{\vec{p}}\,, \end{aligned} \tag{6.13}$$

which implies under parity invariance, that $S_2 = S_4 = S_6 = 0$. To keep the formulae light and insightful, it is useful to reparametrise the quark propagator in the form

$$S(\omega,\vec{p};r,\mu) = \tilde{B}\,\mathbb{1} + (i\omega-\mu)\gamma_0\tilde{A}_0 + i\not{p}\tilde{A}_v + i\gamma_0\not{p}\tilde{C}\,. \tag{6.14}$$

Note that we work in the Weyl basis with $\gamma^*_{0,2} = \gamma^t_{0,2} = \gamma_{0,2}$ and $\gamma^*_{1,3} = \gamma^t_{1,3} = -\gamma_{1,3}$.

Under complex conjugation,[4]

$$\begin{aligned} S(\omega,\vec{p};r,\mu) &\to \gamma_3\gamma_1 S(-\omega,-\vec{p};-r^*,\mu^*)^*\gamma_1\gamma_3 \\ &= \tilde{B}(-\omega,p;-r^*,\mu^*)^*\mathbb{1} + (i\omega-\mu)\gamma_0\tilde{A}_0(-\omega,p;-r^*,\mu^*)^* \\ &\qquad + i\not{p}\tilde{A}_v(-\omega,p;-r^*,\mu^*)^* + i\gamma_0\not{p}\tilde{C}(-\omega,p;-r^*,\mu^*)^*\,, \end{aligned}$$

where we have used $\gamma_3\gamma_1\gamma^*_\mu\gamma_1\gamma_3 = \gamma_\mu$. It follows that

$$\tilde{X}(-\omega,p;-r^*,\mu^*)^* = \tilde{X}(\omega,p;r,\mu)\,, \tag{6.15}$$

for any of the components $\tilde{X} = \tilde{A}_0, \tilde{A}_v, \tilde{B}, \tilde{C}$. Similarly, under charge conjugation,

$$\begin{aligned} S(\omega,\vec{p};r,\mu) &\to \gamma_2\gamma_0 S(-\omega,-\vec{p};-r,-\mu)^{\mathrm{t}}\gamma_0\gamma_2 \\ &= \tilde{B}(-\omega,p;-r,-\mu)^t\,\mathbb{1} + (i\omega-\mu)\gamma_0\,\tilde{A}_0(-\omega,p;-r,-\mu)^t \\ &\qquad + i\not{p}\,\tilde{A}_v(-\omega,p;-r,-\mu)^t + i\gamma_0\not{p}\tilde{C}(-\omega,p;-r,-\mu)^t\,, \end{aligned}$$

having used $\gamma_2\gamma_0\gamma^{\mathrm{t}}_\mu\gamma_0\gamma_2 = -\gamma_\mu$. Charge conjugation invariance gives

$$\tilde{X}(-\omega,p;-r,-\mu)^t = \tilde{X}(\omega,p;r,\mu)\,, \tag{6.16}$$

for, again, any of the components $\tilde{X}$. Combining (6.16) and (6.15), it is

$$\tilde{X}(\omega,p;r^*,-\mu^*)^\dagger = \tilde{X}(\omega,p;r,\mu)\,. \tag{6.17}$$

At this point we can specify to SU(3) and invoke the particular form of the weights $\rho_{1,2,3}$ in the fundamental representation as given in section 3.2. For an imaginary (including the case of zero) chemical potential the background is real, $r\in\mathbb{R}^2$, and thus all components $\tilde{X}_\rho$ are real-valued. Contrarily, the $\tilde{X}_\rho$ are complex in the case of a real chemical potential since the background component r_8 becomes imaginary.

[4] Technically the operation performed is a K-transformation. In terms of the partition function, it is equivalent to a complex conjugation, but in terms of the fermionic field content it involves a transformation of the form $\psi\to\gamma_1\gamma_3\psi$. See Ref. [168] for more details.

It is useful to introduce a class of particular global color rotations, known as Weyl transformations. These are $\mathrm{SU}(N_c)$ matrices $U = e^{\theta}$ with $\theta = i(\theta_\alpha t_\alpha + \theta_{-\alpha} t_{-\alpha})$, for a certain value of θ and where α is a fixed choice of root and t_α the associated generator [167]. On any element Y of the $\mathrm{su}(N_c)$ algebra, the Weyl transformations act as $e^{\theta} Y e^{-\theta}$. In particular, for an infinitesimal transformation of a generator $t^{0^{(j)}}$ in the CSA, one finds

$$t^{0^{(j)}} \to e^{\theta} t^{0^{(j)}} e^{-\theta} = t^{0^{(j)}} - 2\big(\alpha_k t^{0^{(k)}} \alpha_j\big)/\alpha^2 \,. \tag{6.18}$$

It follows that under a Weyl transformation, the background components transform as

$$r_j \to r_j - 2\, r_\alpha\, \alpha_j/\alpha^2 \,. \tag{6.19}$$

Due to the fact that the weights and roots only occur in the form of a product r_κ or r_ρ, shifts in the background of the form (6.19) can be absorbed by appropriate shifts in the roots/weights. For instance, based on Eq. (6.15), it can be worked out that, at real μ,

$$\begin{aligned} \tilde{X}_{\rho_1}(-\omega, p; r, \mu)^* &= \tilde{X}_{\rho_2}(\omega, p; r, \mu) \,, \\ \tilde{X}_{\rho_3}(-\omega, p; r, \mu)^* &= \tilde{X}_{\rho_3}(\omega, p; r, \mu) \,. \end{aligned} \tag{6.20}$$

The previous arguments apply also to the inverse propagator $S^{-1}(\omega, \vec{p}; r, \mu)$, which we parametrize as

$$S^{-1}(\omega, \vec{p}; r, \mu) = B - (i\omega - \mu)\gamma_0 A_0 - i\not{p} A_v - i\gamma_0 \not{p} C \,, \tag{6.21}$$

with the components $X = A_0, A_v, B, C$ obeying the same properties as in Eqs. (6.15), (6.16), and (6.17). With

$$\tilde{X} = \frac{X}{\Delta} \,, \tag{6.22}$$

it is

$$\Delta \equiv B^2 + (\omega + i\mu)^2 A_0^2 + p^2 (A_v^2 - C^2) \,. \tag{6.23}$$

6.3 Complete Rainbow Equations in the LdW Gauge

Given the most general form of the (inverse) propagator in Eq. (6.21) compatible with the underlying symmetries of the thermal system, we now proceed to derive the resulting set of coupled non-linear integral equations for the various tensor components in (6.21) from the rainbow equation (6.1).

In terms of the color-flavor components S_ρ (we leave the index f implicit to lighten notation), the rainbow equation in (6.1) can be written as[5]

$$S_\sigma^{-1}(P) = M_0 - (i\omega + iT\, r_\sigma - \mu)\gamma_0 - i\vec{p}\cdot\vec{\gamma} + g^2 \sum_{\rho,\kappa} \mathcal{D}_{\sigma,\rho\kappa} \int_{\hat{Q}}^{T} \gamma_\mu S_\rho(Q) \gamma_\nu\, G_{\mu\nu}(K_\kappa) \,, \tag{6.24}$$

where $Q = (\hat{\omega}_n, \vec{q})$, $P = (\hat{\omega}, \vec{p})$ and $K_\kappa \equiv P_\sigma - Q_\rho$ is the generalized gluon momentum, with $\hat{\omega}_n$ and $\hat{\omega}$ fermionic Matsubara frequencies. Unlike in the previous chapters, which relied on standard perturbation theory, we cannot use dimensional regularization here. We employ a hard UV cut-off on spatial momenta. The notation is $\int_{\hat{Q}}^{T} f(Q) \equiv T \sum_{n\in\mathbb{Z}} \int^{\Lambda} \frac{d^3q}{(2\pi)^3} f(\hat{\omega}_n, \vec{q})$. The tree-level gluon propagator is $G_{\mu\nu}(K) = P^{\perp}_{\mu\nu}(K)/(K^2 + m^2)$, with $P^{\perp}_{\mu\nu}(K) = \delta_{\mu\nu} - K_\mu K_\mu / K^2$ the transverse projector. Finally, M_0 and g denote the bare quark mass and quark-gluon coupling, respectively.

We gradually evaluate the individual expressions proportional to the different tensor structures in $\gamma_\mu S_\rho(Q) \gamma_\nu\, P^{\perp}_{\mu\nu}(K_\kappa)$. For the various prefactors of matrices $\mathbb{1}, \gamma_0, \vec{\gamma}, \gamma_0\vec{\gamma}$ we find respectively (up to a

[5] We note that the only N_f-dependences in expression (6.24) enter indirectly via non-trivial background values and, potentially, through the running of parameters if one implemented an RG improvement.

global factor of $1/\Delta_\rho(Q)$)

$$
\begin{aligned}
\mathbb{1}: &\qquad 3B^\rho(Q)\,,\\
\gamma_0: &\qquad \hat{A}_0^\rho(Q)\left(1+2\frac{(K_0^\kappa)^2}{K_\kappa^2}\right)+2\hat{A}_v^\rho(Q)\frac{K_0^\kappa}{K_\kappa^2}\vec{k}\cdot\hat{q}\,,\\
\vec{\gamma}: &\qquad 2\hat{A}_0^\rho(Q)\frac{K_0^\kappa}{K_\kappa^2}\vec{k}\cdot\hat{p}+\hat{A}_v^\rho(Q)\left(\hat{p}\cdot\hat{q}+2\frac{(\hat{p}\cdot\vec{k})(\vec{k}\cdot\hat{q})}{K_\kappa^2}\right),\\
\gamma_0\vec{\gamma}: &\qquad \hat{C}_\rho(Q)\left[\hat{p}\cdot\hat{q}\left(1-2\frac{(K_0^\kappa)^2}{K_\kappa^2}\right)-2\frac{(\hat{p}\cdot\vec{k})(\vec{k}\cdot\hat{q})}{K_\kappa^2}\right],
\end{aligned}
$$

where we have introduced $\hat{A}_0^\rho(Q)\equiv(Q_0^\rho+i\mu)A_0^\rho(Q)$, $\hat{A}_v^\rho(Q)\equiv pA_v^\rho(Q)$, $\hat{C}_\rho(Q)\equiv pC_\rho(Q)$, with the generalized frequency $Q_0^\rho=\hat{\omega}_n+Tr_\rho$. After projecting these contributions, we finally end up with the following set of equations:[6]

$$B_\sigma(P) = M_0+3g^2\sum_{\rho,\kappa}\mathcal{D}_{\sigma,\rho\kappa}\int_{\hat{Q}}^T\frac{B_\rho(Q)}{\Delta_\rho(Q)}\frac{1}{K_\kappa^2+m^2}\,, \tag{6.25}$$

$$\hat{A}_0^\sigma(P) = P_0^\sigma+i\mu+g^2\sum_{\rho,\kappa}\mathcal{D}_{\sigma,\rho\kappa}\int_{\hat{Q}}^T\frac{1}{\Delta_\rho(Q)}\frac{1}{K_\kappa^2+m^2}\left\{\hat{A}_0^\rho(Q)\left(1+2\frac{(K_0^\kappa)^2}{K_\kappa^2}\right)+2\hat{A}_v^\rho(Q)\frac{K_0^\kappa}{K_\kappa^2}\vec{k}\cdot\hat{q}\right\}, \tag{6.26}$$

$$\hat{A}_v^\sigma(P) = p+g^2\sum_{\rho,\kappa}\mathcal{D}_{\sigma,\rho\kappa}\int_{\hat{Q}}^T\frac{1}{\Delta_\rho(Q)}\frac{1}{K_\kappa^2+m^2}\left\{2\hat{A}_0^\rho(Q)\frac{K_0^\kappa}{K_\kappa^2}\vec{k}\cdot\hat{p}+\hat{A}_v^\rho(Q)\left(\hat{p}\cdot\hat{q}+2\frac{(\hat{p}\cdot\vec{k})(\vec{k}\cdot\hat{q})}{K_\kappa^2}\right)\right\}, \tag{6.27}$$

$$\hat{C}_\sigma(P) = g^2\sum_{\rho,\kappa}\mathcal{D}_{\sigma,\rho\kappa}\int_{\hat{Q}}^T\frac{\hat{C}_\rho(Q)}{\Delta_\rho(Q)}\frac{1}{K_\kappa^2+m^2}\left\{\hat{p}\cdot\hat{q}\left(1-2\frac{(K_0^\kappa)^2}{K_\kappa^2}\right)-2\frac{(\hat{p}\cdot\vec{k})(\vec{k}\cdot\hat{q})}{K_\kappa^2}\right\}. \tag{6.28}$$

Note that $\hat{C}=0$ is a self-consistent solution, which is equally true for $B=0$ in the chiral limit $M_0=0$. On the other hand, the integrand numerators of the second and third equation are not homogeneous.

Significant technology for tackling similar sets of equations (with $\hat{C}=0$ and $r=0$) has been developed in the literature [16, 97, 284, 285, 286, 287] and we are confident that the system (6.25)-(6.28) can be solved numerically also in the case $\hat{C}\neq 0$, $r\neq 0$. This, however, is beyond the scope of the present thesis. Here, we want to make a first qualitative study by using a drastically simplifed version of these equations which retains only the main relevant ingredients for the physics at hand and allows for maximum analytic control. Our goal is twofold. First, we shall study in this way the qualitative predictions of the CF model for the phase diagram in the chiral limit and the light quark sector. Second, we shall use these simplified equations to make a very first study of the interplay between the chiral degrees of freedom and the background gluon field, across the Columbia plot. The latter study will be the object of chapter 7. We describe and discuss various approximation strategies in the next sections.

6.4 Localization

To discuss our general approximation strategy in the simpler setup, we first turn the background field off, that is, we work in the Landau gauge.

In the chiral limit, $M_0\to 0$, an unbroken chiral symmetry implies both $B=0$ and $C=0$. This also means that a solution with either $B\neq 0$ or $C\neq 0$ signals the spontanous breaking of chiral symmetry. In what follows, we use B as our order parameter for chiral symmetry breaking since $C=0$ remains a consistent solution (which we stick to) even away from the chiral limit. Note that setting $C=0$ is an approximation commonly employed in DSE studies at $T\neq 0$, $\mu\neq 0$ [16, 67]. Moreover, we also set the vector components to their tree-level values, $A_0=A_v=1$.[7] With this ansatz, the rainbow equation (6.25)

[6] We stress that this is a set of twelve (rather than four) coupled equations due to the existence of three distinct weights σ in the fundamental representation of SU(3).

[7] It is worth mentioning that, in the vacuum, the functions A_0 and A_v are, anyway, not well described at the present order in RILO [170]. This is because the LO contributions are accidentally suppressed in the Landau gauge and thus receive substantial two-loop corrections, not included here.

for the quark mass function B reads

$$B(P) = M_0 + 4\,g^2 \int_{\hat{Q}}^{T} \frac{B(Q)}{Q_{i\mu}^2 + B^2(Q)} \frac{1}{[P-Q]^2 + m^2}\,, \tag{6.29}$$

where we have defined the fermionic four-momentum $Q_{i\mu} = (\hat{\omega}_n + i\mu, \vec{q})$ for later convenience. We recall that $B^*(\hat{\omega}, p) = B(-\hat{\omega}, p)$ in the case of a real chemical potential, and $B^*(\hat{\omega}, p) = B(\hat{\omega}, p)$ for an imaginary chemical potential.

We note that Eq. (6.29) is N_f-independent. This can be seen as an artifact of the approximation due to a vanishing background in the Landau gauge. Another route to lifting the flavor blindness could be via the running coupling in a RG-improved analysis (which is however, a subleading effect by $1/N_c$). As outlined in Ref. [170], the RI double expansion can (should) be supplemented with such an RG-improvement. The other sources of N_f dependence appear at higher order in the RILO, e.g., via quark loop corrections to the gluon propagator [16]. However, at this point, we attempt to simplify the equations and refrain from introducing further complications.

In principle, there are many ways to attempt solutions of Eq. (6.29). For instance, one could find a numerical solution for the full momentum dependent mass function $B(Q)$ upon converging iterations of a suitable ansatz function. Instead, we follow a different path to further simplify Eq. (6.29). We impose an approximation scheme called localization [288]. The principle idea is to seek particular momentum values P such that the momentum-dependent mass function $B(P)$, which generically (implicitly) depends on all other momenta Q via the gap equation (6.29), essentially decouples from the remaining momenta and only depends on itself. Typically, this is attempted for vanishing momentum values $P = 0$, which is based on the intuition that the most dominant contributions to the integral in Eq. (6.29) come from the regime of small Q-values. In practice, we replace the momentum-dependent mass function $B(Q)$ in Eq. (6.29) by a momentum-independent constant, $B(Q) \to B(Q = 0) \equiv B$. This procedure of localization is known to correctly grasp the vacuum phenomenology of chiral symmetry breaking. However, in the finite temperature setting of Eq. (6.29), the four-momentum $Q_{i\mu}$ never actually vanishes due to the fermionic nature of the Matsubara sums. This ambiguity allows for *a priori* various possible choices of localization schemes, and in the following two subsections we shall present two particular realizations thereof. However, beforehand, a quick remark is in order.

Once localized (in either form), Eq. (6.29) reduces down to a model description which resembles the formulae treated in the NJL model very closely [86]. The difference manifests itself in the treatment of the gluon propagator, which is taken as static in NJL, which would correspond to the limit of a large gluon mass, whereas a nontrivial momentum dependence remains in the present CF case. We are aware of the apparent similarities of the models and that the NJL model has been employed numerously to study the phase structure of QCD [86, 104, 197, 216, 227]. Nonetheless, we pursue our analysis further seeking to verify whether the CF model allows for an apt description of the phase diagram of QCD. We also understand that the approximations we have implemented in the process are brutally simplistic, and we therefore don't claim any quantitative power. We are motivated by a qualitative analysis via a proof of concept, before in a future study we revoke some of these approximations to focus on the quantitative aspects. Also, gaining intuition with this simplified equations prepares the ground for reintroducing the gluon background.

6.4.1 Physical Localization

The first localization scheme we specify is labelled *physical* and revolves around the retarded component of the quark mass function, which is directly related to the actual pole mass. The retarded mass function is identified as [171]

$$B_R(q_0, q) = B(-i(q_0 - \mu) + 0^+, q)\,, \tag{6.30}$$

where $B(\hat{\omega}_n, q) = B(Q)$ is the Euclidean mass function featuring in Eq. (6.29). Note the presence of the chemical potential in Eq. (6.30), which is in fact essential to obtaining the retarded propagator G_R. This is due to the relation

$$G_R(\omega) \quad = \quad G_M(i\omega_n \to \omega - \mu + i0^+)\,, \tag{6.31}$$

where G_M is the Euclidean Matsubara propagator. Having made the substitution (6.30) in Eq. (6.29), we then localize the resulting equation via the replacement rule

$$B_R(q_0, q) \to B_R(0, 0) \equiv B \in \mathbb{R}\,. \tag{6.32}$$

We insist that in this physical scheme, we can localize directly at $q_0 = 0$ and are no longer restricted by the non-vanishing nature of the fermionic Matsubara frequencies. Once Eq. (6.29) is expressed in terms of the retarded mass function, there is thus no ambiguity in the implementation of the localization procedure. The resulting rainbow equation rewrites in the form

$$B = M_0 + \frac{g^2}{\pi^2} B\Big\{F_{\rm vac}(B) + F_{\rm th}(B)\Big\} \tag{6.33}$$

where the vacuum term is

$$F_{\rm vac}(B) \equiv \int_0^\Lambda {\rm d}q \, \frac{q^2}{\varepsilon_B \varepsilon_m (\varepsilon_B + \varepsilon_m)} \,, \tag{6.34}$$

while the thermal contribution can be found as

$$F_{\rm th}(B) \equiv \frac{2}{B^2 - m^2} \int_0^\infty {\rm d}q \, q^2 \left(\frac{n_{\varepsilon_m}}{\varepsilon_m} + \frac{f_{\varepsilon_B + \mu} + f_{\varepsilon_B - \mu}}{2\varepsilon_B} \right), \tag{6.35}$$

with $\varepsilon_x = \sqrt{x^2 + q^2}$, $f_x = 1/(e^{x/T} + 1)$ is the Fermi-Dirac and $n_x = 1/(e^{x/T} - 1)$ the Bose-Einstein distribution function.

Since the vacuum integral in (6.34) diverges logarithmically with the cutoff, the rainbow equation (6.33) needs to be renormalized appropriately. As this issue occurs already in the chiral limit, one has to employ a coupling renormalization, which is efficiently accounted for by reparametrizing the bare coupling,[8] in the vacuum and in the chiral limit, in terms of a solution for the dynamical mass $B_0 \equiv B(T = 0, \mu = 0)$ via

$$0 = 1 - \frac{g^2}{\pi^2} F_{\rm vac}(B_0) \,. \tag{6.36}$$

Upon substitution in (6.33), this yields,

$$0 = H - B\big[F_{\rm vac}(B_0) - F_{\rm vac}(B) - F_{\rm th}(B)\big] \,, \tag{6.37}$$

where we have defined $H = \pi^2 M_0 / g^2$. For finite values of H, the Eq. (6.37) is UV finite and for fixed values of H, the cutoff Λ can be taken to infinity.

It can easily be shown that

$$F_{\rm vac}(B_0) - F_{\rm vac}(B) = \frac{B^2 \ln(B/m)}{2(B^2 - m^2)} - \frac{B_0^2 \ln(B_0/m)}{2(B_0^2 - m^2)} \,. \tag{6.38}$$

We point out that Eq. (6.33) contains a pole at $B = m$, which is technically regulated by $B^2 - m^2 \to B^2 - m^2 + i0^+$ due to Eq. (6.30), but this limits the range of applicability of the localized equation to values of B away from the pole. Fortunately, all physics underlying the chiral sector and transition can be understood for B values smaller than the $m = 500$ MeV we choose for the gluon mass. Thus we restrict the analysis[9] to $B < m$.

We shall also consider $F_{\rm th}(B)$ in Eq. (6.35), in the limit of vanishing temperature. We have, for $\mu \geq B$,

$$\mathcal{F}_{\rm th}(B) = \frac{B^2/2}{B^2 - m^2} \left[\frac{\mu}{B} \sqrt{\frac{\mu^2}{B^2} - 1} - \cosh^{-1}\left(\frac{\mu}{B}\right) \right], \tag{6.39}$$

and, otherwise, for $\mu < B$, $\mathcal{F}_{\rm th}(B) = 0$.

Employing these analytic expressions, it is easy to verify that the system undergoes a first order transition along the μ-axis. The value of the quark mass function B below the transition, $\mu < \mu_{\rm first}$, is constant, $B = B_0 \equiv B(T = 0 = \mu) = 300$ MeV. For $\mu > \mu_{\rm first}$, chiral symmetry is restored and $B = 0$. This behavior is a manifestation of the Silver-Blaze property [289, 290].

[8] We note that in Eq. (6.36), a symmetry breaking solution, with $B \neq 0$, can only exist for a bare coupling satisfying $g_0^2 > \pi^2 / F_{\rm vac}(0)$. This follows from the fact that $F_{\rm vac}$ as given by Eq. (6.34) is monotonically decreasing with B.

[9] On the other hand, the presence of this pole inhibits us from ever pushing the analysis beyond the light quark regime.

In the following, we discuss how to analyze the phase structure on the basis of the gap equation in (6.37). To this end, it is useful to define the function $\mathcal{R}(B^2)$ as

$$2B\,\mathcal{R}(B^2) \quad \equiv \quad B\big[F_{\rm vac}(B_0) - F_{\rm vac}(B) - F_{\rm th}(B)\big]\,, \tag{6.40}$$

where Eq. (6.37) takes the form $0 = H - 2B\,\mathcal{R}(B^2)$. We further define a potential $W(B^2)$ such that $\partial_B W(B^2) = 2B\,\mathcal{R}(B^2)$, or, equivalently, $W'(B^2) = \mathcal{R}(B^2)$. In the chiral limit, $H = 0$, it allows for the rainbow equation $2B\,\mathcal{R}(B^2) = 0$ to be interpreted as the gap equation of the potential $W(B^2)$. It is in terms of this potential $W(B^2)$ that we analyze the phase structure, where the absolute minimum of $W(B^2)$ corresponds to the physical state of the system.

In particular, in the chiral limit, the requirement for a critical point is that the absolute minimum of the potential be at $B = 0$, with

$$W'(0) = 0\,, \tag{6.41}$$

and, similarly, for a tricritical point,

$$W'(0) = W''(0) = 0\,. \tag{6.42}$$

We point out that Eq. (6.41) is equally the condition determining lower spinodal points, when the transition is first order. In that case, (6.41) holds but the absolute minimum of the potential is not $B = 0$. In that case, the lower spinodal line is accompanied by the upper spinodal line. Both spinodals flank a first order transition line in the chiral phase diagram and all three lines meet at the tricritical point. Upper spinodal points are found from, with $B_{\rm sp} \neq 0$,

$$W'(B^2_{\rm sp}) = W''(B^2_{\rm sp}) = 0\,, \tag{6.43}$$

whereas the first order line satisfies the condition

$$W'(B^2_{\rm first}) \;=\; W(B^2_{\rm first}) - W(0) \;=\; 0\,, \tag{6.44}$$

with $B_{\rm first}$ denoting the position of the non-trivial degenerate minimum at the transition.

Away from the chiral limit, $H \neq 0$, the above conditions need to be modified. To this end, it is convenient to define a new potential in the form

$$V(B) = -HB + W(B^2)\,, \tag{6.45}$$

in terms of which the rainbow equation $0 = H - 2B\mathcal{R}(B^2)$ can be expressed as $V'(B) = 0$. A critical point at location B_c then satisfies

$$V'(B_c) = V''(B_c) = V'''(B_c) = 0\,. \tag{6.46}$$

Similar extensions with respect to $V(B)$, for $H \neq 0$, hold for the respective equations of lower and upper spinodal as well as the first order transition line.

Several important remarks are in order. Firstly, we insist that having a potential at disposal is a necessary condition for a consistent study of the phase structure. While the conditions of (tri)critical and spinodal points don't depend on the potential itself and could be reformulated entirely in terms of the gap equations, the same is not true for the first order line. More importantly, it is via the absolute minimum of the potential that one discriminates between solutions to identify the physical state of the system in the first place. Therefore, knowing a potential, beyond simply its gap equations, is indispensable.

Secondly, we stress that the potentials W and V have been constructed in an effective or practical manner such that its derivatives can be exactly interpreted as the respective gap equations in (6.37). This approach is very efficient in its descriptions of the phase structure and the phenomenological construction of the potentials V and W is very convenient.

Formally, a potential for the rainbow equation in (6.37) can be obtained from the 2PI action in Eq. (6.2), under the condition that one imposes compatible approximations as the ones leading up to Eq. (6.33). In particular, neglecting the gluon background, setting the remaining Dirac components to their tree-level values and localizing the resulting formulae. Moreover, this requires a real time expression of the 2PI action. While in principle envisionable, this undertaking is not necessary for the case discussed above since one obtains easy access to simple potentials, V and W, and for simplicity, we shall stick to the latter.

Finally, we note that the potentials V and W are constructed ambiguously since the solutions of the rainbow equations are not affected, e.g., by multiplying the latter by a strictly positive function. For instance, in the chiral limit, this would yield $W'(B^2) \to f_+(B^2)\mathcal{R}(B^2)$. Since the conditions for spinodal and (tri)critical points only involve derivatives of W and owing to the positivity of f_+, it can easily be shown that these points are independent of the choice of f_+. Contrarily, the position of the first order line, as determined from Eq. (6.44), is explicitly W and thus f_+ dependent. However, because the first order line (regardless of f_+) must always be flanked by spinodal lines (which are f_+ independent), one obtains a reasonable bound for the location of the former in the phase diagram under the condition that the latter are not too far apart. This discussion generalizes to the case of $H \neq 0$ in terms of V. Throughout the analysis performed in the physical localization, we choose $f_+ = 1$. We insist that localizing the 2PI potential typically gives rise to such a function multiplying the gap equation (6.37). However, this function is not guaranteed to be positive (and, in the case of the Euclidean localization to be discuss later, it is not), which leads to spurious solutions.

6.4.2 Euclidean Localization

The second localization scheme we consider is labelled *Euclidean* and directly addresses the issue that in a fermionic context, one cannot simply replace the momentum-dependent mass function $B(Q)$ by its value at $Q = 0$, since the Matsubara frequencies never vanish. In fact, the lowest frequency modes are given by $\pm\hat{\omega}_1$ with $\hat{\omega}_1 = \pi T$. The Euclidean localization scheme is characterized by the replacement $B(Q) \to B(\pm\hat{\omega}_1, 0)$ in Eq. (6.29), where one accounts for both the negative and positive first frequency contribution. However in so doing, one has to consider the problem in the complex plane since $B(\pm\hat{\omega}_1, 0)$ is complex.

We have from Eq. (6.29):

$$B(\hat{\omega}, p) = M_0 + 4g^2 \int_{\hat{Q}}^{T} \frac{B(\hat{\omega}_n, q)}{(\hat{\omega}_n + i\mu)^2 + q^2 + B(\hat{\omega}_n, q)^2} \frac{1}{(\hat{\omega} - \hat{\omega}_n)^2 + (p-q)^2 + m^2} \tag{6.47}$$

and upon evaluating for $\hat{\omega} = \hat{\omega}_1$ and $p = 0$:

$$B(\hat{\omega}_1, 0) = M_0 + 4g^2 \int_{\hat{Q}}^{T} \frac{B(\hat{\omega}_n, q)}{(\hat{\omega}_n + i\mu)^2 + q^2 + B(\hat{\omega}_n, q)^2} \frac{1}{(\hat{\omega}_1 - \hat{\omega}_n)^2 + q^2 + m^2}\,. \tag{6.48}$$

Assuming the sum-integral to be dominated by the region where the propagators underneath the integral get maximal in the $\mu = 0$ case (at $\hat{\omega}_n = \pm\hat{\omega}_1$, $q = 0$ for the first, and at $\hat{\omega}_n = \hat{\omega}_1$, $q = 0$ for the second), we get

$$\begin{aligned} B(\hat{\omega}_1) = M_0 + 2g^2 \int_{\hat{Q}}^{T} & \frac{1}{(\hat{\omega}_1 - \hat{\omega}_n)^2 + q^2 + m^2} \\ & \times \left[\frac{B(\hat{\omega}_1)}{(\hat{\omega}_n + i\mu)^2 + q^2 + B(\hat{\omega}_1)^2} + \frac{B(-\hat{\omega}_1)}{(\hat{\omega}_n + i\mu)^2 + q^2 + B(-\hat{\omega}_1)^2} \right], \end{aligned} \tag{6.49}$$

where we have defined $B(\hat{\omega}, 0) \equiv B(\hat{\omega})$. A similar expression can be obtained for $B(-\hat{\omega}_1) = B(\hat{\omega}_1)^*$. It proves more convenient to work with

$$B_\pm \equiv \frac{B(\hat{\omega}_1) \pm B(-\hat{\omega}_1)}{2}\,. \tag{6.50}$$

In terms of $B_\pm$, the rainbow equation can be rewritten as

$$\begin{aligned} B_\pm = \frac{1 \pm 1}{2} M_0 + g^2 \int_{\hat{Q}}^{T} & \frac{1}{(\hat{\omega}_1 - \hat{\omega}_n)^2 + q^2 + m^2} \\ & \times \left[\frac{B_+ + B_-}{(\hat{\omega}_n + i\mu)^2 + q^2 + (B_+ + B_-)^2} + \frac{B_+ - B_-}{(\hat{\omega}_n + i\mu)^2 + q^2 + (B_+ - B_-)^2} \right. \\ & \left. \pm \frac{B_+ + B_-}{(\hat{\omega}_n - i\mu)^2 + q^2 + (B_+ + B_-)^2} \pm \frac{B_+ - B_-}{(\hat{\omega}_n - i\mu)^2 + q^2 + (B_+ - B_-)^2} \right]. \end{aligned} \tag{6.51}$$

At $\mu = 0$, it is $B_- = 0$. At real μ, B_+ is real and B_- imaginary. As can be checked, these properties are preserved by Eq. (6.51), hence the necessity to keep both $\pm\hat{\omega}_1$ under the sum-integrals. After having

performed the Matsubara sums and the angular integral, Eq. (6.51) can be expressed in the simple form

$$B_\pm = \frac{1\pm1}{2}M_0 + \frac{g^2}{4\pi^2}\Bigg[(B_+ + B_-)\,F_{\hat{\omega}_1}\big(B_+ + B_-;\mu\big) + (B_+ - B_-)\,F_{\hat{\omega}_1}\big(B_+ - B_-;\mu\big) \pm(B_+ + B_-)\,F_{\hat{\omega}_1}\big(B_+ + B_-;-\mu\big) \pm (B_+ - B_-)\,F_{\hat{\omega}_1}\big(B_+ - B_-;-\mu\big)\Bigg], \tag{6.52}$$

where, for notational convenience, we have defined

$$F_{\hat{\omega}_1}(B;\mu) \equiv \int_0^\Lambda \mathrm{d}q \left\{\frac{q^2}{\varepsilon_m}\left(\frac{n_{\varepsilon_m}}{\varepsilon_B^2 - (\varepsilon_m + \mu - i\hat{\omega}_1)^2} + \frac{n_{\varepsilon_m}}{\varepsilon_B^2 - (\varepsilon_m - \mu + i\hat{\omega}_1)^2}\right)\right. \\ \left. -\frac{q^2}{\varepsilon_B}\left(\frac{f_{\varepsilon_B-\mu}}{\varepsilon_m^2 - (\varepsilon_B - \mu + i\hat{\omega}_1)^2} + \frac{f_{\varepsilon_B+\mu}}{\varepsilon_m^2 - (\varepsilon_B + \mu - i\hat{\omega}_1)^2}\right) + \frac{q^2}{\varepsilon_B\varepsilon_m}\,\frac{\varepsilon_B + \varepsilon_m}{(\varepsilon_B+\varepsilon_m)^2 - (\mu - i\hat{\omega}_1)^2}\right\}. \tag{6.53}$$

The equation for B_+ is UV divergent and needs to be renormalized while the equation for B_- is inherently UV finite (for a fixed value of the coupling). We renormalize the former by rewriting the bare coupling in terms of a renormalized one, g_R, in the form

$$\frac{1}{g_R^2} = \frac{1}{g^2} - F_{\mathrm{vac}}(B_*;0)\,, \tag{6.54}$$

where B_* is an arbitrary scale. With this replacement, the equation for B_+ can be rewritten as

$$B_+ = H' + \frac{g_R^2}{4\pi^2}\Bigg[(B_+ + B_-)\,\Delta F_{\hat{\omega}_1}\big(B_+ + B_-;\mu\big) + (B_+ - B_-)\,\Delta F_{\hat{\omega}_1}\big(B_+ - B_-;\mu\big) +(B_+ + B_-)\,\Delta F_{\hat{\omega}_1}\big(B_+ + B_-;-\mu\big) + (B_+ - B_-)\,\Delta F_{\hat{\omega}_1}\big(B_+ - B_-;-\mu\big)\Bigg], \tag{6.55}$$

where we have introduced $H' = Hg_R^2/\pi^2 = M_0\,g_R^2/g^2$ and defined $\Delta F_{\hat{\omega}_1}(B;\mu) = F_{\hat{\omega}_1}(B;\mu) - F_{\mathrm{vac}}(B_*;0)$. Eq. (6.55) is now UV finite, for fixed H, however the replacement (6.54) introduces a cut-off dependence into the originally UV finite equation for B_-. A practical workaround, to be interpreted as part of our approximation scheme, is to simply replace the bare coupling g by the renormalized one, g_R. The equation for B_- then reads

$$B_- = \frac{g_R^2}{4\pi^2}\Bigg[(B_+ + B_-)\,F_{\hat{\omega}_1}\big(B_+ + B_-;\mu\big) + (B_+ - B_-)\,F_{\hat{\omega}_1}\big(B_+ - B_-;\mu\big) -(B_+ + B_-)\,F_{\hat{\omega}_1}\big(B_+ + B_-;-\mu\big) - (B_+ - B_-)\,F_{\hat{\omega}_1}\big(B_+ - B_-;-\mu\big)\Bigg]. \tag{6.56}$$

We stress that the Euclidean localization scheme entails a dependence on the renormalization scale B_* via Eq. (6.55). The renormalized coupling is fixed such that the equation for B_+ attains a solution at $B_0(T=0,\mu=0) = 300$ MeV in the chiral limit.

In the following, we specify how to analyze the phase diagram given the (renormalized) rainbow equations in (6.52), which we schematically write as $\mathcal{R}_\pm = 0$. At this point, we recall that in the case of the physical localization, on the grounds of its rainbow equation, we were able to construct a potential. Based on Eqs. (6.52), in the case of the Euclidean localization, an analogous procedure is not possible and no potential can be inferred. This is due to the fact that the rainbow equations, interpreted as the respective first derivatives of such a potential V (if it existed) in the form $\mathcal{R}_\pm = \partial_{B_\pm} V$, do (in general) not satisfy the necessary Cauchy-Riemann equations. The absence of a potential implies that one cannot discriminate between solutions to identify the physical state of the system. Several comments are due.

Firstly, for certain parameter values, such as either vanishing temperature and/or chemical potential, it is in fact possible to construct a potential. This is based on the realization that in these cases the equation for B_- disappears, leaving behind one single equation for one real-valued variable B_+. This corresponds to the scenario encountered in the physical localization case and the potential (up to factors

f_+) is found as $V = \int \mathcal{R}_+$. However, for a generic situation of non-vanishing temperature and chemical potential, no such potential V exists.

Secondly, it is to be stressed that the absence of a potential is an artifact of our localization procedure. The original rainbow equations do derive from the (2PI) effective action. So a possible alternative to the present approach is to implement the localization procedure directly at the level of the effective potential. This will be discussed in the subsequent section.

Finally, we mention that some instances of the phase diagram are determined from conditions which do not require a potential in the first place. Their formulae merely feature the rainbow equations $\mathcal{R}_\pm$ and various derivatives. Although we insist that it only is via a potential that the physical state of the system can be determined. Nonetheless, we can identify solutions compatible with (tri)critical points *etc.* To this end, we keep the discussion concise at this point and refer to section 7.2 for more details in a similar situation. We employ one of the rainbow equations, say $\mathcal{R}_-(B_+, B_-) = 0$, to determine a relation $B_-(B_+)$, which is then inserted into the second rainbow equation $0 = \mathcal{R}_+\big(B_+, B_-(B_+)\big)$. This defines a reduced potential U in terms of one variable B_+, such that $U'(B_+) \equiv \mathcal{R}_+\big(B_+, B_-(B_+)\big)$. With respect to this reduced potential, in the chiral limit, a critical point is found via the condition

$$U''(0) = 0\,, \tag{6.57}$$

and a tricritical point corresponds to the conditions

$$U''(0) = U^{(4)}(0) = 0\,. \tag{6.58}$$

As before, lower spinodals are characterized by the same condition as the second order points, $U''(0) = 0$, applied in a first order regime. In the latter, there are also upper spinodal points, which are identified upon $U'(B_{\rm us}) = U''(B_{\rm us}) = 0$. Away from the chiral limit, to identify critical points, one lifts $B_\pm = 0$ and instead considers

$$U'(B_c) = U''(B_c) = U'''(B_c) = 0\,. \tag{6.59}$$

6.4.3 Localization at 2PI Level

In this subsection we address the issue of not being able to construct a potential based on the rainbow equations (6.52) in the Euclidean localization scheme. To this end, we consider the 2PI action in Eq. (6.2) and implement approximations which mimic the ones leading up to Eqs. (6.52). In particular, as a first ansatz, we scalarize the structure of the quark propagator S to its simplest component[10]

$$S[B;P] \to \frac{B(P)}{B(P)^2 + P_{i\mu}^2} \to \frac{1}{2}\bigg(\frac{B(\hat\omega_1,0)}{P_{i\mu}^2 + B(\hat\omega_1,0)^2} + \frac{B(-\hat\omega_1,0)}{P_{i\mu}^2 + B(-\hat\omega_1,0)^2}\bigg)\,, \tag{6.60}$$

where in the second step we have restricted the momentum-dependence of the mass function $B(P)$, according to Euclidean localization, to the first fermionic Matsubara frequencies and vanishing spatial momentum. In this setup, one defines a (localized) potential as the 2PI effective action[11]

$$\Gamma_{\rm 2PI}^{\rm Landau} \;=\; -{\rm Tr}\,{\rm Ln}\,S^{-1} - {\rm Tr}\,S_0^{-1}\,S - \frac{1}{2}g^2 C_F \int_{\hat P\hat Q}^T {\rm tr}\Big(\gamma^\mu\,S(P)\gamma^\nu\,S(Q)\Big)G_{\mu\nu}(P-Q)\,, \tag{6.61}$$

evaluated with S given in (6.60). We shall not give the explicit expression here for reasons that become clear below.

Taking derivatives with respect to $B\pm$, we attempt to match the resulting formulae to the expressions in Eqs. (6.51). indeed, it is,

$$\begin{aligned}(\partial_{B_+} + \partial_{B_-})\Gamma_{\rm 2PI}^{\rm Landau} \;=\; 4\int_{\hat P}^T \frac{P_{i\mu}^2 - (B_+ + B_-)^2}{\big[P_{i\mu}^2 + (B_+ + B_-)^2\big]^2}\Bigg[B_+ + B_- - M_0 - 2g^2\int_{\hat Q}^T G_m(Q-P) \\ \times\bigg(\frac{B_+ + B_-}{Q_{i\mu}^2 + (B_+ + B_-)^2} + \frac{B_+ - B_-}{Q_{i\mu}^2 + (B_+ - B_-)^2}\bigg)\Bigg]\,.\end{aligned} \tag{6.62}$$

[10] This approximation can be seen as the analogue of setting to zero all tensor components in the steps leading up to Eq. (6.29), which are not proportional to the identity.

[11] Note that the formalism presented in this subsection in terms of the 2PI action can be extended to LdW gauge, see appendix E for details.

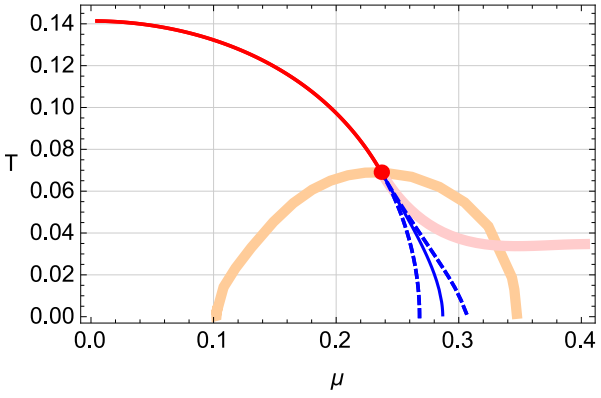

Figure 6.3: Summary of the phase diagram in the chiral limit (all scales in GeV) in the physical localization, with $B_0 = 0.3$ GeV and $m = 0.5$ GeV. The spinodal (dashed) and first (solid) order line are shown in blue, and the second order line and tricritical point in red. The orange band shows the position of the tricritical point in dependence of the gluon mass. The red band corresponds the position of the critical endpoint as a function of nonzero bare quark mass, as further illustrated in Fig. 6.4.

One identifies the interior of the square bracket as the expression one obtains for $B_+ + B_-$ from Eq. (6.51), with the exception that the external momentum is not fixed to the lowest modes but rather integrated over with the weight factor $\big(P^2 - (B_+ + B_-)^2\big)/\big[P^2 + (B_+ + B_-)^2\big]^2$. Similarly for the combination $(\partial_{B_+} - \partial_{B_-})\Gamma^{\text{Landau}}_{\text{2PI}}$, where the integrated factor then corresponds to the formulae of $B_+ - B_-$ in Eq. (6.51) if one simultaneously allows for a change $\mu \to -\mu$. This is typically accounted for upon letting $Q \to -Q$, which does not leave Eq. (6.51) invariant due to a sign introduced in the gluon propagator $G_m(Q-P) \to G_m(-Q-P)$. In contrast, this can be absorbed in $(\partial_{B_+} - \partial_{B_-})\Gamma^{\text{Landau}}_{\text{2PI}}$ by a simultaneous $P \to -P$, which then changes the external weight but completes the matching on the level of the integrated factors:

$$(\partial_{B_+} - \partial_{B_-})\Gamma^{\text{Landau}}_{\text{2PI}} = 4\int_{\hat{P}}^{T} \frac{P^2_{-i\mu} - (B_+ - B_-)^2}{\big[P^2_{-i\mu} + (B_+ - B_-)^2\big]^2}\Bigg[B_+ - B_- - M_0 - 2g^2 \int_{\hat{Q}}^{T} G_m(Q-P) \times\left(\frac{B_+ + B_-}{Q^2_{-i\mu} + (B_+ + B_-)^2} + \frac{B_+ - B_-}{Q^2_{-i\mu} + (B_+ - B_-)^2}\right)\Bigg]. \tag{6.63}$$

The ability to transform $Q \to -Q$ and $P \to -P$ as performed in the 2PI setting is ultimately a consequence of the ansatz (6.60). It introduces a symmetry which is not present in the full underlying theory and therefore constitutes an artifact of the approximation. In fact, the potential in Eq. (6.61) is invariant under $\mu \to -\mu$, which in turns implies that the potential is real-valued if one chooses the variables B_+ and B_- real for any real non-zero μ. This, as explained in sections 6.2 and 6.4.2, is certainly not true in the case of the original theory, where one ought to consider B_+ real and B_- imaginary (which is equally allowed for by the potential in Eq. (6.61)). As a further caveat of the approach presented here, we also insist that the weight factor $\big(P^2 - (B_+ + B_-)^2\big)/\big[P^2 + (B_+ + B_-)^2\big]^2$ is not positive-definite and thus introduces unphysical extrema, which have the tendency to wash out the physical ones for a certain range of parameter values. However, either of these shortcomings is negligible in the chiral limit, where the transition occurs directly at $B_\pm = 0$. As such, we have attempted to locate the tricritical point from various different approaches[12] based on the 2PI potential and never encountered anything resembling its characteristic features. In this respect, we also point out that there is a further issue in the formulae of Eq. (6.61) related to the expression for the two thermal part of the scalar sunset, $S(2n)$, discussed in section B.3.3. This is because the Re ln terms in Eq. (B.50) contain a pole whenever the quark mass attains half the value of the gluon mass. In the heavy quark regime this was never essential. However, it becomes important in the context of chiral symmetry breaking. The pole is regulated by the $i0^+$ present in Eq. (B.50), and must be controlled either analytically or numerically. Despite our efforts we have not found a simple way to get this under control in our numerics.

6.5 Results

We now present our results for the phase diagram as obtained from the physical and Euclidean localization schemes.

[12] For instance, directly at $B = 0$, or by allowing for a small non-zero bare quark mass and the (non-existent) scaling behavior in the near vicinity, or by studying the nature of various contourplots of Eqs. (6.62) and (6.63). Or by manually neglecting the effects of the weight factor in Eqs. (6.62) and (6.63), *etc.* All while trying several renormalization schemes and formats, either via dimensional regularization or a UV-cutoff.

chiral limit	$\mu_{\rm tric}$	$T_{\rm tric}$	$T_{\rm c}(0)$	$\mu_{\rm ls}$	$\mu_{\rm first}$	$\mu_{\rm us}$
Physical loc.	237	69	141	268	287	305
Euclidean loc.	318	64	150	346	365	376
Jakovac *et al.* [103]	≈ 280	≈ 60	140			
Schaefer *et al.* [291]	251	52	142			
Hatta *et al.* [66]	209	107	–			
Qin *et al.* [292] A	140	110	124			
Qin *et al.* [292] B	130	120	133			
Costa *et al.* [216]	286	112	215/6			

Table 6.1: Overview of the numerical results for the various qualitative points in the chiral phase diagram, for the localization schemes considered, in comparison to benchmark literature findings, based upon various approaches based upon the quark model [103, 291], the NJL model [216], and different nonperturbative continuum approaches to QCD [66, 292]. All numbers are given in MeV. For the Euclidean localization, the rainbow equations don't satisfy the Cauchy-Riemann relations and therefore one cannot construct a potential, which in principle inhibits the determination of the $\mu_{\rm first}$-values. However, at $T = 0$, the $\mathcal{R}_-$-equation disappears and one proceeds based solely on $\mathcal{R}_+$, yielding $V = \int \mathcal{R}_+$. We have chosen a value of $B_* \approx 950$ MeV.

Let us first consider the chiral limit. In Fig. 6.3, we summarize the phase diagram in the physical localization scheme. It is coined by the presence of two phases, a chirally broken one in the low temperature and low density region, and a chirally restored phase in the high temperature and high density regime. At vanishing chemical potential the two phases are separated by a a second order transition at the critical temperature $T_c(0)$. For increasing μ, the transition remains second order until the critical line, in red, hits a tricritical point with coordinates $(\mu_{\rm tric}, T_{\rm tric})$, and then turns into the line denoting the lower spinodal, in dashed blue (lower), which eventually ends on the μ-axis at a value $\mu_{\rm ls}$. As mentioned in section 6.4.1, the critical and lower spinodal lines are determined from the same condition in Eq. (6.41). It can easily be reduced to the form

$$\mu^2(T) = m^2 \frac{B_0^2 \ln(B_0/m)}{B_0^2 - m^2} - 4\int_0^\infty dq\, q^2 \frac{n_{\varepsilon_q^m}}{\varepsilon_q^m} - \frac{\pi^2}{3}T^2\,, \tag{6.64}$$

which, as can be verified, is a concave function. A further simplification occurs upon neglecting the bosonic integral, which is justified for sufficiently small temperatures $T/m \ll 1$. The resulting equation yields a fairly adequate reproduction of the complete phase transition line in Fig. 6.3. For a similar result to Eq. (6.64) in a large N_f scenario within the Quark-Meson model, the reader is referred to Ref. [103, 293]. Alongside the lower spinodals, there is an upper spinodal line connecting the tricritical point with the zero temperature axis, at an associated value of the chemical potential denoted by $\mu_{\rm us}$. Together the spinodal lines flank a first order transition line and $\mu_{\rm ls} \leq \mu_{\rm first} \leq \mu_{\rm us}$ must therefore necessarily hold true. In section 6.4.1, it was pointed out that the position of the first order line is not uniquely determined since it depends on the particular potential the localized rainbow equation derives from, *e.g.*, from the choice of the function f_+ described in the previous section. In Fig. 6.3, we depict results corresponding to $f_+ = 1$. However, we also recall that the two spinodal lines are independent of f_+ and since they are not too far apart, this yields a reasonable bound for the entire first order line. Quantitatively, our results in the chiral limit are summarized in Tab. 6.1. We also show the respective findings in the Euclidean localization scheme, for two different values of the renormalization scale.

For a non-zero bare quark mass, chiral symmetry is explicitly broken and the tricritical point becomes critical and moves in the phase diagram as a function of H, as indicated for the physical localization by the red band in Fig. 6.3, and in more detail in Fig. 6.4. This behavior is in qualitative agreement with findings from nonperturbative studies employing the 2PI Effective Potential [66]. The immediate vicinity of the tricritical point is well-described by mean-field exponents, which is the expected behavior since the rainbow equations of both localization schemes are regular at $B = 0$. In Fig. 6.5, we show the quantities $\mu_c(H)$ and $T_c(H)$ for small H, in case of the physical localization.

Further, the second order critical line at $H = 0$ becomes a smooth crossover at $H \neq 0$. In the following, we shall always define the crossover temperature as the point of steepest ascent/descent of the associated order parameter. With this definition, we can determine for which value of H the crossover temperature of the quark mass B becomes $T_s = 170$ MeV in the limit of vanishing potential, $\mu = 0$, since this is the value provided by lattice simulations at the physical point [52, 69, 295]. Within our approach, we treat

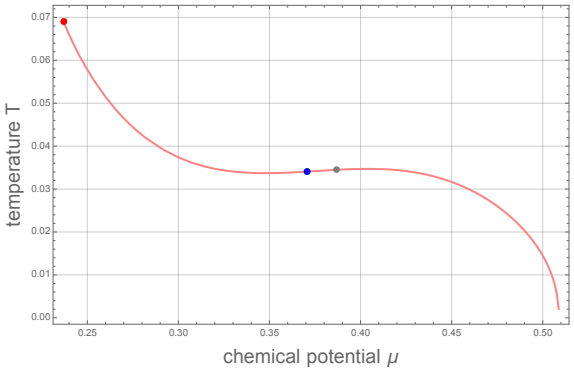

Figure 6.4: Position of the critical point in the physical localization for increasing values of H, starting from the tricritical point in thick red in the chiral limit. The vicinity of the tricritcial point is well-described by mean field scaling exponents, see Fig. 6.5. The blue and gray points correspond to the position of the critical point for physical bare quark mass (see main text), as given by Tab. 6.2, as determined either from B or σ; see text. As can be seen, these alternative choices lead to marginal changes only. The fact that the curve eventually decreases after attaining the physical point instead of rising indefinitely can be attributed to limitations of the physical localization. In particular, due to the presence of the pole at $B = m$, our analysis is restricted to small B-values, that is, to not too large values of H.

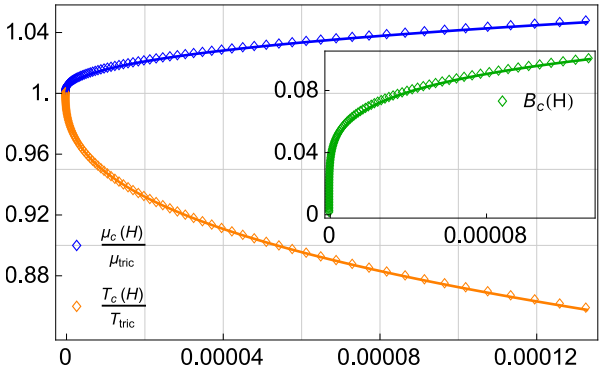

Figure 6.5: The vicinity of the tricritical point in the chiral limit (here for the physical localization) is governed by a scaling behavior of $\mu_c(H)$, $T_c(H)$, and $B_c(H)$ with mean field exponents. The solid lines correspond to power law fits of the form $X_c(H) - X_{\rm tric} \propto H^{\omega_X}$ for $X = \mu, T, B$ with respective exponents $\omega_T = \omega_\mu = 2/5$ and $\omega_B = 1/5$.

Models for CEP	$\mu_c^{\rm phys}$	$T_c^{\rm phys}$
Phys. loc. (B)	371	34
Phys. loc. (σ)	482	23
Fischer *et al.* [101]	168	115
Luecker *et al.* [294]	≈145	≈ 100
Hatta *et al.* [66]	279	95
Tripolt *et al.* [231]	293	10
Ayala *et al.* [224]	315-349	18-45
Cui *et al.* [225]	245	38
Yokota *et al.* [226]	287	5
Contrera *et al.* [227]	319	70
Knaute *et al.* [228]	204	112
Antoniou *et al.* [229]	256	150
Scavenius *et al.* [230] LσM	207	99
Scavenius *et al.* [230] NJL	332	46
Costa *et al.* [216]	332	80
Kovacs *et al.* [217]	320	63

Table 6.2: Coordinates of the critical point in the phase diagram at the *physical point*, $H_{\rm phys}$, obtained once with B and once with σ as the relevant order parameter. All values are in MeV. We compare our findings against many literature computations of the QCD CEP. We distinguish between first-principle and model-based computations.

this particular value of H to correspond to the *physical point*, $H_{\rm phys}$. Once $H_{\rm phys}$ is determined, we can then locate the critical point in the associated phase diagram, see Tab. 6.2. Alternatively, instead of B, one might also consider the quark condensate[13] $\sigma = \langle\bar\psi\psi\rangle$, which in the current approximation can be

[13] In fact, lattice results for the crossover temperature are based on this observable rather than B. Therefore, it would, in principle, be more appropriate to use σ to determine the physical point. The latter is however not well-defined (since UV divergent) in the present localized approximation.

written as

$$\sigma = -4N_f N_c \int_{\hat{P}}^{T} \frac{B(P)}{P_{i\mu}^2 + B^2(P)} = -4N_f N_c \, B \, J_B \,, \tag{6.65}$$

with the first fermionic tadpole defined as $J_B \equiv \int_{\hat{P}}^{T} G_B(P_{i\mu})$ and $G_B(P) = 1/(B^2 + P^2)$. Note that the

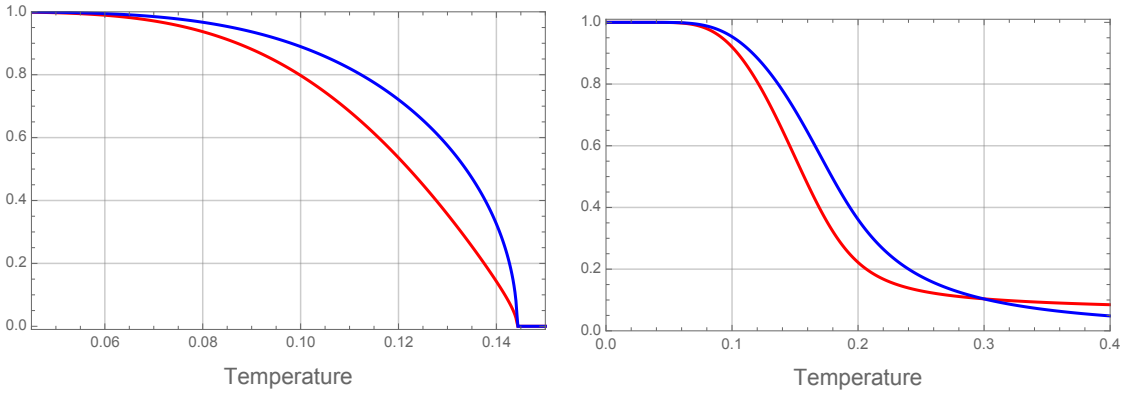

Figure 6.6: Chiral condensate (red) vs. quark mass B (blue) as functions of temperature, for vanishing chemical potential, in the physical localization scheme. All curves are normalized against their zero temperature value. The left plot corresponds to the chiral limit, $H = 0$, whereas for the right plot H is taken at the physical point, *i.e.* such that the quark mass B attains a crossover at $T = 170$ MeV.

vacuum part of the tadpole J_B is given by $J_B(0n) = \frac{1}{8\pi^2}\left(2\Lambda^2 + B^2 \log[B^2/(2\Lambda)^2]\right)$ and thus UV divergent with the cutoff. Since at the current order of approximation we cannot control the renormalization of σ, our naive recipe is to simply subtract the cutoff divergences in $J_B(0n)$. This leaves a scale dependence in $J_B(0n) \to \frac{B^2}{8\pi^2}\log[B^2/\bar{\mu}^2]$, which we choose as $\bar{\mu} = 1$ GeV. For the physical localization scheme, in Fig. 6.4, we show the position of the respective CEPs (as obtained via B or σ) on the curve of critical points in the phase diagram as a function of H. Note that in the chiral limit, for the tricritical point, there is no ambiguity since $B = 0$ is equivalent to $\sigma = 0$. A similar remark applies for the lower spinodal lines in the phase diagram.

We show our results for the CEP in Tab. 6.2 together with a collection of results from various approaches in the literature, ranging from various (PQM, PNJL, *etc.*) models to nonperturbative continuum QCD approaches (2PI, DSE). As can be seen, the community has not yet reached a ballpark consensus on the location of the critical end point in the QCD phase diagram and a wide range of results seem permissible at this point. Our numbers do certainly fall within the group of lower temperatures and larger chemical potentials, and compare well with models [216, 217, 224, 230]. Our agreement with models of NJL type is not surprising, since, as discussed in section 6.4, our localized models closely resemble the NJL formulae.

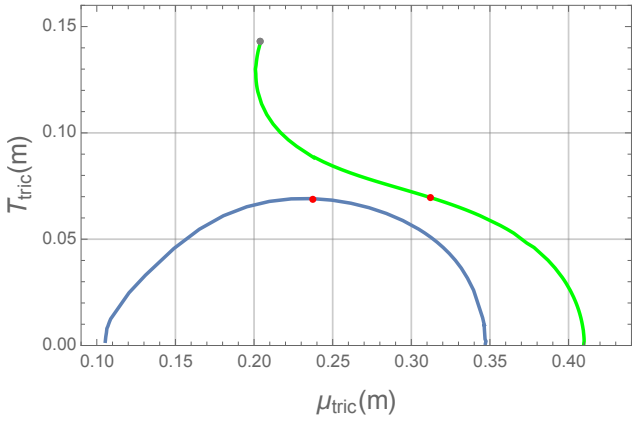

Figure 6.7: Position of the tricritical points in the physical (blue) and Euclidean (green) localization upon varying the gluon mass, where the red points correspond to $m = 500$ MeV, the typical value chosen in the CF model. The gray point corresponds to $m = 0$ and its coordinates can be found in Tab. 6.3, alongside with the remaining other values of $m_{\text{min/max}}$.

Finally, one can study how our findings for the phase diagram depend on the CF mass. While $m = 500$ MeV is the value that globally works best in both the pure YM and the unquenched sector, it is

nonetheless insightful to vary it as a free parameter. For instance, it is interesting to investigate whether a nonzero mass is necessary for having a CEP, or a tricritical point in the chiral limit. Thereby, for each value of m, we always insist on fixing the coupling such that we keep the $T = \mu = 0$ solution B_0 fixed at 300 MeV in the chiral limit.

loc.	Physical	Euclidean
$m_{\min}$	0.088	0
$\mu_{\min}$	0.10	0.205
$T_{\min}$	0	0.143
$m_{\max}$	1.02	0.93
$\mu_{\max}$	0.34	0.407
$T_{\max}$	0	0

Table 6.3: Overview of $m_{\min/\max}$ for both localizations in the chiral limit. Results obtained upon varying the gluon mass, to the upper and lowermost values allowed. We also show the corresponding values of the chemical potential and temperature.

In Fig. 6.7, we trace the position $(\mu_{\rm tric}(m), T_{\rm tric}(m))$ of the tricritical point in the chiral limit. As can be seen, the obtained trajectories are qualitatively quite different, however, the red points (corresponding to m=500 MeV) nonetheless lie rather close to one another. While the physical localization permits for two crossings of the μ-axis, the Euclidean localization only exhibits one. Here, $m_{\rm min,max}$ are defined as the minimum/maximum value of the gluon mass such that there still exists a tricritical point in the phase diagram, *i.e.*, as the value of m when the tricritical point crosses the μ-axis. In the Euclidean localization, one never encounters an $m_{\min}$ and the tricritical point moves to the location denoted in gray in Fig. 6.7 for $m = 0$. This then implies that the existence of a tricritical point imposes constraints on the allowed values of the gluon mass. While in both localization schemes considered here, it can never exceed an upper limit $m_{\max}$, in the Euclidean localization one might take $m \to 0$ without losing the tricritical point. This is not the true for the physical localization which requires a non-zero m.

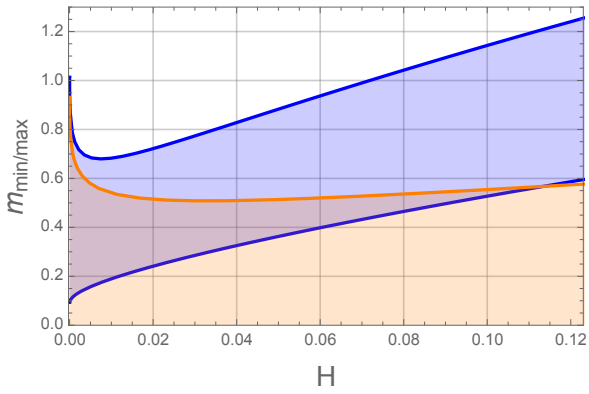

Figure 6.8: We show the evolution of the values $m_{\min}$ and $m_{\max}$ at vanishing temperature as a function of H. The blue curves corresponds to the physical and the orange ones to the Euclidean localization. The respective shaded areas denote the parameter values compatible with the existence of a CEP in the QCD phase diagram. In the non-shaded areas, a CEP is excluded. Scales are given in GeV.

Explicitly, for instance for the physical localization, we can determine the values of $m_{\rm min,max}$ based on analytic considerations from Eqs. (6.38) and (6.39). Letting $x = m/B_0$ and $u = (\ln x^2)/(x^2 - 1)$, one finds the condition $u = 1 + \ln(2u)$, which allows for two real and positive solutions, $u_\pm = u(x_\pm)$, subject to $x_+ x_- = 1$. We find $x_- = \sqrt{u_+/u_-} \approx 0.294$ and $x_+ \approx 3.398$, which give the values shown in Tab. 6.3. To obtain the corresponding values of $y = \mu/B_0$, one resorts to Eq. (6.64) at $T = 0$, $y^2 = x^2 u/2$, yielding $y_- = \sqrt{u_+/2} \approx 0.340$ and $y_+ = y_-/x_- \approx 1.157$. These values again match the numerical results of Tab. 6.3.

The definition of $m_{\rm min,max}$ is trivially extended to the case of non-zero H such that $m_{\rm min,max}(H)$, where the tricritical point is replaced by the CEP. We then show our results for these values in dependence of the symmetry breaking paramter H in Fig. 6.8. Here, we iterate our observation that the existence of a CEP puts an upper bound on the allowed values for the gluon mass in both localization schemes considered, whereas a lower bound only exists for the physical localization.

6.6 Conclusion

In this chapter we have studied the physics of chiral symmetry breaking and its restoration at finite temperature. After some brief introductory comments on the origin and motivation for the rainbow-improved expansion scheme developed in the CF model [170], we have discussed the general structure of the dressed quark propagator at finite temperature. Upon imposing the symmetries of the thermal

system at non-zero density and gluon background, such as parity and charge conjugation invariance, we have worked out the allowed Dirac tensor decomposition of the (inverse) propagator.

Subsequently, we have applied this decomposition to the generalized rainbow equation to derive a set of coupled, non-linear integral equations for the Dirac components of the propagator. In general, these components are complex-valued functions of the four-momentum and explicitly depend on flavor, color, temperature, density and the gluon background.

Before attempting a numerical study of the full structure of these integral equations, we have considered various primary approximation schemes. Our main aim is to develop familiarity with the underlying structure at a simple qualitative level within the CF model, with the intension to eventually extend this work to a more involved treatment, for example the inclusion of a nontrivial gluon background. In so doing, we have introduced a scheme called localization, which amounts to replacing a momentum dependent mass function by a constant, chosen as the value at vanishing momentum. We have specified two implementations of this localization scheme, called physical and Euclidean.

In this context, we have analyzed their predictions for the chiral phase structure, neglecting, at first, the background field, and compared to existing literature findings. Both schemes are in qualitative agreement with the prevalent expected picture, and we further find that quantitatively our values for the tricritical point lie within the ballpark of the vast range of possible locations presented in the literature. Moreover, our simple models are capable of reproducing the tricritical scaling behavior and associated mean field exponents with reasonable accuracy.

In a further step, one can determine the value of the bare quark mass yielding a crossover at zero density and a temperature of 170 MeV, as provided by lattice simulations for QCD at physical quark masses. With this value, one obtains a prediction for the critical endpoint in the QCD phase diagram from our localized models. This calculation can be performed based on either the quark mass function or the condensate as the relevant order parameters, and both methods yield results that are in proximity. More importantly, they range within the literature data from various model studies. This is a remarkable result given the simplicity of our formulation involved.

Finally, we have studied the dependence of both a tricritical point in the chiral limit as well as the CEP for nonzero bare quark masses as a function of the gluon mass. We find that in both models under consideration, their existence is tantamount to the gluon mass value staying below an upper bound beyond which both points vanish off the phase diagram. On the other hand, in one of the two schemes considered, there is additionally a lower bound for the gluon mass. Based on our localizations, we conclude that the necessity of a non-zero gluon mass to allow for a CEP in the QCD phase diagram is observed to be severely scheme-dependent. This issue is certainly an interesting question to investigate in future work and can be definitely answered by solving the original rainbow equations exactly with numerical methods.

Lastly, we mention that a very interesting line of investigation based upon the considerations of this chapter is to introduce a non-trivial gluon background into the localized rainbow equations, permitting a common description of both the order parameters for heavy and light quark physics. This is the topic of the next chapter.

7 Chiral and Deconfinement transition from the Curci-Ferrari Model

In this chapter, we extend the analysis performed in the previous chapter of the chiral transition in terms of the resummed rainbow equations, where it was demonstrated that simple descriptions in the form of localized equations lead to a qualitative agreement with prevalent literature findings. Here, we profit of the simplicity of the localizations considered, and equip the the Euclidean localization with a non-trivial gluon background which thus establishes a link to the Polyakov loop. In this setup, we describe the entire range of the Columbia plot, from the heavy to light quark regime. In so doing, we study the interplay of the chiral and deconfinement transition and analyse the physical point, all from a common approach for the chiral condensate and the Polyakov loop.

In section 7.1, we specify the model, its motivation and characteristics. In particular, we outline some of the challenges that arise in the presence of multiple, colorful quark masses. Further, in section 7.2, we comment on the interplay between the chiral and deconfinement transition and outline explicitly some of the conditions determining the phase structure, which can be generalized to more intricate scenarii. In section 7.3, we showcase our results for the phase structure and the Columbia plot at vanishing chemical potential. Finally, we conclude in section 7.4.

7.1 The Model

We note that both of the two localizations under consideration in chapter 6 are in principle extendable to non-zero gluon background. However, one of the interests of establishing a link to the Polyakov loop is to study the dynamics across the whole Columbia plot, for which the associated B-values become non-zero, and, potentially, large. In this respect, given the pole of the physical localization scheme at $B = m$, it is sensible to merely consider the Euclidean localization scheme at non-trivial gluon background. Its equations in Landau gauge, and for arbitrary values of the renormalization scale B_*, are detailed in section 6.4.2. For nonvanishing background, $r \neq 0$, the quark masses B become colorful quantities and there exists a B^ρ associated to each weight ρ of the fundamental representation.

We begin our derivation of the background-dependent Euclidean localization from the expression in (6.25), where we set all vector components $\hat{A}_0^\rho(P), \hat{A}_v^\rho(P)$ and $\hat{C}_\rho(P)$ to their tree-level values, yielding

$$B_\sigma(P) \;=\; M_0 + 3\,g^2 \sum_{\rho,\kappa} \mathcal{D}_{\sigma,\rho\kappa} \int_{\hat{Q}}^{T} \frac{B_\rho(Q)}{B_\rho(Q)^2 + (\hat{\omega}_n + Tr_\rho + i\mu)^2 + q^2} \frac{1}{(\hat{\omega} - \hat{\omega}_n + Tr_\kappa)^2 + (\vec{p} - \vec{q})^2 + m^2}\,, \tag{7.1}$$

where $\hat{\omega}$ and $\hat{\omega}_n$ denote the external and internal Matsubara frequencies, such that $\hat{\omega} - \hat{\omega}_n$ is bosonic. We evaluate (7.1) for $\hat{\omega} = \hat{\omega}_1$ and zero external momentum, $\vec{p} = 0$. In the same spirit as presented in section 6.4.2, it is conceivable that the first factor of the integrand contributes the strongest for $\hat{\omega}_n = \pm\hat{\omega}_1$ and $q = 0$. Likewise, the second for $\hat{\omega}_n = \hat{\omega}_1$ and $q = 0$. Thus, denoting, as before, $B_\sigma(\hat{\omega}_1) \equiv B_\sigma(\hat{\omega}_1, 0)$, we can approximate the integral by its (supposedly) dominant contributions and obtain a background-extended

version of Eq. (6.49),

$$B_\sigma(\hat{\omega}_1) = M_0 + 3\,g^2 \sum_{\rho,\kappa} \mathcal{D}_{\sigma,\rho\kappa} \int_{\hat{Q}}^{T} \frac{1}{(\hat{\omega}_1 - \hat{\omega}_n + Tr_\kappa)^2 + q^2 + m^2} \times \frac{1}{2}\left[\frac{B_\rho(\hat{\omega}_1)}{B_\rho(\hat{\omega}_1)^2 + q^2 + (\hat{\omega}_n + Tr_\rho + i\mu)^2} + \frac{B_\rho(-\hat{\omega}_1)}{B_\rho(-\hat{\omega}_1)^2 + q^2 + (\hat{\omega}_n + Tr_\rho + i\mu)^2} \right], \tag{7.2}$$

and similarly for $B_\sigma(-\hat{\omega}_1)$. In general, we have that

$$B_\rho(\hat{\omega}, r^*, -\mu^*)^* = B_\rho(\hat{\omega}, r, \mu)\,, \tag{7.3}$$

at which point it becomes apparent that, the resulting equations feature a large amount[1] of complex-valued quark masses. Each of which has to be determined from its own gap equation, which in turn all back-couple to form one large set of coupled integral equations. In a primary attempt, we restrict identically to the scenario of vanishing chemical potential, $\mu = 0$, upon which the equations simplify. This is due to a vanishing r_8 component, and the fact that we can choose $r_3^* = r_3$ such that $B_\rho \in \mathbb{R}$ for all ρ. Further, based on (6.20), it is

$$B_{\rho_1}(-\hat{\omega}, r_3)^* = B_{\rho_2}(\hat{\omega}, r_3) \tag{7.4}$$
$$B_{\rho_2}(-\hat{\omega}, r_3)^* = B_{\rho_1}(\hat{\omega}, r_3) \tag{7.5}$$
$$B_{\rho_3}(-\hat{\omega}, r_3)^* = B_{\rho_3}(\hat{\omega}, r_3) \tag{7.6}$$

and the realness of the quark masses allows for

$$B_{\rho_1}(\hat{\omega}) = B_{\rho_2}(-\hat{\omega}) \equiv B_1 \tag{7.7}$$
$$B_{\rho_2}(\hat{\omega}) = B_{\rho_1}(-\hat{\omega}) \equiv B_2 \tag{7.8}$$
$$B_{\rho_3}(\hat{\omega}) = B_{\rho_3}(-\hat{\omega}) \equiv B_3\,. \tag{7.9}$$

In a next step, we define

$$\mathcal{F}_\kappa^\rho(B) \equiv 4\pi^2 \int_{\hat{Q}}^{T} \frac{1}{(\hat{\omega}_1 - \hat{\omega}_n + Tr_\kappa)^2 + q^2 + m^2} \frac{1}{B^2 + q^2 + (\hat{\omega}_n + Tr_\rho)^2}\,, \tag{7.10}$$

which is worked out as, with $\sigma = \rho + \kappa$,

$$\mathcal{F}_\kappa^\rho(B) = \frac{1}{2}\int_0^\Lambda \mathrm{d}q\, \frac{q^2}{\epsilon_m \epsilon_B}\left[\frac{n_{\epsilon_m + iTr_\kappa} - f_{\epsilon_B + iTr_\rho}}{iTr_\sigma + i\hat{\omega}_1 + \epsilon_B + \epsilon_m} - \frac{f_{\epsilon_B - iTr_\rho} + n_{\epsilon_m + iTr_\kappa}}{iTr_\sigma + i\hat{\omega}_1 - \epsilon_B + \epsilon_m} \right. \\ \left. + \frac{f_{\epsilon_B + iTr_\rho} + n_{\epsilon_m - iTr_\kappa}}{iTr_\sigma + i\hat{\omega}_1 + \epsilon_B - \epsilon_m} + \frac{-n_{\epsilon_m - iTr_\kappa} + f_{\epsilon_B - iTr_\rho}}{iTr_\sigma + i\hat{\omega}_1 - \epsilon_B - \epsilon_m} + \frac{2(\epsilon_m + \epsilon_B)}{-(i\hat{\omega}_1 + iTr_\sigma)^2 + (\epsilon_m + \epsilon_B)^2} \right], \tag{7.11}$$

and which reproduces (6.53) in the limit of vanishing background, for vanishing chemical potential. Its vacuum contribution is

$$\mathcal{F}_{\mathrm{vac}}(B) = \int_0^\Lambda \mathrm{d}q\, \frac{q^2}{\epsilon_m \epsilon_B} \frac{1}{\epsilon_m + \epsilon_B}\,. \tag{7.12}$$

The above permit to nicely rewrite (7.2) as

$$B_\sigma = M_0 + \frac{3}{8\pi^2}\, g^2 \sum_{\rho,\kappa} \mathcal{D}_{\sigma,\rho\kappa} \Big[B_\rho(\hat{\omega}_1)\, \mathcal{F}_\kappa^\rho\big(B_\rho(\hat{\omega}_1)\big) + B_\rho(-\hat{\omega}_1)\, \mathcal{F}_\kappa^\rho\big(B_\rho(-\hat{\omega}_1)\big) \Big]. \tag{7.13}$$

After employing the explicit color dependences in (7.7-7.9), we can turn the color sum $\sum_{\rho,\kappa} \mathcal{D}_{\sigma,\rho\kappa}$ into a vector form

$$\begin{pmatrix} B_1 \\ B_2 \\ B_3 \end{pmatrix} = M_0 + \frac{1}{8\pi^2} g^2 \left[\begin{pmatrix} \mathcal{F}_0^{\rho_1}(B_1) & 3/2\,\mathcal{F}_{\kappa 3}^{\rho_2}(B_2) & 3/2\,\mathcal{F}_{\kappa -2}^{\rho_3}(B_3) \\ 3/2\,\mathcal{F}_{\kappa -3}^{\rho_1}(B_1) & \mathcal{F}_0^{\rho_2}(B_2) & 3/2\,\mathcal{F}_{\kappa 1}^{\rho_3}(B_3) \\ 3/2\,\mathcal{F}_{\kappa 2}^{\rho_1}(B_1) & 3/2\,\mathcal{F}_{\kappa -1}^{\rho_2}(B_2) & \mathcal{F}_0^{\rho_3}(B_3) \end{pmatrix} \right. \\ \left. + \begin{pmatrix} \mathcal{F}_0^{\rho_1}(B_2) & 3/2\,\mathcal{F}_{\kappa 3}^{\rho_2}(B_1) & 3/2\,\mathcal{F}_{\kappa -2}^{\rho_3}(B_3) \\ 3/2\,\mathcal{F}_{\kappa -3}^{\rho_1}(B_2) & \mathcal{F}_0^{\rho_2}(B_1) & 3/2\,\mathcal{F}_{\kappa 1}^{\rho_3}(B_3) \\ 3/2\,\mathcal{F}_{\kappa 2}^{\rho_1}(B_2) & 3/2\,\mathcal{F}_{\kappa -1}^{\rho_2}(B_1) & \mathcal{F}_0^{\rho_3}(B_3) \end{pmatrix} \right] \begin{pmatrix} B_1 \\ B_2 \\ B_3 \end{pmatrix}. \tag{7.14}$$

[1] In principle, there are $N_f \times N_c$ to begin with, and an additional factor 2 due to the distinction between positive and negative first Matsubara frequencies. However, the resulting complex masses all have a mutual complex conjugate partner, thus reducing the number of independent variables by a factor 2 again.

Since the non-thermal pieces in $\mathcal{F}$ are UV divergent, we have to consider some form of renormalization. In section 6.4.1 for vanishing background, the corresponding equation was rendered finite by a coupling renormalization, where the coupling is expressed in dependence of a particular mass shell B_* and further a solution B_0 at vanishing temperature; see (6.54) and surroundings. On the other hand, it can be shown[2] that at non-trivial background, any form of coupling renormalization in (7.14) is not sufficient to turn all three equations for the components B_i simultaneously finite. Therefore, we are forced to employ, by hand, an *ad hoc* renormalization scheme. In this respect, we choose the integrals in (7.14) as being subtracted by a vacuum piece at the scale B_*:

$$\mathcal{F}^{\rho}_{\kappa}(B) \to \mathcal{F}^{\rho}_{\kappa}(B) - \mathcal{F}_{\mathrm{vac}}(B_*) \equiv \Delta\mathcal{F}^{\rho}_{\kappa}(B)\,. \tag{7.15}$$

Categorically, this replacement renders (7.14) finite and thus well-defined, but it still depends on the coupling. Note that at vanishing temperature all B_i's coincide, in which case we divide (7.14) by the coupling and and we call B_0 the corresponding solution in the chiral limit, as we did before in chapter 6. The resulting relation is used to formally replace the coupling by the dimensionful parameter B_0. This recipe eventually leads to

$$\begin{aligned} 0 \;=\; \begin{pmatrix}\mathcal{R}_1\\ \mathcal{R}_2\\ \mathcal{R}_3\end{pmatrix} \equiv\; H + \frac{1}{8}\Bigg[&\begin{pmatrix} \Delta\mathcal{F}^{\rho_1}_{0}(B_1) & 3/2\,\Delta\mathcal{F}^{\rho_2}_{\kappa_3}(B_2) & 3/2\,\Delta\mathcal{F}^{\rho_3}_{\kappa_{-2}}(B_3)\\ 3/2\,\Delta\mathcal{F}^{\rho_1}_{\kappa_{-3}}(B_1) & \Delta\mathcal{F}^{\rho_2}_{0}(B_2) & 3/2\,\Delta\mathcal{F}^{\rho_3}_{\kappa_1}(B_3)\\ 3/2\,\Delta\mathcal{F}^{\rho_1}_{\kappa_2}(B_1) & 3/2\,\Delta\mathcal{F}^{\rho_2}_{\kappa_{-1}}(B_2) & \Delta\mathcal{F}^{\rho_3}_{0}(B_3)\end{pmatrix} \\ &+ \begin{pmatrix} \Delta\mathcal{F}^{\rho_1}_{0}(B_2) & 3/2\,\Delta\mathcal{F}^{\rho_2}_{\kappa_3}(B_1) & 3/2\,\Delta\mathcal{F}^{\rho_3}_{\kappa_{-2}}(B_3)\\ 3/2\,\Delta\mathcal{F}^{\rho_1}_{\kappa_{-3}}(B_2) & \Delta\mathcal{F}^{\rho_2}_{0}(B_1) & 3/2\,\Delta\mathcal{F}^{\rho_3}_{\kappa_1}(B_3)\\ 3/2\,\Delta\mathcal{F}^{\rho_1}_{\kappa_2}(B_2) & 3/2\,\Delta\mathcal{F}^{\rho_2}_{\kappa_{-1}}(B_1) & \Delta\mathcal{F}^{\rho_3}_{0}(B_3)\end{pmatrix} - 8\,\Delta\mathcal{F}_{\mathrm{vac}}(B_0)\Bigg]\begin{pmatrix}B_1\\ B_2\\ B_3\end{pmatrix}, \end{aligned} \tag{7.16}$$

which defines the rainbow equations $\mathcal{R}_i = 0$ that constitute the starting point of our analysis. We have re-introduced the explicit chiral symmetry breaking parameter $H = \pi^2 M_0/g^2$, in terms of the bare mass and the bare coupling. For arbitrary values of the background, (7.16) is B_* dependent, whereas in the limit of vanishing background, it is easily verified that (7.16) becomes B_* independent. With the rainbow equation (7.16) featuring the background r as a dynamical variable, it too needs to be self-consistently determined from its very own *gap* equations. These are derived from the 2PI action specified in chapter 6 and are given in the form

$$\partial_{r_3} V(r,T) \;=\; 0, \tag{7.17}$$

$$\partial_{r_8} V(r,T) \;=\; 0, \tag{7.18}$$

where, as already explained, in case of vanishing chemical potential the latter is trivially solved by $r_8 = 0$ and one remains only with r_3. The potential $V(r,T)$ corresponds to the background field effective potential detailed in Eq. (4.1). Depending on the desired accuracy, two-loop corrections may be included. In a primary attempt, we shall, however, restrict to the one-loop potential. Together with the rainbow equation (7.16), equation (7.17) forms the self-consistent set of equations determining the state of the system. In the following section, we specify how to obtain critical points as well as spinodal lines from this set of equations in terms of two order parameters associated to distinct symmetries, the Polyakov loop and the chiral condensate (or, equivalently, the constituent quark mass). This discussion follows closely a corresponding one in section 6.4.2 and concerns the issue of determining critical points, *etc.*, when the various gap equations for the order parameters do not derive from a common potential.

7.2 Comments on the chiral and deconfinement transition

In the previous section we have obtained a set of gap equations in the form $\mathcal{R}_i = 0$ and $\partial_{r_3} V = 0$, which do not derive from a common potential in the form of first derivatives, since they do not satisfy the necessary Cauchy-Riemann equations. As in the case with $B_\pm$ in chapter 6, this has consequences on the way one defines critical, spinodal points, and so on. For the sake of the argument, we consider a simplified situation with two order parameters, B and ℓ, with their respective gap equations, $R_B = 0$ and $R_\ell = 0$. A generalization to more equations and more parameters (*e.g.* $\bar{\ell}$) is straightforward. Let

[2] The deeper reason for the inability to renormalize all equations simultaneously with the coupling alone is rooted in the fact that the three equations in (7.14) cannot be derived as the first derivatives of some common potential. From first principles, such a potential should of course exist, however due to the approximations implemented here (localization), this realization is lost.

us consider a scenario in which both symmetries, chiral and center, are explicitly broken.[3] This means analyzing a location situated within the Columbia and not on any of its corners.

Employing the gap equation for one of the order parameters, say $\mathcal{R}_B = 0$, determines a function $B(\ell)$ to be inserted into the second equation $\mathcal{R}_\ell(B(\ell),\ell) = 0$, which now merely depends on ℓ. In this way, one conveniently defines a reduced potential $V(\ell)$ such that $V'(\ell) = \mathcal{R}_\ell(B(\ell),\ell)$. In terms of $V(\ell)$, one finds lower spinodal points from the condition (supplemented by $\mathcal{R}_B = \mathcal{R}_\ell = 0$)

$$0 = V''(\ell) \quad \to \quad \partial_\ell \mathcal{R}_\ell \, \partial_B \mathcal{R}_B - \partial_B \mathcal{R}_\ell \, \partial_\ell \mathcal{R}_B = 0 \,. \tag{7.19}$$

Further, a critical point then corresponds to the conditions

$$V'(\ell) = V''(\ell) = V'''(\ell) = 0 \,, \tag{7.20}$$

where the first two equations translate to $\mathcal{R}_B = \mathcal{R}_\ell = 0$ and (7.19). The last condition $V'''(\ell) = 0$ rewrites as (after using (7.19) multiple times)

$$\begin{aligned} 0 \;=\; & \partial_B \mathcal{R}_B \, \partial_B \mathcal{R}_\ell \, \partial_\ell^2 \mathcal{R}_\ell \left[\partial_\ell \mathcal{R}_\ell\right]^{-1} - \partial_B \mathcal{R}_B \, \partial_B \mathcal{R}_\ell \, \partial_\ell^2 \mathcal{R}_B \left[\partial_\ell \mathcal{R}_B\right]^{-1} \\ & -2 \, \partial_B \mathcal{R}_B \, \partial_{B,\ell}^2 \mathcal{R}_\ell + 2 \, \partial_B \mathcal{R}_\ell \, \partial_{B,\ell}^2 \mathcal{R}_B + \partial_\ell \mathcal{R}_B \, \partial_B^2 \mathcal{R}_\ell - \partial_\ell \mathcal{R}_\ell \, \partial_B^2 \mathcal{R}_B \,. \end{aligned} \tag{7.21}$$

Here, we insist on several points. Firstly, one can exchange $\mathcal{R}_B$ and $\mathcal{R}_\ell$ in the above construction, as evident by the symmetric form of the expressions in (7.19) and (7.21). Secondly, in writing (7.21), we assume that the cross-derivatives $\partial_B \mathcal{R}_\ell$ and $\partial_\ell \mathcal{R}_B$ are non-vanishing at the critical point. Otherwise, the situation is a little more subtle. Such instances might occur due to various reasons specific to the particular system under consideration and in such cases it is imperative to choose the correct one of the gap equations to eliminate a suitable order parameter to be placed into the other gap equation. Once again, we insist that these situations arise due to the specific nature of the underlying equations and this issue has to be tackled on a case-by-case basis, and shall not be further discussed here. Finally, we mention that the condition in (7.19) is equivalent to the vanishing of the determinant of the Hessian matrix given as

$$\mathcal{H}(B,\ell) = \begin{pmatrix} \partial_B \mathcal{R}_B & \partial_\ell \mathcal{R}_B \\ \partial_B \mathcal{R}_\ell & \partial_\ell \mathcal{R}_\ell \end{pmatrix} . \tag{7.22}$$

In case the Cauchy-Riemann equations would be satisfied, *i.e.* the gap equations would derive from a common potential, an alternative method to determine critical points is to demand the vanishing of the third directional derivative of the above-mentioned common potential in the direction of the zero eigenvector of the Hessian matrix in (7.22). On easily checks that the latter condition is equivalent to (7.21) if the Cauchy-Riemann condition $\partial_\ell \mathcal{R}_B = \partial_B \mathcal{R}_\ell$ is fulfilled. In the subsequent analysis, in the following section, we shall thus stick to the former alternative, given in (7.21).

7.3 Results

We are now in the position to present our results for the Columbia plot and the phase structure in the case of vanishing chemical potential, for a choice of the scale $B_* = 1$ GeV and a gluon mass of $m = 500$ MeV. First, in section 7.3.1, we verify that the equations in (7.16) reproduce, in the limit of vanishing background, and in the chiral limit, the results of the Euclidean localization scheme of chapter 6 obtained directly in Landau gauge. In section 7.3.2, we locate the heavy quark critical line in the Columbia plot. Finally, in section 7.3.3, we analyse the crossover regime and trace the order parameters as functions of temperature.

7.3.1 Reproducing the Euclidean localization for $r = 0, H = 0$

A necessary consistency check is to verify that the Eqs. (7.16) (numerically) reproduce the critical point at $T = 150$ MeV found in the Euclidean localization scheme in the chiral limit; see Tab. 6.1. We remark that in the limit $r \to 0$, the Hessian matrix attains the form

$$\begin{pmatrix} \partial_{B_j} \mathcal{R}_i & \partial_{r_3} \mathcal{R}_i \\ \partial_{r_3,B_j}^2 V^{(1)} & \partial_{r_3}^2 V^{(1)} \end{pmatrix} \longrightarrow \begin{pmatrix} \partial_{B_j} \mathcal{R}_i & \partial_{r_3} \mathcal{R}_i \\ 0 & \partial_{r_3}^2 V^{(1)} \end{pmatrix} , \tag{7.23}$$

[3] The case of spontaneously broken symmetries is to be treated separately because the conditions for (tri)critical points, *etc.*, are somewhat different due to the underlying symmetries.

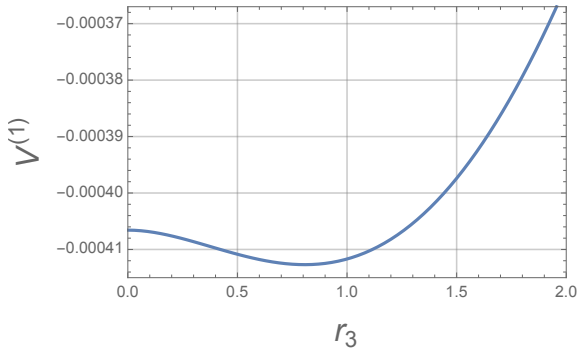

Figure 7.1: The $N_f = 1$ one-loop background effective potential $V^{(1)}$ in the chiral limit and at the *false* critical temperature of 149.5 MeV. Clearly, $r_3 = 0$ corresponds to a local maximum. This serves as an example of the benefits of including a non-trivial gluon background and upgrading the analysis from Landau to LdW gauge.

where $\partial_{B_j}\mathcal{R}_i$ is itself a (3×3) matrix. In the chiral limit for vanishing quark masses, *i.e.* $H, B \to 0$, it is (even at *a priori* non-zero background)

$$\begin{pmatrix} \partial_{B_j}\mathcal{R}_i & \partial_{r_3}\mathcal{R}_i \\ \partial^2_{r_3,B_j}V^{(1)} & \partial^2_{r_3}V^{(1)} \end{pmatrix} \longrightarrow \begin{pmatrix} \partial_{B_j}\mathcal{R}^{\rho^i} & 0 \\ 0 & \partial^2_{r_3}V^{(1)} \end{pmatrix}. \tag{7.24}$$

Demanding that the determinant of the Hessian matrix vanishes, either in the chiral limit and/or at vanishing background, is, thus, equivalent to one of the following conditions:

$$\det \partial_{B_j}\mathcal{R}_i = 0 \tag{7.25}$$

$$\partial^2_{r_3}V^{(1)} = 0\,. \tag{7.26}$$

Setting $r_3 = 0$, Eq. (7.26) is solved for $T \approx \{190, 137, 53\}$ MeV for $N_f = \{1, 2, 3\}$, which corresponds to the temperature below which a non-trivial background has to be accounted for in the chiral limit. Below this temperature, $r_3 = 0$ is a maximum and thus not an equilibrium state of the system. Again at $r = 0$, Eq. (7.25) yields a value $T = 149.5$ MeV,[4] which reproduces the Landau gauge critical point found in Tab. 6.1 for the Euclidean localization scheme. However for $N_f = 1$, the found temperature of 149.5 MeV lies below 190 MeV and thus it is clear that this *false* critical point cannot correspond to physical values. This expectation is confirmed in Fig. 7.1. In turn, we find the correct, physical chiral critical point at a temperature of $T_c = 150$ MeV and $r_3 = 0.793$ upon simultaneously solving (7.25) and $\partial_{r_3}V^{(1)} = 0$.

7.3.2 Locating the heavy quark critical boundary line

In a further step, we tackle the critical boundary line in the top right corner of the Columbia Plot. Our results are summarized in Tab. 7.1, and are aligned with the universality aspects discussed in chapter 5. This is despite the fact that due to the color dependence of the quark masses, the resummed one-loop

critical values	$N_f = 1$	$N_f = 2$	$N_f = 3$
H	505	624	697
r_3	3.305	3.307	3.308
T	177.8	177.8	177.8
B_1	1157.4	1308.3	1395.2
B_2	1274.8	1421.6	1506.0
B_3	1239.4	1388.1	1473.7
$\sum_i B_i/3$	1223.9	1372.7	1458.3

Table 7.1: We show the critical values on the upper boundary line in the top right corner of the Columbia plot. All values (except r_3) are given in MeV.

contribution to the potential in the heavy quark limit writes

$$\beta^4 V^{(1)} = V^{(1)}_{\text{glue}}(\ell, T) - \frac{2}{3}N_f \sum_\rho h(\beta B_\rho)\, e^{ir_\rho}\,, \tag{7.27}$$

which is more intricate than the simpler expression in (5.2). Therefore, *a priori*, the derivation in section 5.1 leading to (5.6) does not apply. Nonetheless, we observe some of the universal properties derived

[4] This value is independent of N_f.

in chapter 5 to be satisfied to reasonable accuracy.[5] For instance, we find an N_f-independent value of the critical temperature. Moreover, we reconstruct the entire critical line from the Bessel relation in Eq. (5.6). This reconstruction is shown in Fig. 7.2, where we have followed the strategy of starting from the $N_f = 3$ values, which typically leads to the closest approximation due to its preferred central position in the Columbia Plot. Also, note that there are three B_i values, each of which can, in principle, serve as

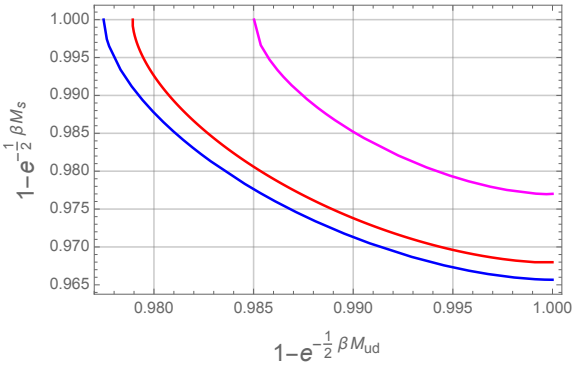

Figure 7.2: Heavy Quark regime of the Columbia Plot. Our reconstructed results (red) from the $N_f = 3$ values in Tab. 7.1 are shown alongside the CF one- (blue) and two-loop (CF2 scheme in purple) analyses in Ref. [168] and chapter 4 respectively. Note that direct comparability of absolute values is infringed by different quark mass renormalizations.

the starting point for the reconstruction. However, they constitute color-dependent objects, and, instead, we focus solely on the color-averaged sum

$$(B_1 + B_2 + B_3)/3\,. \tag{7.28}$$

These values are equally displayed in Tab. 7.1 and are used to obtain the corresponding curve in Fig. 7.2. Finally, the absolute values or the exact location of the the curves in Fig. 7.2 are related to the quark mass renormalization, which is different for the displayed approaches, especially since the renormalization procedure we have implemented in Eq. (7.16) is *ad hoc*. A similar observation was made in section 4.3, where it was argued to be more tentative to compare the respective R_{N_f}-ratios or Y_3 values. In the current setting, choosing $R_{N_f} = \sum_i B_i/(3T_c)$, we find from the values in Tab. 7.1,

$$\begin{aligned} R_3/R_1 &= 1.192\,, \\ R_2/R_1 &= 1.122\,, \\ Y_3 &= 1.575\,, \end{aligned}$$

as compared to $R_3/R_1 = 1.197$, $R_2/R_1 = 1.125$ and $Y_3 = 1.575$ for the CF one-loop and $R_3/R_1 = 1.181$, $R_2/R_1 = 1.115$ and $Y_3 = 1.575$ for the CF two-loop analysis.

7.3.3 Crossover regime

Subsequently, we analyze the phase structure in the $T - H$ plane, which features not only the first order regime and the heavy quark critical point, but also the crossover region. This is shown in Fig. 7.3 for $N_f = 1$, but similar plots can be obtained for $N_f = 2, 3$. We do not indicate the first order transition line itself, since the system of equations in (7.16) and (7.17) does not allow for the construction of a unique associated potential. However, we stress that it must lie between the two spinodal lines, which are in close proximity and merge at the critical point. For H values below critical, we enter the crossover regime. Eventually, for $H = 0$, we also depict the critical point found in the chiral limit. Several remarks are in order. First, we mention that for sufficiently large H values in the crossover regime, the quark masses (as a function of temperature) do in fact exhibit an inflection point. However, due to being far away from the chiral limit, the latter does not associate to a rapid change of the form $B \approx 1$ to $B \approx 0$, with B being schematically normalized by its zero temperature value. This is indicated by the blue stars. Secondly, within the gray band, the quark masses develop two inflection points of comparable size, which means that one can no longer uniquely identify the associated crossover temperature. This situation is illustrated in Fig. 7.4 in the particular case $B_1(T)$.

Additionally, we can also study the behavior of the averaged quark masses, or, alternatively, the condensate σ, and the Polyakov loop as functions of temperature in the crossover region, in dependence of the explicit symmetry breaking parameter H. For convenience, we normalize the averaged quark masses and the condensate by their zero temperature value. Similarly, we normalize the Polyakov loop with respect to its maximum value in the high temperature phase. In Fig. 7.5 we show different scenarii for the background effective potential $V(r, T)$. These are the pure (quark resummed) one-loop potential

[5] In particular, for the values in Tab. 7.1, the relation (5.6) is satisfied with errors contained at 5%.

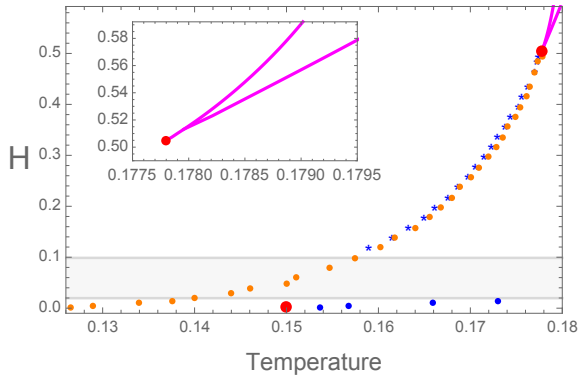

Figure 7.3: Critical points are shown in red, which correspond to the heavy quark boundary line for $N_f = 1$ and the chiral limit. For H values above critical, there are two spinodal lines, shown in purple, of which the inset is a close-up view. For H values below critical, we show the crossover associated to $\sum_i B_i/3$ in blue and to r_3 in orange. Within the gray band, the quark masses exhibit two inflection points, infringing a unique identification of the associated temperature. For the stars, an inflection point is identified, but it does not correspond to a change of phase.

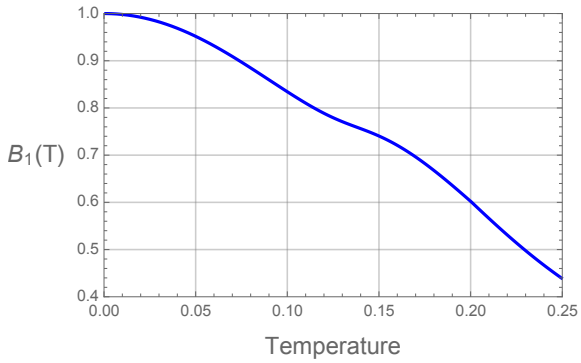

Figure 7.4: We depict the quark mass B_1 as a function of temperature (normalized at zero temperature), for an H value inside the gray band (towards the lower end) displayed in Fig. 7.3. This situation corresponds to the presence of two inflection points of similar significance. The determination of the crossover temperature is therefore ambiguous.

in (4.1), and the addition of the resummed quark sunset terms[6] in (4.7), which contribute at leading order in the RILO expansion scheme via the diagram in Fig. 6.2. We mention that even in the case of the potential $V^{(1)} + V_{\rm q}^{(2)}$, the expression of the Polyakov loop employed in the evaluation of Fig. 7.5 was taken at one-loop level. For all curves, the parameter H has been tuned such that the crossover

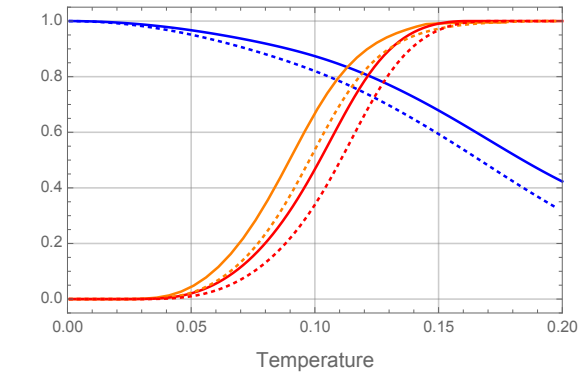

Figure 7.5: We show the averaged quark masses (solid blue) and the Polyakov loop as a function of temperature, for two background effective potentials: $V^{(1)}$ (red) and $V^{(1)} + V_{\rm q}^{(2)}$ (orange). For both potentials, the respective curves for $\sum_i B_i/3$ lie on top of each other. Alternatively, this analysis is performed with the condensate (dashed blue) replacing the quark masses as order parameter (dashed lines). For this plot we have chosen $N_f = 2$.

temperature for the quark masses $\sum_i B_i/3$, or the condensate σ, is at 170 MeV for $N_f = 2$ [295]. In Fig. 7.3, one in principle identifies[7] two corresponding H values. However, the larger leads to B-values around 900 MeV, which is too large to be associated to the physical point, since too close to the YM point. Thus, the larger of the H values is excluded. In the presence of a gluon background, and at the current level of approximation, the condensate is computed as

$$\sigma \;=\; -4N_f \sum_\rho B_\rho \, J^\rho_{B_\rho} \,, \tag{7.29}$$

which entails a UV divergence in the vacuum part of the first fermionic tadpole $J^\rho_{B_\rho} \equiv \int_{\hat{P}}^T G_B(P_{i\mu+Tr_\rho})$

[6] The contribution of the $S(2n)$ terms is neglected as a first approximation. As mentioned in section 6.4.3, this also avoids the pole in the Re ln terms for quark masses attaining half the value of the gluon mass.

[7] Despite the change in N_f, the situation remains qualitatively similar.

and $G_B(P) = 1/(B^2 + P^2)$. Similarly to the discussion in chapter 6, this divergence cannot be controlled in the current setting and we choose to renormalize σ upon subtracting the cutoff dependent terms. We find that all respective curves obtained via the averaged quark masses and the condensate lie in close proximity, and that in all cases the crossover temperatures associated to the Polyakov loop are smaller than the respective values of the chiral order parameters.

7.4 Conclusion

In this chapter we have extended the Euclidean localization scheme presented in chapter 6 to non-trivial gluon background. In so doing, we have developed a model, which establishes a back-coupled link between the condensate and the Polyakov loop and thus allows for the study of the heavy and light quark physics from a common approach. Our results for the whole range of the Columbia plot at vanishing chemical potential are in qualitative agreement with (one of the possibilities of) the expected phase structure. In particular, our findings for the heavy quark boundary line agree well with the universal features described in chapter 5. Moreover, we have traced the Polyakov loop as well as the condensate as a function of temperature in the crossover regime. We find a smaller value of the crossover temperature associated to the Polyakov loops than for the condensate, in both cases under consideration. At the current level of approximation, we conclude that the crossovers associated to the Polyakov loop and the condensate are strongly decoupled effects. In a follow-up study, it would be very insightful to extend the current formalism to non-vanishing values of chemical potential and to treat the resulting, more involved set of coupled gap equations in dependence of more variables. This would allow for an analysis of the possible existence of a CEP in the QCD phase diagram from a first-principle approach accounting simultaneously for the Polyakov loop and the quark condensate in a back-coupled way from the Curci-Ferrari model.

8 Conclusions

Throughout this thesis we have investigated various aspects of infrared QCD, its thermodynamics and phase diagram from the outset of the Curci-Ferrari model. Fundamentally, this particular model is based on the inclusion of a gluon mass term in the Faddeev-Popov Landau gauge-fixed action, and is characterized by allowing for renormalization schemes in which perturbation theory is valid down to arbitrary infrared momentum scales. Prior to the beginning of the thesis, the model had already been developed in its core features and proven to accurately grasp various essential aspects of the physics of QCD correlation functions and YM thermodynamics. Additionally, a first study of the heavy quark phase structure was performed at the one-loop level.

In this context is embedded the research presented in this thesis, which pursues a description of the QCD phase diagram as well as the entire Columbia Plot from the Curci-Ferrari model. As such, the content presented in this thesis is split into two parts, these being the treatment of the heavy quark regime governed by center symmetry, as well as the regime of light quarks characterized by chiral symmetry. Both merit their very own concluding remarks.

With respect to the former, we have computed the two-loop quark-sunset diagram in a massive theory, both in the presence of a non-trivial gluon background field (associated to the Polyakov loop) and at finite temperature and density. We have studied the dynamics at vanishing, imaginary and real chemical potential. Further, we have analyzed the thermodynamic stability of the system at two-loop level. We have also explained why the observed changing monotony of the Polyakov loops as functions of chemical potential is in agreement with their interpretation in terms of free energies. Our results show that the inclusion of the two-loop corrections (drastically) improves the qualitative agreement with lattice benchmarks of the one-loop findings. Quantitatively, a nontrivial challenge in comparing between approaches beyond-one-loop is given by the necessity of quark mass renormalization. In this respect, in terms of less-scheme-dependent quantities—introduced in this thesis—our two-loop results generally indicate a numerical improvement as compared to lattice findings. Moreover, in terms of the thermodynamic aspects, we summarize that most of the unphysical features at one-loop level are rectified by the two-loop corrections, such as positive values of the entropy (s) and energy (e) density at all temperatures, as well as a dramatic decrease in the size of an unphysical branch in the function $s(e)$. Overall, this underlines the robustness of the Curci-Ferrari expansion scheme and, moreover, demonstrates the perturbative nature of the heavy quark corner of the Columbia Plot itself.

In a further study of the heavy quark regime, we have derived some universal features of the critical line in the top right corner of the Columbia Plot. In particular, we discuss models with a confining gluonic sector and which exhibit the dominant fermionic content in the form of a trace log. Performing a large quark mass expansion, we have derived various universal properties, for instance the flavor-independence of the critical temperature or the model-independence of the shape of the critical line, whatever the value of the chemical potential. In this context, we have also developed a set of one-loop Gribov-Zwanziger models, some of which are in qualitative agreement with the structure of the top right corner of the Columbia Plot , and which have successfully been tested against these universal properties. Subsequently, we have verified that some of the universal relations we have derived are accurately satisfied by approaches beyond one-loop order. This, once again, can be interpreted as stemming from the perturbative dynamics underlying the heavy quark regime.

In the light quark regime, we have extended a previous study in the Curci-Ferrari model, which

derives the infamous rainbow equation as the leading order contribution of a simultaneous expansion scheme in small parameters present in the Curci-Ferrari model, notably, the pure-gauge coupling as well as the inverse number of colors. We generalize the rainbow equations to finite density and temperature, as well as to a nontrivial gluon background. Subsequently, based on the Dirac decomposition of the quark propagator at finite temperature, we derive a general set of coupled nonlinear integral equations for its tensor components. In a primary study, we employ various approximation schemes, reducing the equations to be solved to a simpler level. This is motivated by the development of a simple (semi-analytic) setup, which encodes the essential dynamics and has allowed, in a follow-up study, for an easy extension in terms of a gluon background. Our results are in qualitative agreement with findings in the literature and our predictions for the tricritical point in the chiral limit as well as the critical endpoint in the QCD phase diagram range within the ballpark of the existing predictions (although we do not claim predictive power due to the severity of the implemented approximations). Moreover, within the rainbow-improved expansion scheme considered in the Curci-Ferrari model, we have not encountered a first order region in the bottom left corner of the Columbia plot. Instead, we find a second order point in the chiral limit, which is in agreement with one the possible scenarii presented in the introductory chapters. We deduce that the first order region, if it exists, corresponds to a next-to-leading order effect in the rainbow-improved loop expansion.

Lastly, we comment that, in (almost) all situations encountered throughout this thesis, the Curci-Ferrari model has proven a potent description of the infrared dynamics of Landau gauge-fixed QCD, either by perturbative methods or, for the light quark dynamics, by means of controlled resummations.

The work undertaken in this thesis serves as a solid foundation for a large number of interesting follow-up projects. Apart from finishing an unpublished one in terms of a background-extended version of the (approximated) rainbow equations, which allows for a study of the interplay between the Polyakov loops and the chiral condensate, there are several other attractive proposals. As a non-exhaustive list, these include a more involved description of chiral symmetry restoration in the context of a numerical study of the full momentum-dependent equations derived in chapter 6, or to account for contributions that are of next-to-leading order in the RILO expansion scheme. The latter extends the analysis to include effects from mesonic fluctuations or of the chiral anomaly, which are both suppressed at LO. Another interesting line of investigation is the computation of nucleation rates from the Curci-Ferrari model, in particular, for real chemical potential in the saddle point approach. Furthermore, it would be very insightful to compute the quark and gluon spectral functions at finite temperature and chemical potential as a first step towards testing the predictions made by the Curci-Ferrari model for the hadron spectrum in general.

Appendices

A

Generic Matsubara sums

Here, we sketch a proof of the formulae in Eqs. (2.6) and (2.7) for efficiently computing bosonic and fermionic Matsubara sums. To this end, assume a sum of the form

$$T \sum_{n=-N}^{N} F(i\omega_n) \tag{A.1}$$

for some function F, with ω_n either bosonic $\omega_n = 2\pi T n$, or fermionic $\hat{\omega}_n = 2\pi T(n+1/2)$, for some N sufficiently large. Since the Bose-Einstein distribution $n(\zeta) = (e^{\beta\zeta} - 1)^{-1}$ has singularities at $\zeta = i\omega_n$ and similarly the Fermi-Dirac distribution $f(\zeta) = (e^{\beta\zeta} + 1)^{-1}$ for $\zeta = i\hat{\omega}_n$, one can invoke the Residue Theorem and rewrite the sum according to

$$T \sum_{n=-N}^{N} F(i\,\omega_n) \;=\; \frac{-i}{2\pi} \sum_{n=-N}^{N} \oint_{\Gamma_n^{\mathrm{b}}} \mathrm{d}\zeta\, F(\zeta)\, n(\zeta) \tag{A.2}$$

$$T \sum_{n=-N}^{N} F(i\,\hat{\omega}_n) \;=\; \frac{i}{2\pi} \sum_{n=-N}^{N} \oint_{\Gamma_n^{\mathrm{f}}} \mathrm{d}\zeta\, F(\zeta)\, f(\zeta). \tag{A.3}$$

These equations are diagrammatically represented in Fig. A.1. Note that the residues of the distribution

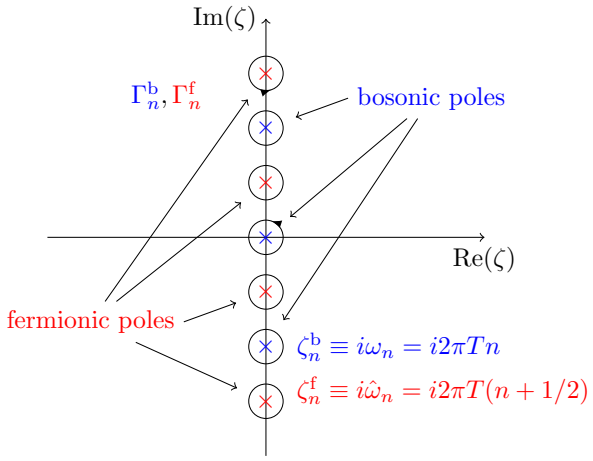

Figure A.1: Diagrammatic representation of Eqs. (A.2) and (A.3). The sum of the anti-clockwise oriented contours encircling the poles is equivalent to the Matsubara sum in Eq. (A.1).

functions at the respective Matsubara frequencies are

$$\mathrm{Res}\,(n(\zeta), i\omega_n) = T \qquad \text{and} \qquad \mathrm{Res}\,(f(\zeta), i\hat{\omega}_n) = -T, \tag{A.4}$$

yielding the opposite signs present in Eq. (A.2) and (A.3).

Furthermore one can now deform the many contours $\Gamma_n^{\mathrm{b,f}}$ and join them together to one big contour

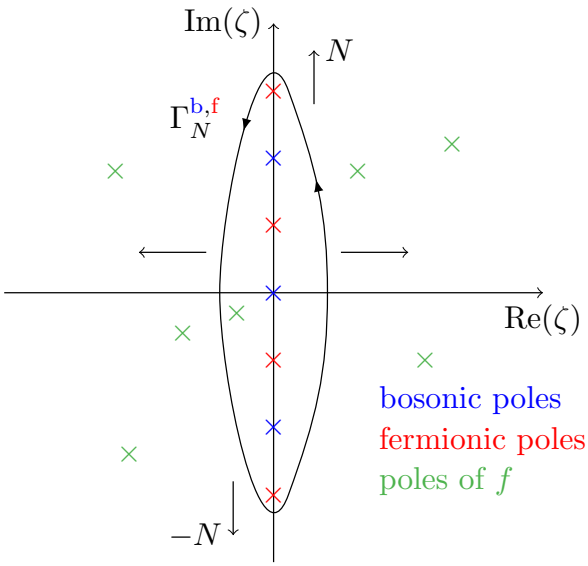

Figure A.2: Same setup as in Fig. A.1 with a deformed contour.

$\Gamma_N^{\mathrm{b,f}}$ as shown in Fig. A.2, upon which

$$T\sum_{n=-N}^{N} F(i\omega_n) = -\frac{i}{2\pi}\oint_{\Gamma_N^{\mathrm{b}}} \mathrm{d}\zeta\, F(\zeta)\, n(\zeta) \tag{A.5}$$

$$T\sum_{n=-N}^{N} F(i\hat{\omega}_n) = \frac{i}{2\pi}\oint_{\Gamma_N^{\mathrm{f}}} \mathrm{d}\zeta\, F(\zeta)\, f(\zeta). \tag{A.6}$$

The contour $\Gamma_N^{\mathrm{b,f}}$ is deformed along the real direction and every time one passes a pole ζ_j of F, a correction term $-\mathrm{Res}\big(F(\zeta)\, n(\zeta), \zeta_j\big)$ has to be added to the RHS of Eq. (A.5) for bosons, and $\mathrm{Res}\big(F(\zeta)\, f(\zeta), \zeta_j\big)$ for fermions in (A.6), such that

$$T\sum_{n=-N}^{N} F(i\omega_n) = -\frac{i}{2\pi}\oint_{\Gamma_N^{\mathrm{b}}} \mathrm{d}\zeta\, F(\zeta)\, n(\zeta) - \sum_{\zeta_j \in \mathrm{Int}\,\Gamma_N^{\mathrm{b}}} \mathrm{Res}\big(F(\zeta)\, n(\zeta), \zeta_j\big) \tag{A.7}$$

and

$$T\sum_{n=-N}^{N} F(i\hat{\omega}_n) = \frac{i}{2\pi}\oint_{\Gamma_N^{\mathrm{f}}} \mathrm{d}\zeta\, F(\zeta)\, f(\zeta) + \sum_{\zeta_j \in \mathrm{Int}\,\Gamma_N^{\mathrm{f}}} \mathrm{Res}\big(F(\zeta)\, f(\zeta), \zeta_j\big). \tag{A.8}$$

Finally, one takes the $N \to \infty$ limit and obtains the given formulae in (2.6) and (2.7), as long as the function F is such that the property

$$\lim_{N\to\infty} \oint_{\Gamma_N^{\mathrm{b,f}}} \mathrm{d}\zeta\, F(\zeta)\, n(\zeta) \to 0, \tag{A.9}$$

or likewise for f, is still satisfied. As previously mentioned in section 2.1, this is the case for almost all physical functions F of interest.

B Computing the Quark Sunset Diagram in the Curci-Ferrari Model

In this appendix we detail the difficulties in the steps to computing the quark-sunset diagram, Fig. 4.1, in the CF model with color-dependent quark masses at finite temperature and chemical potential and in the presence of a non-trivial gluon background.

B.1 Setup

Based on the Feynman rules in section 3.2 the two-loop quark-sunset diagram $V_{\rm q}^{(2)}(r,T,\mu)$ in Fig. 4.1 writes

$$V_q^{(2)}(r,T,\mu) = -\frac{g^2}{2}\sum_f\sum_{\sigma\rho\kappa}\mathcal{D}_{\sigma,\rho\kappa}\int_{\hat{P}}^{T}\int_{Q}^{T} G_m(Q^\kappa)G_{M_f^\rho}(P^\rho)G_{M_f^\sigma}(L^\sigma)\,P^\perp_{\mu\nu}(Q^\kappa) \times \mathrm{tr}\left[\gamma_\mu(i\not{P}^\rho + M_f^\rho)\gamma_\nu(i\not{L}^\sigma + M_f^\sigma)\right], \tag{B.1}$$

where we have employed many previously defined entities which we now briefly recall. We work in dimensional regularization with the convention of $d = 4-2\epsilon$. In section 2.1 we introduced $\int_Q^T f(Q)$ and $\int_{\hat{P}}^T f(P)$ to denote bosonic and fermionic Matsubara sum-integrals respectively. Both the regular momentum conservation $L \equiv P+Q$ as well as the generalized version $L^\sigma = P^\rho + Q^\kappa$ are satisfied. Here, L^σ and P^ρ are of fermionic nature while Q^κ is bosonic. All weights and roots must satisfy $\sigma = \rho+\kappa$ since otherwise $\mathcal{D}_{\sigma,\rho\kappa} \equiv t^\kappa_{\sigma\rho}t^{-\kappa}_{\rho\sigma} = \mathcal{D}_{\rho,\sigma(-\kappa)}$ vanishes. See section 3.2 for more details. The γ_μ are Euclidean matrices and M_f^ρ denotes the quark mass of flavor f associated to the color mode ρ. For simplicity, in the following, we shall drop the subscript f and remember that all masses are explicitly flavor dependent. Finally, $P^\perp_{\mu\nu}$ is the transverse projector and $G_a(b) \equiv 1/(a^2+b^2)$.

As a quick primary outline, the computation of Eq. (B.1) proceeds in two main steps. First, in section B.2, one massages the trace structure until the entire expression is reduced to a combination of scalar-type integrals. In a second step, in section B.3, one performs the Matsubara sums and thus effectively splits the contributions into separate groups based on the number of distribution functions the terms entail.

B.2 Reduction to scalar-type integrals

There are many ways to perform the computation of (B.1), however the line that we will follow is to tackle the trace structure first. To this end, we note

$$\begin{aligned}\gamma_\mu(i\not{P}+M)\gamma_\mu &= (2-d)i\not{P} + d\,M\,,\\ \not{Q}(i\not{P}+M)\not{Q} &= Q^2(-i\not{P}+M) + 2i(P\cdot Q)\not{Q}\,,\end{aligned}$$

which are used in the two terms stemming from the transverse projector under the trace. After taking the trace and gathering similar terms together, one arrives at the intermediate expression

$$V_q^{(2)}(r,T,\mu) = \frac{g^2}{2}\mathrm{tr}\mathbb{1}\sum_f\sum_{\sigma\rho\kappa}\mathcal{D}_{\sigma,\rho\kappa}\Bigg\{-(d-1)\int_{\hat{P}}^T\int_Q^T\Big[P^\rho\cdot L^\sigma + M^\sigma M^\rho\Big]G_m(Q^\kappa)G_{M^\rho}(P^\rho)G_{M^\sigma}(L^\sigma)$$
$$+2\int_{\hat{P}}^T\int_Q^T\Big[Q_\kappa^2\,P^\rho\cdot L^\sigma - (P^\rho\cdot Q^\kappa)(Q^\kappa\cdot L^\sigma)\Big]G_0(Q^\kappa)G_m(Q^\kappa)G_{M^\rho}(P^\rho)G_{M^\sigma}(L^\sigma)\Bigg\}. \quad \text{(B.2)}$$

Further, we need to work a little more on the terms in the square brackets of each line. To treat the first, we can reformulate

$$P^\rho\cdot L^\sigma + M^\rho M^\sigma = \frac{1}{2}\Big[P_\rho^2 + L_\sigma^2 - Q_\kappa^2\Big] + M^\rho M^\sigma = \frac{1}{2}\Big[L_\sigma^2 + M_\sigma^2 + P_\rho^2 + M_\rho^2 - Q_\kappa^2 - m^2\Big] + \frac{m^2}{2} - \frac{(M_\rho - M_\sigma)^2}{2}$$
$$= \frac{1}{2}\Bigg[G_{M^\sigma}^{-1}(L^\sigma) + G_{M^\rho}^{-1}(P^\rho) - G_m^{-1}(Q^\kappa) + m^2 - (M_\rho - M_\sigma)^2\Bigg]. \quad \text{(B.3)}$$

For the second bracket we employ a little trick involving again the transverse projector $P^\perp_{\mu\nu}(Q^\kappa) \equiv \delta_{\mu\nu} - Q^\kappa_\mu Q^\kappa_\nu/Q^2_\kappa$ to find

$$Q_\kappa^2(P^\rho\cdot L^\sigma) - (P^\rho\cdot Q^\kappa)(Q^\kappa\cdot L^\sigma) = Q_\kappa^2\,P^\rho\cdot P^\perp(Q^\kappa)\cdot L^\sigma = Q_\kappa^2\,P^\rho\cdot P^\perp(Q^\kappa)\cdot P^\rho = P_\rho^2 Q_\kappa^2 - (P_\rho\cdot Q_\kappa)^2\,, \quad \text{(B.4)}$$

as well as the realization that $G_0(Q^\kappa)G_m(Q^\kappa) = [G_0(Q^\kappa) - G_m(Q^\kappa)]/m^2$. Making use of all of the above, Eq. (B.2) attains the preliminary form

$$V_q^{(2)}(r,T,\mu) = -\frac{g^2}{4}\mathrm{tr}\mathbb{1}\sum_f\sum_{\sigma\rho\kappa}\mathcal{D}_{\sigma,\rho\kappa}\Bigg\{(d-1)\Big[\big(J^\rho_{M^\rho} + J^\sigma_{M^\sigma}\big)J^\kappa_m - J^\rho_{M^\rho}J^\sigma_{M^\sigma} + (m^2 - (M^\rho - M^\sigma)^2)S^{\kappa\rho\sigma}_{mM^\rho M^\sigma}\Big]$$
$$+\frac{4}{m^2}\Big[I^{\kappa\rho\sigma}_{mM^\rho M^\sigma} - I^{\kappa\rho\sigma}_{0M^\rho M^\sigma}\Big]\Bigg\}. \quad \text{(B.5)}$$

Here, we have defined various scalar-type integrals. In particular, these are the bosonic scalar tadpoles

$$J^\kappa_m \equiv \int_Q^T G_m(Q^\kappa) \quad \text{and} \quad \tilde{J}^\kappa_m \equiv \int_Q^T Q_0^\kappa G_m(Q^\kappa)\,, \quad \text{(B.6)}$$

the fermionic scalar tadpoles[1]

$$J^\rho_M \equiv \int_{\hat{P}}^T G_M(P^\rho) \quad \text{and} \quad \tilde{J}^\rho_M \equiv \int_{\hat{P}}^T P_0^\rho G_M(P^\rho)\,, \quad \text{(B.7)}$$

as well as the fermion–boson scalar sunset

$$S^{\kappa\rho\sigma}_{mM^\rho M^\sigma} \equiv \int_{\hat{P}}^T\int_Q^T G_m(Q^\kappa)G_{M^\rho}(P^\rho)G_{M^\sigma}(L^\sigma)\,. \quad \text{(B.8)}$$

Furthermore we have introduced

$$I^{\kappa\rho\sigma}_{mM^\rho M^\sigma} \equiv \int_{\hat{P}}^T\int_Q^T\Big[P_\rho^2Q_\kappa^2 - (P^\rho\cdot Q^\kappa)^2\Big]G_m(Q^\kappa)\,G_{M^\rho}(P^\rho)\,G_{M^\sigma}(L^\sigma)\,, \quad \text{(B.9)}$$

and the final task in the reduction to purely scalar integrals is to express this quantity $I^{\kappa\rho\sigma}_{mM^\rho M^\sigma}$ entirely in terms of the above-defined tadpoles or scalar sunset. We rewrite the respective terms

$$P_\rho^2Q_\kappa^2G_m(Q^\kappa)\,G_{M^\rho}(P^\rho)\,G_{M^\sigma}(L^\sigma) = G_{M^\sigma}(L^\sigma) - \Big[m^2G_m(Q^\kappa) + M_\rho^2G_{M^\rho}(P^\rho)\Big]G_{M^\sigma}(L^\sigma)$$
$$+ \quad m^2M_\rho^2\,G_m(Q^\kappa)G_{M^\rho}(P^\rho)G_{M^\sigma}(L^\sigma)\,, \quad \text{(B.10)}$$

[1] To keep the notational complication minimal we denote both bosonic and fermionic tadpole integrals by J. They can nonetheless be distinguished either from their respective color modes, *i.e.* fermionic weights or bosonic roots, or from their associated mass in the subscript. This is either the gluon mass for bosonic tadpoles or a quark mass for fermionic ones.

and similarly,

$$\begin{aligned}
&(P^\rho\cdot Q^\kappa)^2 G_m(Q^\kappa)\,G_{M^\rho}(P^\rho)\,G_{M^\sigma}(L^\sigma)\\
&\quad=\frac{m^2+M_\rho^2-M_\sigma^2}{2}(P^\rho\cdot Q^\kappa)G_m(Q^\kappa)G_{M^\rho}(P^\rho)G_{M^\sigma}(L^\sigma)\\
&\qquad+\frac{(P^\rho\cdot Q^\kappa)}{2}\big[G_m(Q^\kappa)G_{M^\rho}(P^\rho)-G_m(Q^\kappa)G_{M^\sigma}(L^\sigma)-G_{M^\rho}(P^\rho)G_{M^\sigma}(L^\sigma)\big]\\
&\quad=\frac{(m^2+M_\rho^2-M_\sigma^2)^2}{4}G_m(Q^\kappa)G_{M^\rho}(P^\rho)G_{M^\sigma}(L^\sigma)\\
&\qquad+\frac{m^2+M_\rho^2-M_\sigma^2}{4}\big[G_m(Q^\kappa)G_{M^\rho}(P^\rho)-G_m(Q^\kappa)G_{M^\sigma}(L^\sigma)-G_{M^\rho}(P^\rho)G_{M^\sigma}(L^\sigma)\big]\\
&\qquad+\frac{(P^\rho\cdot Q^\kappa)}{2}\big[G_m(Q^\kappa)G_{M^\rho}(P^\rho)-G_m(Q^\kappa)G_{M^\sigma}(L^\sigma)-G_{M^\rho}(P^\rho)G_{M^\sigma}(L^\sigma)\big]\,.
\end{aligned}\tag{B.11}$$

Upon substitution, this yields

$$\begin{aligned}
I^{\kappa\rho\sigma}_{mM^\rho M^\sigma}=&-\frac{1}{2}\big[\tilde J^\kappa_m(\tilde J^\rho_{M^\rho}-\tilde J^\sigma_{M^\sigma})-\tilde J^\rho_{M^\rho}\tilde J^\sigma_{M^\sigma}\big]+\frac{M_\sigma^2-m^2-M_\rho^2}{4}J^\kappa_m J^\rho_{M^\rho}+\frac{M_\rho^2-m^2-M_\sigma^2}{4}J^\kappa_m J^\sigma_{M^\sigma}\\
&+\frac{m^2-M_\rho^2-M_\sigma^2}{4}J^\rho_{M^\rho}J^\sigma_{M^\sigma}-\frac{1}{4}\big(m^4+M_\rho^4+M_\sigma^4-2m^2M_\rho^2-2m^2M_\sigma^2-2M_\rho^2M_\sigma^2\big)S^{\kappa\rho\sigma}_{mM^\rho M^\sigma}\,,
\end{aligned}$$

where we have once more relied on the definitions in Eqs. (B.6) to (B.8). Eventually, the fully reduced version of Eq. (B.1) in terms of purely scalar-type integrals takes the intermediate form

$$\begin{aligned}
V_q^{(2)}(r,T,\mu)=&-\frac{g^2}{4}\mathrm{tr}\mathbb{1}\sum_f\sum_{\sigma\rho\kappa}\mathcal{D}_{\sigma,\rho\kappa}\Bigg\{-(d-2)J^\rho_{M^\rho}J^\sigma_{M^\sigma}+J^\kappa_m J^\rho_{M^\rho}\big[d-2+\frac{M_\sigma^2-M_\rho^2}{m^2}\big]+J^\kappa_0 J^\rho_{M^\rho}\frac{M_\rho^2-M_\sigma^2}{m^2}\\
&+J^\kappa_m J^\sigma_{M^\sigma}\big[d-2+\frac{M_\rho^2-M_\sigma^2}{m^2}\big]+J^\kappa_0 J^\sigma_{M^\sigma}\frac{M_\sigma^2-M_\rho^2}{m^2}+\frac{2}{m^2}\big[\big(\tilde J^\kappa_0-\tilde J^\kappa_m\big)\big(\tilde J^\rho_{M^\rho}-\tilde J^\sigma_{M^\sigma}\big)\big]\\
&+\Big[(d-1)\big(m^2-(M^\rho-M^\sigma)^2\big)-\frac{1}{m^2}\big(m^4+M_\rho^4+M_\sigma^4-2m^2M_\rho^2-2m^2M_\sigma^2-2M_\rho^2M_\sigma^2\big)\Big]S^{\kappa\rho\sigma}_{mM^\rho M^\sigma}\\
&+\frac{1}{m^2}\big(M_\rho^4+M_\sigma^4-2M_\rho^2M_\sigma^2\big)S^{\kappa\rho\sigma}_{0M^\rho M^\sigma}\Bigg\},
\end{aligned}\tag{B.12}$$

which concludes the first part of the entire computation.

B.3 Splitting in terms of thermal factors

The strategy to further manage expression (B.12) is to split each of the scalar integrals defined in (B.6)-(B.8) into separate contributions according to the amount of thermal factors it depends on. In order to extract the different thermal and vacuum pieces, one needs to perform the Matsubara sums in each of the terms.
Then, the scalar integrals take the form

$$J^\kappa_m=J_m(0n)+J^\kappa_m(1n),\qquad J^\rho_{M^\rho}=J_{M^\rho}(0n)+J^\rho_M(1n)\tag{B.13}$$

and similarly for the second tadpole types, as well as

$$S^{\kappa\rho\sigma}_{mM^\rho M^\sigma}=S_{mM^\rho M^\sigma}(0n)+S^{\kappa\rho\sigma}_{mM^\rho M^\sigma}(1n)+S^{\kappa\rho\sigma}_{mM^\rho M^\sigma}(2n)\,.\tag{B.14}$$

In the above, the brackets denote the number of Bose-Einstein or Fermi-Dirac distribution functions the various pieces exhibit. Hence, terms labelled by $(0n)$ are the vacuum contributions that inherit all UV divergences. On the other hand, all thermal terms, either $(1n)$ or $(2n)$, are naturally finite. We also point out that all vacuum pieces are entirely medium-independent, and in the absence of an explicit background-dependence we can drop the color-mode superscripts. The only possible source of color-dependence in the vacuum terms enters indirectly via the quark masses.

With the above thermal factor decompositions, one substitutes into the formula in Eq. (B.12). However, a real simplification only occurs in the scenario of having restricted to color-independent fermion

masses.[2] In this limit, the final version of the quark-sunset contribution to the effective potential takes the form

$$\begin{aligned} V_q^{(2)}(r,T,\mu) &= -\frac{1}{4}g^2 N_c C_F \mathrm{tr}\mathbb{1}\sum_f \Big[(d-2)J_{M_f}(0n)\Big(2J_m(0n)-J_{M_f}(0n)\Big) \\ &\qquad +\Big((d-2)m^2+4M_f^2\Big)S_{mM_fM_f}(0n)\Big] \\ &- g^2\mathrm{tr}\mathbb{1}\sum_f\Bigg\{\frac{1}{4}\Big[(d-2)J_{M_f}(0n)+\frac{1}{2}\Big[(d-2)m^2+4M_f^2\Big]I_{M_fM_f}(0n)\Big]\sum_\kappa J_m^\kappa(1n) \\ &\qquad +\frac{C_F}{2}\Big[(d-2)\Big[J_m(0n)-J_{M_f}(0n)\Big]+\Big[(d-2)m^2+4M_f^2\Big]I_{M_fm}(0n)\Big]\sum_\rho J_{M_f}^\rho(1n)\Bigg\} \\ &- \frac{g^2}{2}\mathrm{tr}\mathbb{1}\sum_f\sum_{\sigma\rho\kappa}\mathcal{D}_{\sigma,\rho\kappa}\Bigg\{\Big[J_{M_f}^\rho(1n)+J_{M_f}^\sigma(1n)\Big]J_m^\kappa(1n)-J_{M_f}^\rho(1n)J_{M_f}^\sigma(1n) \\ &\qquad +\frac{1}{m^2}\Big[\tilde{J}_0^\kappa(1n)-\tilde{J}_m^\kappa(1n)\Big]\Big[\tilde{J}_{M_f}^\rho(1n)-\tilde{J}_{M_f}^\sigma(1n)\Big]+(m^2+2M_f^2)S_{mM_fM_f}^{\kappa\rho\sigma}(2n)\Bigg\}. \end{aligned} \tag{B.15}$$

In the following, we gradually detail the explicit computation of all vacuum and thermal pieces.

B.3.1 Bosonic Tadpoles J_m^κ and $\tilde{J}_m^\kappa$

We briefly recall the results for the bosonic tadpoles taken from Ref. [167]. As usual we employ the notation $n_x \equiv (e^{\beta x}-1)^{-1}$ and $\varepsilon_{m,q} \equiv \sqrt{q^2+m^2}$. We denote $\int_q \equiv \mu_r^{2\epsilon}\int \frac{d^{d-1}q}{(2\pi)^{d-1}}$ with the renormalization scale μ_r, and very importantly, we define the rescaled, temperature-dependent background $\hat{r} \equiv Tr$. In terms of these notations, and based on Eq. (2.6), it can be worked out that

$$J_m(0n) = \int_q \frac{1}{2\varepsilon_{m,q}} = -\frac{m^2}{16\pi^2}\left[\frac{1}{\epsilon}+\ln\frac{\bar{\mu}^2}{\mathrm{m}^2}+1+\mathcal{O}(\epsilon)\right], \tag{B.16}$$

$$J_m^\kappa(1n) = \int_q \frac{n_{\varepsilon_{m,q}-i\hat{r}_\kappa}+n_{\varepsilon_{m,q}+i\hat{r}_\kappa}}{2\varepsilon_{m,q}}, \tag{B.17}$$

$$\tilde{J}_m^\kappa(0n) = 0, \tag{B.18}$$

$$\tilde{J}_m^\kappa(1n) = \int_q \frac{n_{\varepsilon_{m,q}-i\hat{r}_\kappa}-n_{\varepsilon_{m,q}+i\hat{r}_\kappa}}{2i}. \tag{B.19}$$

Consequently the massless tadpoles naturally follow, in particular $J_0(0n)=0$. In the first line, $\bar{\mu}^2 \equiv 4\pi e^{-\gamma}\mu_r^2$, where γ is the Euler constant.

B.3.2 Fermionic Tadpoles J_M^ρ and $\tilde{J}_M^\rho$

In analogy to the bosonic tadpoles in the previous subsection, one can similarly treat the fermionic ones. Here, $f_x \equiv (e^{\beta x}+1)^{-1}$ is the Fermi-Dirac distribution, but we otherwise stick to the same conventions as above. After performing the standard Matsubara sums as explained in Eq. (2.7), we find

$$J_M(0n) = \int_p \frac{1}{2\varepsilon_{M,p}} = -\frac{M^2}{16\pi^2}\left[\frac{1}{\epsilon}+\ln\frac{\bar{\mu}^2}{\mathrm{M}^2}+1+\mathcal{O}(\epsilon)\right], \tag{B.20}$$

$$J_M^\rho(1n) = -\int_p \frac{f_{\varepsilon_{M,p}-i\hat{r}_\rho+\mu}+f_{\varepsilon_{M,p}+i\hat{r}_\rho-\mu}}{2\varepsilon_{M,p}}. \tag{B.21}$$

The situation of the second fermionic tadpole is a little more involved, since its Matsubara sum is *a priori* not absolutely convergent. The same issue already occurred in the case of the second bosonic tadpole and Ref. [167] proposed a workaround that lead to the expression in (B.19). Here, we follow the

[2] In case of insisting on color-dependent quark masses, an analogous expression to Eq. (B.15) split in terms of the thermal and vacuum contributions can be achieved, but it follows the exact structure of the formula in Eq. (B.12) and is thus not insightful to be shown.

same logic and subtract a term which yields zero under the symmetric sum $\sum_{-N}^{N}$ due to the $P_0 \to -P_0$ symmetry:

$$\sum_{-N}^{N} P_0^\rho G_M(P^\rho) = \sum_{-N}^{N} \left[P_0^\rho G_M(P^\rho) - P_0 G_M(P)|_{\mu=0} \right]. \tag{B.22}$$

The second tadpole is then obtained in the $N \to \infty$ limit. Eventually,

$$\tilde{J}_M(0n) = 0\,, \tag{B.23}$$

$$\tilde{J}_M^\rho(1n) = -\int_p \frac{f_{\varepsilon_{M,p}-i\hat{r}_\rho+\mu} - f_{\varepsilon_{M,p}+i\hat{r}_\rho-\mu}}{2i}\,. \tag{B.24}$$

B.3.3 Scalar Sunset $S^{\kappa\rho\sigma}_{mM^\rho M^\sigma}$

The reader is pointed towards Ref. [296] for a calculation similar to the one performed in this section. To begin, the scalar sunset

$$S^{\kappa\rho\sigma}_{mM^\rho M^\sigma} = \int_{\hat{P}} \int_Q G_m(Q^\kappa) G_{M^\rho}(P^\rho) G_{M^\sigma}(L^\sigma) \tag{B.25}$$

is reformulated in terms of the spectral representations

$$G_m(Q^\kappa) = \int \frac{dq_0}{2\pi} \frac{\rho_m(q_0,q)}{q_0 - i\omega_n^\kappa}\,, \tag{B.26}$$

$$G_M(P^\rho) = \int \frac{dp_0}{2\pi} \frac{\rho_M(p_0,p)}{p_0 - i\hat{\omega}_n^\rho} = \int \frac{dp_0}{2\pi} \frac{\rho_M(p_0,p)}{p_0 + i\hat{\omega}_n^\rho}\,, \tag{B.27}$$

where $\rho_\alpha(q_0,q) = 2\pi\,\varepsilon(q_0)\,\delta(q_0^2 - \varepsilon_{\alpha,q}^2)$ and where we have invoked the shifted bosonic and fermionic Matsubara frequencies

$$\omega_n^\kappa = \omega_n + \hat{r}_\kappa\,, \tag{B.28}$$

$$\hat{\omega}_n^\rho = \hat{\omega}_n + \hat{r}_\rho + i\mu\,. \tag{B.29}$$

Now, with

$$S^{\kappa\rho\sigma}_{mM^\rho M^\sigma} = T^2 \int_p \int_q \sum_n \sum_m \int_{q_0} \frac{\rho_m(q_0,q)}{q_0 - i\omega_n^\kappa} \int_{p_0} \frac{\rho_{M^\rho}(p_0,p)}{p_0 - i\hat{\omega}_m^\rho} \int_{l_0} \frac{\rho_{M^\sigma}(l_0,l)}{l_0 + i\hat{\omega}_{n+m}^\sigma}\,, \tag{B.30}$$

we are in the position to compute the full (σ) and partial (σ_m) Matsubara sums[3] defined by

$$\sigma \equiv T\sum_m \sigma_m = T^2 \sum_{n,m} \frac{1}{(q_0 - i\omega_n^\kappa)(p_0 - i\hat{\omega}_m^\rho)(l_0 + i\hat{\omega}_{n+m}^\sigma)}\,. \tag{B.31}$$

Making use of $n_{\varepsilon+i\hat{\omega}_m} = -f_\varepsilon$, we find

$$\sigma_m = \frac{1}{p_0 - i\hat{\omega}_m^\rho} \frac{1}{q_0 + l_0 + i\hat{\omega}_m^\rho} \left[n_{q_0 - i\hat{r}_\kappa} + f_{-l_0 - i\hat{r}_\sigma + \mu} \right],$$

and furtherly

$$\sigma = \frac{1}{q_0 + p_0 + l_0} \left[-f_{p_0 - i\hat{r}_\rho + \mu} + f_{-l_0 - q_0 - i\hat{r}_\rho + \mu} \right] \left[n_{q_0 - i\hat{r}_\kappa} + f_{-l_0 - i\hat{r}_\sigma + \mu} \right]. \tag{B.32}$$

We point out that in the limit $q_0 + p_0 + l_0 \to 0$ both the numerator and the denominator of Eq. (B.32) tend to zero to keep σ well-defined. In the subsequent steps it is convenient for the thermal factors to only

[3] Note that the σ defined here is not to be confused with the weight σ. Given their respective occurrences in different positions within the equations, this distinction is easily realized.

depend on one of the variables amongst $\{l_0, p_0, q_0\}$, which is achieved upon using $f_{x+y}\big(1+n_x-f_y\big)=n_x f_y$ to rewrite

$$\sigma = -\frac{1}{q_0+p_0+l_0}\Big[n_{-q_0+i\hat{r}_\kappa} f_{-l_0-i\hat{r}_\sigma+\mu} + f_{p_0-i\hat{r}_\rho+\mu}\big(n_{q_0-i\hat{r}_\kappa} + f_{-l_0-i\hat{r}_\sigma+\mu}\big)\Big]. \tag{B.33}$$

A useful trick to identify the divergent contributions comes from the re-expressions, for q_0 and $p_0 \neq 0$,

$$n_{q_0-i\hat{r}_\kappa} = -\theta(-q_0) + \varepsilon(q_0)\, n_{|q_0|-\varepsilon(q_0)i\hat{r}_\kappa}\,, \tag{B.34}$$

$$f_{p_0-i\hat{r}_\rho+\mu} = \theta(-p_0) + \varepsilon(p_0)\, f_{|p_0|+\varepsilon(p_0)(\mu-i\hat{r}_\rho)}\,, \tag{B.35}$$

where $\theta(x)$ and $\varepsilon(x)$ denote the Heaviside and sign functions respectively.[4]
With the thermal factors split as in (B.34) and (B.35), one encounters the problem that the formerly well-defined σ in Eq. (B.33) picks up divergences at $p_0+l_0+q_0=0$ due to the non-vanishing of some of the newly created numerators. To counteract, we regularize the denominator in the same fashion as in Ref. [166] by

$$\frac{1}{p_0+l_0+q_0} \to \mathrm{Re}\,\frac{1}{p_0+l_0+q_0+i0^+}\,. \tag{B.36}$$

This measure finally leads to the well advertised separation of contributions with varying number of thermal factors, Eq. (B.14). The remainder of the calculation of each contribution is detailed separately in the subsections below.

Finding $S_{mM^\rho M^\sigma}(0n)$

The vacuum piece with no thermal factors explicitly depends neither on the background nor on the temperature or the chemical potential. On the other hand, $S_{mM^\rho M^\sigma}(0n)$ does depend on the mass values involved and thus a medium-dependence is introduced indirectly via the color-dependence of the quark masses.

Alltogether, it reads

$$\begin{aligned} S_{mM^\rho M^\sigma}(0n) = &-\int_p\int_q\int_{q_0}\int_{l_0}\int_{p_0}\rho_m(q_0,q)\rho_{M^\sigma}(l_0,l)\rho_{M^\rho}(p_0,p)\mathrm{Re}\,\frac{1}{q_0+p_0+l_0+i0^+} \\ &\times\Big[-\theta(l_0)\theta(q_0)-\theta(-q_0)\theta(-p_0)+\theta(-p_0)\theta(l_0)\Big]. \end{aligned} \tag{B.37}$$

Integrating over frequencies

$$\begin{aligned} S_{mM^\rho M^\sigma}(0n) = &\sum_{\lambda=\pm}\int_p\int_q \frac{\lambda}{8\varepsilon_{m,q}\varepsilon_{p,M^\rho}\varepsilon_{p+q,M^\sigma}}\mathrm{Re}\Big\{\frac{1}{\varepsilon_{m,q}+\lambda\varepsilon_{p,M^\rho}+\varepsilon_{p+q,M^\sigma}+i0^+} \\ &+\frac{1}{-\varepsilon_{m,q}-\varepsilon_{p,M^\rho}+\lambda\varepsilon_{p+q,M^\sigma}+i0^+}+\frac{1}{-\lambda\varepsilon_{m,q}-\varepsilon_{p,M^\rho}+\varepsilon_{p+q,M^\sigma}+i0^+}\Big\}, \end{aligned} \tag{B.38}$$

where both the p and q integral are individually log-divergent and thus $S_{mM^\rho M^\sigma}(0n)$ features terms of $1/\epsilon^2$ and $1/\epsilon$ in dimensional regularization that need to be renormalized.

In particular, the vacuum sunset can be written in the form [297, 298, 299]:

$$\begin{aligned} S_{mM^\rho M^\sigma}(0n) = &\frac{1}{256\pi^4}\Bigg\{2\Big[m^2\ln\frac{m^2}{\bar{\mu}^2}+M_\rho^2\ln\frac{M_\rho^2}{\bar{\mu}^2}+M_\sigma^2\ln\frac{M_\sigma^2}{\bar{\mu}^2}\Big]-\frac{5}{2}\big(m^2+M_\rho^2+M_\sigma^2\big) \\ &+\frac{1}{2}\Big[\big(m^2-M_\rho^2-M_\sigma^2\big)\ln\frac{M_\rho^2}{\bar{\mu}^2}\ln\frac{M_\sigma^2}{\bar{\mu}^2}+\big(M_\rho^2-M_\sigma^2-m^2\big)\ln\frac{m^2}{\bar{\mu}^2}\ln\frac{M_\sigma^2}{\bar{\mu}^2}+\big(M_\sigma^2-m^2-M_\rho^2\big)\ln\frac{M_\rho^2}{\bar{\mu}^2}\ln\frac{m^2}{\bar{\mu}^2}\Big] \\ &+\mathcal{R}_{mM^\rho M^\sigma}\Big[\mathrm{Li}_2(\mathrm{R_{mM^\rho M^\sigma}})+\mathrm{Li}_2(\mathrm{R_{mM^\sigma M^\rho}})-\ln(\mathrm{R_{mM^\rho M^\sigma}})\ln(\mathrm{R_{mM^\sigma M^\rho}})+\frac{1}{2}\ln\big(\frac{\mathrm{M_\rho^2}}{\mathrm{M_\sigma^2}}\big)\ln\big(\frac{\mathrm{M_\sigma^2}}{\mathrm{m^2}}\big)-\frac{\pi^2}{6}\Big] \\ &+\frac{1}{\epsilon}\Big[m^2\big(\ln\frac{m^2}{\bar{\mu}^2}-\frac{1}{2}\big)+M_\rho^2\big(\ln\frac{M_\rho^2}{\bar{\mu}^2}-\frac{1}{2}\big)+M_\sigma^2\big(\ln\frac{M_\sigma^2}{\bar{\mu}^2}-\frac{3}{2}\big)\Big]-\frac{1}{2\epsilon^2}\Big[m^2+M_\rho^2+M_\sigma^2\Big]\Bigg\}, \end{aligned} \tag{B.39}$$

[4] Note that both $f_{|p_0|+\varepsilon(p_0)(\mu-i\hat{r}\cdot\rho)}$ in general, and $n(|q_0|-\varepsilon(q_0)i\hat{r}\cdot\kappa)$ for r_8 imaginary at real μ, still contain zero-temperature contributions. However, these lead to ultraviolet-finite integrals.

where we have introduced

$$\mathcal{R}_{mM^\rho M^\sigma} \equiv \sqrt{m^4 + M_\rho^4 + M_\sigma^4 - 2m^2M_\rho^2 - 2M_\rho^2M_\sigma^2 - 2m^2M_\sigma^2} \tag{B.40}$$

and

$$R_{mM^\rho M^\sigma} \equiv \frac{m^2 + M_\rho^2 - M_\sigma^2 - \mathcal{R}_{mM^\rho M^\sigma}}{2m^2}\,. \tag{B.41}$$

Similar expressions hold for the respective mass permutations of $R_{mM^\rho M^\sigma}$. The above expression in (B.39) is valid for $m > M^\rho, M^\sigma$ and any other constitution is obtained upon appropriately permuting the mass arguments. Here, Li_2 is the standard notation for the dilogarithm.
In case of a massless gluon the above formulae simplify significantly:

$$\begin{aligned} S_{0M^\rho M^\sigma}(0n) \;=\; \frac{1}{256\pi^4}\Bigg\{ & 2M_\sigma^2 \ln\frac{M_\sigma^2}{\bar\mu^2} + M_\rho^2 \ln\frac{M_\rho^2}{\bar\mu^2}\Big(2 - \ln\frac{M_\sigma^2}{\bar\mu^2}\Big) - \frac{5}{2}\big(M_\rho^2 + M_\sigma^2\big) \\ & + \big(M_\rho^2 - M_\sigma^2\big)\Big[\mathrm{Li}_2\big(\frac{\mathrm{M}_\sigma^2}{\mathrm{M}_\rho^2}\big) - \ln\big(\frac{\mathrm{M}_\rho^2 - \mathrm{M}_\sigma^2}{\bar\mu^2}\big)\ln\big(\frac{\mathrm{M}_\rho^2}{\mathrm{M}_\sigma^2}\big) + \frac{1}{2}\ln^2\big(\frac{\mathrm{M}_\rho^2}{\bar\mu^2}\big) - \frac{\pi^2}{6}\Big] \\ & + \frac{1}{\epsilon}\Big[M_\rho^2\big(\ln\frac{M_\rho^2}{\bar\mu^2} - \frac{1}{2}\big) + M_\sigma^2\big(\ln\frac{M_\sigma^2}{\bar\mu^2} - \frac{3}{2}\big)\Big] - \frac{1}{2\epsilon^2}\left(M_\rho^2 + M_\sigma^2\right)\Bigg\}. \end{aligned} \tag{B.42}$$

Finding $S^{\kappa\rho\sigma}_{mM^\rho M^\sigma}(1n)$

Based on Eqs. (B.34) and (B.35), the terms with one thermal factors are identified as

$$\begin{aligned} S^{\kappa\rho\sigma}_{mM^\rho M^\sigma}(1n) = J^\rho_{M^\rho}(1n)\,\mathrm{Re}\,I_{M^\sigma m}(\varepsilon_{p,M^\sigma} + i0^+, p) + J^\sigma_{M^\sigma}(1n)\,\mathrm{Re}\,I_{M^\rho m}(\varepsilon_{p,M^\rho} + i0^+, p) \\ + J^\kappa_m(1n)\,\mathrm{Re}\,I_{M^\rho M^\sigma}(\varepsilon_{m,q} + i0^+, q)\,, \end{aligned} \tag{B.43}$$

where we have introduced

$$I_{ab}(z;k) \;=\; \int_{q,q_0,l_0} \rho_a(q_0,q)\rho_b(l_0,q+k)\,\frac{\theta(l_0) - \theta(-q_0)}{q_0 + l_0 + z}, \tag{B.44}$$

which is the analytic continuation of the following $T = 0$ integral:

$$I_{ab}(K) \equiv I_{ab}(i\omega;k) = \mu^{2\epsilon}\int \frac{d^dQ}{(2\pi)^d} G_a(Q)G_b(Q+K)\,, \tag{B.45}$$

in the (complex) frequency plane; see Refs. [300, 166] for more details. Note that by definition $I_{ab}(z;k)$ is symmetric under exchange of $a \leftrightarrow b$. Explicit expressions for the thermal parts of the tadpoles can be found in (B.21) and (B.17).
In turn, Eq. (B.45) now enables the definition of the quantities

$$I_{Mm}(0n) \;\equiv\; \mathrm{Re}\,I_{Mm}(\varepsilon_{M,p} + i0^+, p) \tag{B.46}$$

$$I_{M_\rho M_\sigma}(0n) \;\equiv\; \mathrm{Re}\,I_{M_\rho M_\sigma}(\varepsilon_{m,q} + i0^+, q)\,. \tag{B.47}$$

Here, we merely quote the generic result for $\mathrm{Re}\,I_{ab}(\varepsilon_{c,q} + i0^+, q)$, however a detailed derivation alongside a selection of particular sub-cases of interest can be found in appendix C.
We find

$$\begin{aligned} 16\pi^2\,\mathrm{Re}\,I_{ab}(\varepsilon_{c,q} + i0^+, q) \;=\; & \frac{1}{\epsilon} - \frac{1}{2\,c^2}\left(a^2 - b^2\right)\log\left(\frac{a^2}{b^2}\right) + \frac{1}{2}\log\left(\frac{\bar\mu^4}{a^2b^2}\right) + 2 \\ & - \frac{2}{c^2}\begin{cases} -\sqrt{(a+b)^2 - c^2}\sqrt{(a-b)^2 - c^2}\,\tanh^{-1}\left(\frac{\sqrt{(|a|-|b|)^2 - c^2}}{\sqrt{(|a|+|b|)^2 - c^2}}\right) & c^2 \le (|a| - |b|)^2 \\ \sqrt{(|a|+|b|)^2 - c^2}\sqrt{c^2 - (|a|-|b|)^2}\,\tan^{-1}\left(\frac{\sqrt{c^2 - (|a|-|b|)^2}}{\sqrt{(|a|+|b|)^2 - c^2}}\right) & (|a|-|b|)^2 < c^2 < (|a|+|b|)^2 \\ \sqrt{c^2 - (a+b)^2}\sqrt{c^2 - (a-b)^2}\,\tanh^{-1}\left(\frac{\sqrt{c^2 - (|a|+|b|)^2}}{\sqrt{c^2 - (|a|-|b|)^2}}\right) & (|a|+|b|)^2 \le c^2\,. \end{cases} \end{aligned} \tag{B.48}$$

We stress that the result in (B.48) is explicitly q-independent, as it must.

Finding $S^{\kappa\rho\sigma}_{mM^\rho M^\sigma}(2n)$

The last piece to consider is the two thermal factor terms, which we can collect together to obtain

$$\begin{aligned}
S^{\kappa\rho\sigma}_{mM^\rho M^\sigma}(2n) &= -\int_{p_0,p}\rho_{M^\rho}(p_0,p)\varepsilon(p_0)f_{|p_0|+\varepsilon(p_0)(\mu-i\hat{r}_\rho)}\int_{q_0,q}\rho_m(q_0,q)\varepsilon(q_0)n_{|q_0|-\varepsilon(q_0)i\hat{r}_\kappa}\\
&\qquad\times\mathrm{Re}\,G_{M^\sigma}(p_0+q_0+i0^+,|p+q|)\\
&- \int_{p_0,p}\rho_{M^\sigma}(p_0,p)\varepsilon(p_0)f_{|p_0|+\varepsilon(p_0)(\mu-i\hat{r}_\sigma)}\int_{q_0,q}\rho_m(q_0,q)\varepsilon(q_0)n_{|q_0|-\varepsilon(q_0)i\hat{r}_\kappa}\\
&\qquad\times\mathrm{Re}\,G_{M^\rho}(p_0+q_0+i0^+,|p+q|)\\
&+ \int_{p_0,p}\rho_{M^\rho}(p_0,p)\varepsilon(p_0)f_{|p_0|+\varepsilon(p_0)(\mu-i\hat{r}_\rho)}\int_{q_0,q}\rho_{M^\sigma}(q_0,q)\varepsilon(q_0)f_{|q_0|+\varepsilon(q_0)(\mu-i\hat{r}_\sigma)}\\
&\qquad\times\mathrm{Re}\,G_m(p_0+q_0+i0^+,|p+q|)\;. \qquad\text{(B.49)}
\end{aligned}$$

Finally, we can perform the frequency as well as the angular integrals:

$$\begin{aligned}
S^{\kappa\rho\sigma}_{mM^\rho M^\sigma}(2n) &= -\frac{1}{64\pi^4}\sum_{\lambda,\tau\in\{+,-\}}\int_0^\infty dp\frac{p}{\varepsilon_{p,M^\rho}}f_{\varepsilon_{p,M^\rho}+\lambda(\mu-i\hat{r}_\rho)}\int_0^\infty dq\frac{q}{\varepsilon_{m,q}}n_{\varepsilon_{m,q}-i\tau\hat{r}_\kappa}\\
&\qquad\times\mathrm{Re}\,\ln\frac{\varepsilon^2_{p+q,M^\sigma}-\left(\lambda\varepsilon_{p,M^\rho}+\tau\varepsilon_{m,q}+i0^+\right)^2}{\varepsilon^2_{p-q,M^\sigma}-\left(\lambda\varepsilon_{p,M^\rho}+\tau\varepsilon_{m,q}+i0^+\right)^2}\\
&- \frac{1}{64\pi^4}\sum_{\lambda,\tau\in\{+,-\}}\int_0^\infty dp\frac{p}{\varepsilon_{p,M^\sigma}}f_{\varepsilon_{p,M^\sigma}-\lambda(\mu-i\hat{r}_\sigma)}\int_0^\infty dq\frac{q}{\varepsilon_{m,q}}n_{\varepsilon_{m,q}-i\tau\hat{r}_\kappa}\\
&\qquad\times\mathrm{Re}\,\ln\frac{\varepsilon^2_{p+q,M^\rho}-\left(\lambda\varepsilon_{p,M^\sigma}+\tau\varepsilon_{m,q}+i0^+\right)^2}{\varepsilon^2_{p-q,M^\rho}-\left(\lambda\varepsilon_{p,M^\sigma}+\tau\varepsilon_{m,q}+i0^+\right)^2}\\
&+ \frac{1}{64\pi^4}\sum_{\lambda,\tau\in\{+,-\}}\int_0^\infty dp\frac{p}{\varepsilon_{p,M^\rho}}f_{\varepsilon_{p,M^\rho}+\lambda(\mu-i\hat{r}_\rho)}\int_0^\infty dq\frac{q}{\varepsilon_{q,M^\sigma}}f_{\varepsilon_{q,M^\sigma}-\tau(\mu-i\hat{r}_\sigma)}\\
&\qquad\times\mathrm{Re}\,\ln\frac{\varepsilon^2_{m,p+q}-\left(\lambda\varepsilon_{p,M^\rho}+\tau\varepsilon_{q,M^\sigma}+i0^+\right)^2}{\varepsilon^2_{m,p-q}-\left(\lambda\varepsilon_{p,M^\rho}+\tau\varepsilon_{q,M^\sigma}+i0^+\right)^2}\;. \qquad\text{(B.50)}
\end{aligned}$$

Using the explicit formulae in Eq. (B.16)-(B.19), (B.21), (B.24), (B.39), (B.42), (B.43) and (B.50) in Eq. (B.15) finally concludes the computation of the complete quark sunset contribution to the background effective potential.

B.4 Symmetries and Cross-Checks

In this final part we simply collect some basic symmetries and properties displayed by the potential $V_q^{(2)}(r,T,\mu)$ itself as well as some of the entities defined in its derivation. For simplicity and to enlarge the set of allowed symmetries, we restrict to the scenario of color-independent fermion masses. This is because the background r merely enters the expression of the quark sunset contribution in the form of shifts in Matsubara frequencies through scalar products either with roots for bosons, $\pm iT\,r_\alpha$, or with weights for fermions, $\pm iT\,r_\rho$. Most of the symmetries discussed in the follwoing are background induced and rely on the possibility to absorb a shift in the components $r_{3,8}$ by a shift in the color modes,[5] as outlined in section 3.2. This principle globally works since equally the lone color mode-dependence (weights, roots *etc*) of $V_q^{(2)}(r,T,\mu)$ appears in unisono with the background. If however there is a supplementary dependence on these color modes via the fermion masses, most of the subsequent symmetries do no longer hold.

We also point out these symmetries have been proven to be met for the respective one-loop unquenched and two-loop YM terms in Ref. [168, 167], where a more thorough discussion can be found. Thus, they naturally extend to the full potential in Eq. (4.6) and serve as a useful cross-check for our

[5]For instance, a shift in bosonic or fermionic Matsubara frequencies by a multiple of $2\pi T$ can be reabsorbed by a change of the summation variables. Similarly for the expressions in which the Matsubara sums have been explicitly performed. In that case, one deals with the thermal factors $n_{\varepsilon_{m,q}\pm iTr_\alpha}$ or $n_{q\pm iTr_\alpha}$ for bosons or $f_{\varepsilon_{M,q}\pm(\mu-iTr_\rho)}$ for fermions, where the Bose-Einstein and Fermi-Dirac distribution functions are invariant under an imaginary shift of $2\pi T$: $n_{x+2i\pi T}=n_x$, and similarly for f_x.

formulae in the previous section.

Weyl transformations:
To begin, we consider color rotations which preserve the form of the background in Eq. (3.6), called Weyl transformations. In terms of the color modes, they correspond to reflections on axes orthogonal to the roots [167, 301]. In the root-weight diagram displayed in Fig. 3.4, we can see that such reflections lead to permutations of the roots and of weights. In this respect, we remark that the quark-sunset contribution to the potential in Eq. (4.11) features either simple sums over roots κ or weights ρ, or sums over color conserving triplets (σ, ρ, κ) such that $\sigma = \rho + \kappa$. It is easy to check that all Weyl transformation-induced permutations of roots and weights leave either of the types of sums invariant, implying that the potential as a whole remains unchanged.

periodic gauge transformations:
In a similar spirit the potential exhibits an invariance under periodic gauge transformations which protect the background in the form of Eq. (3.6). These transformations are associated to a vector translation of the background $r \to r - 4\pi\alpha'$ for some root α' [167], which results in shifted scalar products

$$r_\alpha \;\to\; r_\alpha - 4\pi\alpha' \cdot \alpha \,, \tag{B.51}$$
$$r_\rho \;\to\; r_\rho - 4\pi\alpha' \cdot \rho \,, \tag{B.52}$$

for bosons and fermions respectively. It is an easy exercise to verify that all of these shifts correspond to multiples of 2π for any combination of roots and weights. Thus, one deduces an invariant quark-sunset contribution in Eq. (4.11).

twisted gauge transformations:
It was shown in Ref. [167] that the pure YM one- and two-loop terms additionally display an invariance under twisted gauge transformations which preserve the background in the form of Eq. (3.6). In analogy to the periodic counterparts in the previous part, the twisted transformations are characterized by a vector translation of the background in the form $r \to r - 4\pi\rho'$ for some weight ρ'. This leads to shifted scalar products as

$$r_\alpha \;\to\; r_\alpha - 4\pi\rho' \cdot \alpha \,, \tag{B.53}$$
$$r_\rho \;\to\; r_\rho - 4\pi\rho' \cdot \rho \,. \tag{B.54}$$

As detailed in the surroundings of Eq. (B.52), the shift in Eq. (B.53) leaves the background potential invariant as it is absorbed as a multiple of 2π. This explains why the YM part of the potential, which solely features products of type r_α, is invariant under twisted gauge transformations. On the other, it is easily checked that the shifts $4\pi\rho' \cdot \rho$ in Eq. (B.54) either yield a value of $4\pi/3$ or $-2\pi/3$. These are not as easily absorbable and the resulting non-invariance of the terms in the quark sector can be interpreted as the manifestation of the explicit breaking of center symmetry.

Roberge-Weiss symmetry:
Given the non-invariance of the quark terms under twisted gauge transformations, one might however remedy the situation upon considering a simultaneous shift in chemical potential. In particular, letting $\mu \to \mu + 2i\pi/3$ yields a global shift in the rescaled (generalized) Matsubara frequency as

$$\beta\hat{\omega}_n^\rho \equiv \beta\hat{\omega}_n + r_\rho + i\mu \;\to\; \beta\hat{\omega}_n + r_\rho + i\mu - 2\pi/3 - \begin{cases} 4\pi/3 \\ -2\pi/3 \end{cases} \tag{B.55}$$

such the total shift can again be absorbed as a multiple of 2π. This is the so-called Roberge-Weiss symmetry.

charge conjugation:
A further significant symmetry of the potential to be discussed is charge conjugation invariance. It is characterized by a simultaneous change of $r \to -r$ and $\mu \to -\mu$. Its invariance is most easily verified in terms of the following identities for the scalar integrals:

$$J_m^\kappa(-r) = J_m^{-\kappa}(r) = J_m^\kappa(r) \,, \tag{B.56}$$
$$\tilde{J}_m^\kappa(-r) = \tilde{J}_m^{-\kappa}(r) = -\tilde{J}_m^\kappa(r) \,, \tag{B.57}$$

$$J_M^\rho(-r,\mu) = J_M^{-\rho}(r,\mu) = J_M^\rho(r,-\mu)\,, \tag{B.58}$$
$$\tilde{J}_M^\rho(-r,\mu) = J_M^{-\rho}(r,\mu) = -\tilde{J}_M^\rho(r,-\mu)\,, \tag{B.59}$$

and

$$S_{mMM}^{\kappa\sigma\rho}(r,\mu) = S_{mMM}^{(-\kappa)(-\sigma)(-\rho)}(-r,\mu) = S_{mMM}^{\kappa\sigma\rho}(r,-\mu)\,. \tag{B.60}$$

complex conjugation:
The final symmetry we explicit is based on complex conjugation and expressed via an invariance of the quark-sunset contribution under a simultaneous transformation of $r \to r^*$ and $\mu \to -\mu^*$. One verifies that

$$J_m^\kappa(r)^* = J_m^\kappa(r^*)\,, \tag{B.61}$$
$$\tilde{J}_m^\kappa(r)^* = \tilde{J}_m^\kappa(r^*)\,, \tag{B.62}$$

$$J_M^\rho(r,\mu)^* = J_M^\rho(r^*,-\mu^*)\,, \tag{B.63}$$
$$\tilde{J}_M^\rho(r,\mu)^* = \tilde{J}_M^\rho(r^*,-\mu^*)\,, \tag{B.64}$$

and

$$S_{mMM}^{\kappa\rho\sigma}(r,\mu)^* = S_{mMM}^{\kappa\rho\sigma}(r^*,-\mu^*)\,, \tag{B.65}$$

upon which the global symmetry for the potential follows. For instance, choosing the background components as $r = (r_3, r_8) \in \mathbb{R}\times\mathbb{R}$ in case of an imaginary chemical potential leads to a real potential. Similarly, it can be checked that the potential remains real at real chemical potential for $r = (r_3, r_8) \in \mathbb{R} \times i\mathbb{R}$, which however also requires the use of complex conjugation, charge conjugation and the Weyl symmetry $r_3 \to -r_3$.

C Derivation of Re $I_{ab}(K)$

In this appendix we detail the computation of the quantity $\mathrm{Re}\, I_{ab}(\varepsilon_{c,q} + i0^+, q)$ which was encountered in the explicit calculation of the one-thermal-factor contribution to the scalar sunset in appendix B.3.3. Therefore, the derivation presented in the following is essential to reducing the intricate quark-sunset structure in Eq. (4.7) to simple and computable analytic expressions. In section C.1 we outline the evaluation of $\mathrm{Re}\, I_{ab}(\varepsilon_{c,q} + i0^+, q)$ in the most general case of real parameters and in C.2 we consider some particular sub-scenarios of physical interest, in some of which the found formulae simplify dramatically.

C.1 Derivation of the general formula

The subsequent derivation operates under the assumption that all masses a, b and c in $\mathrm{Re}\, I_{ab}(\varepsilon_{c,q} + i0^+, q)$ are real. Based on the identification in Eq. (B.45), giving

$$I_{ab}(i\omega; k) \;=\; \mu^{2\epsilon} \int \frac{d^d Q}{(2\pi)^d} G_a(Q) G_b(Q+K)\,, \tag{C.1}$$

it was worked out in Ref. [166, 163] that one can rewrite

$$\mathrm{Re}\, I_{ab}(Q) \;=\; \frac{1}{16\pi^2}\,\mathrm{Re}\left\{\frac{1}{\epsilon} + 2 + \ln\frac{\bar{\mu}^2}{Q^2} - \frac{1}{2}\ln\left(C_{ab}(Q)^2 - \frac{1}{4}\right) + C_{ab}(Q)\,\ln\frac{C_{ab}(Q) - \frac{1}{2}}{C_{ab}(Q) + \frac{1}{2}} + (a \leftrightarrow b)\right\}, \tag{C.2}$$

where eventually one has to replace the four-momentum by $Q^2 = -(c^2 + i0^+)$ and take the real part, such that for instance $\mathrm{Re}\ln\left(\bar{\mu}^2/Q^2\right) \to \ln\left(\bar{\mu}^2/c^2\right)$. In order to similarly capture the correct real parts of the remaining terms, we first have to massage (C.2) some more. We note that the expression in (C.2) is symmetric under exchange of a and b, where the quantity $C_{ab}(Q)$ is given by

$$C_{ab}(Q) = \frac{B_{ab}(Q) + a^2 - b^2}{2Q^2}\,, \tag{C.3}$$

with

$$B_{ab}(Q) = \sqrt{Q^2(Q^2 + 2(a^2+b^2)) + (a^2-b^2)^2}\,. \tag{C.4}$$

For later convenience, it is useful to re-express the C-featuring terms in (C.2) as (for simplicity of notation, we drop the explicit Q-dependence)

$$-\frac{1}{2}\ln\left({C_{ab}}^2 - \frac{1}{4}\right) + (a \leftrightarrow b) \;=\; -\frac{1}{2}\ln\left(C_{ab} - \frac{1}{2}\right)\left(C_{ab} + \frac{1}{2}\right)\left(C_{ba} - \frac{1}{2}\right)\left(C_{ba} + \frac{1}{2}\right), \tag{C.5}$$

$$C_{ab}\,\ln\frac{C_{ab} - \frac{1}{2}}{C_{ab} + \frac{1}{2}} + (a \leftrightarrow b) \;=\; \frac{a^2 - b^2}{2Q^2}\ln\frac{\left(C_{ab} - \frac{1}{2}\right)\left(C_{ba} + \frac{1}{2}\right)}{\left(C_{ab} + \frac{1}{2}\right)\left(C_{ba} - \frac{1}{2}\right)} + \frac{B_{ab}}{2Q^2}\ln\frac{\left(C_{ab} - \frac{1}{2}\right)\left(C_{ba} - \frac{1}{2}\right)}{\left(C_{ab} + \frac{1}{2}\right)\left(C_{ba} + \frac{1}{2}\right)}\,. \tag{C.6}$$

From here, it is easy to check that

$$\left(C_{ab}-\frac{1}{2}\right)\left(C_{ba}+\frac{1}{2}\right) = \frac{B_{ab}^2-(a^2-b^2-Q^2)^2}{4Q^4} = \frac{a^2}{Q^2}\,, \tag{C.7}$$

$$\left(C_{ab}+\frac{1}{2}\right)\left(C_{ba}-\frac{1}{2}\right) = \frac{B_{ab}^2-(b^2-a^2-Q^2)^2}{4Q^4} = \frac{b^2}{Q^2}\,, \tag{C.8}$$

which if applied in (C.5) and (C.6) allows for Eq. (C.2) to be simplified as

$$\mathrm{Re}\, I_{ab}(Q) = \frac{1}{16\pi^2}\,\mathrm{Re}\left\{\frac{1}{\epsilon}+2+\ln\frac{\bar{\mu}^2}{|ab|}+\frac{a^2-b^2}{2Q^2}\ln\frac{a^2}{b^2}+\frac{B_{ab}}{2Q^2}\ln\frac{\left(C_{ab}-\frac{1}{2}\right)\left(C_{ba}-\frac{1}{2}\right)}{\left(C_{ab}+\frac{1}{2}\right)\left(C_{ba}+\frac{1}{2}\right)}\right\}. \tag{C.9}$$

To tackle the last term, after some algebra it can be shown that

$$\left(C_{ab}-\frac{1}{2}\right)\left(C_{ba}-\frac{1}{2}\right) = \frac{1}{2Q^2}\Big[Q^2+a^2+b^2-B_{ab}\Big], \tag{C.10}$$

$$\left(C_{ab}+\frac{1}{2}\right)\left(C_{ba}+\frac{1}{2}\right) = \frac{1}{2Q^2}\Big[Q^2+a^2+b^2+B_{ab}\Big]. \tag{C.11}$$

At this point in the calculation, one needs to be careful since naively taking the real parts with $Q^2 = -(c^2+i0^+)$ might run into branchcuts in the complex Q^2 plane. One way to avoid these subtleties is to identify

$$Q^2+a^2+b^2\mp B_{ab} = \frac{1}{2}\left(\sqrt{Q^2+(a+b)^2}\mp\sqrt{Q^2+(a-b)^2}\right)^2, \tag{C.12}$$

upon which one finds for the expression in (C.9):

$$\begin{aligned}\mathrm{Re}\, I_{ab}(Q) = \frac{1}{16\pi^2}\,\mathrm{Re}\Bigg\{&\frac{1}{\epsilon}+2+\ln\frac{\bar{\mu}^2}{|ab|}+\frac{a^2-b^2}{2Q^2}\ln\frac{a^2}{b^2} \\ &+\frac{\sqrt{Q^2+(a+b)^2}\sqrt{Q^2+(a-b)^2}}{Q^2}\ln\frac{\sqrt{Q^2+(|a|+|b|)^2}-\sqrt{Q^2+(|a|-|b|)^2}}{\sqrt{Q^2+(|a|+|b|)^2}+\sqrt{Q^2+(|a|-|b|)^2}}\Bigg\}.\end{aligned} \tag{C.13}$$

In this form, we are finally in the position to evaluate the real parts. Depending on the relations between the parameters a, b and c, we find different formulae. In particular,

$$\begin{aligned}16\pi^2\ \mathrm{Re}\, I_{ab}(\varepsilon_{c,q}+i0^+,q) = \frac{1}{\epsilon}-\frac{1}{2\,c^2}\left(a^2-b^2\right)\log\left(\frac{a^2}{b^2}\right)+\frac{1}{2}\log\left(\frac{\bar{\mu}^4}{a^2b^2}\right)+2 \\ -\frac{2}{c^2}\begin{cases}-\sqrt{(a+b)^2-c^2}\sqrt{(a-b)^2-c^2}\,\tanh^{-1}\left(\frac{\sqrt{(|a|-|b|)^2-c^2}}{\sqrt{(|a|+|b|)^2-c^2}}\right) & c^2\le(|a|-|b|)^2 \\ \sqrt{(|a|+|b|)^2-c^2}\sqrt{c^2-(|a|-|b|)^2}\,\tan^{-1}\left(\frac{\sqrt{c^2-(|a|-|b|)^2}}{\sqrt{(|a|+|b|)^2-c^2}}\right) & (|a|-|b|)^2<c^2<(|a|+|b|)^2 \\ \sqrt{c^2-(a+b)^2}\sqrt{c^2-(a-b)^2}\,\tanh^{-1}\left(\frac{\sqrt{c^2-(|a|+|b|)^2}}{\sqrt{c^2-(|a|-|b|)^2}}\right) & (|a|+|b|)^2\le c^2\,,\end{cases}\end{aligned} \tag{C.14}$$

which is the expression given in Eq. (B.48).

C.2 Prominent Examples

As an application of the general formula in (C.14), we now give some sub-cases with simplified expressions. The first two are employed in the calculation of the scalar sunset in section B.3.3:

$$\mathrm{Re}\, I_{aa}(\varepsilon_{c,q}+i0^+,q) = \frac{1}{16\pi^2}\left[\frac{1}{\epsilon}+2+\ln\frac{\bar{\mu}^2}{a^2}-2\sqrt{|1-4\frac{a^2}{c^2}|}\begin{cases}\tan^{-1}\sqrt{|1-4\frac{a^2}{c^2}|^{-1}} & 0<c^2<4a^2 \\ \tanh^{-1}\sqrt{|1-4\frac{a^2}{c^2}|} & c^2\ge 4a^2\end{cases}\right],$$

and similarly

$$\begin{aligned}\mathrm{Re}\, I_{ab}(\varepsilon_{b,q}+i0^+,q) &= \frac{1}{16\pi^2}\Bigg[\frac{1}{\epsilon}+2+\ln\frac{\bar{\mu}^2}{b^2}-\frac{a^2}{2b^2}\ln\frac{a^2}{b^2} \\ &\quad + \begin{cases}(-1)\,\frac{a^2}{b^2}\sqrt{4\frac{b^2}{a^2}-1}\ \tan^{-1}\sqrt{4\frac{b^2}{a^2}-1} & 0<\lambda^2<4\\ \frac{a^2}{b^2}\sqrt{1-4\frac{b^2}{a^2}}\ \tanh^{-1}\sqrt{1-4\frac{b^2}{a^2}} & \lambda^2\geq 4\end{cases}\Bigg].\end{aligned} \tag{C.15}$$

It is easily checked that both cases above reduce to the simplest scenarii of

$$\mathrm{Re}\, I_{aa}(\varepsilon_{a,q}+i0^+,q) = \frac{1}{16\pi^2}\left[\frac{1}{\epsilon}+2+\ln\frac{\bar{\mu}^2}{a^2}-\frac{\pi}{\sqrt{3}}\right], \tag{C.16}$$

$$\mathrm{Re}\, I_{a0}(\varepsilon_{0,q}+i0^+,q) = \frac{1}{16\pi^2}\left[\frac{1}{\epsilon}+1+\ln\frac{\bar{\mu}^2}{a^2}\right], \tag{C.17}$$

$$\mathrm{Re}\, I_{00}(\varepsilon_{a,q}+i0^+,q) = \frac{1}{16\pi^2}\left[\frac{1}{\epsilon}+2+\ln\frac{\bar{\mu}^2}{a^2}\right]. \tag{C.18}$$

D

Various limits of the color-degenerate quark-sunset

In this appendix we broadcast a collection of expansions of the quark-sunset contribution $V_q^{(2)}(r,T,\mu)$ in various limits of physical interest. We consider the particular form as given by Eq. (4.18). In the first part, in section D.1, we deal with the most intricate expansion corresponding to large values of temperature and chemical potential. Further we consider the opposite limit of vanishing temperature and density in section D.2. And finally, in section D.3, we treat the atomic nuclei or neutron star situation, in which the temperature goes to zero for a fixed value of chemical potential.

D.1 Taking $\mu, T \to \infty$ while keeping μ/T fixed

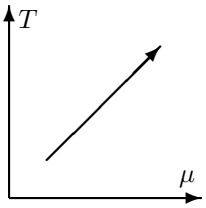

We detail the asymptotics of $V_q^{(2)}(r,T,\mu)$ in the limit of $\mu, T \to \infty$ at a fixed ratio $\hat{\mu} \equiv \mu/T$. The leading behavior is of order $\sim T^4$ and it is convenient to consider the rescaled potential $V_q^{(2)}(r,T,\mu)/T^4$ as a function of $\hat{\mu}$ instead.

The optimal way to proceed is to investigate the asymptotic behavior of the various scalar integrals involved in Eq. (4.18) first. In this respect, we note that the bosonic tadpoles $J_m^\kappa(1n)$ and $\tilde{J}_m^\kappa(1n)$ are by default μ-independent and their expansion is thus equivalent to the pure $T \to \infty$ limit. The respective formulae in this case have been worked out in Ref. [166], which we now recall:

$$J_m^\kappa(1n) \sim \frac{T^2}{2\pi^2} P_2(r_\kappa)\,, \quad \tilde{J}_m^\kappa \sim \frac{T^3}{2\pi^2} P_3(r_\kappa)\,, \tag{D.1}$$

where the P_n's denote the integrals

$$P_{2n+1}(z) \equiv \int_0^\infty dx\, x^{2n}\, \frac{\tilde{n}_{x-iz} - \tilde{n}_{x+iz}}{2i}\,, \tag{D.2}$$

$$P_{2n+2}(z) \equiv \int_0^\infty dx\, x^{2n+1}\, \frac{\tilde{n}_{x-iz} + \tilde{n}_{x+iz}}{2}\,. \tag{D.3}$$

In so doing, we have labelled by $\tilde{n}$ the dimensionless Bose-Einstein distribution function with the temperature formally set to unity. Unlike the formulae presented in Ref. [166], we have opted to not express these integrals in the form of imaginary and real parts, since in the following it is essential to allow for a complex variable z. Written in the form (D.2) and (D.3), the integrals constitute analytic functions of z, unless z is a multiple of 2π. For instance, the functions $P_n(z)$ are analytic over the simply connected open sets $z \in]2\pi n, 2\pi(n+1)[\times\mathbb{R}$ (if considered as subsets of the complex plane) and moreover, for any

$x \in]0, 2\pi[$ a closed form exists as polynomials [253, 166]:

$$P_1(x) = \frac{\pi - x}{2}\,, \tag{D.4}$$

$$P_2(x) = \frac{(\pi - x)^2}{4} - \frac{\pi^2}{12}\,, \tag{D.5}$$

$$P_3(x) = -\frac{(\pi - x)^3}{6} + \frac{\pi^2(\pi - x)}{6}\,, \tag{D.6}$$

$$P_4(x) = -\frac{(\pi - x)^4}{8} + \frac{\pi^2(\pi - x)^2}{4} - \frac{7\pi^4}{120}\,, \ldots \tag{D.7}$$

Naturally, the domain of validity of these polynomial expressions for $P_n(z)$ extends over the entire stripe $]0, 2\pi[\times\mathbb{R}$.[1] Based thereupon, the evaluation of $P_n(z)$ for any z within a different stripe $]2\pi n, 2\pi(n+1)[\times\mathbb{R}$ relies on the periodicity relation $P_n(z + 2\pi) = P_n(z)$. Furthermore, with the sole exception of P_1, all functions P_n are continuous, implying that the respective polynomial expressions are equally applicable on the boundaries of the stripes, in particular at 0 and 2π. On the other hand, this does not hold for $P_1(x)$. However, it can be verified (see below) that the boundary discontinuities of P_1 do not affect the final formula derived for the potential $V_q^{(2)}$ and it is thus permissible to conveniently define $P_1(0)$ and $P_1(2\pi)$ to their respective polynomial values in Eq. (D.4).
In analogy to the bosonic Eqs. (D.2) and (D.3), one might also consider the fermionic integrals:

$$\hat{P}_{2n+1}(z) \equiv -\int_0^\infty dx\, x^{2n}\, \frac{\tilde{f}_{x+iz} - \tilde{f}_{x-iz}}{2i}\,, \tag{D.8}$$

$$\hat{P}_{2n+2}(z) \equiv -\int_0^\infty dx\, x^{2n+1}\, \frac{\tilde{f}_{x+iz} + \tilde{f}_{x-iz}}{2}\,. \tag{D.9}$$

Here, $\tilde{f}$ is the dimensionless Fermi-Dirac distribution with a temperature formally dialed to unity. It satisfies the identity $\tilde{f}_x = -\tilde{n}_{x\pm i\pi}$, which establishes the link

$$\hat{P}_n(z) = P_n(z + \pi)\,. \tag{D.10}$$

It immediately follows that the $\hat{P}_n$'s are polynomials in the stripe $]-\pi, \pi[\times\mathbb{R}$. Alternatively, they can be found from the identity $\tilde{f}_x = \tilde{n}_x - 2\tilde{n}_{2x}$, which yields that

$$\hat{P}_n(z) = \frac{1}{2^{n-1}} P_n(2z) - P_n(z)\,. \tag{D.11}$$

In the limit $T \to \infty$ with $\hat{\mu}$ fixed, it is now an easy deduction to find

$$J_M^\rho(1n) \sim \frac{T^2}{2\pi^2}\hat{P}_2(r_\rho + i\hat{\mu})\,, \quad \tilde{J}_M^\rho \sim \frac{T^3}{2\pi^2}\hat{P}_3(r_\rho + i\hat{\mu})\,. \tag{D.12}$$

Having dealt with all scalar tadpoles, we turn to the two thermal factor contribution of the scalar sunset, $S_{mMM}^{\kappa\rho\sigma}(2n)$. Here, upon rescaling the integration momentum-variables by a factor of T, it is easily argued that $S_{mMM}^{\kappa\rho\sigma}(2n)/T^4 \to 0$ as $T \to \infty$, albeit the value of $\hat{\mu}$.

At this point, we have assembled all necessary ingredients to treat the asymptotic behavior of the full potential in $\lim_{T\to\infty} V_q^{(2)}(r, T, \mu)/T^4$. Clearly, only the products of thermal tadpole contributions give rise to a non-trivial limit and all other terms in Eq. (4.18) vanish.

The piece $[J_{M_f}^\rho(1n) + J_{M_f}^\sigma(1n)]J_m^\kappa(1n)$ leads to

$$\frac{1}{4\pi^4} P_2(r_\kappa)\Big[\hat{P}_2(r_\rho + i\hat{\mu}) + \hat{P}_2(r_\sigma + i\hat{\mu})\Big], \tag{D.13}$$

and similarly for $-J_{M_f}^\rho(1n)J_{M_f}^\sigma(1n)$, which gives

$$-\frac{1}{4\pi^4}\hat{P}_2(r_\rho + i\hat{\mu})\hat{P}_2(r_\sigma + i\hat{\mu})\,. \tag{D.14}$$

[1] In Ref. [166] is specified a recursion relation for the functions $P_n(r)$, which is valid over the complex plane and which allows to alternatively compute $P_n(r)$ directly for $r \in \mathbb{C}$. In this way, it is possible to generate all P_n's by successive integrations of $P_1(r)$. Expanding the thermal factor, one then finds that $P_1(r) = \sum_{k=-\infty}^{\infty}(1 - \delta_{k0})e^{ikr}/2ik = (1/2i)\ln[(1 + e^{-i(r-\pi)})/(1 + e^{i(r-\pi)})] = (1/2i)\ln e^{-i(r-\pi)}$ which equals $(\pi - r)/2$ if the real part of r lies between 0 and 2π.

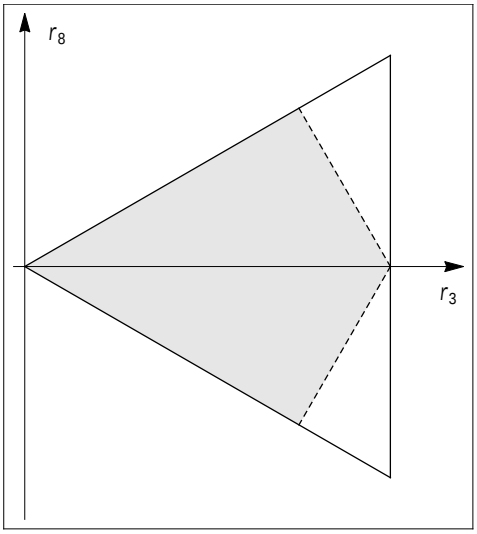

Figure D.1: Inside the fundamental Weyl chamber (equilateral triangle), we show in gray the area over which the polynomial expressions in (D.4)–(D.7) and (D.10) are applicable (under the assumption that one has rewritten the formula for the potential in such a way that only scalar products of the form $r \cdot \alpha^{(j)}$ and $r \cdot \rho^{(j)}$ occur). Moreover, in a quenched scenario the polynomials (D.7) are valid over the entire fundamental Weyl chamber.

Superficially, thermal products of second type tadpoles of the form $\tilde{J}(1n) \times \tilde{J}(1n)$ appear dominant since $\tilde{J}(1n) \sim T^3$. In practice, however, the combination $[\tilde{J}_0^\kappa(1n) - \tilde{J}_m^\kappa(1n)][\tilde{J}_M^\rho(1n) - \tilde{J}_M^\sigma(1n)]/m^2$ in Eq. (4.18) involves a cancellation of the leading T^3 terms of $\tilde{J}_0$ and $\tilde{J}_m$ in the first bracket, such that the overall structure is of the same order as products of first tadpole type. More precisely, for $T \to \infty$ and fixed $\hat{\mu}$,

$$\frac{\tilde{J}_0^\kappa - \tilde{J}_m^\kappa}{m^2} \sim -\left.\frac{d\tilde{J}_m^\kappa}{dm^2}\right|_{m^2=0} = \frac{T}{4\pi^2} P_1(r_\kappa)\,, \tag{D.15}$$

where we have used both the identities

$$\int_Q \omega_n G(Q^\kappa)^2 = -\int_Q \frac{\omega_n}{2q}\frac{d}{dq} G(Q^\kappa) = \int_Q \frac{\omega_n}{2q^2} G(Q^\kappa) \tag{D.16}$$

and called upon the Matsubara sum in Eq. (B.24). Consequently, one identifies the contribution from the term $[\tilde{J}_0^\kappa(1n) - \tilde{J}_m^\kappa(1n)][\tilde{J}_M^\rho(1n) - \tilde{J}_M^\sigma(1n)]/m^2$ as

$$\frac{P_1(r_\kappa)}{8\pi^4}\Big[\hat{P}_3(r_\rho + i\hat{\mu}) - \hat{P}_3(r_\sigma + i\hat{\mu})\Big]. \tag{D.17}$$

Eventually, the asymptotic behavior of the quark-sunset contribution to the potential can be written in the form (a summation over fermionic flavors is implied)

$$\begin{aligned}\lim_{T\to\infty} \frac{V_q^{(2)}(r,T,\mu)}{T^4} \;=\; -\frac{g^2}{2\pi^4}\sum_{\sigma\rho\kappa} \mathcal{D}_{\sigma,\rho\kappa}\Big[&- \hat{P}_2(r_\rho + i\hat{\mu})\hat{P}_2(r_\sigma + i\hat{\mu}) \\ &+ 2P_2(r_\kappa)\hat{P}_2(r_\rho + i\hat{\mu}) \,+\, P_1(r_\kappa)\hat{P}_3(r_\rho + i\hat{\mu})\Big],\end{aligned} \tag{D.18}$$

where we have further simplified the expression calling on $\mathcal{D}_{\sigma,\rho\kappa} = \mathcal{D}_{\rho,\sigma(-\kappa)}$ as well as the even- and oddness of the functions P_{2n} and P_{2n+1} respectively.

D.1.1 Combining with other contributions

It is insightful to add the formula in Eq. (D.18) to the respective counterparts from the one-loop unquenched and one- and two-loop YM contributions. The former, given in Eq. (4.4), has been worked out in Ref. [168], where it was found that at large T and fixed $\hat{\mu}$, the fermion masses are irrelevant and one obtains

$$\lim_{T\to\infty} \frac{V_q^{(1)}(r,T,\mu)}{T^4} = \frac{2N_f}{3\pi^2}\sum_\rho \hat{P}_4(r_\rho + i\hat{\mu})\,. \tag{D.19}$$

Further, the latter have been computed in Refs. [302, 183, 167] as

$$\lim_{T\to\infty} \frac{V_g^{(1)}(r,T)}{T^4} = -\frac{1}{3\pi^2}\sum_\kappa P_4(r_\kappa) \tag{D.20}$$

for the one-loop piece and

$$\lim_{T\to\infty}\frac{V_g^{(2)}(r,T)}{T^4} = \frac{g^2}{4\pi^4}\sum_{\kappa\lambda\tau}\mathcal{C}_{\kappa\lambda\tau}\Big[P_2(r_\kappa)P_2(r_\lambda) + P_1(r_\kappa)P_3(r_\lambda)\Big] \tag{D.21}$$

for the two-loop correction terms. As a remark, we want to stress the apparent similarities in the formulae for the respective glue and quark parts. As a further comment, we point out that these compact expressions can be rewritten more symmetrically by employing the properties of the tensors $\mathcal{C}_{\kappa\lambda\tau}$ and $\mathcal{D}_{\sigma,\rho\kappa}$ as well as of the parity properties of the functions P_n and $\hat{P}_n$. In so doing, it is useful to treat the contributions of zeroes and roots separately, in line with the steps taken in Ref. [167]. Refer to section 3.2.2 for more details on the color modes (zeroes and roots). Eventually, one ends up with

$$\begin{aligned}
\lim_{T\to\infty}\frac{V_g^{(1+2)}(r,T)}{T^4} &= \frac{1}{3\pi^2}\left[d_C P_4(0) + 2{\sum_\alpha}^* P_4(r_\alpha)\right] \\
&+ \frac{g^2}{2\pi^4}{\sum_\alpha}^*\alpha^2\Big\{\big[2P_2(0)+P_2(r_\alpha)\big]P_2(r_\alpha) - P_1(r_\alpha)P_3(r_\alpha)\Big\} \\
&+ \frac{g^2}{\pi^4}{\sum_{\alpha\beta\gamma}}^*\mathcal{C}_{\alpha\beta\gamma}\Big[P_2(r_\alpha)P_2(r_\beta)+P_2(r_\beta)P_2(r_\gamma)+P_2(r_\gamma)P_2(r_\alpha)\Big] \\
&+ \frac{g^2}{2\pi^4}{\sum_{\alpha\beta\gamma}}^*\mathcal{C}_{\alpha\beta\gamma}\Big[P_1(r_\alpha)P_3(r_\beta)+P_1(r_\beta)P_3(r_\gamma)+P_1(r_\gamma)P_3(r_\alpha) \\
&\qquad +P_3(r_\alpha)P_1(r_\beta)+P_3(r_\beta)P_1(r_\gamma)+P_3(r_\gamma)P_1(r_\alpha)\Big],
\end{aligned} \tag{D.22}$$

where we denote by d_C the dimension of the CSA. Also, $\sum_\alpha^*$ sums over all pairs of roots $(\alpha,-\alpha)$ while $\sum_{\alpha\beta\gamma}^*$ sums over all pairs of triplets $((\alpha,\beta,\gamma),(-\alpha,-\beta,-\gamma))$ with $\alpha+\beta+\gamma=0$. In this way, each possible permutation of (α,β,γ) is being counted only once.
In analogy, the quark contribution can be expressed as

$$\begin{aligned}
\lim_{T\to\infty}\frac{V_q^{(1+2)}(r,T,\mu)}{T^4} &= \frac{2N_f}{3\pi^2}\sum_\rho\hat{P}_4(r_\rho+i\hat{\mu}) \\
&- \frac{g^2}{2\pi^4}\sum_\rho\rho^2\Big[2P_2(0)-\hat{P}_2(r_\rho+i\hat{\mu})\Big]\hat{P}_2(r_\rho+i\hat{\mu}) \\
&- \frac{g^2}{\pi^4}{\sum_{\sigma\rho\alpha}}^*\mathcal{D}_{\sigma,\rho\alpha}\Big[P_2(r_\alpha)\hat{P}_2(r_\rho+i\hat{\mu})-\hat{P}_2(r_\rho+i\hat{\mu})\hat{P}_2(r_\sigma+i\hat{\mu}) \\
&\qquad +P_2(r_\alpha)\hat{P}_2(r_\sigma+i\hat{\mu})\Big] \\
&- \frac{g^2}{2\pi^4}{\sum_{\sigma\rho\alpha}}^*\mathcal{D}_{\sigma,\rho\alpha}\Big[P_1(r_\alpha)\hat{P}_3(r_\rho+i\hat{\mu})-P_1(r_\alpha)\hat{P}_3(r_\sigma+i\hat{\mu})\Big],
\end{aligned} \tag{D.23}$$

with $\sum_{\sigma\rho\alpha}^*$ denoting a sum over all pairs of triplets $((\sigma,\rho,\alpha),(\rho,\sigma,-\alpha))$ in agreement with $\sigma=\rho+\alpha$.

Given the formulae in Eqs. (D.22) and (D.23), we insist on the importance of having the scalar products r_α and r_ρ lie in the intervals $\in[0,2\pi]$ and $[-\pi,\pi]$ respectively. This is because an evaluation of the polynomial expressions for the functions P_n in Eqs. (D.4)–(D.7) and for the $\hat{P}_n$ via Eq. (D.10) imposes strict requirements on the range of its input variables. To ensure applicability, one must subtract a sufficient amount of multiples of 2π from r_α and r_ρ. Fortunately, these subtractions leave the integrals (D.2), (D.3), (D.8), and (D.9) invariant. In the following we specify the mechanics of this process, where we restrict to SU(3) and also discuss the pure glue and unquenched situation separately.

In the glue sector, based on the symmetries of the root diagram as shown in Fig. 3.4, it is always possible to rewrite the potential in Eqs. (D.22) and (D.23) solely in explicit dependence on some of the scalar products r_α, for instance the set $r_{\alpha^{(j=1,2,3)}}$, with $\alpha^{(1)}=(1,\sqrt{3})/2$, $\alpha^{(2)}=(1,-\sqrt{3})/2$ and $\alpha^{(3)}=(1,0)$. If we further decompose the background in the form $r=4\pi x_j\rho^{(j)}$, where $\rho^{(1)}=(1,1/\sqrt{3})/2$ and $\rho^{(2)}=(1,-1/\sqrt{3})/2$ are weights of $\mathbf{3}$ and $\bar{\mathbf{3}}$ respectively, the conditions $0<r_{\alpha^{(1,2)}}<2\pi$ become $0<x_{1,2}<1$ since $\alpha^{(j)}\cdot\rho^{(k)}=\delta_{jk}/2$ for $j,k\in\{1,2\}$. Since the values of $4\pi\rho^{(1)}$ and $4\pi\rho^{(2)}$ are identified as two of the edges of the fundamental Weyl chamber, these conditions are satisfied over a region twice as big as this chamber. The third condition reads $0<r_{\alpha^{(3)}}<2\pi$, which is in contrast only satisfied over the

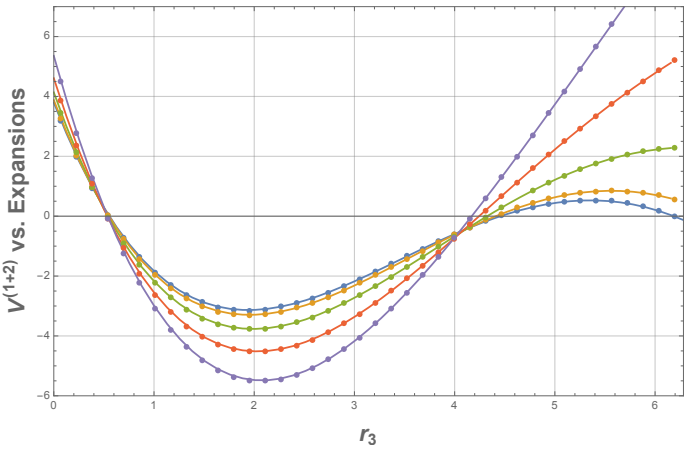

Figure D.2: Comparison of the full potential $V^{(1+2)}(r,T,\mu)$ (dots) against its analytic formulae (solid lines) obtained in the large temperature, $\hat{\mu}$ = fixed limit. The different colors, from blue to purple, correspond to different values of $\hat{\mu} = \{0, 0.5, 1, 1.5, 2\}$. All dots are obtained for a temperature $T = 150m$ (and a degenerate quark mass of 1.9 GeV).

fundamental Weyl chamber itself. It follows that the use of the polynomials (D.4)–(D.7) is justified over the whole Weyl chamber for the pure YM contribution (D.22) under the assumption that it is written in terms of the scalar products $r_{\alpha^{(j)}}$.

In the quark sector, one proceeds in a similar fashion. To begin, it is essential to rewrite the potential in terms of the products $r_{\rho^{(j=1,2,3)}}$, with the same definition of $\rho^{(1,2)}$ as above and $\rho^{(3)} = (0, 1/\sqrt{3})$. In the next step, one identifies the conditions $-\pi < r_{\rho^{(1,2)}} < \pi$ turning into $-1/2 < y_{1,2} < 1/2$, where the numbers y_j constitute the coordinates of r in the basis $\{4\pi\alpha^{(1)}, 4\pi\alpha^{(2)}\}$. Within the fundamental Weyl chamber, these conditions restrict to the shaded area shown in Fig. D.1. Outside this shaded region, it is mandatory to shift either $r_{\rho^{(1)}}$ or $r_{\rho^{(2)}}$ by -2π before using the polynomial expressions. Lastly, the constraint $-\pi < r_{\rho^{(3)}} < \pi$ is fulfilled over the entire fundamental Weyl chamber.

Previously, we have claimed that one actually never encounters the value $P_1(2\pi n)$ in the evaluation of the potential. We are now in the position to outline its underlying reasoning. To this end, assume that $r_\alpha = 2\pi n$. For any $\alpha + \beta + \gamma = 0$, we have $r_\beta = -2\pi n - r_\gamma$ and that the contributions $P_1(r_\alpha)P_3(r_\alpha)$ and $P_1(r_\alpha)(P_3(r_\beta) + P_3(r_\gamma))$ to Eq. (D.22) vanish (because P_3 is periodic and odd), irrespectively of the value of $P_1(2\pi n)$. A similar situation occurs for $\sigma = \rho + \alpha$, which gives that $r_\sigma = r_\rho + 2\pi n$ and it is easily checked that the contribution $P_1(r_\alpha)\hat{P}_3(r_\rho + i\hat{\mu}) - P_1(r_\alpha)\hat{P}_3(r_\sigma + i\hat{\mu})$ to Eq. (D.23) vanishes, irrespectively of the value of $P_1(2\pi n)$.

In the final part, we give some explicit forms for the abstract formulae in Eq. (D.22) and Eq. (D.23), in the reduced situation of vanishing chemical potential such that one can always restrict to the $r_8 = 0$ axis. Up to corrections $\mathcal{O}(g^4)$, we obtain

$$\lim_{T\to\infty} \frac{V_g^{(1+2)}(r,T)}{T^4}\bigg|_{r_8=0} = \frac{135\, r_3^4 - 600\,\pi r_3^3 + 720\,\pi^2 r_3^2 - 256\,\pi^4}{1440\pi^2} + g^2\, \frac{189\, r_3^4 - 912\,\pi r_3^3 + 1584\,\pi^2 r_3^2 - 1152\,\pi^3 r_3 + 256\pi^4}{1536\pi^4}\,, \tag{D.24}$$

and

$$\lim_{T\to\infty} \frac{V_q^{(1+2)}(r,T,\mu=0)}{T^4}\bigg|_{r_8=0} = -\frac{5r_3^4 - 40\pi^2 r_3^2 + 56\pi^4}{480\pi^2} - g^2\, \frac{111 r_3^4 - 264\,\pi r_3^3 - 96\,\pi^2 r_3^2 + 576\,\pi^3 r_3 - 320\pi^4}{4608\pi^4}\,. \tag{D.25}$$

The total potential for $N_f = 1$ is given by

$$\lim_{T\to\infty} \frac{V^{(1+2)}(r,T,\mu=0)}{T^4}\bigg|_{r_8=0} = \frac{15 r_3^4 - 75\,\pi r_3^3 + 105\,\pi^2 r_3^2 - 53\pi^4}{180\pi^2} + g^2\, \frac{57 r_3^4 - 309\,\pi r_3^3 + 606\,\pi^2 r_3^2 - 504\,\pi^3 r_3 + 136\pi^4}{576\pi^4}\,. \tag{D.26}$$

The minimum of the potential in Eq. (D.26) is found as

$$r_3^{\min} = \frac{3g^2}{4\pi} + \mathcal{O}(g^4). \tag{D.27}$$

It is noteworthy that the minimum attains the same value as in the pure Yang-Mills case solely based on Eq. (D.24), which means that unquenching does not affect the high-temperature asymptotics of the Polyakov loop at $\mathcal{O}(g^2)$ for $\mu = 0$.

Finally, we point out that the formulae (93) and (94) of Ref. [167] contain an error which has been corrected in this chapter.

D.2 Taking $\mu, T \to 0$ while keeping μ/T fixed

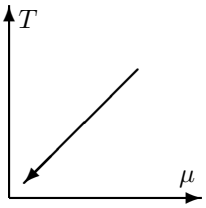

The expansions considered here correspond to the opposite limit as in the previous section. We let $\mu, T \to 0$ while keeping $\hat{\mu} = \mu/T$ fixed. To give some motivation, studying this limit is of interest since there exist to date discrepancies between the findings of analytic approaches as compared to lattice results for the thermodynamic pressure of the system. In particular, the low temperature regime on the lattice is characterized by an exponential suppression [303], whereas in continuum calculations one seems to notoriously end up with a leading T^4 polynomial behavior. This polynomial asymptotics is spearheaded by the presence of the massless ghost modes. These were observed at one-loop order in the CF model [166, 167] and at this point we check if they get modified by the quark sunset contribution.

In the same light as in the previous case, one analyses the scalar integrals and deduces the asymptotic result for the full potential contribution. Doing so, after some simple and non-insightful calculations, one concludes

$$\lim_{T\to 0} \frac{V_q^{(2)}(r,T,\mu)}{T^4} = 0\,, \tag{D.28}$$

which means that there is no correction to the leading ghost loop T^4 (Weiss potential) behavior coming from the fermion sunset in the small temperature regime.[2] While this observation could have been intuited, it still remains a non-trivial check. In fact, it is easy to show that all terms in $\beta^4 V_q^{(2)}$ are exponentially suppressed, either by a term $e^{-\beta m}$ or $e^{-\beta M}$, which is in line with the findings of lattice simulations [303].

D.3 Taking $T \to 0$ while keeping μ fixed

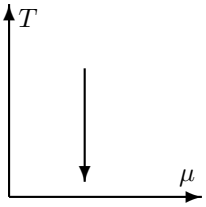

Physically, the limit considered in this part draws inspiration from the situation of atomic nuclei or even the dense cores of neutron stars. In particular, we take $T \to 0$ while simultaneously keeping μ fixed. Similarly to before, we first analyze the individual components, *i.e.*, the scalar integrals, and then assemble the result for the full potential thereafter.

We start by recalling the formulae in Eqs. (B.21) and (B.24), which read for the thermal parts of the first and second fermionic tadpoles

$$J_M^\rho(1n) = -\int_p \frac{f_{\varepsilon_{M,p}-i\hat{r}_\rho+\mu} + f_{\varepsilon_{M,p}+i\hat{r}_\rho-\mu}}{2\varepsilon_{M,p}}\,, \tag{D.29}$$

$$\tilde{J}_M^\rho(1n) = -\int_p \frac{f_{\varepsilon_{M,p}-i\hat{r}_\rho+\mu} - f_{\varepsilon_{M,p}+i\hat{r}_\rho-\mu}}{2i}\,, \tag{D.30}$$

where in the zero temperature limit one identifies $f_{\varepsilon_{M,p}-i\hat{r}_\rho+\mu} \sim e^{-\beta(\varepsilon_{M,p}+\mu)} \to 0$, while on the other hand

$$f_{\varepsilon_{M,p}+i\hat{r}_\rho-\mu} \to \begin{cases} 0 & \varepsilon_{M,p} > \mu \\ \tilde{f}_{ir_\rho} & \varepsilon_{M,p} = \mu \\ 1 & \varepsilon_{M,p} < \mu \end{cases}, \tag{D.31}$$

where we have assumed $M < \mu$ s.t. $\exists\, p^* \in \mathbb{R}^+ : p^* = \sqrt{\mu^2 - M^2}$. Otherwise we have $p^* = 0$ or $p^* \in i\mathbb{R}$ which means that the resulting integrals for the tadpoles vanish. However, since these expressions are

[2] In Refs. [166, 167], a similar observation was made for the respective two-loop glue terms.

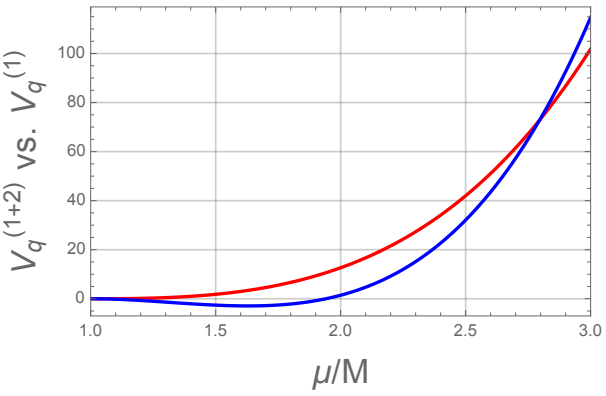

Figure D.3: We plot the one-loop (red) and two-loop (blue) potentials in the limit of vanishing temperature and fixed chemical potential, as a function of μ/M, for a critical three flavor quark mass value of $M \approx 2.19$ GeV, in the scheme CF2. For any $\mu < T$, both curves vanish identically, as explained in the main text.

obtained under the integral and the term $\tilde{f}_{ir_\rho}$ has measure zero, it can be formally dropped and the limiting behavior of Eq. (D.31) essentially reduces to $1 - \Theta(\varepsilon_{M,p} - \mu)$, implying

$$J^\rho_M(1n) \quad \to \quad -\frac{1}{2\pi^2}\int_0^{p^*} \mathrm{d}p\, \frac{p^2}{2\varepsilon_{M,p}} \;=\; \frac{1}{8\pi^2}\Big[-\mu\sqrt{\mu^2-M^2} + M^2 \ln\frac{\sqrt{\mu^2-M^2}+\mu}{M}\Big] \;\equiv\; \mathcal{A}_M(\mu)\,. \tag{D.32}$$

For the second fermionic tadpole we find analogously

$$\tilde{J}^\rho_M(1n) \quad \to \quad \frac{1}{2\pi^2}\int_0^{p^*} \mathrm{d}p\, \frac{p^2}{2i} \;=\; \frac{1}{12\pi^2 i}\big(\mu^2-M^2\big)^{3/2} \;\equiv\; \mathcal{B}_M(\mu)\,. \tag{D.33}$$

We stress that the functions $\mathcal{A}_M(\mu), \mathcal{B}_M(\mu)$ are background independent and merely depend on μ. Further, they are only valid if $M < \mu$, otherwise it must be $\mathcal{A}_M(\mu) = \mathcal{B}_M(\mu) = 0$. Finally, we point out that there exists an alternative (more systematic) approach to obtain these results via taking the formal $T \to 0$ limit as $T\sum_n \to \int_{p_0}$ and subsequent contour integration.

Since both bosonic tadpoles are μ-independent, they vanish in the $T \to 0$ limit, as discussed in the previous section. Therefore, the surviving contributions of the tadpole products are of the form $N_c C_F \mathcal{A}^2_M(\mu)$, where we have used that $\sum_{\sigma\rho\kappa} \mathcal{D}_{\sigma,\rho\kappa} = N_c C_F$.

The last piece to be considered is $S^{\kappa\rho\sigma}_{mMM}(2n)$. In a similar analysis to the one performed above, it is easily shown that all terms involved must vanish unless $M < \mu$. Also, it is not difficult to see that any product of a fermionic and bosonic distribution function must go to zero, which leaves as the only surviving contributions in Eq. (B.50) the products of two fermionic thermal factors. The associated limit is found as

$$S^{\kappa\rho\sigma}_{mM^\rho M^\sigma}(2n) \quad \to \quad \frac{1}{64\pi^4}\int_0^{p^*}\mathrm{d}p\int_0^{q^*}\mathrm{d}q\, \frac{p\,q}{\varepsilon_{m,q}\,\varepsilon_{M,p}}\,\mathrm{Re}\ln\frac{(\varepsilon_{M,q}-\varepsilon_{M,p}+i0^+)^2-\varepsilon^2_{m,p+q}}{(\varepsilon_{M,q}-\varepsilon_{M,p}+i0^+)^2-\varepsilon^2_{m,p-q}}\,, \tag{D.34}$$

where $p^* = q^*$. Clearly, this expression is again background independent and therefore introduces once more a global factor $N_c C_F$ from the color sum.

Finally, collecting together all relevant pieces gives

$$\begin{aligned}\lim_{T\to 0,\,\mu\,\mathrm{fix}} V_q^{(2)}(r,T,\mu) \;&=\; N_c\,\mathrm{tr}\,\mathbb{1}\sum_f M_f^2\,\mathcal{A}_{M_f}(\mu)\left\{\delta Z_{\psi_f} - \frac{\delta M_f}{M_f} + [A_f - B_f](P^2\to -M_f^2)\right\}\\ &+\frac{g^2}{2}N_c C_F\,\mathrm{tr}\mathbb{1}\sum_f\left\{\mathcal{A}^2_{M_f}(\mu) - \frac{m^2+2M_f^2}{64\pi^4}\int_0^{p^*}\mathrm{d}p\int_0^{q^*}\mathrm{d}q\,\frac{p\,q}{\varepsilon_{m,q}\,\varepsilon_{M_f,p}}\,\mathrm{Re}\ln\frac{(\varepsilon_{M_f,q}-\varepsilon_{M_f,p}+i0^+)^2-\varepsilon^2_{m,p+q}}{(\varepsilon_{M_f,q}-\varepsilon_{M_f,p}+i0^+)^2-\varepsilon^2_{m,p-q}}\right\}.\end{aligned}$$

These $\mathcal{O}(g^2)$ corrections can be added to the leading order terms coming from the expression in Eq. (4.4):

$$\lim_{T\to 0,\,\mu\,\mathrm{fix}} V_q^{(1)}(r,T,\mu) \;=\; -\frac{N_c}{48\pi^2}\sum_f\left[2\mu\big(5M_f^2-2\mu^2\big)\sqrt{\mu^2-M_f^2} + 6M_f^4\,\ln\frac{M_f}{\mu+\sqrt{\mu^2-M_f^2}}\right], \tag{D.35}$$

and respective sample results are shown in Fig D.3 for the scheme CF2, as given in Eq. (4.25). Although we remark that an equivalent calculation in the q.o. scheme, defined in Eq. (4.26), has also been performed with virtually non-existent differences. Furtherly, we mention that while the chosen quark mass value (critical for $N_f = 3$) influences the global scale of these curves, their relative shapes seem to be entirely unaffected.

E

2PI Localization in the LdW Gauge

Here, we consider two different formats of the quark propagator, to be used in distinct places of the 2PI potential (6.2). For consistency, in the one-loop terms we stick to the form $S_\rho^{-1} = -i\not{Q}_\rho + B_\rho$, whereas within the sunset we scalarize the quark propagator in the form

$$S_\rho(Q) = B_\rho\, G_{B_\rho}(Q)\,, \tag{E.1}$$

with as usual $G_B(Q) = \frac{1}{B^2+Q^2}$. In both cases we have restricted to propagators diagonal in the Cartan-Weyl basis, see section 6.2 for details. Note that the quark mass functions B_ρ are now weight-dependent. In this way, the 2PI potential reads

$$\Gamma_{\rm 2PI}^{\rm LdW} \;=\; V_g(r,T) - {\rm Tr}\,{\rm Ln}\,S_\rho^{-1} - {\rm Tr}\,S_{0,\rho}^{-1}\,S_\rho + \Phi(S_\rho)\,, \tag{E.2}$$

where the Tr comprises also the sum over weights ρ and flavors f. It is $S_{0,\rho}^{-1} = -i\not{Q}_\rho + M_\rho$, where we adapt an isospin symmetric case, in which all bare masses are chosen as M for all flavors and respective color modes.
Working in an $\overline{\rm MS}$-like scheme,[1] one identifies

$$-{\rm Tr}\,{\rm Ln}\,S_\rho^{-1} \;=\; V_q^{(1)}(r) + \frac{1}{16\pi^2}\sum_{f,\rho} B_\rho^4\left(\frac{3}{2} + \log\frac{\bar\mu^2}{B_\rho^2}\right), \tag{E.3}$$

where the potential $V_q^{(1)}(r)$ was previously encountered in Eq. (4.4), with the difference that the quark masses entering the formulae are now weight-dependent. The supplementary terms are the corresponding vacuum pieces. We further find that

$$-{\rm Tr}\,S_{0,\rho}^{-1}\,S_\rho \;\;\to\;\; -4\sum_{f,\rho} B_\rho M_\rho\, J_{B_\rho}^\rho \tag{E.4}$$

with vacuum contribution

$$-4\sum_{f,\rho} B_\rho M_\rho\, J_{B_\rho}^\rho(0n) \;=\; \frac{1}{4\pi^2}\sum_{f,\rho} B_\rho^3 M_\rho\left(1 + \log\frac{\bar\mu^2}{B_\rho^2}\right), \tag{E.5}$$

and finally

$$\Phi(S_\rho) \;=\; V_q^{(2)}(r)\big|_{S=BG_B} = -6g^2\sum_f\sum_{\sigma\rho\kappa}\mathcal{D}_{\sigma,\rho\kappa}B_\rho B_\sigma\, S^{\kappa\rho\sigma}_{mB_\rho B_\sigma}\,. \tag{E.6}$$

The scalar sunset $S^{\kappa\rho\sigma}_{mB_\rho B_\sigma}$ for different color mode masses is computed in section B.3.3. The variational gap equation for flavor f (flavor index of the B_σ are left implicit) obtained from the potential in Eq. (E.2) by deriving *wrt.* B_σ is of the form

$$0 \;=\; 4\int_P^T \frac{P_\sigma^2 - B_\sigma^2}{(P_\sigma^2+B_\sigma^2)^2}\left[B_\sigma - M_0 - 3\,g^2\sum_{\rho,\kappa}\mathcal{D}_{\sigma,\rho\kappa}\int_Q^T \frac{B_\rho}{B_\rho^2+Q_\rho^2}\frac{1}{K_\kappa^2+m^2}\right], \tag{E.7}$$

[1] It can be shown that the potential in Eq. (E.2) is not renormalizable within the local approximations considered here. Our strategy is thus to drop all $1/\epsilon$ poles in dim. reg. This procedure can be interpreted as being part of the original approximation scheme of the 2PI potential.

where the expression in the square brackets corresponds to Eq. (6.25) with the values of the scalar functions in Δ_ρ set appropriately to agree with our chosen form of the quark propagator in Eq. (E.1).

We stress that the respective contribution from $S^{\kappa\rho\sigma}_{mB_\rho B_\sigma}(2n)$ in Eq. (E.6) faces the same regulator-related challenge as discussed in the section 6.4.3 for the pure Landau gauge counterpart.

We mention that while many solutions to the gap equations $\partial\Gamma^{\mathrm{LdW}}_{\mathrm{2PI}}/\partial r = 0$ and $\partial\Gamma^{\mathrm{LdW}}_{\mathrm{2PI}}/\partial B_\rho = 0$ do in fact exist, none of them are in agreement with the expected pattern of the chiral phase structure as explained in chapter 2. Most solutions do not display any form of chiral restoration or any transition at all. In a few particular scenarii, a second order transition in the chiral limit and at vanishing chemical potential could be identified, however due to the uncontrollable inconsistencies related to the regulator in $S(2n)$ terms, a further analysis was never pursued.

Bibliography

[1] D. J. Gross and F. Wilczek. Ultraviolet Behavior of Nonabelian Gauge Theories. Phys. Rev. Lett., 30:1343–1346, 1973. [,271(1973)].

[2] H. D. Politzer. Reliable Perturbative Results for Strong Interactions? Phys. Rev. Lett., 30:1346–1349, 1973. [,274(1973)].

[3] J. Blumlein, H. Bottcher, and A. Guffanti. Non-singlet QCD analysis of deep inelastic world data at O(alpha(s)**3). Nucl. Phys., B774:182–207, 2007.

[4] K. Nakamura et al. Review of particle physics. J. Phys., G37:075021, 2010.

[5] J. L. Kneur and A. Neveu. $Lambda_{\rm MS}^{\rm QCD}$ from Renormalization Group Optimized Perturbation. Phys. Rev., D85:014005, 2012.

[6] A. Deur, S. J. Brodsky, and G. F. de Teramond. The QCD Running Coupling. Prog. Part. Nucl. Phys., 90:1–74, 2016.

[7] K. G. Wilson. Confinement of quarks. Phys. Rev. D, 10:2445–2459, Oct 1974.

[8] C. Ratti. Lattice QCD and heavy ion collisions: a review of recent progress. Rept. Prog. Phys., 81(8):084301, 2018.

[9] R. Gupta. Introduction to lattice QCD: Course. In Probing the standard model of particle interactions, 1997.

[10] O. Philipsen. Lattice QCD at finite temperature and density. Eur. Phys. J. ST, 152:29–60, 2007.

[11] A. Bazavov et al. Nonperturbative QCD Simulations with 2+1 Flavors of Improved Staggered Quarks. Rev. Mod. Phys., 82:1349–1417, 2010.

[12] C. T. H. Davies et al. High precision lattice QCD confronts experiment. Phys. Rev. Lett., 92:022001, 2004.

[13] F. J. Dyson. The s matrix in quantum electrodynamics. Phys. Rev., 75:1736–1755, Jun 1949.

[14] J. Schwinger. On the green's functions of quantized fields. i. Proceedings of the National Academy of Sciences, 37(7):452–455, 1951.

[15] C. D. Roberts and A. G. Williams. Dyson-Schwinger equations and their application to hadronic physics. Prog. Part. Nucl. Phys., 33:477–575, 1994.

[16] C. S. Fischer. QCD at finite temperature and chemical potential from Dyson-Schwinger equations. Prog. Part. Nucl. Phys., 105:1–60, 2019.

[17] R. Alkofer and L. von Smekal. The Infrared behavior of QCD Green's functions: Confinement dynamical symmetry breaking, and hadrons as relativistic bound states. Phys. Rept., 353:281, 2001.

[18] E. S. Swanson. A Primer on Functional Methods and the Schwinger-Dyson Equations. AIP Conf. Proc., 1296(1):75–121, 2010.

[19] U. Ellwanger, M. Hirsch, and A. Weber. The Heavy quark potential from Wilson's exact renormalization group. Eur. Phys. J., C1:563–578, 1998.

[20] C. Wetterich. Exact evolution equation for the effective potential. Phys. Lett., B301:90–94, 1993.

[21] T. R. Morris. The Exact renormalization group and approximate solutions. Int. J. Mod. Phys., A9:2411–2450, 1994.

[22] J. Polchinski. Renormalization and Effective Lagrangians. Nucl. Phys., B231:269–295, 1984.

[23] J. Berges, N. Tetradis, and C. Wetterich. Nonperturbative renormalization flow in quantum field theory and statistical physics. Phys. Rept., 363:223–386, 2002.

[24] H. Gies. Introduction to the functional RG and applications to gauge theories. Lect. Notes Phys., 852:287–348, 2012.

[25] B. Delamotte. An Introduction to the nonperturbative renormalization group. Lect. Notes Phys., 852:49–132, 2012.

[26] J. M. Pawlowski. Aspects of the functional renormalisation group. Annals Phys., 322:2831–2915, 2007.

[27] J. M. Pawlowski, D. F. Litim, S. Nedelko, and L. von Smekal. Infrared behavior and fixed points in Landau gauge QCD. Phys. Rev. Lett., 93:152002, 2004.

[28] U. Heinz and R. Snellings. Collective flow and viscosity in relativistic heavy-ion collisions. Ann. Rev. Nucl. Part. Sci., 63:123–151, 2013.

[29] U. W. Heinz. The Strongly coupled quark-gluon plasma created at RHIC. J. Phys., A42:214003, 2009.

[30] K. Fukushima and T. Hatsuda. The phase diagram of dense QCD. Rept. Prog. Phys., 74:014001, 2011.

[31] B. Mohanty. STAR experiment results from the beam energy scan program at RHIC. J. Phys., G38:124023, 2011.

[32] H.-T. Ding, F. Karsch, and S. Mukherjee. Thermodynamics of strong-interaction matter from Lattice QCD. Int. J. Mod. Phys., E24(10):1530007, 2015.

[33] M. M. Aggarwal et al. An Experimental Exploration of the QCD Phase Diagram: The Search for the Critical Point and the Onset of De-confinement. 2010.

[34] P. Senger. Nuclear matter physics at NICA. Eur. Phys. J., A52(8):217, 2016.

[35] T. Ablyazimov et al. Challenges in QCD matter physics –The scientific programme of the Compressed Baryonic Matter experiment at FAIR. Eur. Phys. J., A53(3):60, 2017.

[36] T. Sakaguchi. Study of high baryon density QCD matter at J-PARC-HI. Nucl. Phys., A967:896–899, 2017.

[37] S. Weissenborn, I. Sagert, G. Pagliara, M. Hempel, and J. Schaffner-Bielich. Quark Matter In Massive Neutron Stars. Astrophys. J., 740:L14, 2011.

[38] A. Kurkela, E. S. Fraga, J. Schaffner-Bielich, and A. Vuorinen. Constraining neutron star matter with Quantum Chromodynamics. Astrophys. J., 789:127, 2014.

[39] Sz. Borsányi et al. Calculation of the axion mass based on high-temperature lattice quantum chromodynamics. Nature, 539(7627):69–71, 2016.

[40] A. M. Polyakov. Thermal Properties of Gauge Fields and Quark Liberation. Phys. Lett., 72B:477–480, 1978.

[41] G. 't Hooft. On the Phase Transition Towards Permanent Quark Confinement. Nucl. Phys., B138:1–25, 1978.

[42] P. de Forcrand, M. D'Elia, and M. Pepe. A Study of the 't Hooft loop in SU(2) Yang-Mills theory. Phys. Rev. Lett., 86:1438, 2001.

[43] P. Giovannangeli and C. P. Korthals Altes. 't Hooft and Wilson loop ratios in the QCD plasma. Nucl. Phys., B608:203–234, 2001.

[44] H. Reinhardt and D. Epple. The 't Hooft loop in the Hamiltonian approach to Yang-Mills theory in Coulomb gauge. Phys. Rev., D76:065015, 2007.

[45] L. Fister and J. M. Pawlowski. Confinement from Correlation Functions. Phys. Rev., D88:045010, 2013.

[46] K. Kashiwa and R. D. Pisarski. Roberge-Weiss transition and ?t Hooft loops. Phys. Rev., D87(9):096009, 2013.

[47] C. Korthals-Altes, A. Kovner, and Misha A. Stephanov. Spatial 't Hooft loop, hot QCD and Z(N) domain walls. Phys. Lett., B469:205–212, 1999.

[48] B. Svetitsky. Symmetry Aspects of Finite Temperature Confinement Transitions. Phys. Rept., 132:1–53, 1986.

[49] L. Susskind. Lattice Models of Quark Confinement at High Temperature. Phys. Rev., D20:2610–2618, 1979.

[50] S. L. Glashow and S. Weinberg. Breaking chiral symmetry. Phys. Rev. Lett., 20:224–227, 1968.

[51] T. Banks and A. Casher. Chiral Symmetry Breaking in Confining Theories. Nucl. Phys., B169:103–125, 1980.

[52] Y. Aoki, Z. Fodor, S. D. Katz, and K. K. Szabo. The QCD transition temperature: Results with physical masses in the continuum limit. Phys. Lett., B643:46–54, 2006.

[53] M. A. Stephanov. QCD phase diagram: An Overview. PoS, LAT2006:024, 2006.

[54] G. Endrodi, Z. Fodor, S. D. Katz, and K. K. Szabo. The QCD phase diagram at nonzero quark density. JHEP, 04:001, 2011.

[55] M. A. Stephanov, K. Rajagopal, and E. V. Shuryak. Event-by-event fluctuations in heavy ion collisions and the QCD critical point. Phys. Rev., D60:114028, 1999.

[56] R. Alkofer, C. S. Fischer, F. J. Llanes-Estrada, and K. Schwenzer. The Quark-gluon vertex in Landau gauge QCD: Its role in dynamical chiral symmetry breaking and quark confinement. Annals Phys., 324:106–172, 2009.

[57] M. A. Stephanov. QCD phase diagram and the critical point. Prog. Theor. Phys. Suppl., 153:139–156, 2004. [Int. J. Mod. Phys.A20,4387(2005)].

[58] B.-J. Schaefer, J. M. Pawlowski, and J. Wambach. The Phase Structure of the Polyakov–Quark-Meson Model. Phys. Rev., D76:074023, 2007.

[59] Z. Fodor and S. D. Katz. Critical point of QCD at finite T and mu, lattice results for physical quark masses. JHEP, 04:050, 2004.

[60] P. de Forcrand, S. Kim, and O. Philipsen. A QCD chiral critical point at small chemical potential: Is it there or not? PoS, LATTICE2007:178, 2007.

[61] K. Rajagopal and F. Wilczek. Static and dynamic critical phenomena at a second order QCD phase transition. Nucl. Phys., B399:395–425, 1993.

[62] B. Mohanty and J. Serreau. Disoriented chiral condensate: theory and experiment. Phys. Rept., 414:263–358, 2005.

[63] M. A. Stephanov. Non-Gaussian fluctuations near the QCD critical point. Phys. Rev. Lett., 102:032301, 2009.

[64] P. de Forcrand. Simulating QCD at finite density. PoS, LAT2009:010, 2009.

[65] M. D'Elia. High-Temperature QCD: theory overview. Nucl. Phys., A982:99–105, 2019.

[66] Y. Hatta and T. Ikeda. Universality, the QCD critical / tricritical point and the quark number susceptibility. Phys. Rev., D67:014028, 2003.

[67] C. D. Roberts and S. M. Schmidt. Dyson-Schwinger equations: Density, temperature and continuum strong QCD. Prog. Part. Nucl. Phys., 45:S1–S103, 2000.

[68] K. Fukushima and C. Sasaki. The phase diagram of nuclear and quark matter at high baryon density. Prog. Part. Nucl. Phys., 72:99–154, 2013.

[69] P. de Forcrand and O. Philipsen. The QCD phase diagram for small densities from imaginary chemical potential. Nucl. Phys., B642:290–306, 2002.

[70] M. D'Elia and M. Lombardo. Finite density QCD via imaginary chemical potential. Phys. Rev., D67:014505, 2003.

[71] M. D'Elia, S. Mukherjee, and F. Sanfilippo. QCD Phase Transition in a Strong Magnetic Background. Phys. Rev., D82:051501, 2010.

[72] S. Borsányi, Z. Fodor, C. Hoelbling, S. D. Katz, S. Krieg, and K. K. Szabo. Full result for the QCD equation of state with 2+1 flavors. Phys. Lett., B730:99–104, 2014.

[73] L. D. McLerran and B. Svetitsky. Quark Liberation at High Temperature: A Monte Carlo Study of SU(2) Gauge Theory. Phys. Rev., D24:450, 1981.

[74] J. Braun, H. Gies, and J. M. Pawlowski. Quark Confinement from Color Confinement. Phys. Lett., B684:262–267, 2010.

[75] J. Braun, L. M. Haas, F. Marhauser, and J. M. Pawlowski. Phase Structure of Two-Flavor QCD at Finite Chemical Potential. Phys. Rev. Lett., 106:022002, 2011.

[76] C. S. Fischer, L. Fister, J. Luecker, and J. M. Pawlowski. Polyakov loop potential at finite density. Phys. Lett., B732:273–277, 2014.

[77] C. S. Fischer, J. Luecker, and J. M. Pawlowski. Phase structure of QCD for heavy quarks. Phys. Rev., D91(1):014024, 2015.

[78] F. E. Canfora, D. Dudal, I. F. Justo, P. Pais, L. Rosa, and D. Vercauteren. Effect of the Gribov horizon on the Polyakov loop and vice versa. Eur. Phys. J., C75(7):326, 2015.

[79] M. Quandt and H. Reinhardt. Covariant variational approach to Yang-Mills Theory: effective potential of the Polyakov loop. Phys. Rev., D94(6):065015, 2016.

[80] H. Reinhardt, G. Burgio, D. Campagnari, E. Ebadati, J. Heffner, M. Quandt, P. Vastag, and H. Vogt. Hamiltonian approach to QCD in Coulomb gauge - a survey of recent results. Adv. High Energy Phys., 2018:2312498, 2018.

[81] J. I. Kapusta. Quantum Chromodynamics at High Temperature. Nucl. Phys., B148:461–498, 1979.

[82] M. Quandt and H. Reinhardt. A covariant variational approach to Yang-Mills Theory at finite temperatures. Phys. Rev., D92(2):025051, 2015.

[83] U. S. Gupta and V. K. Tiwari. Revisiting the Phase Structure of the Polyakov-quark-meson Model in the presence of Vacuum Fermion Fluctuation. Phys. Rev., D85:014010, 2012.

[84] P. Kovacs, Z. Szep, and G. Wolf. Existence of the critical endpoint in the vector meson extended linear sigma model. Phys. Rev., D93(11):114014, 2016.

[85] R. D. Pisarski and V. V. Skokov. Chiral matrix model of the semi-QGP in QCD. Phys. Rev., D94(3):034015, 2016.

[86] Michael Buballa. NJL model analysis of quark matter at large density. Phys. Rept., 407:205–376, 2005.

[87] R. D. Pisarski. Quark gluon plasma as a condensate of SU(3) Wilson lines. Phys. Rev., D62:111501, 2000.

[88] K. Kashiwa, R. D. Pisarski, and V. V. Skokov. Critical endpoint for deconfinement in matrix and other effective models. Phys. Rev., D85:114029, 2012.

[89] O. Philipsen. Lattice QCD at non-zero temperature and baryon density. In Modern perspectives... Proceedings, Intern. School, 93rd Session, Les Houches, France, 2009, pages 273–330, 2010.

[90] P. de Forcrand and O. Philipsen. The Chiral critical line of N(f) = 2+1 QCD at zero and non-zero baryon density. JHEP, 01:077, 2007.

[91] P. de Forcrand and O. Philipsen. Constraining the QCD phase diagram by tricritical lines at imaginary chemical potential. Phys. Rev. Lett., 105:152001, 2010.

[92] O. Kaczmarek, F. Karsch, E. Laermann, C. Miao, S. Mukherjee, P. Petreczky, C. Schmidt, W. Soeldner, and W. Unger. Phase boundary for the chiral transition in (2+1) -flavor QCD at small values of the chemical potential. Phys. Rev., D83:014504, 2011.

[93] P. Cea, L. Cosmai, M. D'Elia, A. Papa, and F. Sanfilippo. The critical line of two-flavor QCD at finite isospin or baryon densities from imaginary chemical potentials. Phys. Rev., D85:094512, 2012.

[94] P. Cea, L. Cosmai, and A. Papa. Critical line of 2+1 flavor QCD. Phys. Rev., D89(7):074512, 2014.

[95] C. Bonati, P. de Forcrand, M. D'Elia, O. Philipsen, and F. Sanfilippo. Chiral phase transition in two-flavor QCD from an imaginary chemical potential. Phys. Rev., D90(7):074030, 2014.

[96] R. Bellwied, S. Borsányi, Z. Fodor, J. Guenther, S. D. Katz, C. Ratti, and K. K. Szabo. The QCD phase diagram from analytic continuation. Phys. Lett., B751:559–564, 2015.

[97] G. Eichmann, H. Sanchis-Alepuz, R. Williams, R. Alkofer, and C. S. Fischer. Baryons as relativistic three-quark bound states. Prog. Part. Nucl. Phys., 91:1–100, 2016.

[98] J. Braun, L. Fister, J. M. Pawlowski, and F. Rennecke. From Quarks and Gluons to Hadrons: Chiral Symmetry Breaking in Dynamical QCD. Phys. Rev., D94(3):034016, 2016.

[99] C. S. Fischer, J. Luecker, and J. A. Mueller. Chiral and deconfinement phase transitions of two-flavour QCD at finite temperature and chemical potential. Phys. Lett., B702:438–441, 2011.

[100] C. S. Fischer and J. Luecker. Propagators and phase structure of Nf=2 and Nf=2+1 QCD. Phys. Lett., B718:1036–1043, 2013.

[101] C. S. Fischer, J. Luecker, and C. A. Welzbacher. Phase structure of three and four flavor QCD. Phys. Rev., D90(3):034022, 2014.

[102] G. Eichmann, C. S. Fischer, and C. A. Welzbacher. Baryon effects on the location of QCD's critical end point. Phys. Rev., D93(3):034013, 2016.

[103] A. Jakovac, A. Patkos, Z. Szep, and P. Szepfalusy. T - mu phase diagram of the chiral quark model from a large flavor number expansion. Phys. Lett., B582:179–186, 2004.

[104] K. Fukushima. Phase diagrams in the three-flavor Nambu-Jona-Lasinio model with the Polyakov loop. Phys. Rev., D77:114028, 2008. [Erratum: Phys. Rev.D78,039902(2008)].

[105] T. K. Herbst, J. M. Pawlowski, and B.-J. Schaefer. The phase structure of the Polyakov-quark-meson model beyond mean field. Phys. Lett., B696:58–67, 2011.

[106] S. Resch, F. Rennecke, and B.-J. Schaefer. Mass sensitivity of the three-flavor chiral phase transition. Phys. Rev., D99:076005, 2019.

[107] R. D. Pisarski and F. Wilczek. Remarks on the Chiral Phase Transition in Chromodynamics. Phys. Rev., D29:338–341, 1984.

[108] A. Bazavov et al. Equation of state in (2+1)-flavor QCD. Phys. Rev., D90:094503, 2014.

[109] A. Bazavov et al. Equation of state and QCD transition at finite temperature. Phys. Rev., D80:014504, 2009.

[110] L. von Smekal. Universal Aspects of QCD-like Theories. Nucl. Phys. Proc. Suppl., 228:179–220, 2012.

[111] S. Borsányi, Z. Fodor, C. Hoelbling, S. D. Katz, S. Krieg, C. Ratti, and K. K. Szabo. Is there still any T_c mystery in lattice QCD? Results with physical masses in the continuum limit III. JHEP, 09:073, 2010.

[112] F. Cuteri, C. Czaban, O. Philipsen, and A. Sciarra. Updates on the Columbia plot and its extended/alternative versions. EPJ Web Conf., 175:07032, 2018.

[113] I. M. Singer. Some Remarks on the Gribov Ambiguity. Commun. Math. Phys., 60:7–12, 1978.

[114] V. N. Gribov. Quantization of Nonabelian Gauge Theories. Nucl. Phys., B139:1, 1978. [,1(1977)].

[115] H. Neuberger. NONPERTURBATIVE BRS INVARIANCE. Phys. Lett., B175:69–72, 1986.

[116] D. Zwanziger. Renormalizability of the critical limit of lattice gauge theory by BRS invariance. Nucl. Phys., B399:477–513, 1993.

[117] N. Vandersickel and D. Zwanziger. The Gribov problem and QCD dynamics. Phys. Rept., 520:175–251, 2012.

[118] D. Dudal, J. A. Gracey, S. P. Sorella, N. Vandersickel, and H. Verschelde. A Refinement of the Gribov-Zwanziger approach in the Landau gauge: Infrared propagators in harmony with the lattice results. Phys. Rev., D78:065047, 2008.

[119] H. Neuberger. Nonperturbative BRS Invariance and the Gribov Problem. Phys. Lett., B183:337–340, 1987.

[120] D. Zwanziger. Local and Renormalizable Action From the Gribov Horizon. Nucl. Phys., B323:513–544, 1989.

[121] D. Dudal, S. P. Sorella, N. Vandersickel, and H. Verschelde. New features of the gluon and ghost propagator in the infrared region from the Gribov-Zwanziger approach. Phys. Rev., D77:071501, 2008.

[122] D. Zwanziger. Nonperturbative Modification of the Faddeev-popov Formula and Banishment of the Naive Vacuum. Nucl. Phys., B209:336–348, 1982.

[123] D. Zwanziger. Nonperturbative Faddeev-Popov formula and infrared limit of QCD. Phys. Rev., D69:016002, 2004.

[124] D. Zwanziger. Covariant Quantization of Gauge Fields Without Gribov Ambiguity. Nucl. Phys., B192:259, 1981.

[125] D. Kroff and U. Reinosa. Gribov-Zwanziger type model action invariant under background gauge transformations. Phys. Rev., D98(3):034029, 2018.

[126] J. Serreau and M. Tissier. Lifting the Gribov ambiguity in Yang-Mills theories. Phys. Lett., B712:97–103, 2012.

[127] J. Serreau, M. Tissier, and A. Tresmontant. Covariant gauges without Gribov ambiguities in Yang-Mills theories. Phys. Rev., D89:125019, 2014.

[128] J. Serreau, M. Tissier, and A. Tresmontant. Influence of Gribov ambiguities in a class of nonlinear covariant gauges. Phys. Rev., D92:105003, 2015.

[129] G. Curci and R. Ferrari. On a Class of Lagrangian Models for Massive and Massless Yang-Mills Fields. Nuovo Cim., A32:151–168, 1976.

[130] M. Tissier and N. Wschebor. Infrared propagators of Yang-Mills theory from perturbation theory. Phys. Rev., D82:101701, 2010.

[131] M. Tissier and N. Wschebor. An Infrared Safe perturbative approach to Yang-Mills correlators. Phys. Rev., D84:045018, 2011.

[132] U. Reinosa, J. Serreau, M. Tissier, and N. Wschebor. How nonperturbative is the infrared regime of Landau gauge Yang-Mills correlators? Phys. Rev., D96(1):014005, 2017.

[133] Ph. Boucaud, J. P. Leroy, A. Le Yaouanc, J. Micheli, O. Pene, and J. Rodriguez-Quintero. The Infrared Behaviour of the Pure Yang-Mills Green Functions. Few Body Syst., 53:387–436, 2012.

[134] I. L. Bogolubsky, E. M. Ilgenfritz, M. Muller-Preussker, and A. Sternbeck. Lattice gluodynamics computation of Landau gauge Green's functions in the deep infrared. Phys. Lett., B676:69–73, 2009.

[135] F. D. R. Bonnet, P. O. Bowman, D. B. Leinweber, and A. G. Williams. Infrared behavior of the gluon propagator on a large volume lattice. Phys. Rev., D62:051501, 2000.

[136] F. D. R. Bonnet, P. O. Bowman, D. B. Leinweber, A. G. Williams, and J. M. Zanotti. Infinite volume and continuum limits of the Landau gauge gluon propagator. Phys. Rev., D64:034501, 2001.

[137] A. Cucchieri and T. Mendes. Constraints on the IR behavior of the ghost propagator in Yang-Mills theories. Phys. Rev., D78:094503, 2008.

[138] V. G. Bornyakov, V. K. Mitrjushkin, and M. Muller-Preussker. SU(2) lattice gluon propagator: Continuum limit, finite-volume effects and infrared mass scale m(IR). Phys. Rev., D81:054503, 2010.

[139] T. Iritani, H. Suganuma, and H. Iida. Gluon-propagator functional form in the Landau gauge in SU(3) lattice QCD: Yukawa-type gluon propagator and anomalous gluon spectral function. Phys. Rev., D80:114505, 2009.

[140] A. Maas. Describing gauge bosons at zero and finite temperature. Phys. Rept., 524:203–300, 2013.

[141] O. Oliveira and P. J. Silva. The lattice Landau gauge gluon propagator: lattice spacing and volume dependence. Phys. Rev., D86:114513, 2012.

[142] A. Cucchieri and T. Mendes. What's up with IR gluon and ghost propagators in Landau gauge? A puzzling answer from huge lattices. PoS, LATTICE2007:297, 2007.

[143] A. Maas. Two and three-point Green's functions in two-dimensional Landau-gauge Yang-Mills theory. Phys. Rev., D75:116004, 2007.

[144] A. Cucchieri and T. Mendes. Electric and magnetic Landau-gauge gluon propagators in finite-temperature SU(2) gauge theory. PoS, FACESQCD:007, 2010.

[145] A. Cucchieri and T. Mendes. Electric and Magnetic Screening Masses around the Deconfinement Transition. PoS, LATTICE2011:206, 2011.

[146] R. Aouane, V. G. Bornyakov, E. M. Ilgenfritz, V. K. Mitrjushkin, M. Muller-Preussker, and A. Sternbeck. Landau gauge gluon and ghost propagators at finite temperature from quenched lattice QCD. Phys. Rev., D85:034501, 2012.

[147] A. Maas, J. M. Pawlowski, L. von Smekal, and D. Spielmann. The Gluon propagator close to criticality. Phys. Rev., D85:034037, 2012.

[148] P. J. Silva, O. Oliveira, P. Bicudo, and N. Cardoso. Gluon screening mass at finite temperature from the Landau gauge gluon propagator in lattice QCD. Phys. Rev., D89(7):074503, 2014.

[149] J. M. Cornwall. Dynamical Mass Generation in Continuum QCD. Phys. Rev., D26:1453, 1982.

[150] P. Bicudo, D. Binosi, N. Cardoso, O. Oliveira, and P. J. Silva. Lattice gluon propagator in renormalizable ξ gauges. Phys. Rev., D92(11):114514, 2015.

[151] A. C. Aguilar, D. Binosi, and J. Papavassiliou. Gluon and ghost propagators in the Landau gauge: Deriving lattice results from Schwinger-Dyson equations. Phys. Rev., D78:025010, 2008.

[152] D. Dudal, J. A. Gracey, S. P. Sorella, N. Vandersickel, and H. Verschelde. The Landau gauge gluon and ghost propagator in the refined Gribov-Zwanziger framework in 3 dimensions. Phys. Rev., D78:125012, 2008.

[153] C. S. Fischer, A. Maas, and J. M. Pawlowski. On the infrared behavior of Landau gauge Yang-Mills theory. Annals Phys., 324:2408–2437, 2009.

[154] K. Kondo. A low-energy effective Yang-Mills theory for quark and gluon confinement. Phys. Rev., D84:061702, 2011.

[155] S. Strauss, C. S. Fischer, and C. Kellermann. Analytic structure of the Landau gauge gluon propagator. Phys. Rev. Lett., 109:252001, 2012.

[156] P. Watson and H. Reinhardt. Leading order infrared quantum chromodynamics in Coulomb gauge. Phys. Rev., D85:025014, 2012.

[157] M. Q. Huber. Gluon and ghost propagators in linear covariant gauges. Phys. Rev., D91(8):085018, 2015.

[158] F. Gao, S. Qin, C. D. Roberts, and J. Rodriguez-Quintero. Locating the Gribov horizon. Phys. Rev., D97(3):034010, 2018.

[159] D. Dudal, O. Oliveira, and N. Vandersickel. Indirect lattice evidence for the Refined Gribov-Zwanziger formalism and the gluon condensate $\langle A^2 \rangle$ in the Landau gauge. Phys. Rev., D81:074505, 2010.

[160] M. Peláez, M. Tissier, and N. Wschebor. Three-point correlation functions in Yang-Mills theory. Phys. Rev., D88:125003, 2013.

[161] M. Peláez, M. Tissier, and N. Wschebor. Two-point correlation functions of QCD in the Landau gauge. Phys. Rev., D90:065031, 2014.

[162] M. Peláez, M. Tissier, and N. Wschebor. Quark-gluon vertex from the Landau gauge Curci-Ferrari model. Phys. Rev., D92(4):045012, 2015.

[163] U. Reinosa, J. Serreau, M. Tissier, and N. Wschebor. Yang-Mills correlators at finite temperature: A perturbative perspective. Phys. Rev., D89(10):105016, 2014.

[164] J. A. Gracey, M. Peláez, U. Reinosa, and M. Tissier. Two loop calculation of Yang-Mills propagators in the Curci-Ferrari model. Phys. Rev., D100(3):034023, 2019.

[165] U. Reinosa, J. Serreau, M. Tissier, and N. Wschebor. Deconfinement transition in SU(N) theories from perturbation theory. Phys. Lett., B742:61–68, 2015.

[166] U. Reinosa, J. Serreau, M. Tissier, and N. Wschebor. Deconfinement transition in SU(2) Yang-Mills theory: A two-loop study. Phys. Rev., D91:045035, 2015.

[167] U. Reinosa, J. Serreau, M. Tissier, and N. Wschebor. Two-loop study of the deconfinement transition in Yang-Mills theories: SU(3) and beyond. Phys. Rev., D93(10):105002, 2016.

[168] U. Reinosa, J. Serreau, and M. Tissier. Perturbative study of the QCD phase diagram for heavy quarks at nonzero chemical potential. Phys. Rev., D92:025021, 2015.

[169] J. I. Skullerud, P. O. Bowman, A. Kizilersu, D. B. Leinweber, and A. G. Williams. Nonperturbative structure of the quark gluon vertex. JHEP, 04:047, 2003.

[170] M. Peláez, U. Reinosa, J. Serreau, M. Tissier, and N. Wschebor. Small parameters in infrared quantum chromodynamics. Phys. Rev., D96(11):114011, 2017.

[171] M. Laine and A. Vuorinen. Basics of Thermal Field Theory. Lect. Notes Phys., 2016.

[172] J. I. Kapusta. Finite-temperature Field Theory. Cambridge University Press, Cambridge, 1989.

[173] J. I. Kapusta and C. Gale. Finite-Temperature Field Theory: Principles and Applications. Cambridge University Press, Cambridge, 2006.

[174] M. Le Bellac. Thermal Field Theory. Cambridge Monographs on Mathematical Physics. Cambridge University Press, 2011.

[175] L. G. Yaffe and B. Svetitsky. First Order Phase Transition in the SU(3) Gauge Theory at Finite Temperature. Phys. Rev., D26:963, 1982.

[176] B. Svetitsky and L. G. Yaffe. Critical Behavior at Finite Temperature Confinement Transitions. Nucl. Phys., B210:423–447, 1982.

[177] S. Gupta, K. Huebner, and O. Kaczmarek. Polyakov loop in different representations of SU(3) at finite temperature. Nucl. Phys., A785:278–281, 2007.

[178] R. A. Brandt, F. Neri, and M. Sato. Renormalization of Loop Functions for All Loops. Phys. Rev., D24:879, 1981.

[179] O. Jahn and O. Philipsen. The Polyakov loop and its relation to static quark potentials and free energies. Phys. Rev., D70:074504, 2004.

[180] A. Dumitru, Y. Hatta, J. Lenaghan, K. Orginos, and R. D. Pisarski. Deconfining phase transition as a matrix model of renormalized Polyakov loops. Phys. Rev., D70:034511, 2004.

[181] S. L. Adler. Axial-vector vertex in spinor electrodynamics. Phys. Rev., 177:2426–2438, Jan 1969.

[182] G. 't Hooft. Symmetry Breaking Through Bell-Jackiw Anomalies. Phys. Rev. Lett., 37:8–11, 1976. [,226(1976)].

[183] D. J. Gross, R. D. Pisarski, and L. G. Yaffe. QCD and Instantons at Finite Temperature. Rev. Mod. Phys., 53:43, 1981.

[184] C. Vafa and Edward Witten. Restrictions on Symmetry Breaking in Vector-Like Gauge Theories. Nucl. Phys., B234:173–188, 1984.

[185] A. Pich. Chiral perturbation theory. Rept. Prog. Phys., 58:563–610, 1995.

[186] E. Laermann and O. Philipsen. The Status of lattice QCD at finite temperature. Ann. Rev. Nucl. Part. Sci., 53:163–198, 2003.

[187] G. Endrodi, Z. Fodor, S. D. Katz, and K. K. Szabo. The Nature of the finite temperature QCD transition as a function of the quark masses. PoS, LATTICE2007:182, 2007.

[188] P. de Forcrand and O. Philipsen. The QCD phase diagram for three degenerate flavors and small baryon density. Nucl. Phys., B673:170–186, 2003.

[189] F Karsch, E Laermann, and Ch Schmidt. The Chiral critical point in three-flavor QCD. Phys. Lett., B520:41–49, 2001.

[190] A. Bazavov et al. The chiral and deconfinement aspects of the QCD transition. Phys. Rev., D85:054503, 2012.

[191] M. Fromm, J. Langelage, S. Lottini, and O. Philipsen. The QCD deconfinement transition for heavy quarks and all baryon chemical potentials. JHEP, 01:042, 2012.

[192] H. Saito, S. Ejiri, S. Aoki, T. Hatsuda, K. Kanaya, Y. Maezawa, H. Ohno, and T. Umeda. Phase structure of finite temperature QCD in the heavy quark region. Phys. Rev., D84:054502, 2011. [Erratum: Phys. Rev.D85,079902(2012)].

[193] U. M. Heller. Recent progress in finite temperature lattice QCD. PoS, LAT2006:011, 2006.

[194] Y. Aoki, S. Borsányi, S. Durr, Z. Fodor, S. D. Katz, S. Krieg, and K. K. Szabo. The QCD transition temperature: results with physical masses in the continuum limit II. JHEP, 06:088, 2009.

[195] D. H. Rischke. The Quark gluon plasma in equilibrium. Prog. Part. Nucl. Phys., 52:197–296, 2004.

[196] K. Fukushima. Chiral effective model with the Polyakov loop. Phys. Lett., B591:277–284, 2004.

[197] D. Nickel. Inhomogeneous phases in the Nambu-Jona-Lasino and quark-meson model. Phys. Rev., D80:074025, 2009.

[198] F. Cuteri, O. Philipsen, and A. Sciarra. QCD chiral phase transition from noninteger numbers of flavors. Phys. Rev., D97(11):114511, 2018.

[199] S. Aoki, H. Fukaya, and Y. Taniguchi. Chiral symmetry restoration, eigenvalue density of Dirac operator and axial U(1) anomaly at finite temperature. Phys. Rev., D86:114512, 2012.

[200] A. Pelissetto and E. Vicari. Relevance of the axial anomaly at the finite-temperature chiral transition in QCD. Phys. Rev., D88(10):105018, 2013.

[201] M. Grahl and D. H. Rischke. Functional renormalization group study of the two-flavor linear sigma model in the presence of the axial anomaly. Phys. Rev., D88(5):056014, 2013.

[202] A. Butti, A. Pelissetto, and E. Vicari. On the nature of the finite temperature transition in QCD. JHEP, 08:029, 2003.

[203] P. de Forcrand and M. D'Elia. Continuum limit and universality of the Columbia plot. PoS, LATTICE2016:081, 2017.

[204] A. Pelissetto, A. Tripodo, and E. Vicari. Landau-Ginzburg-Wilson approach to critical phenomena in the presence of gauge symmetries. Phys. Rev., D96(3):034505, 2017.

[205] A. Roberge and N. Weiss. Gauge Theories With Imaginary Chemical Potential and the Phases of QCD. Nucl. Phys., B275:734–745, 1986.

[206] C. Bonati, P. de Forcrand, M. D'Elia, O. Philipsen, and F. Sanfilippo. Constraints on the two-flavor QCD phase diagram from imaginary chemical potential. PoS, LATTICE2011:189, 2011.

[207] C. Bonati, G. Cossu, M. D'Elia, and F. Sanfilippo. The Roberge-Weiss endpoint in $N_f = 2$ QCD. Phys. Rev., D83:054505, 2011.

[208] A. Dumitru, R. D. Pisarski, and D. Zschiesche. Dense quarks, and the fermion sign problem, in a SU(N) matrix model. Phys. Rev., D72:065008, 2005.

[209] G. Aarts. Introductory lectures on lattice QCD at nonzero baryon number. J. Phys. Conf. Ser., 706(2):022004, 2016.

[210] R. V. Gavai and S. Gupta. Pressure and nonlinear susceptibilities in QCD at finite chemical potentials. Phys. Rev., D68:034506, 2003.

[211] Sz. Borsányi, G. Endrodi, Z. Fodor, S. D. Katz, S. Krieg, C. Ratti, and K. K. Szabo. QCD equation of state at nonzero chemical potential: continuum results with physical quark masses at order mu^2. JHEP, 08:053, 2012.

[212] A. Bazavov et al. The QCD Equation of State to $\mathcal{O}(\mu_B^6)$ from Lattice QCD. Phys. Rev., D95(5):054504, 2017.

[213] J. N. Guenther, R. Bellwied, S. Borsányi, Z. Fodor, S. D. Katz, A. Pasztor, C. Ratti, and K. K. Szabo. The QCD equation of state at finite density from analytical continuation. Nucl. Phys., A967:720–723, 2017.

[214] J. Langelage and O. Philipsen. The deconfinement transition of finite density QCD with heavy quarks from strong coupling series. JHEP, 01:089, 2010.

[215] L. Haas, R. Stiele, J. Braun, J. Pawlowski, and J. Schaffner-Bielich. Improved Polyakov-loop potential for effective models from functional calculations. Phys. Rev., D87(7):076004, 2013.

[216] P. Costa, M. C. Ruivo, and C. A. de Sousa. Thermodynamics and critical behavior in the Nambu-Jona-Lasinio model of QCD. Phys. Rev., D77:096001, 2008.

[217] P. Kovacs and Zs. Szep. Influence of the isospin and hypercharge chemical potentials on the location of the CEP in the mu(B) - T phase diagram of the SU(3)(L) x SU(3)(R) chiral quark model. Phys. Rev., D77:065016, 2008.

[218] R. Stiele and J. Schaffner-Bielich. Phase diagram and nucleation in the Polyakov-loop-extended Quark-Meson truncation of QCD with the unquenched Polyakov-loop potential. Phys. Rev., D93(9):094014, 2016.

[219] B. W. Mintz, R. Stiele, R. O. Ramos, and J. Schaffner-Bielich. Phase diagram and surface tension in the three-flavor Polyakov-quark-meson model. Phys. Rev., D87(3):036004, 2013.

[220] W. Busza, K. Rajagopal, and W. van der Schee. Heavy Ion Collisions: The Big Picture, and the Big Questions. Ann. Rev. Nucl. Part. Sci., 68:339–376, 2018.

[221] Y. Yin. The QCD critical point hunt: emergent new ideas and new dynamics. 2018.

[222] X. Dong, Y.-J. Lee, and R. Rapp. Open Heavy-Flavor Production in Heavy-Ion Collisions. 2019.

[223] A. Sirunyan et al. Multiparticle correlation studies in pPb collisions at $\sqrt{s_{\mathrm{NN}}}$ = 8.16 TeV. 2019.

[224] A. Ayala, S. Hernandez-Ortiz, and L. A. Hernandez. QCD phase diagram from chiral symmetry restoration: analytic approach at high and low temperature using the Linear Sigma Model with Quarks. Rev. Mex. Fis., 64(3):302–313, 2018.

[225] Z. Cui, J. Zhang, and H. Zong. Proper time regularization and the QCD chiral phase transition. Sci. Rep., 7:45937, 2017.

[226] T. Yokota, T. Kunihiro, and K. Morita. Spectral functions in functional renormalization group approach – analysis of the collective soft modes at the QCD critical point –. In ERG Miramare, Trieste, Italy, September 19-23, 2016, 2016.

[227] G. A. Contrera, A. . Grunfeld, and D. Blaschke. Supporting the search for the CEP location with nonlocal PNJL models constrained by Lattice QCD. Eur. Phys. J., A52(8):231, 2016.

[228] J. Knaute, R. Yaresko, and B. Kaempfer. Holographic QCD phase diagram with critical point from Einstein-Maxwell-dilaton dynamics. Phys. Lett., B778:419–425, 2018.

[229] N. G. Antoniou, F. K. Diakonos, X. N. Maintas, and C. E. Tsagkarakis. Locating the QCD critical endpoint through finite-size scaling. Phys. Rev., D97(3):034015, 2018.

[230] O. Scavenius, A. Mocsy, I. N. Mishustin, and D. H. Rischke. Chiral phase transition within effective models with constituent quarks. Phys. Rev., C64:045202, 2001.

[231] R.-A. Tripolt, L. von Smekal, and J. Wambach. Flow equations for spectral functions at finite external momenta. Phys. Rev., D90(7):074031, 2014.

[232] T. K. Herbst, J. M. Pawlowski, and B.-J. Schaefer. Phase structure and thermodynamics of QCD. Phys. Rev., D88(1):014007, 2013.

[233] M. G. Alford, A. Schmitt, K. Rajagopal, and T. Schaefer. Color superconductivity in dense quark matter. Rev. Mod. Phys., 80:1455–1515, 2008.

[234] I. A. Shovkovy. Two lectures on color superconductivity. Found. Phys., 35:1309–1358, 2005. [,260(2004)].

[235] M. G. Alford, K. Rajagopal, and F. Wilczek. Color flavor locking and chiral symmetry breaking in high density QCD. Nucl. Phys., B537:443–458, 1999.

[236] M. G. Alford. Color superconducting quark matter. Ann. Rev. Nucl. Part. Sci., 51:131–160, 2001.

[237] M. Baldo and L. S. Ferreira. Nuclear liquid-gas phase transition. Phys. Rev. C, 59:682–703, Feb 1999.

[238] J. Pochodzalla et al. Probing the nuclear liquid - gas phase transition. Phys. Rev. Lett., 75:1040–1043, 1995.

[239] J. de Boer, K. Skenderis, P. van Nieuwenhuizen, and A. Waldron. On the renormalizability and unitarity of the Curci-Ferrari model for massive vector bosons. Phys. Lett., B367:175–182, 1996.

[240] G. 't Hooft. A Two-Dimensional Model for Mesons. Nucl. Phys., B75:461–470, 1974.

[241] T. Maskawa and H. Nakajima. Spontaneous Symmetry Breaking in Vector-Gluon Model. Prog. Theor. Phys., 52:1326–1354, 1974.

[242] T. Maskawa and H. Nakajima. Spontaneous Breaking of Chiral Symmetry in a Vector-Gluon Model. 2. Prog. Theor. Phys., 54:860, 1975.

[243] V. A. Miransky. Dynamics of Spontaneous Chiral Symmetry Breaking and Continuum Limit in Quantum Electrodynamics. Nuovo Cim., A90:149–170, 1985.

[244] A. Cucchieri, D. Dudal, T. Mendes, and N. Vandersickel. Massive gluon propagator at zero and finite temperature. 2012.

[245] P. J. Silva and O. Oliveira. The lattice gluon propagator in Landau gauge at zero and finite temperature. 2013. [PoSConfinementX,045(2012)].

[246] F. Canfora, P. Pais, and P. Salgado-Rebolledo. Gribov gap equation at finite temperature. Eur. Phys. J., C74:2855, 2014.

[247] B. S. DeWitt. Quantum Theory of Gravity. 2. The Manifestly Covariant Theory. Phys. Rev., 162:1195–1239, 1967. [,298(1967)].

[248] L. F. Abbott. The Background Field Method Beyond One Loop. Nucl. Phys., B185:189–203, 1981.

[249] L. F. Abbott. Introduction to the Background Field Method. Acta Phys. Polon., B13:33, 1982.

[250] P. M. Lo, B. Friman, and K. Redlich. Polyakov loop fluctuations and deconfinement in the limit of heavy quarks. Phys. Rev., D90(7):074035, 2014.

[251] K. Fukushima and V. Skokov. Polyakov loop modeling for hot QCD. Prog. Part. Nucl. Phys., 96:154–199, 2017.

[252] T. K. Herbst, J. Luecker, and J. M. Pawlowski. Confinement order parameters and fluctuations. 2015.

[253] A. Dumitru, Y. Guo, and C. P. Korthals Altes. Two-loop perturbative corrections to the thermal effective potential in gluodynamics. Phys. Rev., D89(1):016009, 2014.

[254] U. Reinosa. A perturbative approach to the confinement-deconfinement phase transition. EPJ Web Conf., 129:00032, 2016.

[255] K. Fukushima and Y. Hidaka. A Model study of the sign problem in the mean-field approximation. Phys. Rev., D75:036002, 2007.

[256] H. Nishimura, M. C. Ogilvie, and K. Pangeni. Complex saddle points in QCD at finite temperature and density. Phys. Rev., D90(4):045039, 2014.

[257] H. Nishimura, M. C. Ogilvie, and K. Pangeni. Complex Saddle Points and Disorder Lines in QCD at finite temperature and density. Phys. Rev., D91(5):054004, 2015.

[258] A. Folkestad and J. O. Andersen. Thermodynamics and phase diagrams of Polyakov-loop extended chiral models. Phys. Rev., D99(5):054006, 2019.

[259] J. Maelger, U. Reinosa, and J. Serreau. Perturbative study of the QCD phase diagram for heavy quarks at nonzero chemical potential: Two-loop corrections. Phys. Rev., D97(7):074027, 2018.

[260] C. Itzykson and J. B. Zuber. Quantum Field Theory. International Series In Pure and Applied Physics. McGraw-Hill, New York, 1980.

[261] S. Caracciolo, A. Pelissetto, and A. Rago. Two loop critical mass for Wilson fermions. Phys. Rev., D64:094506, 2001.

[262] O. Kaczmarek, F. Karsch, P. Petreczky, and F. Zantow. Heavy quark anti-quark free energy and the renormalized Polyakov loop. Phys. Lett., B543:41–47, 2002.

[263] F. Canfora, A. Giacomini, P. Pais, L. Rosa, and A. Zerwekh. Comments on the compatibility of thermodynamic equilibrium conditions with lattice propagators. Eur. Phys. J., C76(8):443, 2016.

[264] J. Serreau and U. Reinosa. Perturbative aspects of the phase diagram of QCD with heavy quarks. EPJ Web Conf., 137:07024, 2017.

[265] J. Maelger, U. Reinosa, and J. Serreau. Universal aspects of the phase diagram of QCD with heavy quarks. Phys. Rev., D98(9):094020, 2018.

[266] M. Fromm, J. Langelage, S. Lottini, M. Neuman, and O. Philipsen. Phase transitions in heavy-quark QCD from an effective theory. 2012. [J. Phys. Conf. Ser.432,012033(2013)].

[267] P. Cooper and D. Zwanziger. Local QCD Action at Finite Temperature. Phys. Rev., D93(10):105026, 2016.

[268] P. Cooper and D. Zwanziger. Spectral decomposition of the ghost propagator and a necessary condition for confinement. Phys. Rev., D93(10):105024, 2016.

[269] D. Dudal and D. Vercauteren. Gauge copies in the Landau-DeWitt gauge: A background invariant restriction. Phys. Lett., B779:275–282, 2018.

[270] N. Vandersickel. A Study of the Gribov-Zwanziger action: from propagators to glueballs. PhD thesis, Gent U., 2011.

[271] J. Maelger, U. Reinosa, and J. Serreau. Rainbows in the QCD phase diagram. 2019.

[272] B. Lucini and M. Panero. SU(N) gauge theories at large N. Phys. Rept., 526:93–163, 2013.

[273] M. J. Teper. SU(N) gauge theories in (2+1)-dimensions. Phys. Rev., D59:014512, 1999.

[274] G. Eichmann, R. Alkofer, I. C. Cloet, A. Krassnigg, and C. D. Roberts. Perspective on rainbow-ladder truncation. Phys. Rev., C77:042202, 2008.

[275] H. J. Munczek. Dynamical chiral symmetry breaking, Goldstone's theorem and the consistency of the Schwinger-Dyson and Bethe-Salpeter Equations. Phys. Rev., D52:4736–4740, 1995.

[276] P. Maris, C. D. Roberts, and P. C. Tandy. Pion mass and decay constant. Phys. Lett., B420:267–273, 1998.

[277] P. Maris and C. D. Roberts. Dyson-Schwinger equations: A Tool for hadron physics. Int. J. Mod. Phys., E12:297–365, 2003.

[278] S. Qin, L. Chang, Y. Liu, C. D. Roberts, and D. J. Wilson. Investigation of rainbow-ladder truncation for excited and exotic mesons. Phys. Rev., C85:035202, 2012.

[279] C. S. Fischer and R. Alkofer. Nonperturbative propagators, running coupling and dynamical quark mass of Landau gauge QCD. Phys. Rev., D67:094020, 2003.

[280] P. Maris and P. C. Tandy. Bethe-Salpeter study of vector meson masses and decay constants. Phys. Rev., C60:055214, 1999.

[281] J. M. Cornwall, R. Jackiw, and E. Tomboulis. Effective Action for Composite Operators. Phys. Rev., D10:2428–2445, 1974.

[282] H. van Hees and J. Knoll. Renormalization in selfconsistent approximations schemes at finite temperature. 1. Theory. Phys. Rev., D65:025010, 2002.

[283] J.-P. Blaizot, E. Iancu, and U. Reinosa. Renormalization of Phi derivable approximations in scalar field theories. Nucl. Phys., A736:149–200, 2004.

[284] V. Gigante, J. H. Alvarenga Nogueira, E. Ydrefors, C. Gutierrez, V. A. Karmanov, and T. Frederico. Bound state structure and electromagnetic form factor beyond the ladder approximation. Phys. Rev., D95(5):056012, 2017.

[285] E. Ydrefors, J. H. Alvarenga Nogueira, V. A. Karmanov, and T. Frederico. Solving the three-body bound-state Bethe-Salpeter equation in Minkowski space. Phys. Lett., B791:276–280, 2019.

[286] T. Frederico, G. Salmé, and M. Viviani. Quantitative studies of the homogeneous Bethe-Salpeter Equation in Minkowski space. Phys. Rev., D89:016010, 2014.

[287] A. Bender, Craig D. Roberts, and L. Von Smekal. Goldstone theorem and diquark confinement beyond rainbow ladder approximation. Phys. Lett., B380:7–12, 1996.

[288] G. Marko, U. Reinosa, and Z. Szep. O(N) model within the Φ-derivable expansion to order λ^2: On the existence and UV/IR sensitivity of the solutions to self-consistent equations. Phys. Rev., D92(12):125035, 2015.

[289] T. D . Cohen. Functional integrals for QCD at nonzero chemical potential and zero density. Phys. Rev. Lett., 91:222001, 2003.

[290] G. Marko, U. Reinosa, and Z. Szep. Bose-Einstein condensation and Silver Blaze property from the two-loop Φ-derivable approximation. Phys. Rev., D90(12):125021, 2014.

[291] B.-J. Schaefer and J. Wambach. The Phase diagram of the quark meson model. Nucl. Phys., A757:479–492, 2005.

[292] S. Qin, L. Chang, H. Chen, Y. Liu, and C. D. Roberts. Phase diagram and critical endpoint for strongly-interacting quarks. Phys. Rev. Lett., 106:172301, 2011.

[293] A. Jakovac, A. Patkos, Zs. Szep, and P. Szepfalusy. Analytic determination of the T - mu phase diagram of the chiral quark model. Acta Phys. Hung., A22:355–362, 2005.

[294] J. Luecker, C. S. Fischer, L. Fister, and J. M. Pawlowski. Critical Point and Deconfinement from Dyson-Schwinger Equations. PoS, CPOD2013:057, 2013.

[295] F. Karsch, E. Laermann, and A. Peikert. Quark mass and flavor dependence of the QCD phase transition. Nucl. Phys., B605:579–599, 2001.

[296] G. Marko and Zs. Szep. Influence of the Polyakov loop on the chiral phase transition in the two flavor chiral quark model. Phys. Rev., D82:065021, 2010.

[297] S. P. Martin. Evaluation of two loop selfenergy basis integrals using differential equations. Phys. Rev., D68:075002, 2003.

[298] C. Ford and D. R. T. Jones. The Effective potential and the differential equations method for Feynman integrals. Phys. Lett., B274:409–414, 1992. [Erratum: Phys. Lett.B285,399(1992)].

[299] F. A. Berends and J. B. Tausk. On the numerical evaluation of scalar two loop selfenergy diagrams. Nucl. Phys., B421:456–470, 1994.

[300] J.-P. Blaizot and U. Reinosa. Isolating vacuum amplitudes in quantum field calculations at finite temperature. Nucl. Phys., A764:393–422, 2006.

[301] J.-B. Zuber. Invariances in Physics and Group Theory. IRMA Lect. Math. Theor. Phys., 23:307–324, 2015.

[302] N. Weiss. The Effective Potential for the Order Parameter of Gauge Theories at Finite Temperature. Phys. Rev., D24:475, 1981.

[303] J. Engels, F. Karsch, H. Satz, and I. Montvay. Gauge Field Thermodynamics for the SU(2) Yang-Mills System. Nucl. Phys., B205:545–577, 1982.

université PARIS-SACLAY | ÉCOLE DOCTORALE PHENIICS

Titre : Points de vue perturbatifs sur le diagramme de phases de la chromodynamique quantique

Mots clés : Chromodynamique Quantique, Température finie, Densité finie, Confinement, Brisure de symétrie chirale

Résumé : L'étude du diagramme des phases de la Chromodynamique Quantique (QCD) et des transitons associées (déconfinement et restoration de la symétrie chirale) représentent des défis majeurs de la Physique moderne et nombreuses sont les approches théoriques qui visent à en sonder les multiples facettes. Du fait de l'intensité de l'interaction forte dans les régimes d'énergie pertinents pour les transitions susmentionnées, ces approches sont en général de nature nonperturbative, la théorie des perturbations étant réputée inapplicable à ces échelles. Il est, cependant, bien établi que le point de départ de la théorie usuelle des perturbations, basée sur la procédure de fixation de jauge de Faddeev-Popov, est ambigu à ces échelles (ambiguïté de Gribov). Dans ce contexte, une approche perturbative modifiée, basée sur le Lagrangien de Curci et Ferrari, a été proposée, via l'ajout phénoménologique d'un terme de masse effectif pour le gluon en jauge de Landau. Cette approche a été testée avec succès, notamment dans sa capacité à reproduire les fonctions de corrélation de la théorie Yang-Mills (et QCD dans la limite de quarks lourds) et la thermodynamique à temperature et potentiel chimique non nuls.
Dans cette thèse, nous avons testé la robustesse de ces résultats en évaluant la structure de phase de la QCD avec quarks lourds au deuxième ordre de la théorie des perturbations dans le modèle de Curci-Ferrari et en comparant nos résultats à ceux d'approches nonperturbatives. Nos résultats indiquent que, dans ce régime de quarks lourds, le diagramme de phases est contrôlée perturbativement. Nous avons également étendu notre étude au cas de la QCD avec quarks légers en utilisant un schéma de resommation qui exploite la présence de petits paramètres dans le régime infrarouge de la QCD. Dans le secteur des quarks, cette démarche donne lieu à la resommation des fameux diagrammes dits "arc-en-ciel". Ici, nous généralisons ce formalisme à temperature et densité non nulles et en presence d'un champ de fond gluonique. Nous réalisons une toute première étude qualitative des prédictions du modèle CF concernant l'existence possible d'un point critique dans le diagramme de phases de QCD sur la base d'une version simplifiée des équations générales ainsi obtenues.

Title : Perturbative perspectives on the Phase diagram of Quantum ChromoDynamics

Keywords : Quantum Chromodynamics, Finite Temperature, Finite Density, Confinement, Chiral symmetry breaking

Abstract : Unravelling the structure of the QCD phase diagram and its many aspects such as (de)confinement and chiral symmetry breaking, is one of the big challenges of modern theoretical physics, and many approaches have been devised to this aim. Since perturbation theory is believed to cease feasibility at low energy scales, these approaches treat the relevant order parameters, the quark condensate and the Polyakov loop, non-perturbatively. However, it is also well-established that the starting point for perturbation theory, the Fadeev-Popov gauge-fixing procedure, is inherently ill-defined in the infrared due to the presence of Gribov ambiguities. In this context, a modified perturbative approach based on the Curci-Ferrari Lagrangian has been introduced, where a phenomenologically motivated effective gluon mass term is added to the Landau gauge-fixed action. Prior to the beginning of the thesis, this approach has proven extremely fruitful in its descriptions of (unquenched) Yang-Mills correlation functions and thermodynamics at (non)zero temperature and density.
Throughout the thesis we extend this analysis to the entire phase structure of QCD and QCD-like theories and test the validity of the model in various regimes of interest. For instance, to further a previous one-loop study in the regime of heavy quark masses, we have computed the two-loop quark sunset diagram in the presence of a non-trivial gluon background in a finite temperature and density setting. We come to the conclusion that the physics underlying center symmetry is well-described by our perturbative model with a seemingly robust weak-coupling expansion scheme. Furthermore, we study the regime of light quarks by means of a recently proposed resummation scheme which exploits the presence of actual small parameters in the Curci-Ferrari description of infrared QCD. In the quark sector, this leads to the renown rainbow equations. We extend this first-principle setup to non-zero temperature, chemical potential, and gluon background. We perform a first qualitative analysis of the prediction of the model concerning the possible existence of a critical endpoint in the QCD phase diagram by using a simplified version of these general equations.

Université Paris-Saclay
Espace Technologique / Immeuble Discovery
Route de l'Orme aux Merisiers RD 128 / 91190 Saint-Aubin, France